UNIVERSITY OF LEEDS

Modelling Ice Sheets and Sea Level During the Penultimate Deglaciation and the Last Interglacial:
Uncertainty, Sensitivity, and Calibration

Oliver Pollard

The University of Leeds
School of Earth and Environment

December 2023

Submitted in accordance with the requirements for the degree of

Doctor of Philosophy

Intellectual Property

The candidate confirms that the work submitted is his own, except where work which has formed part of jointly authored publications has been included. The contribution of the candidate and the other authors to this work has been explicitly indicated below. The candidate confirms that appropriate credit has been given within the thesis where reference has been made to the work of others.

Research from the publication Pollard et al., 2023, *Quantifying the Uncertainty in the Eurasian Ice-Sheet Geometry at the Penultimate Glacial Maximum (Marine Isotope Stage 6).*, The Cryosphere, 17(11), pp.4751-4777., doi: https://doi.org/10.5194/tc-17-4751-2023, jointly authored with Natasha L.M. Barlow, Lauren Gregoire, Natalya Gomez, Víctor Cartelle, Jeremy C. Ely, Lachlan C. Astfalck, has been included in this thesis as Chapter 3. OGP produced the computational experimental design (alongside NLMB, LJG, NG, and LCA); wrote and executed the code required for preparing the experiments, creating modified shear stress maps, extracting and generating ice-sheet margins, output processing and analytics, and filtering parameter spaces; modified and ran the ICESHEET model, and trained Gaussian processes emulators; visualised and analysed the results and wrote the manuscript with contributions from all other authors (including major contributions from NLMB and LJG). NLMB acquired the funding, was the source of the idea behind the work, supervised the work throughout, provided expertise in palaeo datasets, and made major contributions to the interpretation of results. LJG co-supervised and provided expertise in numerical experimental design, Bayesian uncertainty quantification, ideas for many of the computational solutions developed, majorly contributed to interpretation of results and the subsequent direction of experimental investigation. NG co-supervised and provided expertise in glacial isostatic adjustment, contributed to experimental design decision, and made particular contributions to the treatment of topography. VC expanded the Last Deglaciation Eurasian shear stress map to encompass the region covered by the Penultimate Glacial Maximum Eurasian ice sheet, provided expertise on geomorphological features in the southern North Sea as well as in the design of shear stress modifications. JCE provided the Last Deglaciation Eurasian shear stress

map, shear stress value ranges, and contributed expertise surrounding shear stress, ice-sheet model operation, and experimental design. LCA provided expertise in Bayesian uncertainty quantification, large ensemble experiments, and implausibility metrics.

The work within Chapter 4 was led and undertaken by Oliver G. Pollard and included contributions from Natasha L.M. Barlow, Lauren J. Gregoire, and Natalya Gomez. OGP designed the experiments, ran the model simulations, performed the analysis, produced the figures, and wrote the text. NLMB advised on the Penultimate Deglaciation experimental design, contributed to the interpretation of results, and edited the manuscript. LJG advised on the experimental design and presentation of results. NG provided expertise on glacial isostatic adjustment, contributed to the ideas behind required Python tools, and advised on the focus of the work and results.

The work within Chapter 5 was led and undertaken by Oliver G. Pollard and included contributions from Natasha L.M. Barlow, Lauren Gregoire, and Natalya Gomez. NLMB was the source of the idea behind the work, provided expertise in relative sea-level data, and suggested changes to the text. LJG helped to design the Antarctic parameterisation and suggested changes to the text. NG provided the Deconto Antarctic ice-sheet model data, advised on the experimental design, and provided expertise on parameter ranges.

This PhD thesis has received funding from the European Research Council (ERC) under the European Union's Horizon 2020 research and innovation programme (grant agreement no. 802281) and forms a contribution to the RISeR project. The author has, therefore, benefited from collaboration within the RISeR project, though all work contained within (unless otherwise stated) is his own.

Acknowledgements

First and foremost, I would like to thank my brilliant supervisors, Natasha Barlow, Lauren Gregoire, and Natalya Gomez, for their years of guidance, encouragement, and generosity. I would especially like to thank Tasha for her steadfast support and patience, Lauren for her passion and belief in my work, and Natalya for her enthusiasm and expertise.

I am fortunate to have collaborated with Lachlan Astfalck, Jeremy Ely, and Víctor Cartelle, without whom this work would not have been possible. I would especially like to thank Lachy for his invaluable statistical know-how and grounding advice. I would also like to say a special thank you to Sarah Bradley, Chris Clark, and the research group at Sheffield for sharing their expertise; Amy McGuire, Graham Rush and the RISeR team; and to Ruza Ivanovic for ever-stimulating discussions and honest advice.

Thank you to Yvan Romé, Suzie Robinson, Sam Sherriff-Tadano, Richard Fewster, Violet Patterson, Brooke Snoll, and the rest of the Leeds Climate-Ice research group; and the unforgettable list of characters in Priestley Office 11.06 who kept work a fun and enjoyable place to be.

I could not have completed this thesis without my wonderful and supportive friends; this journey would not have been the same without you.

Finally, thank you to my family for their unwavering care and love, especially to my Mum and Dad, for whom I'm ever grateful. I would like to dedicate this thesis to the memory of my Grandad Bob, who encouraged me to study maths and who, in the face of a challenge, I often think of and smile.

Abstract

Antarctica's contribution to future global mean sea level rise is likely to be significant, and yet the rate, magnitude, and timing of this contribution beyond 2300 is poorly understood as predicted future melt scenarios are outside the window of modern observations. The Last Interglacial period was the last time in Earth's history that the global mean sea level was higher than today, driven, in part, by a smaller than present-day Antarctic ice sheet and could, therefore, provide constraints on scenarios and mechanisms of future ice-sheet melt. The Last Interglacial evolution of Antarctic ice-sheet geometry resulted in a particular global pattern, or fingerprint, of Antarctic-driven sea-level change, subsequently recorded in records of Last Interglacial relative sea levels. Records from certain Eurasia regions may be sensitive to this fingerprint and could be used to help uncover Last Interglacial Antarctic ice-sheet evolution. However, for this analysis, the complex contribution of glacial isostatic adjustment to Eurasian Last Interglacial relative sea-level records must be quantified.

This thesis explores uncertainty in the Penultimate Glacial Maximum and subsequent Penultimate Deglaciation of the Eurasian ice sheet, the predominant driver of Eurasian glacial isostatic adjustment during the Last Interglacial, using a simple, calibrated ice-sheet model, resulting in a Penultimate Glacial Maximum volume of 48 ± 8 m SLE. The sensitivity of Eurasian Last Interglacial relative sea level is quantified with respect to ice-sheet and Earth model uncertainty in which the latter is found to be dominant. A suite of Last Interglacial Antarctic ice-sheet scenarios are developed to determine regional sensitivity to Antarctic ice-sheet changes, revealing a particularly strong influence in Wales, Atlantic, and English Channel regions. Finally, Bayesian history matching is applied to compare a relative sea-level ensemble against a Last Interglacial sea-level database, suggesting an Antarctic ice-sheet melt contribution of 3.2 - 9.3 m (*likely*, 66th percentile). However, when compared against relative sea-level data, none of the modelled scenarios are found to be implausible. More work is needed to constrain the large model-data uncertainties before rates, timings and East vs West contributions of the Antarctic ice sheet during the Last Interglacial can be identified.

Contents

List of Figures

List of Tables

Abbreviations

AIS Antarctic Ice Sheet

EAIS East Antarctic Ice Sheet

EMIC Earth-System Models Of Intermediate Complexity

GCM General Circulation Models

GIA Glacial Isostatic Adjustment

GIN Greenland-Iceland-Norwegian

GMSL Global Mean Sea Level

GNSS Global Navigation Satellite System

GrIS Greenland Ice Sheet

LGM Last Glacial Maximum

LGP Last Glacial Period

LHS Latin Hypercube Sample

LIG Last Interglacial

MIS Marine Isotope Stage

PGM Penultimate Glacial Maximum

PGP Penultimate Glacial Period

PREM Preliminary Reference Earth Model

RCP Representative Concentration Pathway

RSL Relative Sea Level

SLE Sea-level Equivalent

VLM Vertical Land Motion

WAIS West Antarctic Ice Sheet

WALIS World Atlas Of Last Interglacial Shorelines

Chapter 1

Introduction

1.1 Motivation

Climate change-driven global mean sea level (GMSL) rise presents a direct and existential threat to coastal ecosystems, infrastructure, and communities around the world. Current GMSL is rising at a rate of 3.6 mm yr^{-1} and accelerating, driven primarily by anthropogenic forcings (IPCC, 2022). During the 20th century, thermal expansion and glacier melt were the primary sources of GMSL rise, but as polar temperatures continue to rise, ice-sheet melt is becoming the dominant contributor (Gregory et al., 2013). By the year 2300, high greenhouse-gas emission scenarios place plausible GMSL at 2 - 7 m above present day (IPCC, 2022), and cannot rule out the possibility of even higher sea-level rise when poorly understood ice-sheet retreat mechanisms are accounted for (Edwards et al., 2019). Numerical modelling studies have reported that the Antarctic ice sheets may contribute up to 4 m of this projected rise by 2300 (Lowry et al., 2021) but there is a high degree of uncertainty on both the magnitude and timing of contributions predicted by Antarctic ice-sheet simulations (DeConto et al., 2021). Global sea-level change as a result of ice-mass loss is highly spatially variable and the spatial pattern is determined by the sources of ice-sheet melt (Tamisiea et al., 2014). Therefore, constraining the potential location(s) and rate of ice sheet mass loss is essential for making informed predictions about the coastal locations most at risk of sea-level inundation.

Poorly understood mechanisms of ice-sheet retreat under a warming climate are a major source of uncertainty for predictions of long-term ice-sheet melt derived from numerical models, since data describing the response of such mechanisms lie outside of the window of modern observations (Pattyn and Morlighem, 2020; Robel et al.,

2019). However, the present day is far from the only time in Earth's history that the Antarctic ice sheet has been subjected to the effects of a warming climate. By turning to the palaeo record, which contains evidence from previous such warming events, it may be possible to undercover the past response of Antarctica under climate stresses similar to those of today. The most recent such warm period was the Last Interglacial (LIG) (Marine Isotope Stage (MIS) 5e; 130-116 ka) which saw GMSL between 5 - 10 m above that of present-day (IPCC, 2022). Driven by polar temperatures 3 - 5 °C above pre-industrial values (Capron et al., 2014), the LIG was the last time in Earth's history that the Greenland and Antarctic ice sheets were smaller than today (Dutton et al., 2015) and so presents an opportunity to study ice-sheet behaviour under a climate forcing similar to that projected under future emission scenarios (Overland et al., 2014). While the Greenland and Antarctic ice sheets may have been smaller during the LIG, questions remain as to their relative contributions to GMSL change as well as the location and geometry of ice retreat.

Ice-sheet mass changes and global ocean geometry are intrinsically linked via the influence of gravitational, rotational, and glacial isostatic adjustment (GIA) processes, meaning that ice-mass change from a particular ice-sheet will generate a characteristic spatial pattern of sea level, known as a sea-level fingerprint (Mitrovica et al., 2009; Hay et al., 2014). Numerical predictions of sea-level fingerprints have shown that some areas within the Eurasian region are particularly sensitive to ice-mass changes in Antarctica while being relatively insensitive to the effects of Greenland ice-sheet melt, meaning that sea-level records in such regions are well placed to disentangle the LIG contributions of these ice sheets (Barnett et al., 2023). The elevation of former LIG sea levels are recorded in sediments and geology at sites across the Eurasian region (Rovere et al., 2023b) but values recovered from these sites are the combined result of numerous geophysical processes, known collectively as relative sea level (RSL), that must be corrected for in order to isolate the Antarctic fingerprint. Of these processes, the influence of GIA from ice-sheet changes during the Penultimate Glacial Maximum (PGM) is of particular importance to LIG RSL.

In this study, we focus on quantifying uncertainty in the Eurasian ice-sheet evolution, in the model of the solid Earth we use, in the timing of the Penultimate deglaciation, and in their result on northwest Eurasian GIA and RSL. We utilise this information to isolate the Antarctic sea-level fingerprint recorded within LIG RSL records and, as a result, constrain the possible contributions and melt-geometries of Antarctica during the LIG. Uncovering the LIG Antarctic sea-level fingerprint would, therefore, provide insights into the rates, magnitudes, and timings of LIG Antarctic ice-mass loss.

1.1.1 Research Questions

The overall objectives of this thesis can be summarised by the following research questions:

RQ1: Can an uncertainty framework, utilising a simple ice-sheet model, be used to explore the range of uncertainty in ice-sheet geometry during the Penultimate Deglaciation?

RQ2: How much does uncertainty in the ice-sheet and Earth models affect our ability to understand relative sea level during the Last Interglacial?

RQ3: Can a regional Eurasian relative sea-level dataset be used to identify the fingerprint of Antarctic ice-sheet melt during the Last Interglacial?

1.1.2 Research Objectives

In order to investigate these research questions, my thesis research chapters (3, 4, 5) will tackle five identified research objectives (Table 1.1).

Table 1.1: Research objectives and the relevant thesis chapters in which they are applied.

	Objective	Chapter(s)
OBJ1	Generate a range of plausible Eurasian ice-sheet geometries during the Penultimate Deglaciation.	3, 4
OBJ2	Quantify the uncertainty in Eurasian LIG RSL that arises from uncertainties in ice-sheet histories and Earth model inputs.	4
OBJ3	Determine the spatiotemporal sensitivity of Eurasian LIG RSL to parameterisations of ice-sheet and Earth model inputs.	4
OBJ4	Parameterise LIG Antarctic melt scenarios and produce an ensemble of resultant LIG RSL reconstructions in order to explore the sensitivity of the Eurasian LIG RSL to Antarctic fingerprints.	5
OBJ5	Utilise a compilation of sea-level data to produce a best-fitting subset of the Eurasian LIG RSL ensemble and analyse favoured Antarctic melt scenarios.	5

1.2 Review of the Current Literature

1.2.1 The Last Interglacial

1.2.1.1 Climate

The LIG period was characterised by higher sea levels, smaller ice sheets and warmer polar temperatures than present, making it an attractive period of study for the calibration of future warming scenarios and the subject of extensive research (Dutton and Lambeck, 2012). In contrast to the Anthropogenic forcing driving modern-day changes, it is widely agreed upon that the primary driver of LIG surface temperature increases was the particular configuration of Earth's orbit at this time. Berger (1988) first outlined the intrinsic link between orbit and climate on the timescale of glacial-interglacial cycles and Berger and Loutre (1991) calculated that orbital eccentricity during the LIG had a value of almost twice that of modern day. This difference resulted in an increase in incoming solar insolation at the top of the atmosphere for summer months in the Northern Hemisphere (Otto-Bliesner et al., 2013), a pattern that is both stronger in magnitude and which occurred earlier in the interglacial than during the Holocene (Yin and Berger, 2015; Shi et al., 2022). The resulting temperature anomalies have been clearly detected in the extensive global proxy dataset of Turney and Jones (2010), in which 263 ice, marine, and terrestrial sequences were analysed to conclude that average surface temperature during the LIG was 1.5 °C above present. The polar proxy compilation of Capron et al. (2014) reveals an even greater temperature increase at the polar regions of between 3 - 5 °C above present. Numerical modelling efforts have applied Earth-System Models of Intermediate Complexity (EMIC) and, more recently, complex General Circulation Models (GCM) to the reconstruction of LIG climate (Otto-Bliesner et al., 2013; Herold et al., 2012), but, as highlighted in the model-data inter-comparison paper by Lunt et al. (2013), there remains ongoing disagreement between simulated and proxy reconstructions of global average surface temperature anomalies. Despite this, Lunt et al. (2013) found the ensemble of climate models showed clear annual Arctic and summer seasonal Northern Hemispheric warming during the LIG.

1.2.1.2 Sea Level

Accompanying higher surface temperatures, GMSL during the LIG was likely far higher than that of today (Kopp et al., 2009; Dutton and Lambeck, 2012; Dyer et al., 2021), but estimates vary as to the magnitude, timing, and structure of the highstand. Kopp et al. (2009) applied a Bayesian statistical model to a selection of 42 sea-level indicators, including procedures that accounted for vertical land motion

(VLM), to suggest that LIG GMSL reached at least 6.6 m (95% probability), likely exceeded 8 m (67% probability) but was unlikely to have exceeded 9.4 m (33% probability). Dutton and Lambeck (2012) compiled a database of 711 U-Th dated LIG outcrops which, combined with numerical ice-sheet reconstructions based on the work of Lambeck et al. (2006), supported the conclusions of Kopp et al. (2009) to suggest a 5.5 - 9 m highstand. More recently, Dyer et al. (2021) has proposed a lower estimate of 1.2 - 5.3 m by using Bayesian inversion techniques to infer a posterior distribution of GMSL time series from Bahamian RSL records, rekindling the debate on the feasibility of higher magnitude LIG highstand (the highest value of GMSL during the LIG). The IPCC AR6 report assessed it is virtually certain that LIG GMSL was higher than today, and likely 5 - 10 m higher (*medium confidence*) (Fox-Kemper et al., 2021).

While the question of constraining maximum GMSL remains uncertain, there is ongoing debate surrounding the timing of the LIG sea-level highstand as well as the number of highstand peaks that occurred. Far-field records from the Seychelles and Australia, both of which are thought to be reasonably representative of GMSL since they are situated well away from large ice-sheet mass changes, have been interpreted to suggest opposing models of LIG highstand timing. Dutton et al. (2015) analysed sea-level data from Seychelles fossil corals and found that the GMSL maximum had been reached by 128.6 ± 0.8 ka, and similar conclusions were drawn by Dyer et al. (2021) who suggested an early highstand prior to 121 ka and likely prior to 125 ka. However, O'Leary et al. (2013) analysed fossil coral reefs in Western Australia and concluded, in contrast, that a large, late LIG highstand had occurred. In studying LIG sea-level variability, Kopp et al. (2013) combined a global sea-level database with 250 models of GIA to statistically assess the likelihood of inter-LIG GMSL variability and concluded that a double-peaked highstand likely occurred at some point within the LIG accompanied by a 4 m fall in GMSL. By contrast, Barlow et al. (2018) argued that insufficient evidence was available to validate the rapid rates of ice-sheet regrowth required to support a 4 m GMSL fluctuation, and thus a double-peaked highstand, instead suggesting that such patterns could be explained by uncertainties in the GIA modelling. Sea-level records from the Red Sea, with chronologies determined by association with proxy-based age models, have been interpreted by Rohling et al. (2019) to suggest the occurrence of many smaller inter-LIG oscillations. While higher GMSL during the LIG can partially be explained by the contribution of thermal expansion, with McKay et al. (2011) suggesting a contribution of no more than 0.4 ± 0.3 m, all estimates of the LIG highstand point to a sizable contribution from the Greenland Ice Sheet (GrIS) and/or Antarctic Ice Sheet (AIS).

1.2.1.3 Greenland and Antarctic Ice Sheets

The sea-level record points to a substantial GrIS and AIS ice-sheet contribution to LIG GMSL rise but the relative contribution and evolution of each ice sheet remains highly uncertain (Figure 1.1A). The AIS has long been suggested as the most likely contributor of ice-sheet melt, primarily due to the marine-based West Antarctic Ice Sheet (WAIS)'s proposed vulnerability to Southern Ocean warming (Turney et al., 2020; Fogwill et al., 2014; Golledge et al., 2012). Coupled climate-ice simulations by DeConto and Pollard (2016) suggest that the WAIS may have contributed 6 - 7.5 m to GMSL during the early LIG. Clark et al. (2020) suggests a lower contribution of around 3 m but agrees that this was primarily due to an early WAIS collapse between 127 ka and 124 ka, driven by subsurface ocean warming. Pan et al. (2021) demonstrated that post-glacial rebound of bedrock under marine sectors of WAIS may contribute up to an additional 1 m of GMSL rise via water expulsion as the local ocean basin shrinks, and this effect may amplify the estimates of DeConto and Pollard (2016), Clark et al. (2020), and others by up to 30%. The East Antarctic Ice Sheet (EAIS) has typically been assumed to be relatively stable under ocean forcing due to bedrock elevation being mostly above the elevation of the sea surface. Work looking at the modern-day ice sheet has even suggested EAIS ice volume growth in response to temperature forcing since changes in precipitation patterns can cause a positive surface mass balance in the region (Harig and Simons, 2015). However, simulations performed by Fogwill et al. (2014) have shown that changes in Southern-Hemispheric wind patterns could drive local surface warming that can, in turn, drive a 3 - 5 m LIG contribution from EAIS, showing that EAIS stability cannot be assumed in all warming scenarios (Figure 1.1B).

Dynamic ice-sheet modelling of the GrIS was first applied by Letréguilly et al. (1991) whereby a $\delta^{18}O$ derived climate-forcing was used to suggest a 1 - 2 m GrIS contribution to the LIG highstand. A similar conclusion was drawn by Stone et al. (2013) in their work utilising a large ensemble of climate-driven ice-sheet simulations of the GrIS, constrained with Greenland ice-core data, to suggest the Greenland ice sheet likely made a small contribution of 0.6 m (90% probability) to GMSL, and no more than 3.5 m (10% probability). Interpretation of climate-proxy records from ice-core data remains a key source of uncertainty in GrIS modelling and was used by Cuffey and Marshall (2000) to infer a GrIS contribution of up to 5.5 m, and thus a relatively small AIS contribution, via a coupled ice-and-heat flow ice-sheet model (Huybrechts et al., 1991). More recent modelling efforts have utilised data from large GrIS ice-core proxy-data acquisition projects, such as the North Greenland Eemian Ice Drilling (NEEM) (NEEM community members, 2013) and Greenland Ice Sheet Project 2 (GISP2) (Meese et al., 1997), to suggest contributions ranging from 2 - 3.4

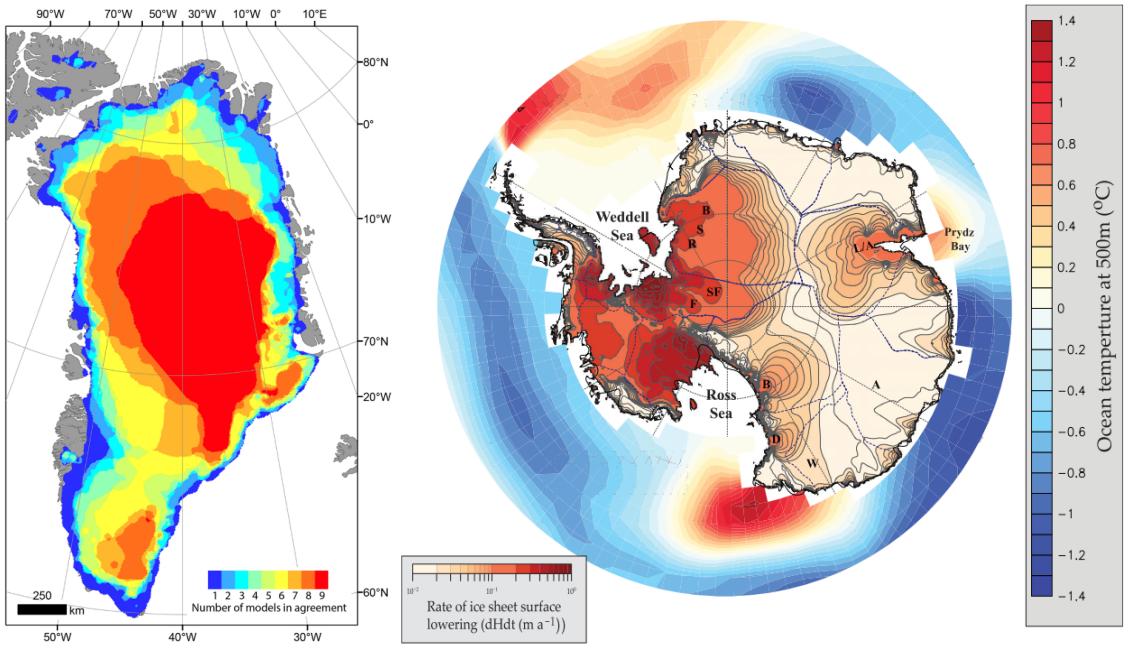

Figure 1.1: (A) Agreement of 9 numerical models of the minimum GrIS configuration during the LIG, including those of (Otto-Bliesner et al., 2006; Yau et al., 2016). Figure from Haywood et al. (2019), Figure 4. (B) Rates of AIS thinning at 135 ka generated from an independent glacial cycle ocean forcing. Also shown are the Southern Ocean temperature anomalies at 500 m depth. Image from Fogwill et al. (2014), Figure 6.

m (Otto-Bliesner et al., 2006), 5.1 m (Yau et al., 2016), and 3 m (Sommers et al., 2021), demonstrating the wide range of disagreement in the configuration of the GrIS and it's contribution to LIG GMSL.

1.2.2 Relative Sea Level

1.2.2.1 Sea-Level Records and Local Processes

While GMSL is a useful quantity for describing large-scale changes to the ocean system, the global pattern of sea level is highly spatially non-uniform and is influenced by processes that act on many spatiotemporal orders of magnitude (Milne et al., 2009; Kemp et al., 2011; Dutton et al., 2015). The value of sea level at a particular location and time is defined as the difference in elevation between the sea surface and the Earth's topography and is referred to as RSL (Gregory et al., 2019). A RSL value, therefore, deviates from GMSL as it represents the summed contribution of all sea-level processes that have acted at that location.

RSL indicators are geological data points which record the elevation of past sea level. A single sea-level index point consists of three components: i) current elevation and geospatial position; ii) the difference between the current elevation and past

RSL; and iii) the age of the indicator (Rovere et al., 2016). Examples of palaeo sea-level indicators include: marine terraces, which may contain sedimentary features or biological indicators that indicate the presence of marine or terrestrial environment (Muhs et al., 2021); coral reef terraces, where species of coral can be used to infer sea-level depth from their expected living-depth range (Pedoja et al., 2018); and beach deposits (Sainz de Murieta et al., 2021). The difference between the present-day elevation of these features compared to the palaeo indicator can be used to infer a RSL, resulting in a value reflecting the influence of numerous geophysical processes.

The geological record has been extensively studied for LIG RSL indicators (Cohen et al., 2022; Rovere et al., 2016). The recently published World Atlas of Last Interglacial Shorelines (WALIS) compilation database by Rovere et al. (2023b) contains over 4500 globally distributed MIS 5e RSL sea-level data points, primarily from geomorphological records such as marine terraces, shoreline angles and tidal notches. Despite their relative abundance, the use of RSL data to draw conclusions about the magnitude and rates of LIG global sea-level change remains inherently difficult due to the influence of local, site-specific, geodynamic processes that cause their sea-level value to deviate from the present day elevation of the indicator. While the influence of a particular process is highly dependent on location, on the timescales of glacial-interglacial cycles four processes are typically dominant in affecting changes in RSL, each of which will be discussed in turn: active tectonics, dynamic topography, sediment isostasy, and GIA (Figure 1.2) (Woodworth et al., 2019; Yokoyama and Purcell, 2021).

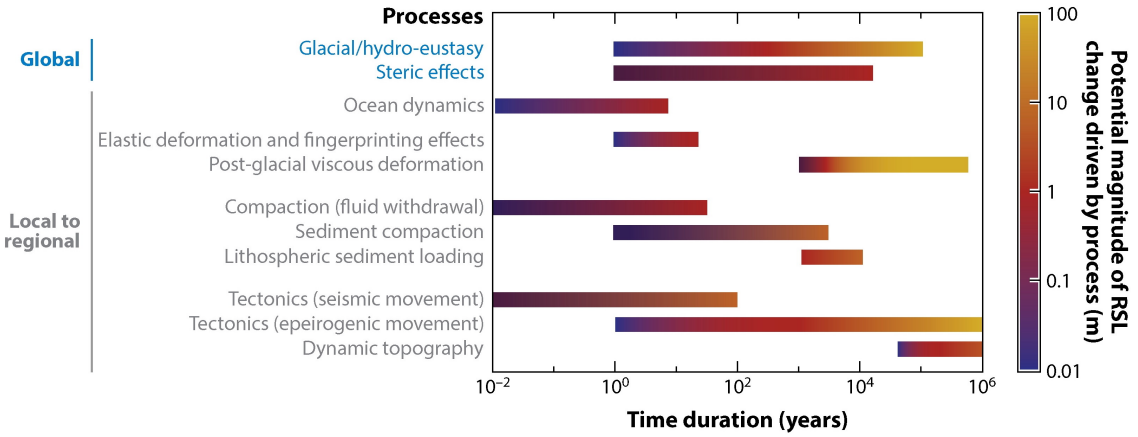

Figure 1.2: The range of processes that can affect RSL values are shown with their magnitude of influence over different timescales. Image from Horton et al. (2018), Figure 1A.

Active tectonics occur on timescales $\mathcal{O}(10^0)$ - $\mathcal{O}(10^6)$ years and result in topographic deformation due to crustal plate movement, and can contribute to RSL in areas close to active plate margins. Pedoja et al. (2011) analysed a compilation of MIS

5e shoreline data above global plate boundaries and found that their elevation, on average, was 45 m above present-day sea level. Studies correcting RSL for use in GMSL estimate often exclude sites suspected of a high active tectonics contribution due to difficulties in isolating the contribution from other processes such as GIA. The work by Simms et al. (2020) found that at terrace formations in southern California, an area of high tectonic activity, the contribution from active tectonics of 0.66 ± 0.2 m ka^{-1} which, for LIG records, represents up to $\sim$ 90 m of VLM that must be accounted for and, more importantly, contributes a significant additional source of uncertainty to corrected RSL indicators. While active tectonics is restricted to plate boundary locations, dynamic topography is the process of topographic deformation that results from mantle flow and can have a global influence on timescales $\mathcal{O}(10^{4.5})$ - $\mathcal{O}(10^{6})$ years (Flament et al., 2013). Austermann et al. (2017) demonstrated that dynamic topography can make a multi-metre contribution to LIG RSL records and corrections have since been applied to records at sites such as Australia (Rovere et al., 2023a) and Madagascar (Stephenson et al., 2019).

Sediment isostasy encompasses two phenomena related to the redistribution of sediment deposits and which act on timescales $\mathcal{O}(10^{0})$ - $\mathcal{O}(10^{4})$ years: subsidence, referring to the local land subsidence that results from the build-up of sediment load; and compaction, which is the effective land lowering that results from sediment reducing in volume (Brain, 2016). Volume reduction can occur *in situ* by processes such as; consolidation, whereby water is expelled from between the sediment grains; self-weight, in which particles viciously rearrange; or by biochemical processes acting on organic sediments (Brain, 2016). Wolstencroft et al. (2014) investigated the role of sediment in controlling subsidence rates in the Mississippi Delta, which is experiencing modern-day sea-level rise of 10 mm yr $^{-1}$, and found that, while sediment loading contributed only a fraction ($\sim$ 0.5 mm yr^{-1}) to the total, the large subsidence rates could likely be explained by significant ongoing sedimentary compaction. The influence of Holocene sediment compaction has been studied and quantified at other river deltas sites across the world, contributing land subsidence rates of up to 20 mm yr $^{-1}$ in the Mekong Delta, Vietnam (Zoccarato et al., 2018), 15 mm yr $^{-1}$ in the Po Delta, Italy (Teatini et al., 2011), and 4.5 mm yr $^{-1}$ in the Nile Delta, Egypt (Marriner et al., 2012). In another study, offshore core data from the southern North Sea show that deltaic sediments deposited by surrounding river basins create a large sediment load, driving rates of subsidence of up to 3 mm yr^{-1} since the LIG (Cohen et al., 2022). However, this is minor compared to the final and most influential vertical-land deformation process driving RSL change at sites close to former ice-sheet loads, GIA.

1.2.2.2 Glacial Isostatic Adjustment

Over the timescales of glacial-interglacial cycles, the primary driver of RSL spatial variability is GIA (Whitehouse, 2018; Farrell and Clark, 1976). More accurately, GIA refers to a collection of geophysical processes that result in ice and water mass changes and which drive the complex feedback between ocean water volume, perturbations of the Earth's rotational axis, Earth's gravitational field, and viscoelastic deformation of the solid Earth (Milne and Mitrovica, 1998; Mitrovica and Milne, 2003). The effects of GIA in regions under previous ice-sheet loads are so pronounced that positive rates of VLM of greater than 10 mm yr^{-1}, driven by ice-sheet changes during the Last Deglaciation, continue to this day. Such rates are so high that they can be observed on human timescales without sophisticated scientific measurements (Whitehouse, 2018). Observations of RSL change dating back to AD 1563 are recorded in coastal rocks around Sweden (Ekman, 2009), and which Celsius (1743) used to produce the first GIA calculations, although which he incorrectly assumed was due to a fall in GMSL.

After Lyell (1835) deduced that sea-level change was non-uniform across Sweden, a catalogue of developments proceeded through the 19th and 20th centuries in an attempt to explain the processes underpinning variations in land uplift rates. Jamieson (1865) first suggested that ice sheets may have driven subsidence; Woodward (1888) developed the mathematics behind geoid deformation due to the redistribution of surface ice-sheet mass; the realisation of the importance of both ice mass changes and the resulting deformation on sea-level change (Nansen, 1921; Daly, 1925); and the eventual expression of complete ice-ocean loading and Earth deformation feedbacks as expressed by Farrell and Clark (1976) in the Sea Level Equation. In modern GIA modelling, the Sea Level Equation has been extended to account for changes in ocean area due to the changes in ocean basin geometry as the ocean surface geometry changes, as well as from grounded ice-sheet advance and retreat into the ocean basin (Mitrovica and Milne, 2003). In addition, perturbations to the Earth's axis of rotation due to changes in the Earth's mass distribution, which elicit complex feedbacks between ocean mass redistribution and solid Earth deformation, have been incorporated (Milne and Mitrovica, 1998).

1.2.2.3 Numerical Sea-Level Models

Gravitationally self-consistent numerical sea-level models are able to generate spatiotemporal predictions of global RSL values by solving the Sea Level Equation (Spada and Stocchi, 2007; Kendall et al., 2005; Farrell and Clark, 1976). Here, we follow Spada and Stocchi (2007) to outline the key mathematical derivation of

this equation. We begin by defining absolute sea level $SL(\hat{x}, t)$ at a time t and position vector $\hat{x} = (\theta, \psi)$, where θ is colatitude and ψ is longitude, as the difference between the height of two bounding surfaces, with reference to the centre of the Earth. We define the geoid as $R^{ss}(\hat{x}, t)$, the geometry of the ocean surface as a result of self-consistent gravitational attraction and in the absence of ocean-atmosphere dynamics; and the solid Earth surface $R^{se}(\hat{x}, t)$. $SL(\hat{x}, t)$ is therefore simply,

$$SL(\hat{x}, t) = R^{ss}(\hat{x}, t) - R^{se}(\hat{x}, t). \tag{1.1}$$

In the context of palaeo timescales, sea-level change S is defined as the difference between the absolute sea level at a given time t and some remote time t_r such that,

$$S(\hat{x}, t) = SL(\hat{x}, t) - SL(\hat{x}, t_r), \tag{1.2}$$

and defines RSL when t_r is present day and t is some time in the past. For simplicity, we now denote the time t of each quantity by a subscript and drop the explicit $\hat{x}$ dependence. By Equations 1.1 and 1.2,

$$\begin{aligned} S_t &= SL_t - SL_{t_r}, && (1.3)\\ &= R^{ss}_t - R^{se}_t - R^{ss}_{t_r} + R^{se}_{t_r}, && (1.4)\\ &= \left(R^{ss}_t - R^{ss}_{t_r}\right) - \left(R^{se}_t - R^{se}_{t_r}\right), && (1.5)\\ &= N_t - U_t, && (1.6) \end{aligned}$$

where N is the sea-surface variation and U is the vertical solid surface displacement. This is the simplest form of the Sea Level Equation and it shows the dependence between geoid, solid Earth, and sea-level change. To make this equation useful for producing numerical solutions of ice-sheet-driven sea-level changes these relationships must be expanded to explicitly demonstrate the bounding surface geometry dependence for a specified Earth surface mass loading (ice sheets and the ocean).

Farrell and Clark (1976) saw that sea-surface variation could be represented as an equipotential surface and thus take the form,

$$N_t = \frac{\phi(\hat{x}, t)}{\gamma} + c(t), \tag{1.7}$$

where $\frac{\phi(\hat{x},t)}{\gamma}$ is the spatially variable geoid height variation, γ is gravity at the Earth's surface, ϕ is the total variation of the gravity potential, and c is a time variable constant introduced to conserve ice-sheet mass. The Sea Level Equation can then be

written

$$S_t = \frac{\phi_t}{\gamma} - U_t + c(t). \tag{1.8}$$

Conservation of mass can be expressed using ice-sheet change m_i and ocean mass change m_o such that,

$$m_i(t) + m_o(t) = 0, \tag{1.9}$$

where m_i is simply the spatial integration of S which, by Equation 1.8, can be expressed as,

$$m_o(t) = \int_o \rho_w S dA = \int_o \rho_w \left(\frac{\phi}{\gamma} - U + c \right) dA, \tag{1.10}$$

where dA is the area element over the Earth's surface and ρ_w is the density of water. Combining with Equation 1.9,

$$\int_o \rho_w \left(\frac{\phi}{\gamma} - U + c(t) \right) dA = -m_i \tag{1.11}$$

$$\implies A_0 \rho_w c(t) = -m_i - \int_o \rho_w \left(\frac{\phi}{\gamma} - U \right) dA \tag{1.12}$$

$$\implies c(t) = -\frac{m_i}{A_o \rho_w} - \overline{\left(\frac{\phi}{\gamma} - U \right)}, \tag{1.13}$$

where A_0 is the modern ocean area and the overbar represents spatially averaged over the ocean surface. Therefore, the Sea Level Equation can be written as,

$$S = \left(\frac{\phi}{\gamma} - U \right) - \frac{m_i}{\rho_w A_0} - \overline{\left(\frac{\phi}{\gamma} - U \right)}. \tag{1.14}$$

In the case of a rigid ($U_t = 0$), non-self-gravitating ($\phi_t = 0$) Earth, this form of the Sea Level Equation has the simple solution,

$$S_t = -\frac{m_i}{\rho_w A_0} = S^E, \tag{1.15}$$

where S^E is eustatic sea-level change driven purely by ice-sheet-driven ocean-volume change.

Let $I(\hat{x}, t)$ be the change in ice-sheet thickness such that,

$$I(\hat{x}, t) = T(\hat{x}, t) - T_0(\hat{x}), \tag{1.16}$$

where $T(\hat{x}, t)$ is ice-sheet thickness and $T_0(\hat{x})$ is a reference ice-sheet thickness such that $m_i(t)$ can be expressed as,

$$m_i(t) = \int_i \rho_i I dA. \tag{1.17}$$

We can then define the total Earth surface load change $\mathcal{L}$ as a combination of ice and ocean-load changes,

$$\mathcal{L}(\hat{x}, t) = \rho_i I(\hat{x}, t) + \rho_w S(\hat{x}, t) O(\hat{x}, t), \tag{1.18}$$

where $O(\hat{x}, t)$ is the ocean function with value 1 where there is ocean or grounded ice, and 0 otherwise. The solid Earth (N) and gravitational potential (ϕ) response to this load change is given by convolution with the associated Green's functions such that,

$$\begin{Bmatrix} U \\ \phi \end{Bmatrix} (\hat{x}, t) = \rho_i \begin{Bmatrix} G_u \\ G_\phi \end{Bmatrix} \otimes_i I + \rho_w \begin{Bmatrix} G_u \\ G_\phi \end{Bmatrix} \otimes_o S. \tag{1.19}$$

By introducing the Green's function $\frac{G_s}{\gamma} = \frac{G_\phi}{\gamma} - G_u$ we can express the gravitationally self-consistent, Green's function form of the Sea Level Equation,

$$S = \frac{\rho_i}{\gamma} G_s \otimes_i I + \frac{\rho_w}{\gamma} G_s \otimes_o S - \frac{m_i}{A_o \rho_w} - \frac{\rho_i}{\gamma} \overline{G_s \otimes_i I} + \frac{\rho_w}{\gamma} \overline{G_s \otimes_o S}. \tag{1.20}$$

In this form, the Sea Level Equation is a linear (in the case of non-migrating shorelines, in which case A_0 will have S dependence), integral, implicit equation for S. Ice-sheet load changes are represented by I, which can be decomposed as spherical harmonics to solve for the convolution $G_s \otimes_i I$, while the dependence of deformation on mantle rheology appears in the load-deformation coefficients, which must be calculated to solve G_s. Analytical solutions to this equation are not known in general. However, the development of techniques such as the pseudo-spectral approach has enabled general approximate numerical solutions to be developed that have also extended their implementations to enable migrating shorelines and rotational feedback (Mitrovica and Milne, 2003).

Numerical solutions of the Sea Level Equation for the purposes of GIA modelling have been extensively applied in the modern literature to a variety of scientific challenges, including: investigating the rheological structure of the Earth (Peltier and Drummond, 2008); identifying the spatial pattern of global RSL, and how it deviates from GMSL (Milne and Mitrovica, 2008); inverting GIA uplift rates to reconstruct past ice-sheet changes (Mitrovica and Peltier, 1992; Peltier, 2004; Peltier et al., 2015); interpreting palaeo sea-level records to infer GMSL (Barnett et al., 2023; Dyer et al., 2021); to infer future ice-sheet dynamics and mass loss (Gomez et al., 2015; Yousefi et al., 2022; Pan et al., 2021); and for correctly interpreting modern-day ice-sheet observational data (Riva et al., 2009; Peltier, 2009). In all

cases, GIA models rely on two pieces of information: the evolution of global ice-sheet thickness and the rheological structure of the solid Earth.

1.2.2.4 Rheology of the Earth

If the Earth was a rigid body and topography was fixed then, on the timescales of glacial cycles, the effects of GIA due to ice-sheet melt would be near instantaneous: the ocean volume would increase through meltwater flux, as would the volume of the basin via grounding line retreat, and the ocean geoid would be reshaped by perturbation to the Earth's gravitational field and axis of rotation. However, the longevity, spatial complexity, and highly coupled nature of GIA effects stem from the viscoelastic response of the solid Earth to surface load changes. Each instance of surface mass redistribution excites deformation in the solid Earth, which compounds with ongoing deformation from previous load changes and drives further redistribution of surface mass.

The magnitude and duration of response of GIA to surface loading is dependent on the viscoelastic structure of the solid Earth and yet this structure is highly spatio-temporally complex and uncertain. Investigations into the thickness of the lithosphere, using measurements of the seismic wave relative velocities, have found that its thickness can vary by an order of magnitude globally (Gung et al., 2003; Pasyanos, 2010), while models of Earth's mantle structure find that dynamic, chaotic convection patterns can generate four orders of magnitude difference in viscosity values accompanied by a highly spatiotemporally variable pattern (Heister et al., 2017). If lateral variations are neglected, Dziewonski and Anderson (1981) showed that it is possible to estimate the radially variable, depth-averaged elastic and density structure of the solid Earth through studying a compilation of seismological measurements, resulting in the influential Preliminary Reference Earth Model (PREM) model.

Numerical GIA simulations typically assume the solid Earth behaves as a linear Maxwell viscoelastic body and represent the predefined viscous structure as viscoelastic Love numbers that result from a method of spectral decomposition originally developed by Love (1909) (Peltier, 1974; Mitrovica and Peltier, 1992). The simplest rheological models assume a purely elastic Earth (Wahr et al., 1998) and, since elastic deformations dominate over short timescales ($\mathcal{O}(10^3)$ yr), this can be an appropriate simplification when modelling mass changes over timescales much less than the expected Maxwell response time, such as week-by-week ice-mass changes observed by the GRACE satellite (Wahr et al., 1998). However, when modelled processes occur on timescales similar to that of the Maxwell response time, viscous

effects become non-negligible, giving rise to the need for a more complex viscoelastic model.

1D viscoelastic models are represented by a radial viscosity profile which typically represents the lithosphere as a region of exceptionally high viscosity of a prescribed thickness. Refinement of viscosity values beyond the lithosphere is typically achieved through comparison against either observed rebound rates or sea-level data. In the first approach, Bayesian inversion is employed to invert GIA rebound data and thus constrain a best-fitting radial viscosity profile (Peltier, 1996; Lambeck et al., 2017; Peltier, 2004). Alternatively, viscosity values can be calibrated against compilations of RSL records (Bradley et al., 2023). Both approaches are complicated by the relative sparsity and high uncertainties in sea level and rebound datasets in addition to the need to make assumptions about the evolution of past ice-sheet loads to drive the GIA model.

The assumption of a laterally invariant viscoelastic structure made by 1D rheology models is problematic for studies of GIA in regions such as Antarctica where Kaufmann et al. (2005), based on seismology studies by Ritzwoller et al. (2001), identified a large difference in mantle viscosity between the East and West portions of the continent which can have important consequences for GIA (Powell et al., 2020). Kaufmann et al. (2005) demonstrated that the inclusion of 3D GIA made only a small contribution to uncertainty in Antarctic mass changes, but van der Wal et al. (2015) expanded their approach to include uncertainty in the derivation of 3D viscosity profiles from seismic data, and found reduced mass balance estimates from GRACE satellite data as a result. More recently, Yousefi et al. (2022) demonstrated that including 3D rheology models in Antarctica increased far-field sea-level estimates by up to 20% for simulation runs between 2100 and 2500. A number of studies have also found considerable influence from the inclusion of 3D GIA on reconstructions of past RSL when compared to the use of globally-averaged 1D viscosity profiles (Bagge et al., 2021; Li et al., 2022; Pan et al., 2022; Austermann et al., 2021). The work by Pan et al. (2022) focused on RSL reconstructions at the Last Glacial Maximum (LGM) and, in testing a suite of 40 3D GIA configurations, found that RSL predictions at the LGM can differ from 1D-derived reconstructions by up to an average of 3 m at far-field sites and, in some locations, by up to 11 m. This work agreed with the conclusions drawn by Bagge et al. (2021) in which a set of 18 3D GIA models was used to show that 3D mantle viscosity variation can be a significant influence on Last Deglaciation RSL reconstructions. Austermann et al. (2021) was the first to demonstrate the potential significance of 3D viscosity and laterally varying lithospheric thickness in the reconstruction of LIG RSL and, in their work, 1D and 3D GIA-driven RSL reconstructions differed $\mathcal{O}(10)$ m in the near

field (regions close to former ice sheets) and $\mathcal{O}(1)$ m in far-field locations. However, models of 3D GIA contain considerable degrees of freedom which are difficult to constrain, such as the prescription of mineral properties, radial viscosity profiles, and the conversion relationship between seismic velocity and temperature variations to estimate the Earth's thermal structure. As such, the inclusion of 3D GIA in RSL reconstruction has been shown to introduce significant additional RSL uncertainty (Li et al., 2022) which, owing to the expensive computational requirements, are highly challenging to explore. In light of these limitations, and with the suggestion that suitable 1D radial viscosity profiles can be used to locally approximate the 3-D GIA result at specific sites (Austermann et al., 2017), it is often sufficient to utilise 1D reconstructions for applications to the LIG.

1.2.2.5 Sea-Level Fingerprints

The geometry of the ocean surface is intrinsically linked to the particular mass distribution of the Earth system. Rapid ice-sheet melt acts to perturb the Earth's gravitational field and, through the reduced gravitational attraction between the shrinking ice mass and the ocean, cause RSL to fall close to the melting ice sheet while rising further afield (Mitrovica et al., 2009). The source of ice-sheet melt results in a particular pattern of sea-level change, known as a fingerprint. Hay et al. (2014) computed the fingerprints that would result from the collapse of GrIS, WAIS and marine sectors of the EAIS during the LIG (Figure 1.3).

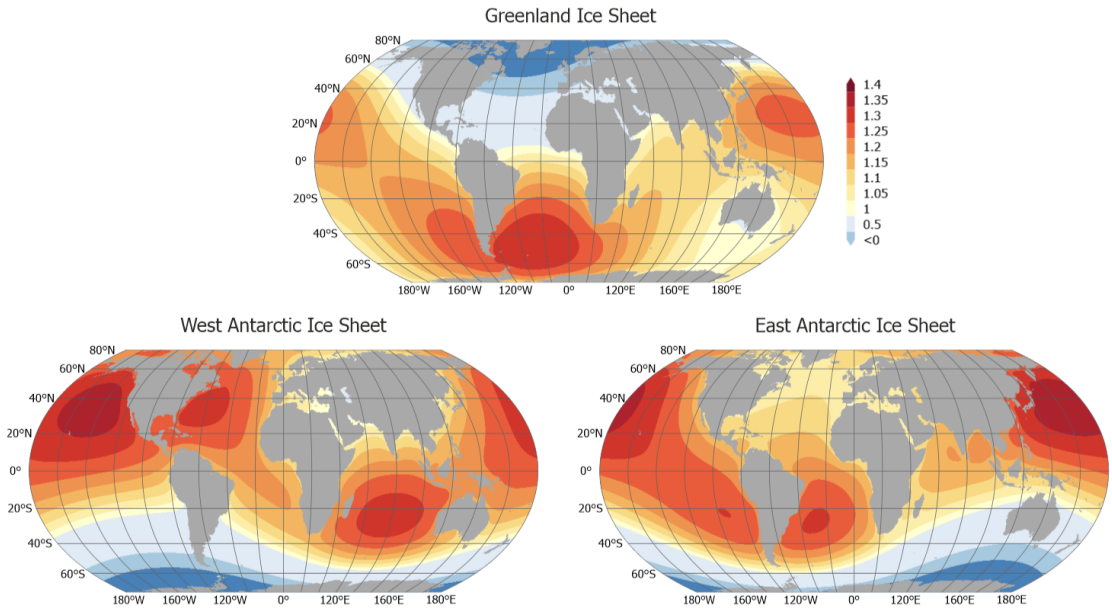

Figure 1.3: Sea-level fingerprints as a result of ice-sheet mass loss from GrIS, EAIS and WAIS. Image from Barlow and Rush (2022), based upon the modelling by Hay et al. (2014).

Sea-level fingerprints, if detected in RSL records, can be inverted to uncover sources of ice-sheet melt. Meltwater Pulse 1A, a rapid period of ice-sheet melt that occurred during the Last Glacial Period (LGP), has been the subject of numerous fingerprint inversion studies in attempts to isolate the dominant meltwater source. Work by Clark et al. (2002) compared RSL records from Barbados and the Sunda Shelf against calculated sea-level fingerprints of the North American Laurentide ice-sheet and WAIS, concluding a small North American and large AIS contribution. Later work by Lin et al. (2021) applied a similar approach but instead drew an opposing conclusion, ruling out a large AIS contribution on the grounds of incompatibility with Scottish isolation basin records, instead proposing that North American sources dominated melt. Utilising sea-level fingerprints to identify sources of ice-sheet melt requires that local processes affecting RSL records are quantified and corrected for, including the significant contribution of GIA driven by past and future ice-sheet loading. Studies have utilised the theory of sea-level fingerprints to aid the interpretation of RSL data, such as the work by Barnett et al. (2023) in which the estimated AIS fingerprint value in Eurasia was used to invert Eurasian RSL data points into estimated values of LIG AIS melt. Similarly, O'Leary et al. (2013) used geospatial fingerprinting information to draw conclusions as to the differing magnitudes of GrIS and AIS melt required to attain their inferred LIG GMSL highstand. In both cases, such studies are limited to utilising fingerprints via their assumed local magnitude of influence rather than calculating their effects directly from models of AIS melt. By not reconstructing the actual fingerprint but scaling local signals by the fingerprint's assumed magnitude, these studies do not explore the range of possible fingerprinting patterns that may result from alternative evolutions of ice-sheet melt.

1.2.3 Late Quaternary Ice Sheets

The Quaternary Period (2.6 Ma - present), comprising of the current Holocene (11.7 ka - present) and the Pleistocene Epochs, has been characterised by the repeated cyclic inception, advance and retreat of large-scale ice sheets, known as glacial-interglacial cycles, across much of the Northern Hemisphere (Ehlers and Gibbard, 2004). The LGP, separating the LIG from the present day, was the most recent and well-documented glacial period due to the relative abundance of surviving geomorphological evidence for constraining ice-sheet extent, configuration and evolution (Clark and Mix, 2002; Dalton et al., 2020; Hughes et al., 2016). Batchelor et al. (2019) developed a series of Northern Hemispheric ice-sheet extents from a compilation of over 180 previous studies looking at empirical and modelling evidence for past ice-sheet configurations. Their work suggested that the Laurentide ice sheet was by far the largest Northern Hemispheric ice mass at the LGM ($\sim 14 \times 10^6$

km^2) in comparison to the Eurasian ($\sim 6 \times 10^6$ km^2), Cordilleran ($\sim 2 \times 10^6$ km^2) and Greenland ($\sim 3 \times 10^6$ km^2) ice sheets at this time. The maximum extent of the Greenland and Antarctic ice sheets are constrained by the size of their respective continental shelves and, as a result, their ice-sheet margins during previous glacial periods are typically better constrained due to this physical limitation (Simpson et al., 2009; Denton and Hughes, 2002). By contrast, the extent of Eurasian and North American ice sheets during past glacial periods must be constrained by empirical evidence for ice-sheet extent and, therefore, are typically more uncertain. Despite this, the expansive North American and Eurasian ice sheet margins at the LGM have been well documented by regional studies. The LGM Eurasian ice sheet extent estimated by Batchelor et al. (2019) is in agreement with the previous DATED-1 empirical data compilation study by Hughes et al. (2016) which focuses on the Eurasian region. During PGM (correlated to MIS 6, 191-123 ka), the Laurentide, Greenland, and Cordilleran ice sheets were likely similar in extent to that of the LGM but the Eurasian ice sheet was likely far larger, equal in size to that of the Laurentide ($\sim 14 \times 10^6$ km^2) (Batchelor et al., 2019; Ehlers and Gibbard, 2004; Ehlers et al., 2011; Toucanne et al., 2009) (Figure 1.4). There is a greater sparsity of empirical evidence for past ice-sheet extents prior to and smaller than the maximum LGM extent, due to this evidence being overwritten by subsequent glaciation, thus limiting studies of the Penultimate Deglaciation ice-sheet margin evolution.

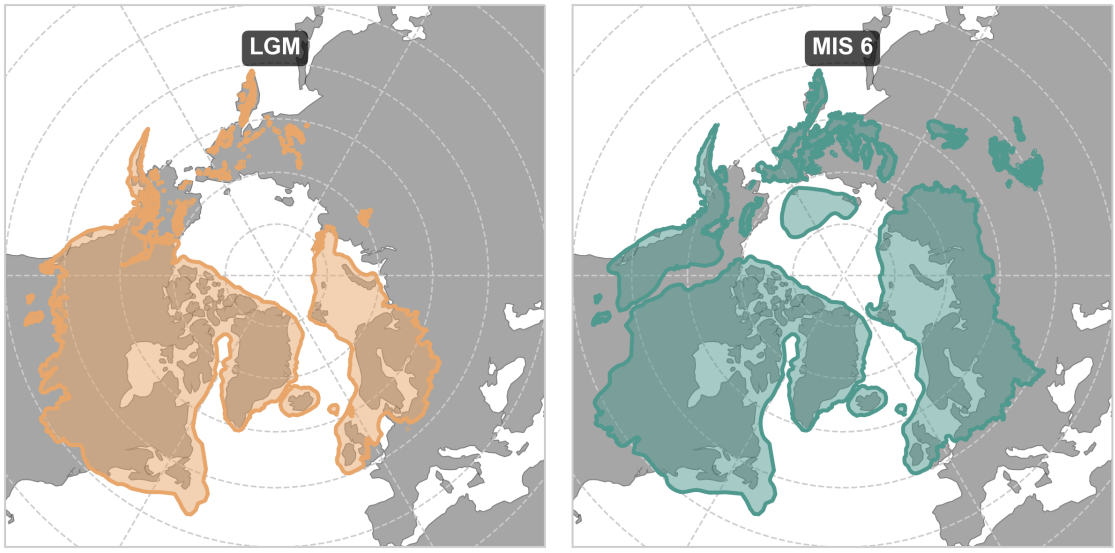

Figure 1.4: The maximum extent of Northern hemisphere ice-sheets during the LGM and PGM as constructed by Batchelor et al. (2019).

The evolution of global ice sheet thickness forms the second essential input to the Sea Level Equation for reconstructions of past RSL changes. Due to the long-term impacts of GIA, ice-sheet changes can have a significant impact on RSL long after they originally occurred and the sensitivity analysis by Dendy et al. (2017) demonstrated

that LIG sea level was sensitive to at least three glacial cycles worth of ice-sheet loading. While geomorphological evidence can be used to describe the extent and provide limits on their thickness, reconstructing 3D ice-sheet geometries requires the use of numerical models.

1.2.3.1 Numerical Ice-Sheet Models

Reconstructions of ice-sheet thickness are a vital component in the modelling of past sea-level changes but there is little empirical evidence available to constrain past ice-sheet geometry. Instead, work has focused on utilising available geological constraints on ice-sheet extent, VLM and RSL data in combination with numerical modelling to estimate ice-sheet thickness. Ice-sheet numerical modelling studies typically adopt one of three main approaches: GIA inversion (Lambeck et al., 2017; Peltier et al., 2015), dynamic ice-sheet modelling (Tarasov et al., 2012; Patton et al., 2017), or simple ice-sheet modelling (Gowan et al., 2021; Fisher et al., 1985) (Figure 1.5). GIA inversion models combine modern VLM measurements with models of Earth's viscoelastic structure in order to estimate the ice-sheet load required to generate recorded uplift rates. The ICE-6G global ice-sheet reconstruction of Peltier et al. (2015) is the result of GIA inversion applied to a global set of VLM data to produce global ice-sheet thickness history spanning from 26 ka until the present day. In this work, Peltier et al. refined previous iterations of their ICE models, such as ICE-5G (Peltier, 2004), by better constraining their viscoelastic Earth model through comparison of the ice-sheet history against more extensive records of RSL data. ICE-6G suggests maximum Eurasian and North American ice-sheet volumes of 22 m SLE and 88 m SLE, respectively, and expanded Greenland and Antarctic volumes of 2 m SLE and 13 m SLE, respectively, compared with modern day. This method has been applied by Lambeck et al. (2006) for time periods earlier than the LGM in their regional study of Eurasia. In that work, they suggest a smaller LGM Eurasian volume of 18 m SLE but a far larger PGM configuration of 52.5 m SLE. In later work, Lambeck et al. (2017) switch focus to the North American ice sheet and infer LGM and PGM volumes of 68 m SLE and 85 m SLE, respectively. While GIA inversion techniques are often consistent with empirical constraints from rebound and sea-level data, they do not guarantee physical consistency with known ice-sheet physics (Stuhne and Peltier, 2015), leading other studies to prefer dynamic ice-sheet modelling.

3D thermodynamic ice-sheet models, driven by climate forcing, present an alternative approach to reconstructing 3D time-evolving ice-sheet geometries. Spanning the LGM to present day, the GLAC-1D ice-sheet history used for the Paleoclimate Modelling Intercomparison Project (PMIP) 4, outlined by Ivanovic et al. (2016), has

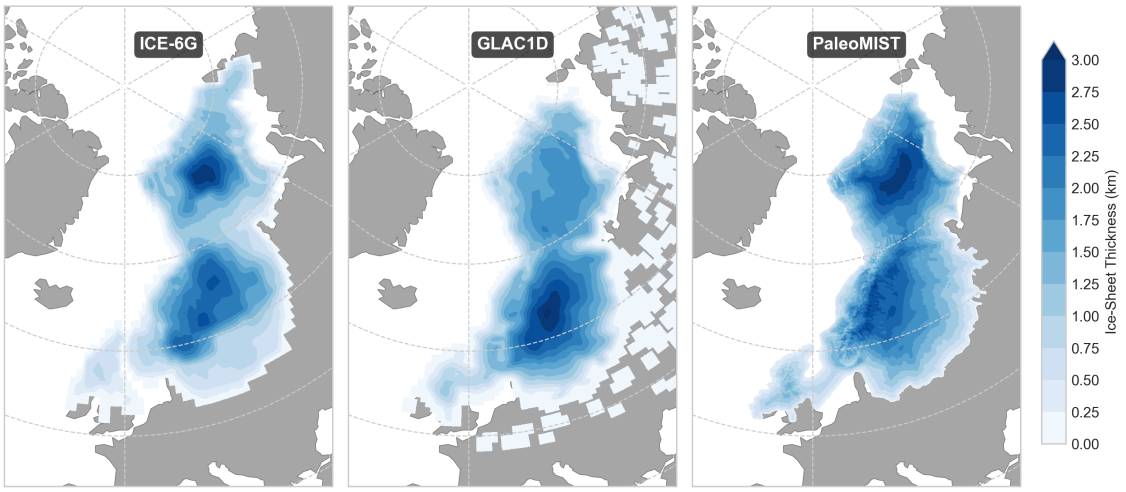

Figure 1.5: The LGM Eurasian ice-sheet configuration as constructed by the ICE-6G GIA inversion (Peltier et al., 2015), GLAC-1D dynamic (Tarasov et al., 2012), and PaleoMIST simple (Gowan et al., 2021) ice-sheet models.

adopted a combination of regional ice-sheet reconstructions each of which has been produced by thermodynamic ice-sheet simulations strongly nudged to fit constraints from 2D reconstructions of ice extent, near-field sea level data, melt-water history, and climate evolution. Compared with GIA inversion modelling each of the Eurasian and North American (Tarasov et al., 2012), Antarctic (Briggs et al., 2014), and Greenland (Tarasov and Peltier, 2002) components have fewer degrees of freedom available with which to best-fit observational constraints in order to enforce ice-sheet physics and prescribed climate forcing within their models. Patton et al. (2016) focused their dynamic ice-sheet modelling towards the build-up and, in later work, retreat (Patton et al., 2017) of the LGM Eurasian ice sheet and concluded a volume estimate of 17 m SLE, lower than those produced by GIA inversion.

Limited dynamic modelling studies have focused on the PGM due to large uncertainties in climate forcing and available data constraints. Despite this, the PGM model of Peyaud (2006), used by Colleoni (2009), utilised the 2D ice-sheet margin of Svendsen et al. (2004) as a target configuration for their dynamic ice-sheet model with which to tune a climate forcing input which resulted in a very large 70 m SLE Eurasian and inferred 78 m SLE North American PGM ice-sheet volume (Colleoni et al., 2016). The PMIP4 Penultimate Deglaciation protocol also utilised dynamic ice-sheet modelling by adopting the work of Abe-Ouchi et al. (2007), this time forced by outputs of a GCM, as boundary conditions for transient climate simulations. While dynamic models ensure more physically plausible ice-sheet geometries, they are also dependent on the reliability of the climate-forcing used.

GIA inversion models can only be reconstructed where there is abundant, spatially diverse and high quality VLM and RSL data; while dynamic ice-sheet simulations are expensive to run and dependent on large assumptions about climate. An alternative approach is the use of **simple ice-sheet modelling** in which ice-sheet geometries are generated based upon the assumptions of steady-state, perfectly-plastic ice flow physics without accounting for the influence of dynamic ice-sheet processes (Nye, 1952; Reeh, 1982; Fisher et al., 1985). Nye (1952) first proposed that the surface gradient of a perfectly plastic ice sheet was directly related to shear stress at the ice-bed interface and that, combined with a prescribed ice-sheet centre, could be used to estimate ice-sheet thickness. The Nye (1952) method, which originally assumed invariant topography beneath the ice sheet, was expanded on by Fisher et al. (1985) to allow for variable topography and basal shear stress beneath the ice sheet by enabling changes in the estimated direction of ice-sheet flowlines, the hypothetical path that traces the flow of ice from the interior of an ice sheet to the margin. In the same work, Fisher et al. (1985) applied their model to reconstructing the Laurentide ice sheet. Subsequently, Gowan et al. (2016a) used this formulation to develop the ICESHEET model which is able to generate 3D ice-sheet geometries using an iterative process to calculate thickness profiles along flowlines that are generated at regular intervals within the prescribed ice margin. Gowan et al. (2016b) first applied ICESHEET to the reconstruction of the Western portion of the LGM Laurentide ice-sheet before going on to develop the global ice-sheet history PaleoMIST (Gowan et al., 2021) spanning 80 ka to present day.

1.3 Summary

GMSL is rising and accelerating, but as ice-sheet melt becomes the dominant contributor to sea-level rise the uncertainty surrounding the Greenland and Antarctic response to a warmer climate becomes more pressing to resolve. Modelling and data studies of the LIG have helped to shed light on spatiotemporal patterns of warm temperatures, high sea levels, and small ice sheets, helping to uncover the value this time period presents to inform the prediction of future warming scenarios. In particular, previous research suggests that smaller Greenland and/or Antarctic ice sheets likely drove higher than present LIG sea levels but the source, magnitude, and timing of their contribution remains uncertain. As the abundance of studies generating LIG sea-level records has increased, along with their accessibility through the development of generalised databases, so too has our understanding of the breadth of processes that can affect our interpretation of such records. In particular, the significant contribution of GIA to near-field sites can dominate their RSL signal, leading to potentially large uncertainties surrounding their correction

for such processes. Despite this, exciting developments in the modelling community have begun to explore the theoretical possibility of identifying sea-level fingerprints of LIG ice-sheet changes, but the largest challenge remains uncertainty in the Earth's rheology and ice-sheet history. While numerous ice-sheet and sea-level modelling approaches have been developed to marry simulations with observational data, much work still remains to understand LIG sea-level and to harness the information it may hold about future ice-sheet melt in a warming world.

To address these research gaps, this thesis utilises the opportunity afforded by northwest Europe's sensitivity to the source of LIG ice-sheet melt whilst capturing and quantifying uncertainties that result from studying a location proximal to a former ice load. The following chapter gives an overview of the tools and techniques required to perform this work (Chapter 2). Next, I describe the development of a Eurasian ice-sheet load (Chapter 3 and 4) and subsequently determine the sensitivity of LIG sea level to the range of parameters influencing regional GIA (Chapter 4). Finally, I assess and calibrate Eurasian RSL models to European sea level data with the aim of fingerprinting Antarctic melt during the LIG (Chapter 5).

Chapter 2

Tools and Techniques

The work within this thesis is focused on the use of an ice-sheet and sea-level model to produce simulations of northwest Eurasian RSL during the LIG. Various tools and techniques were employed to produce model inputs, perform analysis, and enable a complete model workflow, as summarised in Figure 2.1. While the details of these methods are given in each chapter, this chapter outlines key aspects of the tools and techniques that I utilised and developed.

2.0.1 Numerical Models

A numerical model is a mathematical representation of some real-world system for which approximate solutions can be generated with the use of numerical methods. A collection of computer code that implements such numerical methods is referred to as a simulator (or model). Models often require input data to describe the physical state of a system, determine system behaviour, or describe internal characteristics of numerical solutions, but the true value of these inputs are often uncertain. Because of this, it is common to decompose input data into a series of (usually scalar) values known as model parameters. The range of possible parameter values is referred to as a parameter range and the combined space that contains all possible combinations of input parameters is referred to as a **parameter space**. For deterministic models, this parameter space maps to the space of all possible model outputs within the given bounds of parameter uncertainty.

Many problems that use numerical models require knowledge of the possible range of output values across a model parameter space, but since determining the model output that corresponds to each input parameter combination requires running the model, it can be computationally expensive to densely explore this space. Techniques have been

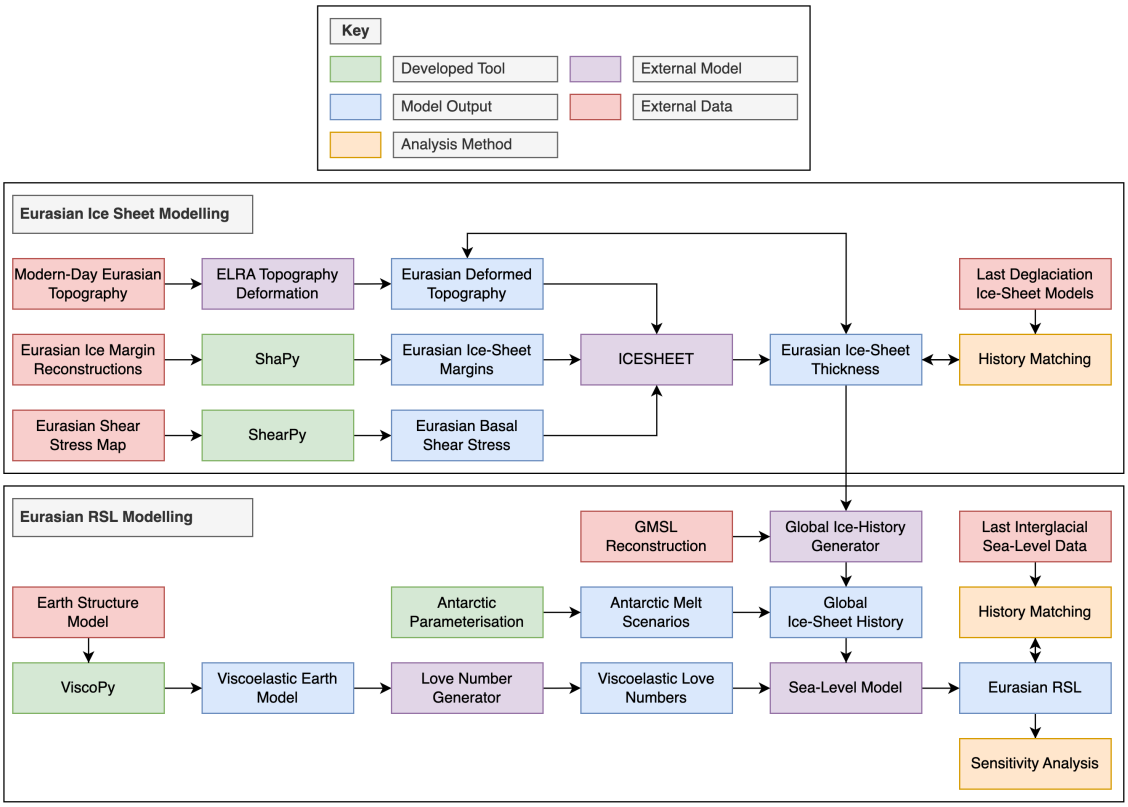

Figure 2.1: Flowchart visualising how the models and tools used in this thesis interlink.

developed to efficiently explore a model parameter space including Latin hypercube sampling (Mckay et al., 2000), used throughout this thesis. When generating N samples, latin hypercube sample (LHS) works by first dividing each dimension of the model parameter space into N equal parts. Within each division, the algorithm then generates a random value along each dimension, producing a LHS. The space-filling properties of this design can be further improved upon by modifying the initial sample to maximise the distance between all points, known as a maximin LHS (Williamson, 2015). The maximin LHS design used in this work ensures that the parameter space is quasi-randomly but evenly explored. In this thesis, we explore our parameter space designs for both an ice-sheet and sea-level model, which will now be briefly described in turn.

2.0.1.1 Gowan ICESHEET Model

This thesis utilises the simple ice-sheet model known as ICESHEET, developed by Gowan et al. (2016a), for our Penultimate Deglaciation simulations of the Eurasian ice sheet. ICESHEET assumes a steady-state, perfectly plastic ice-sheet rheology (i.e. the flow of ice) in order to calculate ice elevation along paths of ice flow, known as flowlines. As detailed in Gowan et al. (2016a), the basis of this theory was originally

developed by Nye (1952) in which ice-sheet elevation E along a flowline was related to basal shear stress at the base of the ice τ_o by the surface gradient,

$$\frac{dE}{ds} = \frac{\tau_o}{\rho_i g H}, \tag{2.1}$$

where s is the distance along the ice flowline, g is the acceleration due to gravity, H is the ice-sheet thickness, and ρ_i is the density of ice. This formulation can be used to calculate E along a flowline if the centre of the ice sheet is known and if both τ_o and bedrock topography B are assumed to be constant. These equations were subsequently expanded by Reeh (1982) and Fisher et al. (1985) to allow for changes in flowline direction, such that,

$$\left(\frac{dE}{ds}\right)^2 = \left(\frac{\partial E}{\partial x}\right)^2 + \left(\frac{\partial E}{\partial y}\right)^2, \tag{2.2}$$

where x and y are the directions parallel and perpendicular to the ice-sheet margin respectively.

Substituting Equation 2.1 into Equation 2.2 produces,

$$\left(\frac{H_f}{E-B}\right)^2 = \left(\frac{\partial E}{\partial x}\right)^2 + \left(\frac{\partial E}{\partial y}\right)^2, \tag{2.3}$$

where H_f is the characteristic thickness given by,

$$H_f = \frac{\tau_o(x,y)}{\rho_i g}. \tag{2.4}$$

Through the method of characteristics, Equation 2.3 can be expressed in terms of the partial derivatives $p = \partial_x E$ and $q = \partial_y E$, to arrive at the following system of differential equations,

$$\frac{dy}{dx} = \frac{q}{p}, \tag{2.5}$$

$$\frac{dE}{dx} = \frac{H_f^2}{(E-B)^2 p}, \tag{2.6}$$

$$\frac{dq}{dx} = \frac{H_f^2}{p(E-B)^3}\left(\frac{\partial B}{\partial y} - q\right) + \left(\frac{H_f}{p(E-B)^2}\right)\frac{\partial H_f}{\partial y}. \tag{2.7}$$

The ICESHEET model is a computational implementation of numerical solutions to these three equations solved by iteratively generating ice-elevation contours (Figure 2.2). ICESHEET works by first sampling an ice-sheet margin for a series of coordinates to be used as flowline termination locations. For each coordinate, ICESHEET calculates a flowline direction and elevation (for the margin, this elevation

is assumed to be 1 m) before traversing each flowline vector until a new, specified elevation value is reached. The flowline directions and coordinates corresponding to these flowline vector positions are then used to assemble a new elevation contour, with routines in place to deal with issues such as polygon crossover and separation (Figure 2.2). This process is repeated until all flowline calculations have terminated before the resulting series of polygons, represented as a collection of coordinates, that describe the elevation contours of the ice sheet are outputted to a text file.

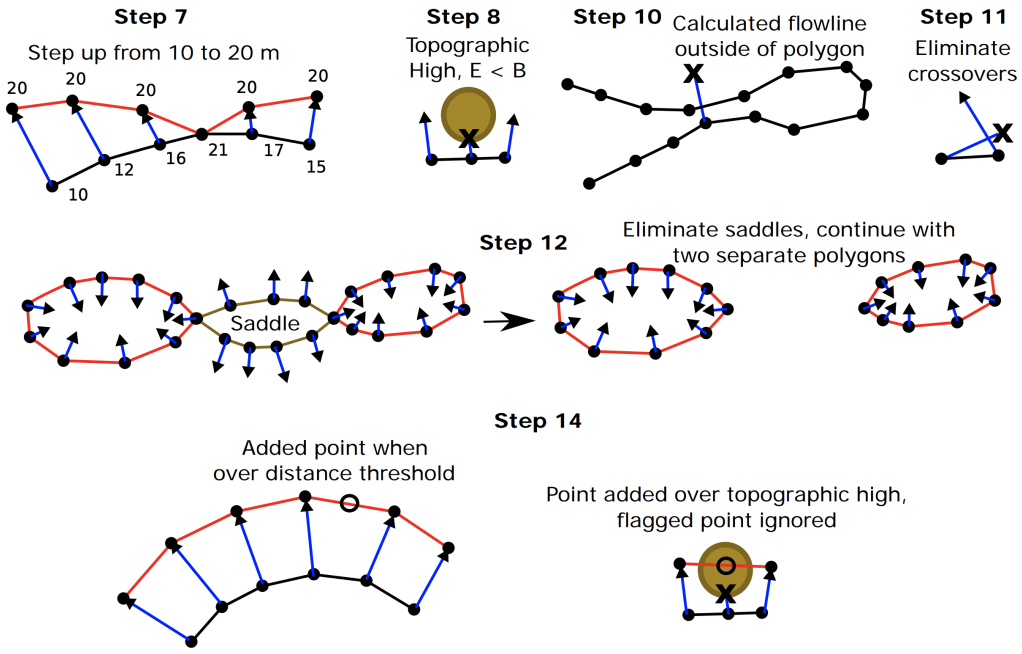

Figure 2.2: Visualisation of key steps in ICESHEET's numerical implementation of ice-sheet flowline profiles. From Gowan et al. (2016a), Figure 1.

ICESHEET allows the user to specify the resolution of reconstructions through two parameters: the elevation interval, used to determine the elevation spacing between contour calculations; and the minimum spacing, describing the minimum distance between flowline coordinates along each polygon. In this work, the elevation coordinate data outputted from ICESHEET is interpolated onto the same model grid on which the input data is defined with the use of the Python-based Scipy interpolation library.

2.0.1.2 Kendall Sea-Level Model

The sea-level model used in this work is based on the numerical implementation described by Kendall et al. (2005) that uses a pseudo-spectral approach to calculate numerical solutions to the Sea Level Equation (Equation 1.20) (Mitrovica and Peltier, 1991). Spectral, in this case, refers to the mathematical transformation of a quantity

originally defined in the spatial domain (such as ice-sheet thickness and topographic deformation) to the spectral domain. This can be especially useful for quantities defined on the surface of a sphere since any such quantity $\chi(\theta, \psi, t)$ for t is time, colatitude θ, and longitude ψ can be expressed as,

$$\chi(\theta, \psi, t) = \sum_{l=0}^{\infty} \sum_{m=-l}^{l} \chi_{lm}(t) Y_{lm}(\theta, \psi), \tag{2.8}$$

where l is the spherical harmonic degree, m is the spherical harmonic order, Y_{lm} is the spherical harmonic function, χ_{lm} are time-evolving scaling factors. In the case of the Sea Level Equation, the pseudo-spectral approach refers to the fact that solutions to spatially variable sea-level change are computed in the spectral domain, as this is numerically more efficient, while aspects that require spatial filtering (such as ocean masking) are mathematically simpler to perform in the space domain (Gomez et al., 2010). Thus, the Kendall et al. (2005) implementation performs calculations in both domains, transforming quantities as necessary.

In general, it is not possible to retain the complete spherical harmonic representation of a spatial quantity, as shown in Equation 2.8, since this would require storing spherical harmonic degrees from 0 to ∞. Instead, the sea-level model allows the user to specify a maximum spherical harmonic degree and order at which to truncate the decomposition. To aid the spherical harmonic transformation, the sea-level spatial model grid used for input and output quantities is defined on the Gauss–Legendre latitudinal nodes of corresponding maximum harmonic degree order.

The spherical formulation of the Sea Level Equation solves for the deformation of the solid Earth to an arbitrary surface load through the use of viscoelastic Love number theory (Peltier, 1974). This theory requires expressing the spatial viscoelastic Earth structure in terms of Love number spectra, which characterise the impulse response of a Maxwell Earth. In this thesis, the Love number spectra are calculated up to the same specified maximum harmonic degree via the collocation method implemented by Jerry Mitrovica (pers comms.) and outlined in Mitrovica and Peltier (1992).

2.0.2 Python Tools

2.0.2.1 ShearPy

ShearPy is a Python-based tool that I have developed to generate shear-stress inputs to the ICESHEET model. This tool interfaces with a database of shear-stress regions that each consists of a region ID, time period, and geometry in order to easily generate maps with specified shear-stress values. *ShearPy* allows for shear-stress map

inputs to be generated in a layer-like fashion. Each layer of the map is treated as a separate Python object and *ShearPy* implements 'magic methods' in corresponding object classes to allow arithmetic and logical operations between layers. The program includes options to make reproducible ensembles more convenient, such as a 'combine pattern string' option that executes a pre-defined series of combination operations that can easily be stored as metadata.

In addition, *ShearPy* implements a number of geospatial operations that can manipulate the geographic extent of layers (such as defining a maximum internal extent for ice streaming) and generate new layers (such as cold-based ice and hybrid ice streaming) based on ice-sheet margin position. Other features include convenient access to shear stress geometries by ID, region, or type; in-built plotting tools to pre-view operations; and the ability to rapidly reprojection and rasterisation of shear-stress vectors onto a model grid.

ShearPy is made publicly available here: https://github.com/oliverpollard/ShearPy

2.0.2.2 ShaPy

Work within this thesis required the ability to interpolate between two closed polygons. To achieve this, I have developed a Python module for this purpose, named *ShaPy*, that is able to calculate a mapping between coordinates from an exterior to an interior polygon. This point mapping can then be used to define a corresponding set of vectors that describe the path each exterior polygon coordinate should take to reach its corresponding interior point. Using this method, my module can generate an intermediary polygon for any specified interpolation value s corresponding to a normalised distance d along the interpolation vectors with $d = 0$ and $d = 1$ corresponding to the original exterior and interior polygons respectively. In the standard mode, the program will perform linear interpolation, such that $d = s$, but I also included additional functionality in ShaPy to allow for non-linear interpolation rates (e.g. $d = s^2$), as shown in Figure 2.3, and variable vector interpolation rates that depend on the angular position of the vector's corresponding exterior coordinate.

ShaPy operation takes 6 key operations, numbered corresponding to the illustrations in Figure 2.3:

1. The exterior and interior polygon geometries are loaded into the program.

2. Equally spaced coordinates are generated along both the interior and exterior polygon perimeters. The number of coordinates sampled is specified by the user through the *sample_size* parameter.

3. An initial mapping of polygon coordinates, from exterior to interior, is generated by matching each exterior coordinate to the interior point with the minimum linear distance. This procedure does not guarantee that all interior coordinates are mapped to an exterior coordinate.

4. For each sequence of unmapped interior coordinates, an equal number of new exterior coordinates are inserted in an equidistant sequence between bounding mappings, and mapped to the interior coordinates

5. Each mapping is associated with an interpolation 'power' which determines the distance along the connecting line that a new coordinate will be generated at for a given interpolation 'value'.

6. An interpolated polygon is generated by joining all interpolated coordinates.

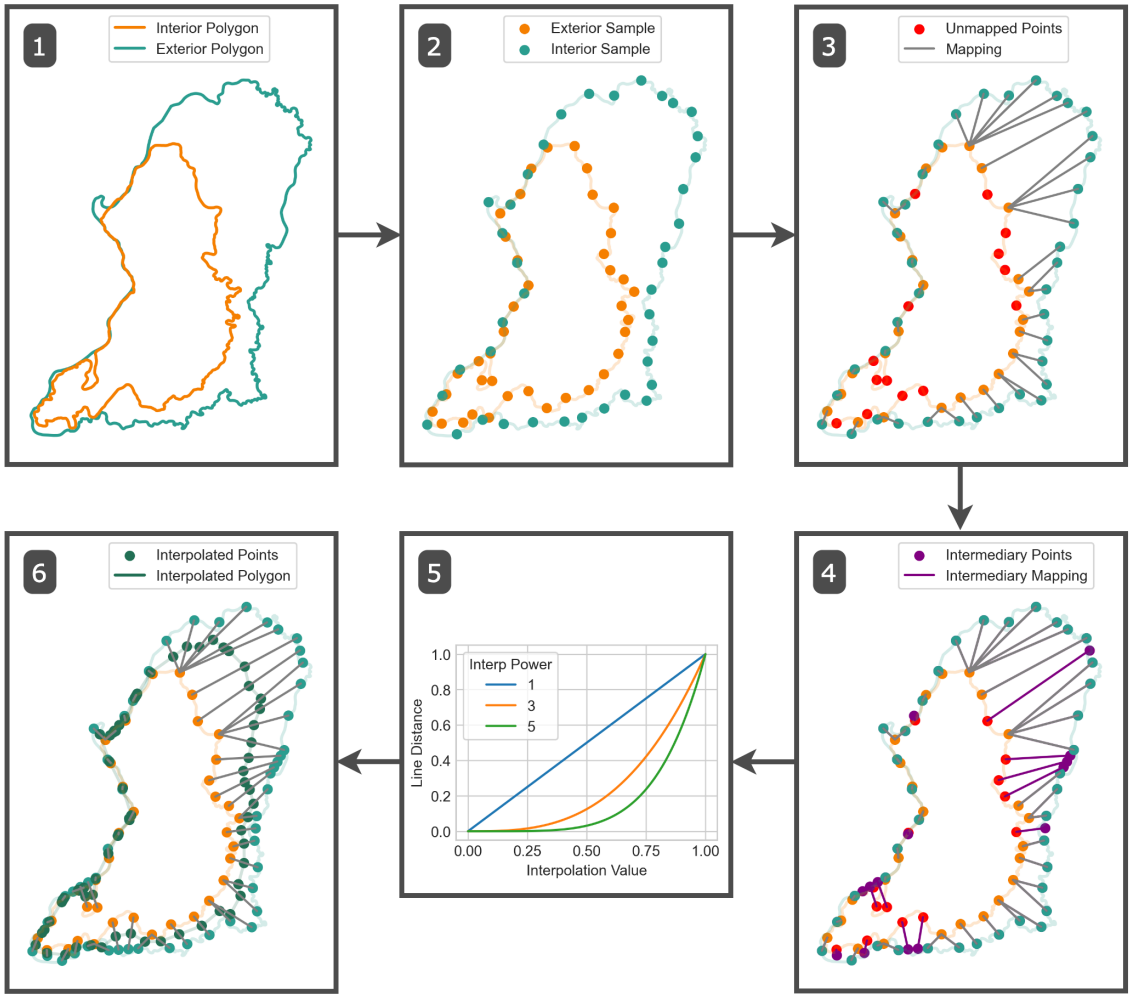

Figure 2.3: Schematic illustrating the key steps in the shape interpolation algorithm developed and implemented with ShaPy.

ShaPy has been developed as an object-orientated Python module that exposes the polygon coordinate sampling methods with a user-accessible *PolygonSampler* object and the polygon interpolation methods with a *PolygonInterp* object.

ShaPy is made publicly available here: https://github.com/oliverpollard/ShaPy

2.0.2.3 ViscoPy

In developing large ensembles of sea-level model outputs, I was required to produce systematic variations in the viscoelastic Earth structure that respected parameter discontinuity values imposed by the Preliminary Reference Earth Model (PREM) (Dziewonski and Anderson, 1981). To achieve this, I developed a Python module, named *ViscoPy*, that could quickly and easily generate 1D viscoelastic Earth structures with user-specified viscosity values and region divisions; depth-variable model resolution; and imposed PREM elastic and density structure discontinuity locations. My module is built around the *ModelGenerator* object that, once initialised, can be used to rapidly generate Earth structures by providing a list of viscosity values and boundaries to the *generate* method which then returns a table of Earth property values. The module has in-built *load* and *save* functions, and uses the same file structure as is required by the Mitrovica love-number generator (described in Section 2.0.1.2) for easy use with the sea-level model.

ViscoPy is made publicly available here: https://github.com/oliverpollard/ViscoPy

2.0.3 Uncertainty Quantification and Statistical Modelling

In the context of numerical modelling, uncertainty quantification is the process of assessing and quantifying uncertainties associated with model output values. This section will briefly review some key concepts that are important for this research. First, I review the two key categories of model uncertainty: parametric uncertainty, resulting from input parameter boundary condition uncertainty; and structural uncertainty, as a result of mathematical assumptions, physical simplifications, missing processes, or numerical implementations (Smith, 2013; Parker, 2013). Next, I review three statistical modelling techniques: sensitivity analysis, used to identify the most important parameters contributing to parametric uncertainty; history matching, reducing the size of the model parameter space to only include regions that can best fit observations, accounting for model parametric and structural uncertainty; and Gaussian process emulation, a statistical model that makes this analysis possible without the need to run thousands of numerical model simulations. These are powerful methodologies that are commonly used to understand and quantify the uncertainty that results from large numerical modelling experiments.

2.0.3.1 Parametric Uncertainty

The assessment of parametric uncertainty typically requires performing a large ensemble of simulations that explores different possible combinations of input parameter values, referred to as a perturbed parameter ensemble (PPE) (Murphy et al., 2007). The use of PPEs to quantify parametric uncertainty in palaeo ice-sheet and sea-level models is an underdeveloped field due to the computational requirements, difficulty in constraining parameter ranges, and lack of observational constraints. In particular, parametric uncertainty assessments in dynamic ice-sheet models are limited by the computational requirements of running a fully coupled climate model within a large-ensemble framework. Such studies instead make assessments based on perturbations to parameters controlling surface mass balance as a simple approximation to the impacts of climate uncertainty. However, examples are more common in studies that focus on ice-sheet changes since the Last Deglaciation, since more observational constraints are available against which model output ranges can be compared. Recent examples of such studies include the work by Gandy et al. (2023) in which parametric uncertainty in the extent of the North American ice sheet at the LGM was quantified with the use of a 280-member PPE. This ensemble was generated with a LHS of 13 parameters controlling ice sheet albedo, ice sheet dynamics, atmospheric, and oceanic parameters within a coupled climate-ice model. Some studies have quantified parametric uncertainty in ice-sheet models prior to the Last Deglaciation, such as the work by Stone et al. (2013), which assessed the parametric uncertainty in thermo-mechanical ice-sheet model simulations of GrIS during the LIG. Their work used 500-member LHS to explore 5 uncertain parameters but were unable to assess the impact of structural climate model error on their simulations.

2.0.3.2 Structural Uncertainty

Accurately assessing structural uncertainty can be much more challenging than exploring parametric uncertainty. Studies often try to capture structural error by determining the mismatch between model outputs and observed data. However, due to uncertainties in modelled physical processes and numerical implementations, it is not guaranteed that a numerical model can match observational constraints even with a perfect choice of input parameters and well-constrained observations. It can be difficult to directly compare spatiotemporal outputs from palaeo ice-sheet and sea-level models against observation data since such data is generally sparsely available. Despite this, methods have been developed to directly compare spatiotemporal ice-sheet thickness outputs against geochronological data (Ely et al., 2019), ice-sheet flow direction compared against lineations left within the geomorphological record (Archer et al., 2023), and modelled margins against moraine positions (Li

et al., 2008). Despite these efforts, direct comparison of spatiotemporal ice-sheet and sea-level model outputs in order to quantify the full spatiotemporal structure of the structural model error remains challenging. More typically, spatiotemporal fields are summarised by some choice of metric (such as total ice-sheet volume or RSL at a particular location) in order to be comparable against corresponding data reconstructions, including modelled ice-sheet area and volume (Gregoire et al., 2016; Gandy et al., 2023) and RSL reconstructions (Gowan et al., 2021; Tarasov and Peltier, 2002; Peltier, 2004). In these instances, discrepancies between modelled summary metrics and observations are assumed to be representative of the model-structural uncertainty. In the case of multiple sources of observation, it can be useful to apply a method capable of combining these summaries into a single metric describing model-data fit. One such method is known as history matching, which uses the implausibility metric to describe the distance between the model and data, normalised by the total model-data uncertainty (Gandy et al., 2023; Bower et al., 2010; Vernon et al., 2022; Williamson et al., 2013).

2.0.3.3 Sensitivity Analysis

The number of simulations required for a PPE to properly assess parametric uncertainty is highly dependent on the specifics of the numerical model being assessed. Typically this number increases with the number of model parameters under assessment. In order to allow for a more focused assessment of uncertainty, PPEs can be restricted to include only those parameters that significantly contribute to uncertainty in a model output of interest, a process known as sensitivity analysis. Sensitivity analysis attributes model output uncertainty to input variations (Pianosi et al., 2016) and can be used to reduce the dimensions of model parameter spaces required to explore parametric uncertainty (Saltelli et al., 2007, 2010). Sensitivity analysis can be performed by varying each model parameter individually (known as one-at-a-time experiments) or through more sophisticated methods, such as **Sobol sensitivity analysis** (Sobol', 1990), that are able to quantify the relative contribution (or sensitivity index) of a parameter to the overall output variance. Examples of sensitivity analysis performed in the context of palaeo-ice-sheet modelling include the work by Briggs et al. (2013) quantifying sensitivity to 31 thermo-mechanical ice-sheet model parameters governing the AIS deglaciation.

2.0.3.4 History Matching

History matching is a procedure used to identify areas of a model's parameter space that are able to fit observational constraints within a specified magnitude of model and data uncertainty, referred to as the 'not ruled out yet' (NROY) subset of the

parameter space (Vernon et al., 2022; Williamson et al., 2013; Bower et al., 2010). The first step in this procedure is to perform sensitivity analysis on the model parameters, identifying those to which the model output of interest is most sensitive. This allows the analysis to proceed with a reduced dimensionality parameter space, enabling it to be explored with a greater density for the same number of samples. Next, the parameter space is explored by running a large ensemble of simulations from parameter combinations sampled from this space, using a space-filling design such as LHS. Since running a numerical model can often be computationally expensive, it is common to then explore a far larger LHS sample of the parameter space using an approximate statistical representation of the numerical model (known as an emulator), trained on the original LHS of model outputs. Finally, for each parameter combination tested, each model output can then be summarised with a scalar implausibility value, which represents the model's ability to fit observations for a given parameter combination, normalised by the total uncertainty. These implausibility values can be used to identify the NROY portion of the parameter space that is able to fit observations within some specified distance tolerance. If needed, the NROY space can then be further refined with successive waves of history matching (Vernon et al., 2022).

To understand the implausibility measure, first consider the true value of some quantity of interest y that we have modelled as $f(\hat{p})$ for parameter combination $\hat{p}$. We consider, here, two sources of error. First, assume we have observed at some value z and observational error e, such that $y + e = z$. Next, since our numerical model is not a perfect representation of the real world, all predictions $f(\hat{p})$ are separated from y by model structural discrepancy ϵ such that, for the hypothetical perfect parameter combination $\hat{p}^*$, $y = f(\hat{p}^*) + \epsilon$. The implausibility of parameter combination $\hat{p}$ is then given by,

$$I(\hat{p}) = \sqrt{\frac{(E(f(\hat{p})) - z - E(\epsilon))^2}{Var(e) + Var(\epsilon) + Var(f(\hat{p}))}} \tag{2.9}$$

where E is the expectation, Var is the variance, $E(\epsilon)$ is the expected model bias, $Var(\epsilon)$ is the variance of structural error, and $Var(f(\hat{p}))$ is the emulator error in the case that f is an emulation of our original numerical model. If $f(\hat{p})$ is known exactly, that is, we have observed the actual model output, then $Var(f(\hat{p})) = 0$. Values of $I(\hat{p})$ are then given in terms of standard deviations of the overall model and data uncertainty. It is typical to rule out parameter combinations that have implausibility of greater than 3, following the Pukelsheim (2012) three-sigma rule typically used in Bayesian history matching, in order to identify the remaining NROY parameter space best able to explain observations (Andrianakis et al., 2015; Williamson et al., 2015).

2.0.3.5 Gaussian Process Emulation

In performing uncertainty quantification or sensitivity analysis, it is often necessary to perform large-ensembles of model outputs that would be computationally infeasible to acquire directly from a numerical model. In this instance, model outputs can be approximated with the use of a fast, surrogate statistical model referred to as an emulator that is trained on a smaller subset of model outputs. One such type of emulator is a Gaussian process, a non-parametric model defined as a collection of random variables, any finite subset of which follows a multivariate Gaussian distribution (Rasmussen and Williams, 2006; Astfalck et al., 2019). At a high level, a Gaussian process places a probability distribution over the infinite possible set of functions that may explain our data. This distribution first takes the form of a *prior* distribution constraining the subset of the function space to those with characteristics that we believe may best fit the process in question (such as smoothness, periodicity, and differentiability). This *prior* information is encoded within a covariance matrix Σ which is generated by a choice of covariance function, or kernel, for a given set of function characteristic requirements. After generating some model output values, this *prior* distribution and associated Σ can be updated to a *posterior* distribution that further narrows the subset of functions to those that can also explain our specific data (Rasmussen and Williams, 2006). Together, Σ and a mean function μ fully define the Gaussian process statistical model. The need to emulate numerical models has made the Gaussian process a popular tool within the Earth sciences and has been used in a variety of applications that have required dense model output sampling (Gilford et al., 2020; Pollard et al., 2016; Edwards et al., 2021).

2.1 Summary

This section has provided a brief outline of key methods and tools used throughout this thesis for the investigation of northwest Eurasian RSL during the LIG. Chapters 3 and 4 show how the simple ICESHEET model can be applied to the Penultimate Deglaciation of the Eurasian ice sheet while Chapters 4 and 5 apply the sea-level model to investigate the sensitivity, uncertainty, and calibration of RSL outputs. This work begins by investigating the range of plausible Eurasian ice-sheet geometries at the PGM with the use of a simple ice-sheet model and refined with the use of Bayesian history matching.

Chapter 3

Quantifying the Uncertainty in the Eurasian Ice-Sheet Geometry at the Penultimate Glacial Maximum (Marine Isotope Stage 6)

This chapter has been published as Pollard et al., 2023, *Quantifying the Uncertainty in the Eurasian Ice-Sheet Geometry at the Penultimate Glacial Maximum (Marine Isotope Stage 6).*, The Cryosphere, 17(11), pp.4751-4777., doi: https://doi.org/10.5194/tc-17-4751-2023.

3.1 Abstract

The North Sea LIG sea level is sensitive to the fingerprint of mass loss from polar ice sheets. However, the signal is complicated by the influence of glacial isostatic adjustment driven by Penultimate Glacial Period (PGP) ice-sheet changes, and yet these ice-sheet geometries remain significantly uncertain. Here, we produce new reconstructions of the Eurasian ice sheet during the PGM by employing large ensemble experiments from a simple ice-sheet model that depends solely on basal sheer stress, ice extent, and topography. To explore the range of uncertainty in possible ice geometries, we use a parameterised shear-stress map as input that has been developed to incorporate bedrock characteristics and the influence of ice-sheet basal processes. We perform Bayesian uncertainty quantification, utilising Gaussian process emulation, to calibrate against global ice-sheet reconstructions of the Last Deglaciation and rule out combinations of input parameters that produce unrealistic

ice sheets. The refined parameter space is then applied to the PGM to create an ensemble of constrained 3D Eurasian ice-sheet geometries. Our reconstructed PGM Eurasian ice-sheet volume is 48 ± 8 m SLE. We find that the Barents-Kara Sea region displays both the largest mean volume and volume uncertainty of 24 ± 8 m SLE while the British-Irish sector volume of 1.7 ± 0.2 m SLE is smallest. Our new workflow may be applied to other locations and periods where ice-sheet histories have limited empirical data.

3.2 Introduction

The LIG (MIS 5e; 130 - 116 ka) was the last time in Earth's history that the Greenland and Antarctic ice sheets were smaller than today (Dutton et al., 2015), during a time when polar temperatures were 3-5 °C above pre-industrial values (Capron et al., 2014), raising the global mean sea level by 5-10 m above present values (IPCC, 2022). The timing, magnitude and spatial pattern of LIG sea-level changes are, in large part, caused by ice-mass changes during the interglacial as well as by those that occurred during the preceding glacial (MIS 6, 191-123 ka) cycle (Dendy et al., 2017; Rohling et al., 2008, 2019). The effect of ice-sheet melt on sea-level change is complex due to feedbacks between ocean water volume, perturbations of the Earth's rotational axis, Earth's gravitational field, and viscoelastic deformation of the solid Earth due to changing ice and water loads (Milne and Mitrovica, 1998). Together, these processes are termed GIA (Farrell and Clark, 1976; Mitrovica and Milne, 2003; Whitehouse, 2018), and form the primary drivers of spatially variable RSL change on glacial-interglacial timescales.

Regional LIG RSL changes are a consequence of the distribution and timing of terrestrial ice-mass deglaciation during the preceding glacial. Last Deglaciation ice-sheet histories included in GIA reconstructions are well constrained by a wealth of geological data (Clark and Mix, 2002; Dalton et al., 2020; Hughes et al., 2016) and tested against comprehensive RSL databases (e.g., Peltier, 2004; Shennan et al., 2006; Stuhne and Peltier, 2017; Tarasov et al., 2012). By contrast, for glacial periods prior to the LGM, including the Penultimate Deglaciation (typically correlated to the end of MIS 6 and, regionally in Europe, the late Saalian glacial phase) that preceded the LIG, a paucity of geomorphological and chronological constraints for ice extent, thickness, and volume means that older ice-sheet reconstructions are much harder to constrain. This presents a significant source of uncertainty for studies that focus on ice and water loading changes during the LIG (Barlow et al., 2018; Düsterhus et al., 2016). One notable uncertainty in the PGP ice history is the Eurasian ice sheet, as its extent was thought to have been significantly larger during the PGM

than the LGM (Batchelor et al., 2019; Svendsen et al., 2004) (Figure 3.1). Geological data suggest that the preceding glacial Eurasian ice sheet was typified by more than one period of ice advance during late Saalian. In western Europe two significant phases of ice advance occurred; the Drenthe (ca. 175-160 ka) which extended south of the LGM ice extent in the Netherlands, and the latter Warthe readvance (ca. 150-140 ka) which terminated within the limits of the Drenthe glacial maximum (Toucanne et al., 2009; Ehlers et al., 2011; Ehlers and Gibbard, 2004). To the east, a period of Saalian ice advance in central Russia deposited the extensive Moscow till, which is now commonly ascribed to MIS 6 (Shik, 2014), although chronological uncertainty means it remains unresolved how this glacial deposition correlates to the advance/retreat phases in the west. It is reasonable to assume that the Penultimate Deglaciation of the Eurasian ice sheet may have been asynchronous, as it was during the Last Deglaciation (Patton et al., 2017), with parts of the ice sheet reaching its maximum position at the same time as other areas retreated. This difference in timing and extent would result in a differing pattern of solid Earth displacement and RSL change during the LIG, in both the near and far field, compared to the Holocene (Cohen et al., 2022; Dendy et al., 2017; Lambeck et al., 2006; Rohling et al., 2008). However, to better constrain this, more chronological data are needed to reconstruct the spatially variable timing and extent of the ice load during the PGP across Europe (Lauer and Weiss, 2018).

Previous work reconstructing the configuration of the Eurasian ice sheet has primarily focused on the Last Deglaciation (Clark et al., 2022; Gowan et al., 2021; Patton et al., 2016; Peltier et al., 2015; Tarasov et al., 2012) with some notable exceptions extending to the Penultimate Deglaciation (Colleoni et al., 2016; Lambeck et al., 2006). Ice-sheet reconstructions can be categorised as either 2D, which aim to outline the ice sheet extent, or 3D, where the geometry (thickness and extent) of the ice sheet is estimated. Detailed 2D reconstructions of the Last Deglaciation have been compiled from available geomorphological constraints describing the full chronological evolution of the ice sheet at high temporal resolutions of up to 0.5 ka (Batchelor et al., 2019; Hughes et al., 2016). By contrast, 2D reconstruction efforts for the Penultimate Deglaciation Eurasian ice sheet are more limited and have focused on the maximum asynchronous ice limit during the Penultimate Glacial Cycle, since intermediary deglaciation margins are difficult to constrain and date with the available geomorphological evidence (Batchelor et al., 2019; Svendsen et al., 2004). 2D reconstructions are limited in their application to GIA modelling since they do not provide ice thickness information.

Three main approaches have been employed to estimate 3D Eurasian ice-sheet geometry, and therefore ice thickness and volume: GIA inversion, dynamic ice-sheet

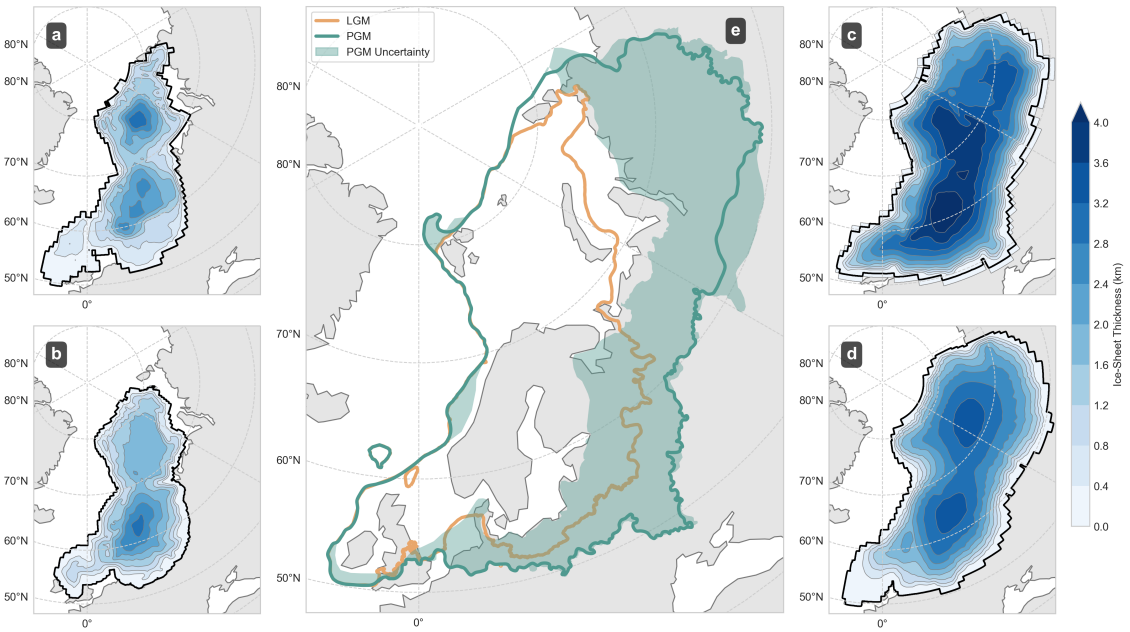

Figure 3.1: LGM and PGM Eurasian ice-sheet reconstructions: (a) 26 ka ICE-6G (Peltier et al., 2015) and (b) 21 ka GLAC-1D (Tarasov et al., 2012) reconstructed Eurasian ice-sheet thickness at their respective maximum Eurasian ice-volume configurations during the Last Glacial Maximum. PGM maximum (140 ka) Eurasian ice-sheet thickness from (c) Colleoni (2009) and (d) Lambeck et al. (2006). (e) Comparison of ice margins from Batchelor et al. (2019), with the green band showing the area between the MIS 6 maximum and MIS 8 best-estimate margins.

modelling, and simple ice-sheet modelling. In the first, solutions to the inverse GIA problem are calculated by tuning a combination of global ice reconstruction, radially varying Earth viscosity, and lithospheric thickness to fit a global set of RSL records and modern Global Navigation Satellite System (GNSS) data. This method has been applied in the generation of numerous Eurasian ice-sheet reconstructions during the Last Deglaciation (Lambeck et al., 2006; Peltier, 2004; Peltier et al., 2015) while also having been applied to the Penultimate Deglaciation (Lambeck et al., 2006). By design, GIA inversion ice-sheet load solutions are consistent with empirical constraints on rebound and sea-level data, when combined with the corresponding adopted viscoelastic Earth structure, but do not ensure physical consistency with known ice-sheet physics, often leading to physically implausible reconstructions.

In the second approach, 3D thermodynamic ice-sheet models, driven by climate forcing, are used to model 3D time-evolving ice-sheet geometry. This approach has been applied to the PGM in combination with a prescribed climate forcing to produce a 3D Eurasian ice-sheet reconstruction that, at equilibrium, matches the Svendsen et al. (2004) Eurasian ice margins (Colleoni, 2009; Colleoni et al., 2016; Peyaud, 2006). In turn, this reconstruction has been used to drive ice-sheet sensitivity experiments (Wekerle et al., 2016). Similarly, Abe-Ouchi et al. (2007)

used a dynamic ice-sheet model, driven by a general circulation model, to model Northern Hemisphere ice sheets over late Quaternary glacial cycles, which are used as boundary conditions for transient climate simulations of PMIP4 (Menviel et al., 2019). In other work, climate-driven thermodynamic ice-sheet simulations have been performed by Tarasov et al. (2012) and Patton et al. (2017), nudged to fit constraints from 2D reconstructions, near-field sea-level data, meltwater history, and climate evolution. While dynamic models ensure more physically plausible ice-sheet geometries they are also dependent on the reliability of the climate forcing used.

Finally, the simple ice-sheet model approach is designed to generate ice geometries that approximate the profile of a steady-state ice sheet for a given margin. This technique has been used in both regional reconstructions, such as the Last Deglaciation of the western Laurentide (Gowan et al., 2016b), as well as global ice-sheet margins (Gowan et al., 2021) during the Last Deglaciation.

The large uncertainties and limited data available from which to constrain the pattern and timing of the Penultimate Deglaciation of the Eurasian ice sheet (Rohling et al., 2017; Ehlers et al., 2011; Hughes et al., 2011) means it must be tackled with robust and efficient methods of uncertainty quantification and parameter sampling for the problem to be tractable (Andrianakis et al., 2015; Astfalck et al., 2021; Williamson et al., 2013). LGM studies show it is possible to use uncertainty quantification techniques, combined with 3D dynamic ice-sheet modelling, to estimate a range of plausible ice-sheet histories (Gregoire et al., 2016; Tarasov et al., 2012; Gandy et al., 2021). However, reliance on poorly constrained rebound data required for GIA inversion modelling (Lambeck et al., 2006) or assumptions of highly uncertain climate data used in dynamic ice-sheet simulations (Abe-Ouchi et al., 2007; Peyaud, 2006) make these approaches challenging to constrain for the Penultimate Deglaciation and give only a very limited view of possible pasts with no grasp on the vast range of plausibility. In addition, computational requirements make quantification of uncertainties intractable if the models used are too complex. Therefore, the fast execution speeds and small number of input parameters make simple ice-sheet modelling a well-suited approach for tackling the challenges of the PGM within a Bayesian uncertainty quantification framework.

In this paper, we develop a new technique to generate plausible Eurasian ice-sheet geometries for the PGM where we have little information on ice thickness and dynamics, accounting for uncertainty, and provide an ensemble of ice sheets that have been systematically tested. We utilise ICESHEET, a simple ice-sheet model whose minimal input requirements enables the production of large ensemble simulations with controlled sources of uncertainty (Gowan et al., 2016a). We demonstrate how the 2D,

uncertain shear-stress input to the model can be parameterised and systematically varied to produce an ensemble of physically consistent ice-sheet geometries. We then test and calibrate the model and input shear-stress map on the Last Deglaciation to rule out implausible input parameters and produce a new simulation of the Eurasian Last Deglaciation in the process. Finally, we apply the information gained from this process to produce ensembles of ice-sheet geometries for the PGM that can serve as input to subsequent GIA modelling to robustly quantify uncertainties.

3.3 Models and Methods

3.3.1 ICESHEET Simulator

ICESHEET is an ice-sheet model (Gowan et al., 2016a) that assumes steady-state conditions and a simple, perfectly plastic ice-sheet rheology to rapidly generate physically plausible ice-sheet reconstructions from only three 2D model inputs: ice-sheet margins, regional topography, and basal shear stress (based upon the physics first developed by Nye (1952), Reeh (1982), and Fisher et al. (1985)). Using an iterative process, ICESHEET calculates thickness profiles along flowlines that are generated at regular intervals within the prescribed ice margin. Flowline positions, and thus the ice-sheet thickness profile, are dependent on the 2D input topography and shear-stress maps (Gowan et al., 2016b). The shear-stress map serves as a tuning input that can be calibrated or inverted to produce a target ice-sheet geometry, although significant uncertainties exist in determining basal shear stress (Sect. 3.3.2).

The model has been applied where large uncertainty in inputs required for dynamic ice-sheet models, such as climate, have reduced the confidence in using the outputs of such models as inputs to sea-level models due to misfits against ice extent and volume distributions that impact GIA, and where large numbers of runs are required making computational efficiency paramount, such as in the exploration of variable global ice-sheet configurations (Gowan et al., 2021). Limited constraints on climatic conditions, the requirement for large ensemble simulations to explore the range of plausible scenarios, and a need for well-defined sources of uncertainty make ICESHEET an ideal choice for exploring uncertainty in ice-sheet configurations during the PGM.

Two model parameters determine the resolution of a reconstruction with ICESHEET: contour elevation interval and flowline spacing. For our reconstructions, we use values of 20 m and 5000 m respectively in order to balance compute time with resolution. The 2D model inputs are defined on a Lambert Azimuthal Equal Area (LAEA) projection centred on lat 90°, long 0°, using the WGS84 ellipsoid, and with boundaries defined at -1265453 m to 4159547 m in the x direction and -4722734.8

m to 1352265.2 m in the y direction with no x or y offsets, covering the Eurasian region at a resolution of 5 km. In the following subsections, we describe the set-up and inputs to simulations of the Last Deglaciation and PGM.

3.3.2 Uncertainty Quantification

ICESHEET, owing to the large uncertainties in the shear-stress input, is capable of producing a wide range of ice-sheet geometries for both the Last Deglaciation and the PGM. While it is useful to retain some of this possible set of geometries for the purpose of uncertainty quantification, not all simulations will fall within our expectations of plausible Eurasian configurations. Existing GIA reconstructions provide constraints on ice-sheet thickness during the Last Deglaciation and it is desirable to transpose this information to the PGM through model calibration. Bayesian uncertainty quantification techniques exist to explore uncertainty and calibrate physical models (Astfalck et al., 2021). However, because the primary input of ICESHEET is the 2D, extremely heterogeneous, and poorly constrained basal shear-stress matrix, “out-of-the-box” methods for sampling uncertain model inputs are unsuitable. Moreover, due to the major simplifications applied within ICESHEET, this 2D input should not only represent ice basal shear stress linked with bedrock geology, but should also encompass the effect of missing ice surface mass balance and the influence of basal processes. Thus, a bespoke framework for quantifying past ice-sheet uncertainty with simple ice-sheet models such as ICESHEET is needed.

We first employ ICESHEET to produce a new simulated history of the Last Deglaciation that we then calibrate against independently derived, regionally aggregated volume metrics for the Last Deglaciation by employing a Bayesian uncertainty quantification method called "history matching". History matching allows us to identify regions of the ICESHEET input parameter space for which ICESHEET simulations are able to match the regional volume estimates that are expressed in published reconstructions (used here as an “observation”) given the uncertainty in the model and target data (Williamson et al., 2015). This space is referred to as the "not ruled out yet" (NROY) space and, once identified using the Last Deglaciation constraints, can then also be applied to refine our set of reconstructions for the PGM where empirical constraints on published models are far more limited. This procedure also allows us to identify systematic differences between the geometry simulated by ICESHEET and those reconstructed through GIA modelling, thus testing the capability of our modelling approach in providing meaningful ice geometries for use in sea-level and climate simulators.

3.3.3 Model Set-Up for the Last Deglaciation

We consider two spatiotemporal reconstructions of Eurasian ice-sheet thickness and regional topography during the Last Glacial Period: GLAC-1D (Tarasov et al., 2012) and ICE-6G (Peltier et al., 2015). These reconstructions have been selected as they are widely used, well regarded, and more accessible than others (Ivanovic et al., 2016; Lambeck et al., 2006; Menviel et al., 2019) while also representing two contrasting modelling methodologies that are both independent of the ICESHEET methodology (Gowan et al., 2021). GLAC-1D is the result of a large ensemble of thermodynamic ice-sheet simulations driven by climate reconstructions that have been nudged and selectively refined to fit RSL records. It is provided every 0.1 ka at a spatial resolution of lat 0.25˚and long 0.5˚(Tarasov et al., 2012). ICE-6G is a solution to the inverse GIA problem and is provided at 0.5 ka after 21 ka, and 1.0 ka before, with spatial resolution of lat 1°, long 1°(Peltier et al., 2015). ICE-6G provides a better fit to sea-level records than GLAC-1D, but the ice geometry is not compatible with ice-sheet physics (Stuhne and Peltier, 2017), while GLAC-1D provides glaciological consistent ice-sheet geometries that account for ice-flow physics and climate forcing (Tarasov and Peltier, 2002). Both reconstructions account for GIA effects, provide accompanying topography inputs, match against RSL data, and include a range of time slices that span the full deglaciation.

We extract the ice margin from each Last Deglaciation reconstruction, for use as input to ICESHEET, to ensure that we are able to accurately compare the difference between thickness slices generated by ICESHEET and those of the reconstruction considered. To do this, we reproject and interpolate each reconstruction onto the same model grid as ICESHEET before applying an algorithm that produces ice-margin geometries from the gridded thickness data (Appendix 3.9.1).

When using ICESHEET to simulate past ice sheets, the input topography needs to be adjusted for GIA. Since our aim is to reproduce ICE-6G and GLAC-1D volumes, we simply use the topography deformation fields provided by each model, reprojected onto our model grid. We run the ICESHEET model with topography and margins from GLAC-1D and ICE-6G, at 22, 20, 18, and 16 ka. These times are chosen since they capture a range of ice-sheet deglaciation thickness and extent configurations while excluding the very thick slices >22 ka, which are poorly constrained by sea-level data, and those of small extent after 16 ka which are less relevant for producing the extensive PGM. We label these simulations ICESHEET_{1D} and ICESHEET_{6G}.

3.3.4 Model Set-Up for the Penultimate Glacial Maximum

3.3.4.1 Ice-Sheet Margin

We generate a range of possible ice-sheet margins based on the late Quaternary ice extent maps produced by Batchelor et al. (2019) derived from a compilation of empirical and modelling evidence, which for MIS 6 includes 25 empirical extent outlines, 40 empirical point-source data points, and 5 modelled ice extents. Batchelor et al. (2019) produce minimum, best-estimate, and maximum extent margins for MIS 6 which primarily differ in extent in Siberia (Figure 3.1). In this work we select three margins in order to explore the uncertainty in the PGM configuration of the Eurasian ice sheet (Figure 3.1). We use the MIS 6 best-estimate margin noting that this represents the maximum extent the ice sheet would have reached at any one time between ca. 190 and 132 ka; however, in the west it most likely corresponds with the Drenthe stage (>150 ka) given the extensive southern ice sheet position in western Europe and the North Sea. We also utilise the MIS 6 maximum margin to explore the uncertainties in the maximum Siberian extent. Given the potential for a smaller ice sheet during the latter part of the Saalian complex (which is not captured in the minimum MIS 6 margin of Batchelor et al. (2019)) we use their MIS 8 best-estimate map as a proxy for a late Saalian ice extent where the maximum ice position in western Europe was further to the north during the Warthe substage (<150 ka). This provides a starting point by which to explore the uncertainty in the PGM configuration, which can only be furthered with improved temporal and spatial constraints.

Margin extent is included as a continuous parameter in our experimental design that varies between 0 and 1, where values of 0, 0.5, and 1 correspond to the minimum (MIS 8 best-estimate), most likely (MIS 6 best-estimate), and maximum (MIS 6 maximum) extents respectively. Values that fall between these points represent intermediary margins between the three configurations which we generate by employing a novel shape-interpolation algorithm we have developed for this purpose. Since the Batchelor et al. (2019) MIS 6 best-estimate reconstruction is restricted to the subset of their data that they judge to have the highest reliability, we apply a normal probability distribution to our margin extent parameter, centred around 0.5, to ensure that margins closest to this best estimate are most common in our ensemble.

3.3.4.2 Topography

For simulations of the Last Deglaciation, we employ pre-existing models of topography changes due to GIA as provided with the adopted GLAC-1D and ICE-6G ice histories for use as input to ICESHEET. For the PGM no such pre-existing GIA deformation

model exists for our ice load and yet GIA-driven changes in topography beneath the ice sheet play an important role in determining ice-sheet geometry, contributing up to a 20% increase in total ice volume over the Penultimate Glacial cycle relative to a simulation where topography remains fixed (Gowan, 2014). In order to account for GIA, we first estimate the topographic deformation field that would result from the solid Earth underneath the Eurasian ice sheet being at (or close to) isostatic equilibrium with the ice load. To estimate this fully compensated topography associated with a given load, we adopt the fully relaxed form of the simple Elastic Lithosphere Relaxing Asthenosphere (ELRA) model (Huybrechts and de Wolde, 1999):

$$
\begin{aligned}
w_q(r) &= \frac{qAL^2}{2\pi D}\mathrm{kei}\left(\frac{r}{L}\right) \\
q &= \rho_i g h \\
L &= \left(\frac{D}{\rho_b g}\right)^{\frac{1}{4}}
\end{aligned}
$$

where h is the thickness of the ice, g is the acceleration due to gravity (9.81 m s^{-2}), ρ_i is the density of ice (916 kg m^{-3}), q is the applied ice load, w_q is the solid earth response to loading at a radial distance r from the load, A is the area of an applied load cell, L is the flexural rigidity length scale, ρ_b is the bedrock density (3300 kg m^{-3}), and D is the flexural rigidity of the lithosphere (1025 N m).

The assumption of full compensation could be considered reasonable, given the lack of constraints during this time, if the ice-sheet maximum configuration endured for a sufficiently long duration. However, in order to account for the possibility of partial deformation, we include a continuous scaling parameter in our ensemble that scales the fully relaxed deformation field, ranging between 0.475 and 1, for a given ice-sheet load such that lower values result in a smaller magnitude of deformation. The lower bound of this parameter is constrained by comparing the (partially relaxed) topography at 20ka predicted in the GLAC-1D model to a calculation of the fully compensated topography that would result from inputting the GLAC-1D ice cover at 20ka and modern topography into the equations above.

In order to approximate topography deformation at the PGM, we begin by reprojecting the RTopo-2 modern-day global topography (Schaffer et al., 2016), originally provided at a 0.5 degree resolution in latitude-longitude coordinates, onto the LAEA model domain, interpolating onto our chosen Eurasian grid at a 5 km spacing, and applying a 1σ Gaussian blur in order to smooth any sudden changes in elevation. This smoothing is required because ICESHEET can fail to run if large topography

gradients are present when calculating flowline shapes. Following the approach of Gowan et al. (2021), we run ICESHEET with this modern-day topography to calculate an initial ice-sheet thickness which is then used as the load input to the ELRA model in order to calculate the resulting deformed topography. This new deformed topography is then scaled by the topography parameter before being used as input in a second iteration run of ICESHEET in order to calculate the resulting ice-sheet thickness.

3.4 Parameterising the Shear-Stress Input Map

The primary control and biggest source of uncertainty in ICESHEET is the 2D input shear-stress map. The presence, composition, and thickness of deformable sediments underneath an ice sheet impacts the friction at the ice-bed interface, which, in turn, affects the flow of ice and thus the local ice-sheet thickness and geometry. Nye (1952) originally related these quantities by balancing the shear stress at the base of the ice sheet with the driving stress which, after expansion by Reeh (1982) and Fisher et al. (1985), was modified to include the impact of topography. Studies employing this theory have used surface geology data to develop maps of shear stress (Fisher et al., 1985; Gowan et al., 2021, 2016b).

The shear stress values can be calibrated or inverted to match a target ice geometry or varied to predict a range of plausible geometries. However, random sampling of such 2D inputs within the context a Bayesian uncertainty quantification framework presents a significant challenge since the number of independent parameters likely make experiments computationally unfeasible. To simplify this problem, studies typically employ one of two approaches to deal with 2D inputs: random error field generation, or parameter decomposition. In the first approach, each value within the 2D input is modelled as having an error described by a probability density function and spatial autocorrelation which, together, allows for the random generation of 2D error fields. When summed with the original values, error fields represent possible realisations of the 2D input (Zhao and Kowalski, 2020). Alternatively, the approach of parameter decomposition aims to reduce the number of parameters by collecting groups of values with similar properties that together could be assumed to represent spatial collections of homogeneous behaviour, and that can therefore be varied as a single parameter.

In a similar manner to parameter decomposition, previous studies have divided their study area into a set of geographic regions that are each assumed to have the same internal average shear-stress value (Gowan et al., 2021, 2016b). The shear-stress

values are chosen to reflect a combination of known accumulation rates, with lower values used for areas that have higher moisture scarcity; evidence of ice thickness including GPS uplift rates; knowledge of underlying sediments which inform the deformability of the bed; topographic elevation (Fisher et al., 1985; Gowan et al., 2016b; Reeh, 1982); and, in some cases, modified in order to fit a database of known RSL data (Gowan et al., 2021, 2016b). However, this approach still produces a complex mosaic of independent regions that are too numerous to incorporate into a Bayesian uncertainty framework. To overcome this, we also decompose our study area into geographic regions of similar shear stress, derived from geological maps and satellite data but we choose not to follow the approach of previous work in converging on a single tuned shear-stress input. This is because, firstly, such an approach results in a single 'best-fit' ice-sheet simulation output and, secondly, lacks the possibility of rigorous uncertainty quantification since such analysis with many independently varying shear-stress regions becomes intractable. Therefore, we instead opt to incorporate the uncertainty inherent in the shear-stress values of similar regions, enabling the production of a range of ice-sheet simulations by propagating uncertainty through our ensemble.

3.4.1 Sediment Distribution

In this paper, we adapt a basal shear-stress map, developed for Eurasia during the Last Deglaciation, utilised in Gandy et al. (2018) and Clark et al. (2022). This map was constructed by dividing the bed of the Eurasian ice sheet into distinct surface geological and geomorphological units, in consultation with geological mapping, sediment thickness maps, and the distribution of glacial landforms observed by satellite imagery and digital elevation models. In the original map, five landscape categories were distinguished: i) palaeo-ice streams; ii) marine sediments; iii) thick and iv) thin terrestrial Quaternary sediments, as indicated by subglacial bedforms and on sediment maps; and v) exposed bedrock surface (Gandy et al., 2018).

Due to uncertainties in the identification of such sediment categories during the PGM, we modify the original map in four ways to make it applicable to modelling the Penultimate Deglacial history and to keep our quantification of uncertainties tractable: (i) merging the original continuous sediment and discontinuous sediment categories into a single 'onshore' category to reflect the lack of evidence to constrain the location of regions of discontinuous sediment during the PGP; (ii) defining the underlying sediment type for each ice-streaming region so that their length may be altered and the underlying sediment revealed (Sect. 3.4.2); (iii) adding additional ice-streaming regions in the eastern sector and creating a separate ice streaming layer for the PGM (Sect. 3.4.3); (iv) expanding the southerly and easterly extent of the

map to encompass the greater Eurasian PGM ice-sheet extent. Regions within our adapted map are therefore categorised by their underlying sediment in the absence of ice streaming (Figure 3.2a) as well as their potential to ice stream during the PGM and Last Deglaciation (Figure 3.2b)

Each category has an associated shear-stress value uncertainty range, derived from our expert judgement, and described in Table 3.1. The larger extent of the Eurasian ice sheet during the PGP means that we require a shear-stress map that extends further south, into Continental Europe, and further east towards Siberia. We designed these additional regions based on a digitally compiled maps of geology (Persits et al., 1997) alongside modern satellite imagery. Our final shear-stress map for Eurasia for the PGP consists of 740 categorised regions (Figure 3.2).

3.4.2 Ice Streaming

Ice streams are corridors of fast-flowing ice that occur towards the exteriors of ice sheets and significantly reduce local ice thickness (Stokes and Clark, 2001). It is important that these regions are represented explicitly in ICESHEET, as the model lacks the dynamic mechanisms needed to generate ice streams on its own (Hindmarsh, 2009; Gandy et al., 2019), and thus they are instead included as areas of very low shear stress. This enables ICESHEET to capture their main effect for GIA models, to reduce regional ice thickness. Evidence for the configuration of historic ice streaming relies on the identification of flow patterns, shapes, and deformed bed conditions within the geomorphological record (Stokes and Clark, 2001, 1999). Ice-stream margin features can be dated (e.g. radiocarbon, cosmogenic nuclide, or optically stimulated luminescence) in order to infer the time the associated ice stream was active (Bentley et al., 2010; Stokes et al., 2015). Identifying and dating ice-streaming regions during the PGP poses a greater challenge compared to the Last Glacial Period as the period pre-dates the application of ^{14}C methods and much of the sediment left behind by streaming has been removed by subsequent glacial activity. This is especially true for the southern margin of the Eurasian ice sheet (Joon et al., 1990; Laban, 1995; Sokołowski et al., 2021). By comparison, the extent-limiting influence of the continental shelf break and topography of troughs on the shelf increases confidence that ice streaming in the northern PGP Eurasian ice sheet was similar to those of the Last Glacial Period.

We represented ice streams in our shear-stress map with a low shear stress value. To reflect the differences in streaming configurations as well as the disparity in geospatial constraints between the two glacial periods, we produce two separate maps of ice streaming during the Last Glacial Period and the PGP. The PGP layer is identical to

the Last Glacial Period layer in the north, except for the addition of two streaming regions in the northeast, since the Eurasian ice sheet reached a similar extent during both glaciations (Figure 3.1). However, we completely remove ice streaming along the southern region in the PGM sheet stress map since evidence constraining streaming positions during the PGP is sparse, while the larger extent of the PGM ice sheet (Figure 3.1) means the mapped Last Glacial Period ice streams do not apply as they would terminate within the interior of the ice sheet.

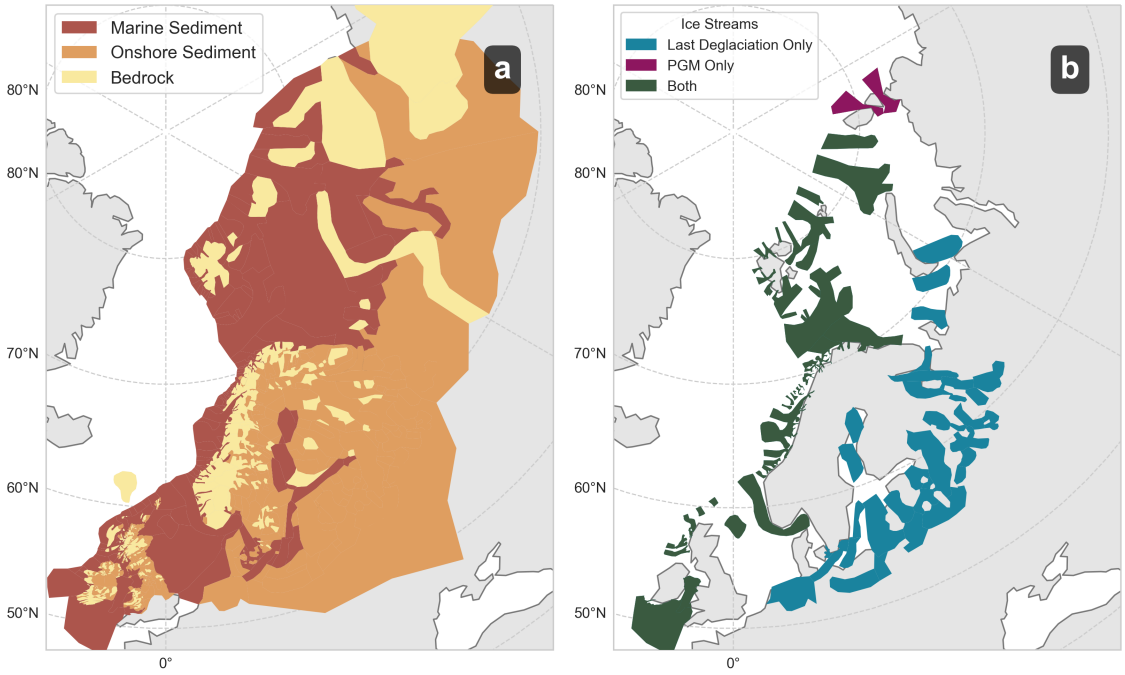

Figure 3.2: Components of the shear-stress Map: (a) Underlying sediment category, which is used in the absence of overlying basal modification, shown for each region. (b) Regions capable of ice streaming, which is represented in our model by a low shear stress, for the Last Deglaciation (blue), for PGM (purple), and for both (green).

3.4.3 Ice-Sheet Influence on Basal Conditions

Prescribing shear-stress values based on geological surface type ignores the influence of basal conditions on sliding (Tsai et al., 2015; Weertman, 1957). However, the basal conditions can influence the effective shear stress and, in turn, affect the geometry of an ice sheet. In order to better capture ice-sheet basal interactions we account for the influence of three such effects: cold based ice, active ice streaming, and hybrid ice streaming. The first approximates the effects on basal conditions when ice becomes frozen to the surface in the central interiors of large ice sheets (Bierman et al., 2015). Cold-based ice has a high effective shear stress whether the bed is made of hard bedrock or soft sediment. The cold-based ice modification introduces this idea through two parameters. The first controls the size of the cold-based region (modelled as distance of unfrozen region from the margin), ranging from between

300 and 1000 km (Figure 3.3b). The upper limit matches the maximum distance from the margin at the PGM, resulting in no cold-based ice, while the lower limit stops cold-based ice forming at the margin within the range of likely ice streaming. Secondly, we control the shear stress value of the region with a parameter ranging between 120 and 200 kPa.

Ice streaming occurred at different times and locations through the Last Deglaciation of the Eurasian ice sheet (Figure 3.2b). Ice streaming is also likely to have occurred during periods of ice-sheet advance or retreat throughout the Preceding Glacial (Lang et al., 2018), but a limited amount of geomorphological evidence means it is much harder to constrain when and where. As discussed above, it is not sufficient to simply use the LGM ice-stream locations, as these ice streams may not reach the PGM margin and it is not realistic to have an ice stream that terminates within the ice sheet. We therefore introduce an "active ice-streaming distance" parameter for the northern portion of the ice sheet to restrict ice streaming to within a particular distance of the margin ranging between 0 and 1000 km, based upon work by Margold et al. (2015), and thus induce a marginal dependence on the previously static shear-stress input (Figure 3.3a). We also introduce a hybrid ice-streaming modification to represent the shear-stress values that would result from streaming at the southern margin without exact prescription of stream locations. We define a distance from the margin that represents the average length of an ice stream ranging between 0 and 600 km (Margold et al., 2015; Stokes and Clark, 1999) (Figure 3.3c), and also prescribe a shear-stress range whose minimum and maximum values are dependent on the shear-stress values for ice streaming and onshore sediment respectively, acting as a proxy for ice-stream density.

In addition to better capturing the resulting shear-stress implications of basal-driven interactions, the introduction of these three basal modifications allows us to expand the range of ice-sheet geometries and volumes that can be produced by ICESHEET for a given margin; and to improve the physical plausibility of the shear-stress input by increasing the dimension of our parameter space improving our ability to calibrate the model output and widen the range of uncertainty that can be considered. In total, we describe our shear-stress input through 9 parameters.

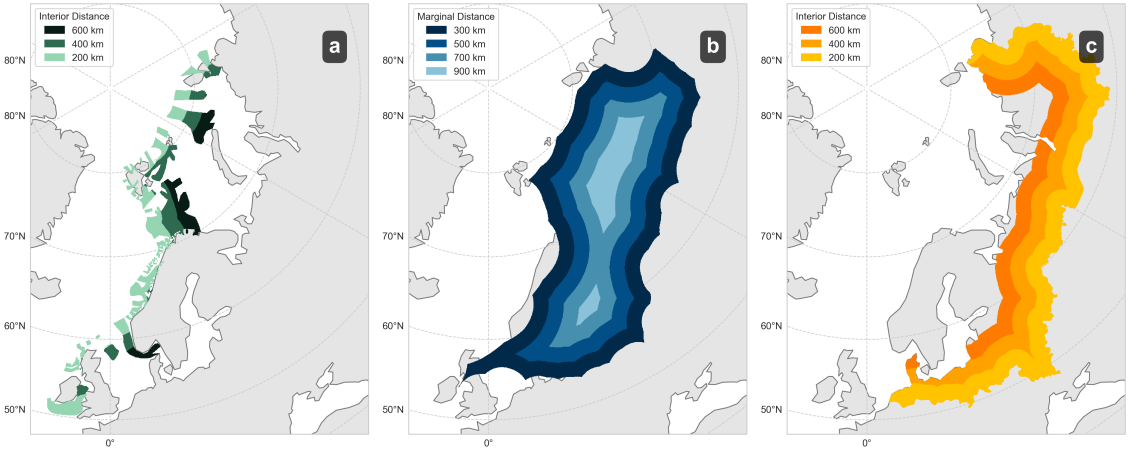

Figure 3.3: Shear-stress basal modifications demonstrated using the PGM map and margin: (a) Map of active PGM ice streams for different values of the interior distance parameter. (b) Map of PGM cold-based region for a range of marginal distances, which introduces a frozen bed sector at the interior of an ice sheet. (c) Map of PGM hybrid ice-streaming region for a range of interior distances that approximates ice streaming at the southern margin of the ice sheet.

Table 3.1: Parameters controlling the model inputs for ICESHEET and their corresponding value ranges sampled in our ensemble of simulations.

Parameter Name	Value	Unit	Model Input	Time Period
Margin Extent	0.0 – 1.0	1	Margin	PGM
Topographic Deformation	0.475 - 1.0	1	Topography	PGM
Marine Sediment Shear Stress	10 – 30	kPa	Shear Stress	PGM & LD
Onshore Sediment Shear Stress	30 – 100	kPa	Shear Stress	PGM & LD
Bedrock Shear Stress	100 – 150	kPa	Shear Stress	PGM & LD
Ice Streaming Shear Stress	5 – 20	kPa	Shear Stress	PGM & LD
Ice Streaming Interior Distance	0 – 1000	km	Shear Stress	PGM & LD
Cold Based Ice Shear Stress	120 – 200	kPa	Shear Stress	PGM & LD
Cold Based Ice Marginal Distance	300 – 1000	km	Shear Stress	PGM
Hybrid Ice Streaming Shear Stress	5 – 100	kPa	Shear Stress	PGM
Hybrid Ice Streaming Marginal Distance	0 – 600	km	Shear Stress	PGM

3.5 Last Deglaciation Reconstruction and Calibration

3.5.1 Ensemble Design

We employ a random LHS design to select a 200-member set of input parameter values from the 7D parameter space controlling the shear-stress input (Table 3.1), after excluding hybrid ice-streaming shear-stress and marginal distance parameters since the position of southern margin ice streams are prescribed for the LGM (Figure 3.2b). LHS is a design method, common in Bayesian uncertainty quantification, that efficiently explores the input parameter space to construct ensembles of model simulations (Gregoire et al., 2016; Williamson et al., 2013, 2015). It is typical to sample a minimum of 10x the number of parameters, but a higher sample density is beneficial, particularly if parameter ranges are wide and poorly constrained, hence our large sample design. For each reconstruction and time period, this parameter set is used in combination with the extracted ice margin to generate a corresponding shear-stress map. We run 200 simulations for each reconstruction and each of the 4 selected time periods (22, 20, 18, 16 ka), totalling 1600 simulations (Figure 3.5 and Figure 3.10).

3.5.2 Calculating Implausibility

GIA models are sensitive to regional distributions of ice-mass loading more so than localised differences in the ice-sheet profile. Since our work is aimed towards developing a GIA ice-sheet input, we choose to assess and calibrate ICESHEET against the ice-sheet volume integrated over three ice-sheet regions which allows us to assess volume difference at a regional scale, rather than over the whole ice sheet or cell-by-cell: Barents-Kara Sea, British-Irish, and Fennoscandia (Figure 3.10). To assess the model simulations against ICE-6G and GLAC-1D, we use an implausibility metric routinely used in history matching (Williamson et al., 2013). The implausibility is akin to a root mean square error normalised by a measure of acceptable discrepancy between a given observation z and modelled value $\mathcal{F}(\hat{p})$, where $\mathcal{F}$ is the model and $\hat{p}$ is a set of model parameters, for a quantity of interest (e.g ice volume) given the known uncertainty in the observation and model limitations. The difference between an observation z and the real system y is quantified by the observational error e, such that $z = y + e$, while the difference between the modelled value at the theoretical best set of input parameters $\hat{p}^*$ and y is quantified as the structural model discrepancy ϵ, such that $\mathcal{F}(\hat{p}^*) + \epsilon = y$ (Vernon et al., 2022; Bower et al., 2010; Williamson et al., 2017). Additionally, it is often necessary to be able to

predict values of $\mathcal{F}(\hat{p})$ by training an emulator $f(\hat{p})$, such that $\mathcal{F}(\hat{p}) = f(\hat{p}) + \omega(\hat{p})$, where $\omega(\hat{p})$ is the emulation uncertainty, to facilitate denser sampling of the model parameter space than is feasible through direct model runs. Here, we emulate multiple quantities i corresponding to volumes of the Eurasian ice sheet over each of the three regions for each time step and margin series. For each quantity i, the implausibility I_i of the model for a given parameter combination $\hat{p}$ is expressed as

$$I_i(\hat{p}) = \sqrt{\frac{(E(f_i(\hat{p})) - E(\epsilon_i) - z_i)^2}{F(Var(e_i) + Var(\epsilon_i)) + Var(\omega(\hat{p}))}}, \tag{3.1}$$

where E is the expectation (i.e. mean), Var is the variance, and F is a scaling factor for the model and observational uncertainties (see explanation below).

In lay terms, the implausibility represents the discrepancy between the "best guess" (i.e. expectation) of the model emulator $E(f_i(\hat{p}))$ and the observation z_i, accounting for systematic model bias (represented by the term $E(\epsilon_i)$) and scaled by the sum of the uncertainties in the observation, model and emulator. Thus, implausibility is large if the discrepancy between model and observation is large relative to the uncertainties.

As explained at the start of this section, the quantities of interest that we emulate and calculate implausibility for are the ice-sheet volumes at each simulated time, region, and margin series (GLAC-1D and ICE-6G), resulting in 24 quantities. We derive the "observed" regional ice volumes z_i for each of these quantities from the ICE-6G and GLAC-1D reconstructions; obtain each set of $\mathcal{F}_i(\hat{p})$ from the corresponding ICESHEET model ensemble; and train a Gaussian process emulator f_i for each quantity, resulting in 24 emulators of ice volume.

$E(f_i(\hat{p}))$ and $Var(\omega(\hat{p}))$ are calculated as the mean and variance from the emulated volumes $f_i(\hat{p})$, where $Var(\omega(\hat{p})) = 0$ and $E(f_i(\hat{p})) = \mathcal{F}_i(\hat{p})$ for values of input parameters $\hat{p}$ run in the original ICESHEET ensembles. The model bias $E(\epsilon_i)$ and structural uncertainty $Var(\epsilon_i)$ are estimated as the mean and variance of the residuals from the 20 ICESHEET ensemble members with the lowest RMSE against the corresponding GLAC-1D and ICE-6G thickness fields. Since we only have two target reconstructions of ice volume from GLAC-1D and ICE-6G, we choose to estimate $Var(e_i)$ as half the difference between the GLAC-1D and ICE-6G volumes for a given region and time, knowing that this quantity underestimates the true uncertainty in the observations. We therefore choose to augment the observation and model structural uncertainties by 20%, by setting $F = 1.2$. The choice of regional ice-sheet volumes as our metrics, the selection of the F value, and judgement of

their impacts of parameter space refinement, comprise an iterative process and other applications may choose different metrics or tolerance for model discrepancy.

Following from Equation 3.1, we combine our implausibility metrics into a single implausibility $I(\hat{p})$ for a given set of input parameters $\hat{p}$ such that,

$$I(\hat{p}) = \frac{1}{N} \sum_{i} I_i(\hat{p}), \tag{3.2}$$

where $N = 24$ is the total number of implausibility metrics. In other words, the overall implausibility is set as the mean of the implausibilities calculated for each time, region and margin.

$I(\hat{p})$ is therefore an average measure of how well a particular set of input parameters is able to produce an output via ICESHEET that matches our expectation of ice-sheet volume for each region, time, and margin considered. We restrict our NROY space to parameter values that correspond to model runs with implausibility $I(\hat{p})$ less than 3, following the Pukelsheim (2012) three-sigma rule typically used in Bayesian history matching (Andrianakis et al., 2015; Williamson et al., 2015).

3.5.3 Results

GLAC-1D and ICE-6G reconstructions have volume estimates of comparable magnitudes for each time considered, with ICE-6G having a volume of 105.0%, 97.0%, 112.5% and 115.3% of that of GLAC-1D for 22, 20, 18, and 16 ka respectively. However, the extent of ICE-6G is larger with an area of 120.4%, 118.6%, 133.4%, and 143.2% of that of GLAC-1D for 22, 20, 18, and 16 ka respectively. It appears that producing the smaller ICE-6G area-to-volume ratio is challenging for ICESHEET when used with our shear-stress map. This means that, prior to correcting for an estimate of model bias, nearly all ICESHEET_{6G} ensemble members overestimate the volume of ICE-6G margins, whereas the ICESHEET_{1D} distributions commonly encompass the target GLAC-1D volume. Overall, for most regions and times, the reconstruction target ice volume falls within the distributions of modelled volumes, often towards the lower values. There is a significant lack of overlap between the ICE-6G target ice-sheet volume and the reconstructed volume using ICE-6G margins in the British-Irish sector. This model-data discrepancy is accounted for in the prescription of the model bias correction (Equation 3.1) which reduces the influence of this misfit on the overall implausibility metric. The algorithm used to extract ice-sheet margins from the target reconstructions leads to some differences in extent, such as an overestimation in the Barents Sea extent at 16 ka (Figure 3.5i,j). This is a result of the smoothing procedure applied during margin creation which can lead

to underestimation where there are small thickness protrusions, and overestimation at some concave margin edges.

Before applying our criteria for implausibility, we find that the 200-member ensemble generated for the Last Deglaciation has a mean implausibility of 4 ± 2. After removing members with implausibility of greater than 3, we find that 116 members have been excluded, leaving 42% of parameter points within the NROY space, and a new mean implausibility of 2.1 ± 0.4. The NROY space favours reduced ice-sheet volumes with all times considered for ICESHEET$_{1D}$ and ICESHEET$_{6G}$ exhibiting a reduction in average total volume compared with the original distributions (Figure 3.4). In this work, we express ice-sheet volumes in terms of sea-level equivalent (SLE) volume which we calculate by dividing a given ice-sheet volume by modern ocean area. We find that the largest mean percentage reduction in volume is for the Fennoscandian region of the ICESHEET$_{6G}$ 18 ka margin at -16%, while the least reduced is the British-Irish region of the ICESHEET$_{1D}$ 16 ka margin at -4%. The maximum volume across all margins and times is reduced from 29.7 m to 21.1 m after history matching, with the minimum increased slightly from 8.7 to 8.9 m SLE (Figure 3.4).

Prior to applying the bias correction fields, ice-sheet thickness in the interior of the Barents-Kara Sea region is consistently underestimated over all margins and times, potentially due to the lack of modelled dynamics that are important for marine ice sheets, but shows lower variance than other regions (Figure 3.13). The largest variance occurs in ice-sheet thickness in the centre of the Fennoscandian region. However, thickness in this region appears to be over-estimated in ICE-6G and under-estimated in GLAC-1D simulations. In addition, both target reconstructions position ice-sheet domes slightly towards the marine margins and exhibit thinner continental marginal ice. This likely reflects the larger accumulation of snow closer to the coast and the influence of a rain shadow in reducing accumulation towards the interior. By contrast, since ICESHEET does not see the effect of climate on the ice-sheet geometry, our simulated position of the ice dome is very central, yet this discrepancy is consistent between model and reconstructions and of a similar order of magnitude to the discrepancy between the two target reconstructions. The ice thickness at the margin is systematically greater in our simulations than in both reconstructions. Because of our choice of metric, history matching against regional volume, we therefore prefer ice sheets that are thinner in the interior and thicker at the edges but a different target metric would rank simulations differently, such as max thickness which would likely select thinner overall simulations. Regional differences also exist in post-history matching mean model performance after removal of the model bias field. GLAC-1D and ICE-6G remain respectively under and overestimated, while the primary misfit is now in the centre of the Fennoscandian

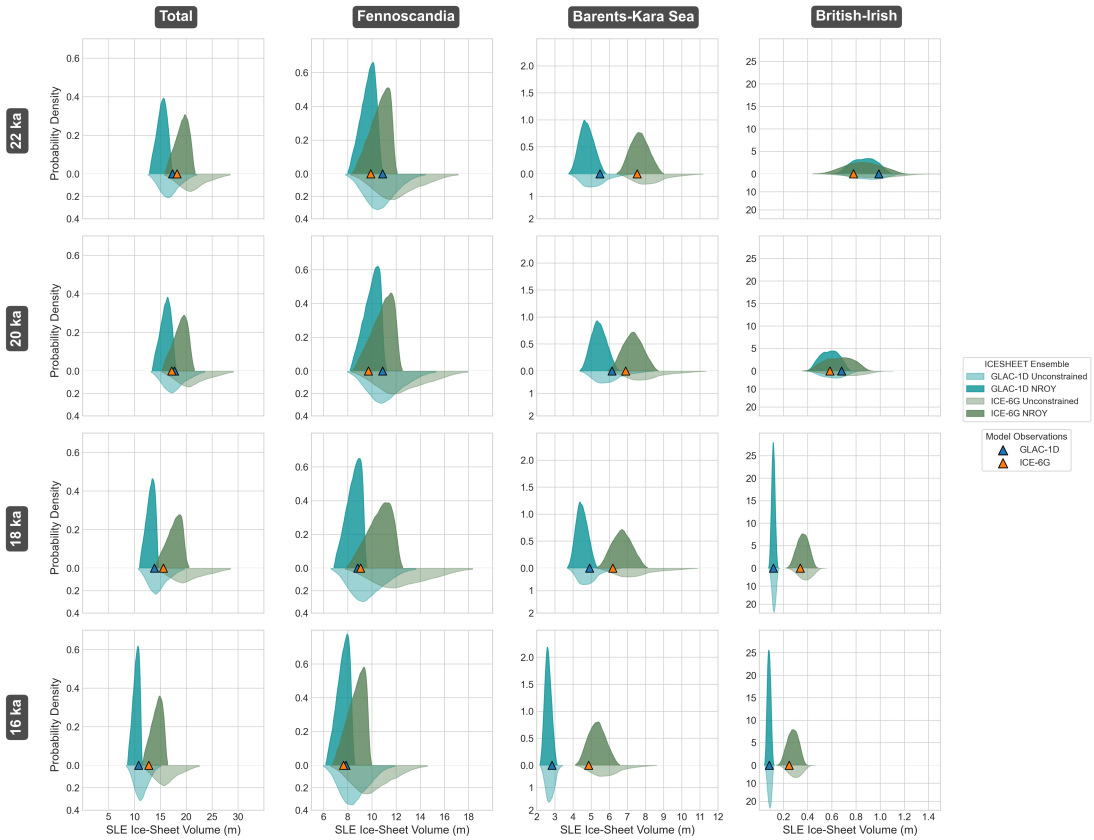

Figure 3.4: Deglacial ice-sheet volume probability density functions, derived from a 10^5-member sample from the quantity's associated Gaussian process emulator, for each region (total, Barents-kara Sea, Fennoscandia and British-Irish) and time (16, 18, 20, and 22 ka) after correcting for model bias. ICESHEET$_{1D}$ (blue) and ICESHEET$_{6G}$ (green) are shown separately for both before (lighter shade, below) and after (dark shade, above) applying the history matching NROY parameter constraint. The blue and orange triangles show the target regional ice volumes from the ICE-6G and GLAC-1D reconstructions respectively.

ice sheet, likely due to the large disagreement between GLAC-1D and ICE-6G in this region.

To better understand the relationship between implausibility and the shear-stress input parameter values, we generate an optical depth image which reveals the shape of the NROY region within our parameter space (Figure 3.6). This image shows the density of NROY parameter values, and the minimum implausibility, across each of the 21 faces of the 7D parameter hypercube. Each face is associated with a parameter pair and consists of 1600 (40x40) pixels. For a given face, each pixel represents 2 fixed values for the 2 parameters associated with the face, and the pixel NROY density and minimum implausibility values are derived from a 1000-member random sample of the 5 remaining unfixed parameters. Each 1000-member sample is evaluated using the 24 Gaussian process emulators in order to calculate their

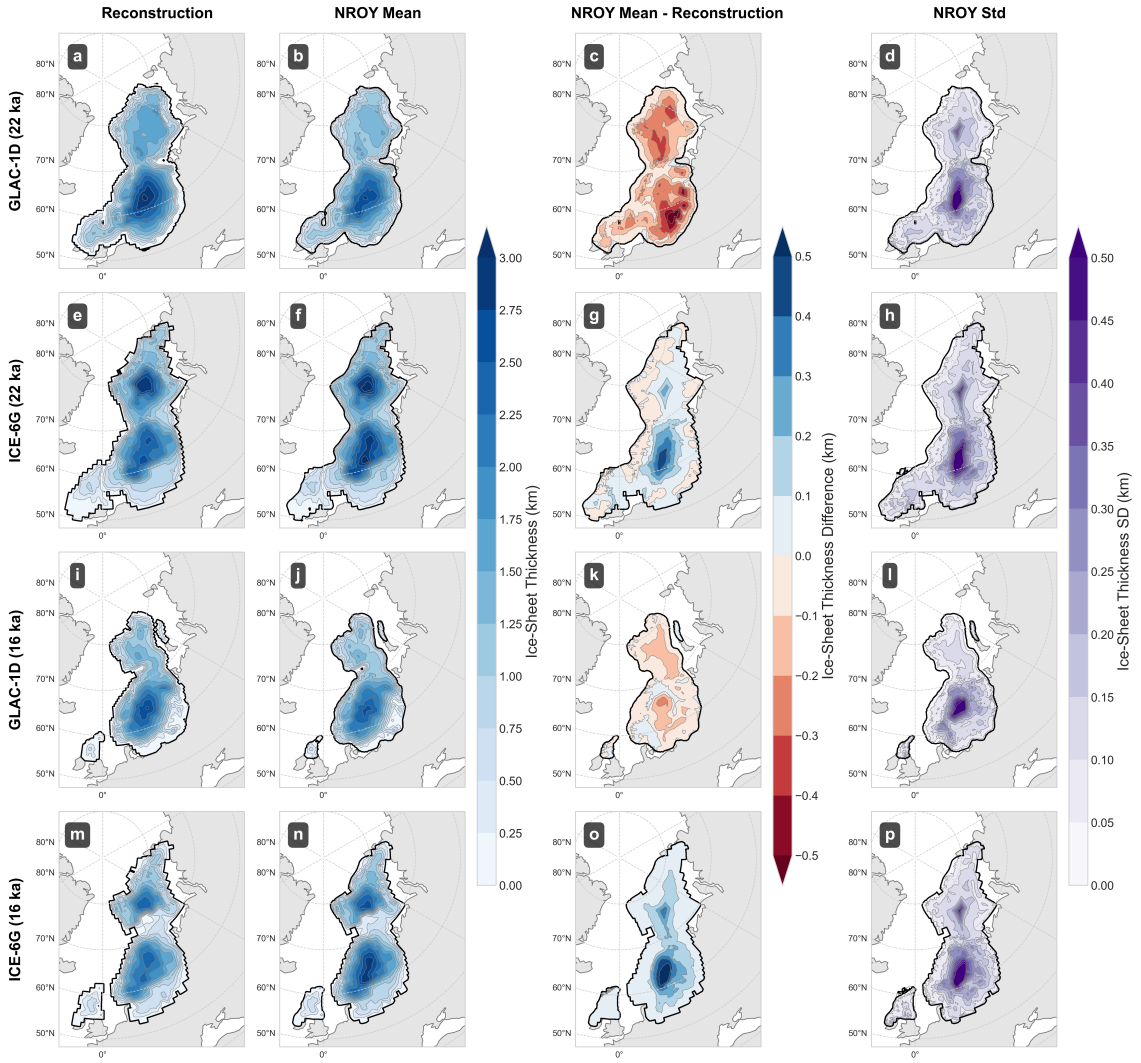

Figure 3.5: Comparison of the constrained NROY ensemble of ICESHEET$_{1D}$ and ICESHEET$_{6G}$ simulations, with model bias removed, against the GLAC-1D (first row: a-d) and ICE-6G (second row: e-h) reconstructions respectively, for the 22 ka time slice. (a) GLAC-1D target reconstruction. (b) Mean of the NROY ensemble of ICESHEET model outputs, with model bias removed, using the margin derived from a. (c) Difference between our ensemble mean (b) and the target reconstruction (a). (d) Standard deviation of this ensemble. Panels (i)-(p) are as in (a)-(h) but for the 16 ka time slice.

associated implausibility values, meaning that each face in the 21-face image is the result of 38.4 million emulator evaluations.

Our analysis reveals that there is a slight preference for lower ice-stream and marine shear-stress values and a relatively strong preference for onshore shear stress values (Figure 3.6). This is likely due to the smaller ice-sheet geometries that these lower values result in. Bedrock shear-stress values show no clear relationship indicating insensitivity of our regional ice-sheet volume metrics to this parameter. This may

be due to the small relative area covered by bedrock, in contrast to other types of shear-stress categories, resulting in a limited impact on ice-sheet volume.

We see a strong indication that lower values of onshore sediment shear stress (mean of 55.3 ± 19.6 kPa), and higher values of cold-ice interior distance (mean of 786 ± 138 km) are favourable (Figure 3.6). A large value of the cold-ice interior distance parameter will produce a smaller area of cold-based ice, since this distance is defined from the margin inwards, and thus such runs will produce smaller ice-sheet volumes that have lower implausibility. In addition, lower overall shear-stress values are shown to be more realistic in most cases but we do not see the same relationship with cold-ice shear stress and bedrock, as this model seems insensitive to these parameters. Finally, a preference for higher values of ice-streaming interior distance (mean of 627 ± 244 km), indicates that longer ice streams, and therefore thinner ice, are preferred. We find that these parameter distributions are common throughout the deglaciation, but with a stronger influence of cold-ice interior distance for smaller ice sheets in the later deglaciation stages. We hypothesise that is a result of the ice sheet being in a state of climate disequilibrium in the later stages of the deglaciation which may have caused a thick yet narrow ice-sheet geometry due to ice melt at the margins while the thick interior is still present. We also observe a larger influence of marine sediment shear stress on models with a greater margin extent because smaller extents have less ice that covers marine sediments.

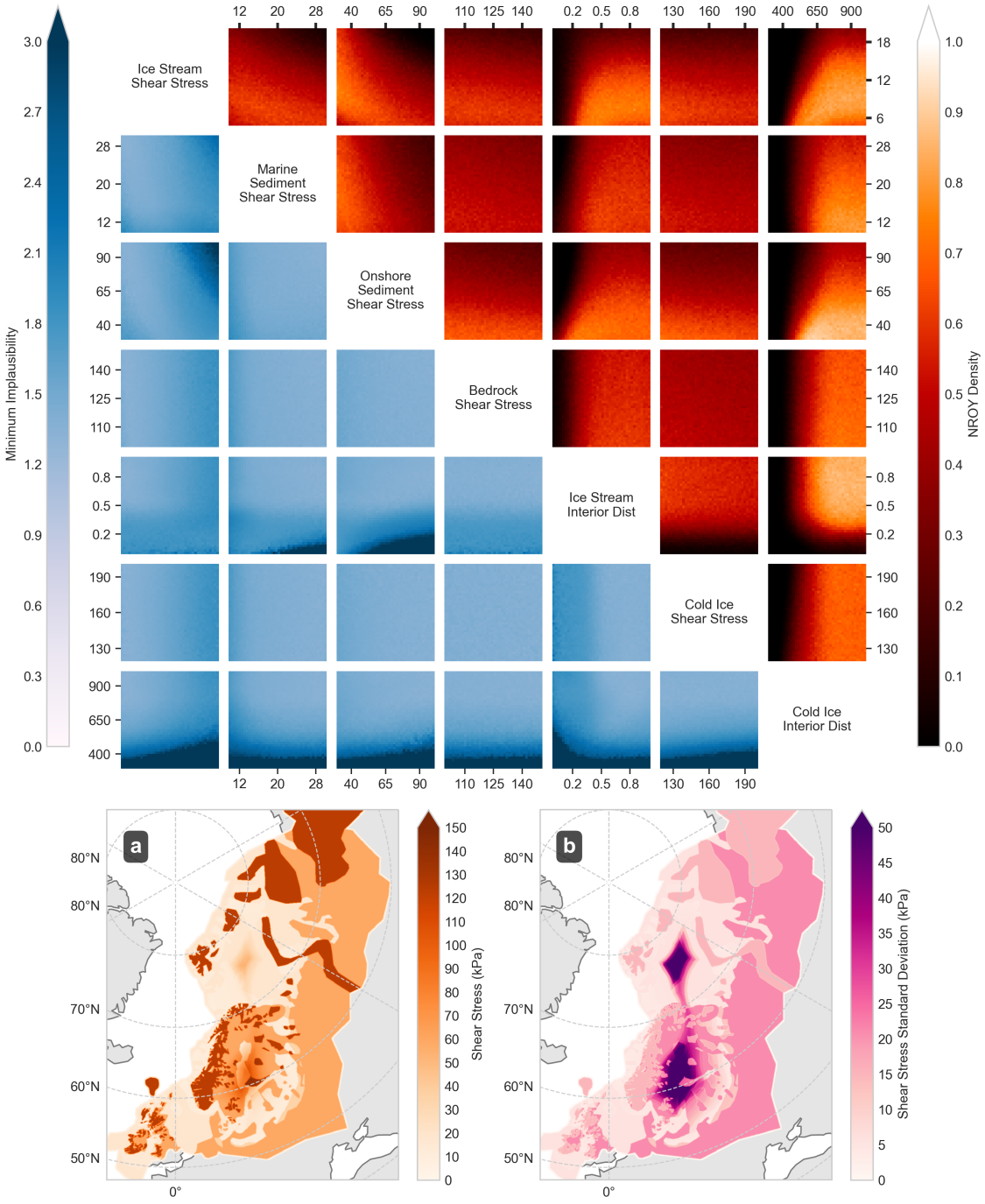

Figure 3.6: Shape of the NROY parameter space (Sect. 4.2) for the Last Deglaciation. Density of the NROY space (reds) and the minimum implausibility value (blues) shown for each face of the 7D hypercube. Each panel is composed of 40x40 pixels, while the value at each cell is derived from a 1000-member random sample of 24 Gaussian process volume emulators (1 for each time, margin, and region) in order to calculate the resulting implausibility and derive a value for each pixel. Maps show the resulting mean (a) and standard deviation (b) of the NROY shear-stress map input averaged over ICESHEET$_{6G}$ and ICESHEET$_{1D}$ at 22 ka .

3.6 Application to the Penultimate Glacial Maximum

3.6.1 Initial Model of the Penultimate Glacial Maximum Eurasian Ice Sheet

In order to model the configuration of the PGM Eurasian ice sheet, and to include new parameters controlling hybrid ice streaming, marginal extent, and topographic deformation, we first generate a new 1000-member, uniform LHS sample of the model parameter ranges as detailed in Table 3.1. Our initial ensemble iteration of PGM ice-sheet simulations is run using modern-day topography (Schaffer et al., 2016) (initially ignoring the topographic deformation parameter), and the 1000-member set of generated shear-stress map and ice-sheet margin inputs, based on work by Batchelor et al. (2019) (Figure 3.1e), as described in Sect. 3.3.4.2. While the margin extent parameter was initially sampled as uniform, in order to aid in training of the Gaussian process emulator, the following volume estimates are reported from an emulation-derived sample of 10^5 parameters using a normal range for the margin extent parameter, centred on 0.5 with a standard deviation of 0.1.

Over the full ensemble, this produces an ice sheet with a volume of 45 ± 15 m SLE (Figure 3.7a) which falls below the ≈ 70 m SLE value by Colleoni et al. (2016) and within range of the 52.5 m SLE value of Lambeck et al. (2006) and the 33.2 m SLE of de Boer et al. (2013), within uncertainty. Next, we apply corrections for glacial isostatic adjusted topography to the ensemble, and utilise our Last Deglaciation history matching (Sect. 3.5) to refine our PGM ice-sheet reconstruction.

3.6.2 Effects of Glacial Isostatic Adjustment

Previous research has shown the importance of accounting for GIA when simulating ice sheets with the ICESHEET model (Gowan, 2014) and therefore we must account for this in our simulations, using the approach outlined in Sect. 3.3.4.2. We find that, after applying the simple deformation model, scaling the magnitude of deformation by the topography deformation parameter, our mean deformed topography is depressed by a total volume of $4 \pm 1 \times 10^6$ km^3 compared to modern-day topography which, if this space were filled with ice, would be equivalent to 9 ± 4 m SLE. On average, the region covered by ice is depressed by 0.1 ± 0.2 km compared with modern day, with areas close to the interior of the ice sheet experiencing the highest levels of deformation, with a maximum depression of 1.2 ± 0.2 km (Figure 3.11). All topography underneath the ice-sheet mass is depressed by applying ELRA but variation in this depression

is minimal at the exterior regions of the ice since the model is less sensitive to the smaller changes in ice thickness at the peripheries of the ice sheet.

Deformed topography has a non-negligible impact on the distribution of ice volume in our ensemble with mean volume increasing from 45 ± 15 m SLE to 50 ± 16 m SLE (Figure 3.7). A single iteration of the ELRA topography, combined with the deformation scaling parameter, allows us to account for the first-order effects of GIA, with our experiments finding that subsequent iterations produce ice volume changes of an order of magnitude less than the first.

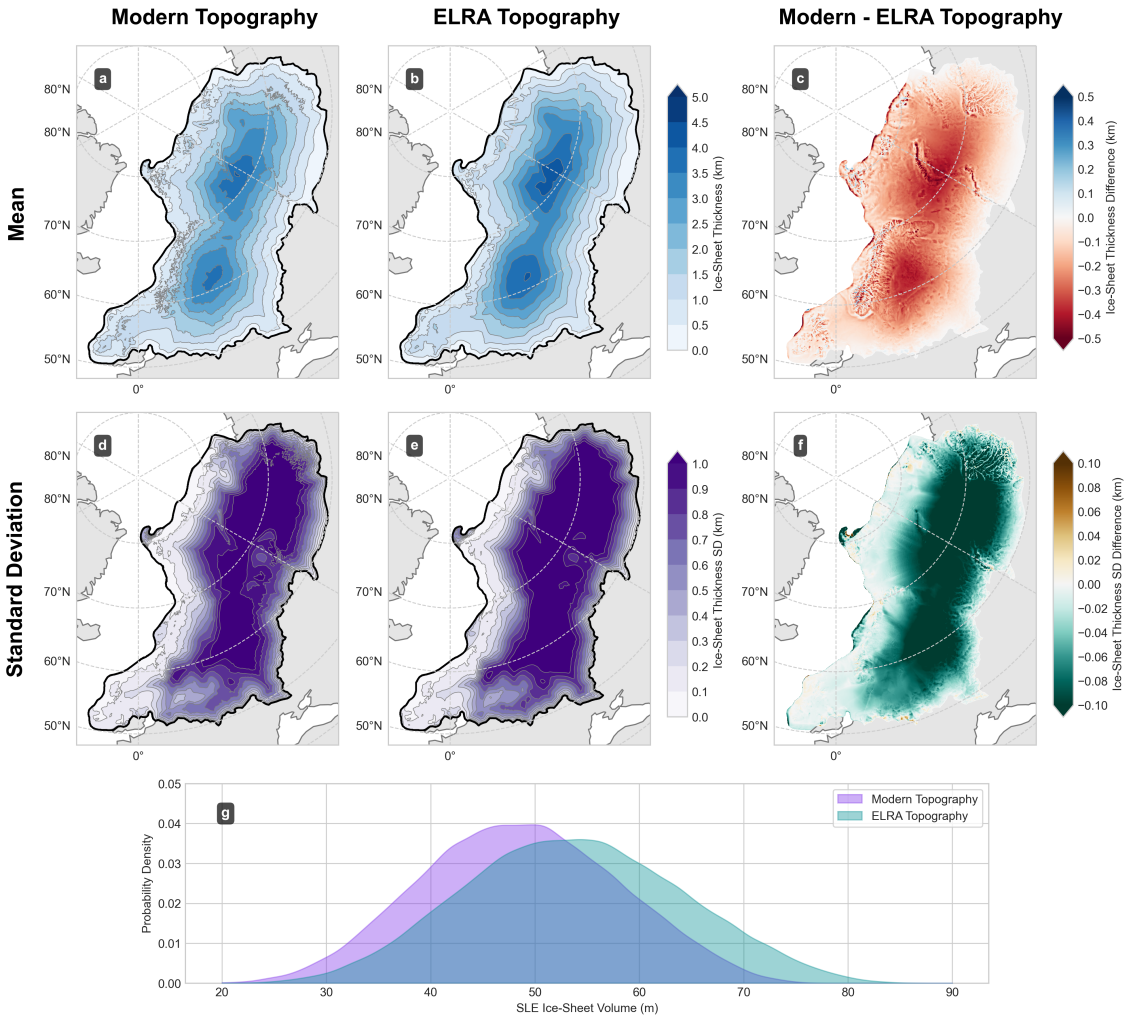

Figure 3.7: Impact of ELRA topography deformation on PGM ice thickness. Mean thickness across the full ensemble using modern-day topography (a) and ELRA deformation respectively (b). (c) Difference in the ensemble mean thickness between ELRA adjusted and modern topography simulations. (d)-(f) as (a)-(c) but showing ensemble standard deviation. (g) Distributions of PGM ice sheet volume in the ensemble run with modern topography (purple) and ELRA adjusted topography (green).

3.6.3 Reconstruction of the Penultimate Glacial Maximum Eurasian Ice Sheet

We are now able to refine our initial 1000-member LHS ensemble of Eurasian PGM ice-sheet geometries by utilising information gained from our previous history matching procedure against the Last Deglaciation. As in Sect. 3.5.2, we compile our best estimate reconstruction of the PGM with quantified uncertainty by excluding members that have an implausibility of greater than 3. The implausibility values for PGM sample members are derived by utilising the 24 Gaussian process emulators trained on each volume metric, as in Sect. 3.5.2, for the 7 common parameters. We account for the presence of a bias term in our initial implausibility by subtracting a scalar bias of 1.76 m from all PGM volumes. This bias was calculated as a result of scaling the NROY PGM volume mean by the mean Last Deglaciation percentage bias at 20 ka.

Applying the NROY constraint acts to reduce the mean of our ice-sheet thickness ensemble from 2.0 ± 0.4 km to 1.8 ± 0.3 km (Figure 3.9). Much of this reduction in volume is from favouring ice sheets with a thinner interior (Figure 3.8). The pre-history matched mean maximum thickness of 4.8 ± 1.0 km, occurring in the interior, decreases to 4.3 ± 0.9 km, but with slightly thicker ice at the southern margin, compared with the maximum ice thickness over North America at the LGM of 3.38 km, and present-day Greenland and Antarctica at 3.14 km and 4.01 km respectively (Tarasov et al., 2012). After history matching, we see the highest variation in thickness in the NROY subset is in the central eastern portion of the ice sheet, except for the Barents Sea region where cold-based ice is present through many of the accepted ensemble members (Figure 3.8). In addition, we find that history matching favours a reduction in the shear stress value for the interior of the ice sheet, but an increase in the Siberian sector, while the exterior shear-stress values remain similar (Figure 3.12). Our mean PGM regional ice-sheet volume is 24 ± 8 m SLE for the Barents-Kara Sea (27 ± 9 m SLE pre-history matching), 19 ± 6 m SLE for Fennoscandia (21 ± 7 m SLE pre-history matching), and 1.7 ± 0.2 m SLE for the British-Irish region (1.8 ± 0.2 m SLE pre-history matching). We find the 5th and 95th percentile of our NROY ice-sheet volume distribution for the PGM to be 35 m SLE and 62 m SLE respectively. Our lower value is comparable to the Eurasian ice volume simulated with dynamic ice-sheet modelling by de Boer et al. (2013) of 33.2 m SLE, and our peak probability (48 m SLE) close to the reconstruction by Lambeck et al. (2006) (52.5 m SLE) using GIA inversion methods. The dynamic ice-sheet model output which results in a 70 m SLE PGM Eurasian ice sheet by Colleoni (2009) exceeds our maximum. Similarly, the simulation developed by Abe-Ouchi

et al. (2013), and subsequently used in the PMIP protocol (Menviel et al., 2019), is within the 99th percentile, but greater than our 95th percentile ($\approx$ 64 m SLE).

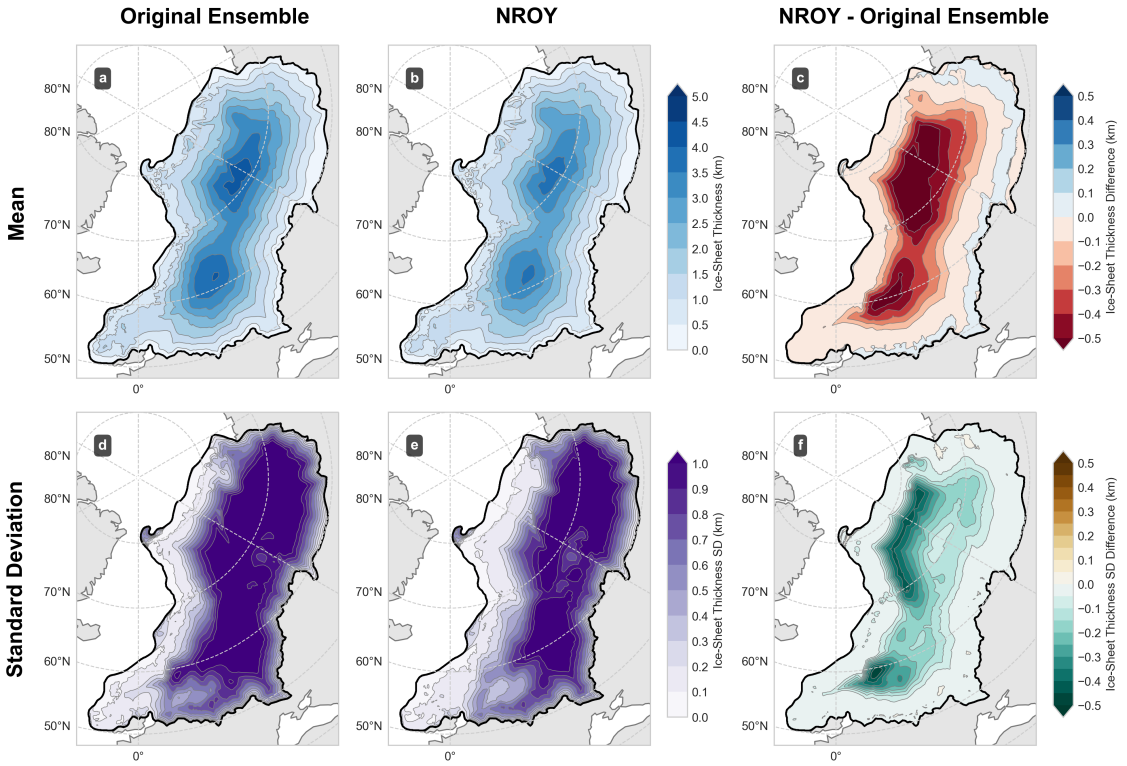

Figure 3.8: Ensemble mean ice-sheet thickness before and after history matching (a) full ensemble and (b) NROY subset, and the difference between these means (c). (d)-(f) are as (a)-(c) but for the standard deviation instead of mean. Applying constraints on the Last Deglaciation leads to ice sheets with smaller volumes in the ice interior, but slightly thicker ice at the margins.

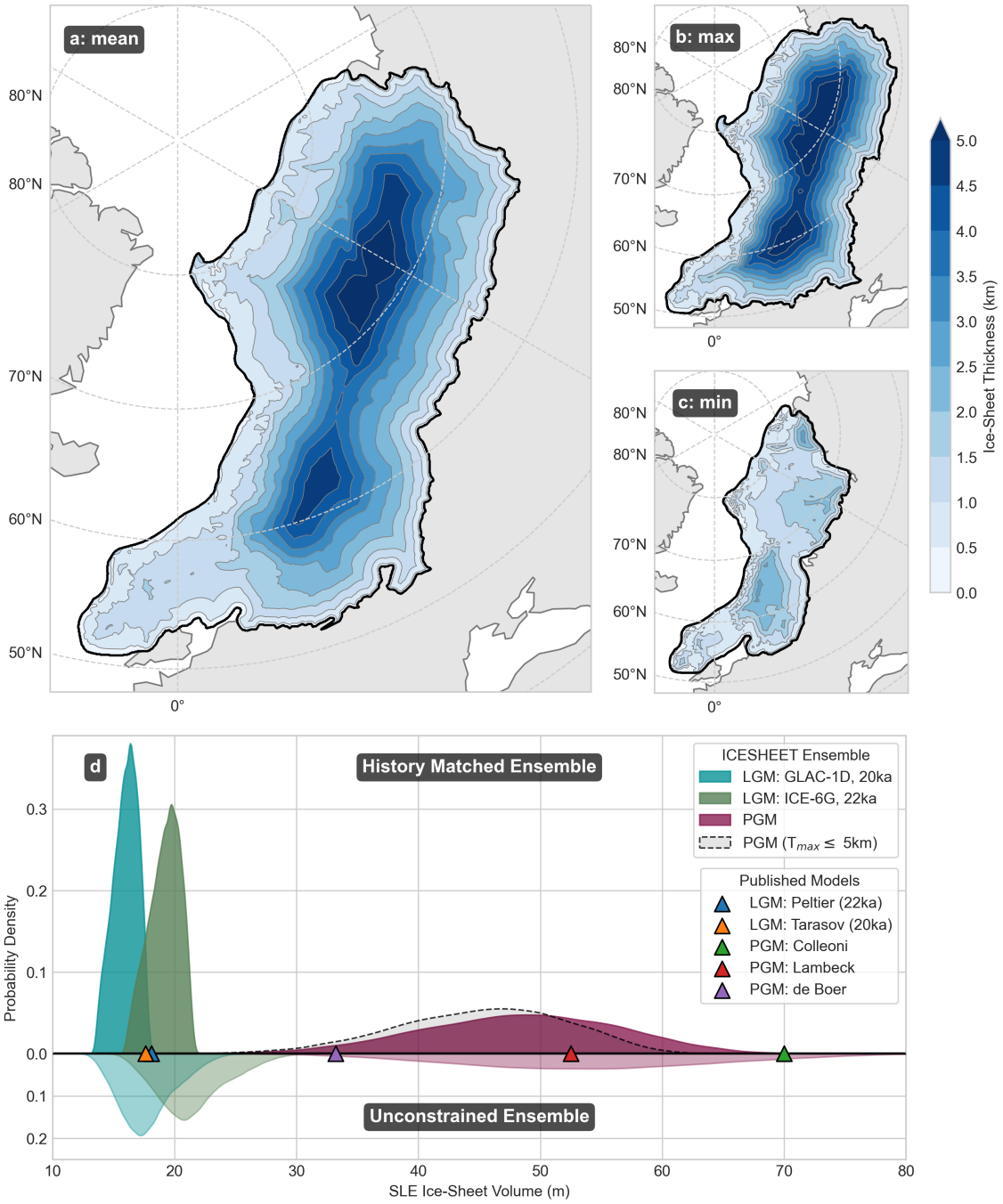

Figure 3.9: (a) PGM Eurasian ice-sheet thickness ensemble member from the constrained ensemble (NROY), having been refined using information leveraged from history matching against the Last Deglaciation, with total ice-sheet volume closest to the probability distribution mean (48 m SLE). Smallest (b) and largest (c) PGM NROY ensemble members after history matching. (d) Probability density functions of unconstrained (bottom, lighter shade) and history matching constrained (top, darker shade) ice-sheet volumes for ensembles of the 20 ka GLAC-1D (blue) and 22 ka ICE-6G Last Glacial Maximum margins and the PGM (purple) compared against published ice-sheet dynamic simulation reconstructions from the corresponding time periods (Colleoni, 2009; Lambeck et al., 2006; de Boer et al., 2013; Peltier et al., 2015; Tarasov et al., 2012). Dashed grey line shows alternative probability density function when we constrain to simulations with ≤ 5 km maximum thickness.

3.7 Discussion

ICESHEET (Gowan et al., 2016a) is able to produce simple, perfectly plastic, steady-state ice-sheet reconstructions with minimal number of inputs. Such reconstructions are appropriate inputs for calculating RSL change since GIA modelling is less sensitive to the specific surface geometry of an ice sheet and more sensitive to the regional load distribution and evolution. Utilising a history-matching approach and a large ensemble to explore a range of controlling shear-stress parameters, we produced an ICESHEET-derived set of simulations for the Last Deglaciation of the Eurasian ice sheet (17 ± 2 m SLE at 22 ka, averaged across ICE-6G and GLAC-1D margins). These results provide an alternative ice model independent of climate forcing or the need to fit with RSL data, and provide ice-sheet thickness estimates not offered from geomorphologically constrained margin reconstructions (Batchelor et al., 2019; Hughes et al., 2016). These LGM outputs then help to constrain a reconstruction of the PGM Eurasian ice sheet, where constraints on ice-sheet extent, thickness and basal conditions are far more limited. Our final model outputs suggest an ice-sheet volume of 48 ± 8 m SLE, which is 2 - 3.5 times larger than that for the Eurasian ice sheet at the LGM. Between the LGM and PGM simulations, the Barents-Kara Sea region has the highest average percentage increase in volume at +245% (from 7 ± 1 m to 24 ± 8 m SLE), followed by the British-Irish region at +170% (from 0.6 ± 0.1 m to 1.7 ± 0.2 m SLE) and the Fennoscandia at +63% (from 11 ± 2 m to 19 ± 6 m SLE). If we combine our Eurasian ice-sheet reconstruction for the PGM with LGM values of the other ice sheets averaged from ICE-6G (Peltier et al., 2015) and GLAC-1D (Tarasov et al., 2012) (9.5 m, 78.8 m and 72.9 m SLE excess ice volumes of the Greenland, Antarctic, and Laurentide ice sheets respectively), we arrive at an ice volume that is 7 m SLE higher than the value suggested by the delta ^{18}O curve for MIS 6 (Waelbroeck et al., 2002). This would suggest that balancing the total ice volume during the PGM would require a $\approx 10\%$ decrease in the size of the Laurentide ice sheet compared to the LGM. This spatial difference in the distribution of ice load between the LGM and PGM across Eurasia and North America has significant implications for the pattern and magnitude of LIG sea level (Dendy et al., 2017), compared to the Holocene. It should be noted that this simple comparison is made to illustrate the implications of our results on the relative size of the Laurentide ice sheet, but with the caveat that the relationship between global average sea level and global ice-sheet volume is more complicated than implied here, due to the effects of ocean-load-driven bathymetry changes and ice-sheet-driven topography changes modifying ocean basin volumes. This mean that estimates of global mean sea level are dependent on assumptions of the viscoelastic response of the Earth, and may in fact differ by up to 20 m from the estimate used here (Gowan et al., 2021).

One limitation of our approach is that ICESHEET does not represent dynamic ice-sheet processes or climate information that may be important for defining spatial variations in Eurasian ice geometry at the PGM. In our reconstruction, the location of ice domes remain central relative to the ice-sheet margin, which in turn is prescribed as a maximum synchronous extent and, by extension, volume. By contrast, Colleoni (2009) do include dynamics in their ice-sheet reconstruction but a near implausible total SLE ice-sheet volume of 70 m (since this would require a Laurentide ice sheet 40% smaller than at the LGM which seems unlikely), combined with large uncertainties on required climate inputs, casts doubt on the reliability of this simulation for use in climate and GIA model inputs. By utilising a range of ice margins (Figure 3.1) our outputs do consider the potential varying size of the Eurasian ice sheet maximum during the late Saalian (Ehlers et al., 2011), although analysis of the consequence of spatial and temporal variations during the Penultimate Deglaciation on GIA must be considered in future work.

The use of a shear-stress map to represent bed friction, decomposed into key parameters, provides a flexible framework for reconstruction of Quaternary Eurasian ice-sheet geometries since the parameter space can be easily and quickly explored to produce large ensembles of simulations that span the uncertainty in this input. Ice-sheet processes at the bed often manifest as a change in basal shear stress (Knight, 1997) and approximations to the basal implications of such processes can be incorporated into this framework, for example by approximating the presence of cold-based ice. Uncertainty in the location of sediment types, bedrock and ice streaming remains a challenge but we find that the use of variable density regions, such as the hybrid ice-streaming component employed in the southern sector of the ice sheet, have a strong control on the implausibility metric and can therefore be used to effectively explore the impact of these uncertainties. The shear-stress map is an attempt to represent a complex distribution of basal properties (Knight, 1997). Our work has expanded this methodology to include the cold-based ice and active ice-streaming basal modifications which have had a strong impact on the implausibility metric, improving the simulation fit during history matching when applied to the Last Deglaciation, with the exception of the British ice sheet (Figure 3.4) where simulation mismatch is likely due to discrepancies in ice-margin extraction. By extension, this approach also worked to better refine our reconstructions at the PGM. The modelling framework could be further improved by validating these modifications against other ice-sheet models, such as for the Laurentide and Greenland ice sheets.

By employing history matching, leveraging information from models of the Last Deglaciation, we were able to refine the ensemble mean for our PGM ensemble from 50 ± 16 m to 48 ± 8 m SLE. This approach reduced the size of our original parameter

space, which had initially produced a broad range of ice-sheet volumes, by 58% and revealed a tendency for our ensemble to overestimate ice-sheet thickness since our refined ensemble preferred thinner ice sheets. This technique could be improved in a number of ways. The average relative distance in regional volume metrics derived between our two target reconstructions is 15.9%. However, some metrics are much more uncertain, such as the volume of the British-Irish ice sheet at 20 ka, which has a relative distance of 76.0%. It would be beneficial to extend the model comparisons beyond GLAC-1D and ICE-6G, such as in the work by Patton et al. (2017). In addition, the GLAC-1D target reconstruction is itself derived from an ensemble of simulation (Tarasov et al., 2012). Therefore, the observation metric uncertainty could be more accurately accounted for in our procedures if the original ensembles from which the target reconstructions are derived could be obtained.

A possible criticism of our work is that the PGM ice sheet we are predicting with our model is "out of sample" compared to the Last Deglaciation that we have calibrated the model on since the PGM ice sheet is larger than at the LGM. This is a very common situation in modelling uncertainty quantification work. We believe this analysis is robust to this issue since the ice-sheet volume is correlated with extent meaning that, since our simulations are based on the same shear-stress map and modifications, the history matched parameter space is applicable for simulation of both the Last Deglaciation and the PGM. However, given the larger PGM margin, ICESHEET is able to generate ice-sheet thickness values that may be physically implausible (greater than 5 km). We investigate the effect that constraining to simulations that have a maximum thickness of ≤ 5 km has on our PGM volume probability density function (Figure 3.9) and find that this results in a reduced volume estimate of 45 ± 7 m SLE.

This work has demonstrated the benefit of using simpler ice-sheet models with a Bayesian uncertainty quantification framework to explore the range of uncertainty in periods when there are highly uncertain ice-sheet geometries. This workflow, using ICESHEET and history matching, could be applied to other regions (e.g. Laurentide) or times (e.g. the large MIS 12 ice sheets) where there are also large uncertainties in extent, thickness and timing.

3.8 Conclusions

By employing a simple ice-sheet model we were able to investigate the range of physically plausible PGM ice geometries for the Eurasian ice sheet. The primary control on geometry changes are due to the 2D shear-stress map input that we

decompose into 9 parameters controlling regional shear-stress values and the shear-stress influence of key basal processes. By employing a Latin hypercube sampling technique, we explore the range of possible ice-sheet thickness distributions over this parameter space. We find that our model procedure generates a PGM ice-sheet ensemble with a total SLE volume range of 50 ± 16 m SLE. In order to refine this ensemble range, we employ a history matching procedure, leveraging information from previously published reconstructions of the Last Deglaciation, in order to rule out combinations of input parameter values that produce unrealistic ice sheets.

This work is aimed at producing ice-sheet simulations to be used as input to sea-level models and thereby assess ice-sheet geometry at a regional scale that ignores local details in the thickness profile. History matching rules out 58% of our parameter space and heavily favoured parameter combinations that lead to smaller ice-sheet configurations. We applied the refined parameter space (NROY space) to our original PGM ensemble, reducing the mean and uncertainty on our range of PGM volume to 48 ± 8 m SLE. This refinement reflects the preference for smaller Eurasian ice sheets found in the Last Deglaciation history matching procedure and points at the tendency for ICESHEET driven by a parameterised shear-stress map to overestimate ice-sheet thickness. This work is currently limited to a single synchronous maximum but can be applied to develop reconstructions of ice extent and thickness over a full deglacial cycle that can in turn serve as input into a GIA model for predicting changes in RSL. The rate and timing of the deglaciation are important factors in the pattern and magnitude of RSL change during deglaciation and the subsequent interglacial and, despite the lack of chronological constraints, producing a full Penultimate Deglaciation history for Eurasia remains an important challenge to overcome in future work.

3.9 Appendix

3.9.1 Figures and Margin Extraction Algorithm

In order to perform a history matching procedure with ICESHEET we require that the ice-sheet margins used as input be approximately equivalent to those of the reconstructions we are comparing with. Margins are not provided explicitly with either the ICE-6G or GLAC-1D reconstructions and thus we instead developed a simple algorithm to extract margins from gridded ice-sheet thickness rasters. The procedure is as follows:

For each reconstruction and time period, we first reproject and interpolate the ice-thickness and topography fields from their native grid to our LAEA model grid using

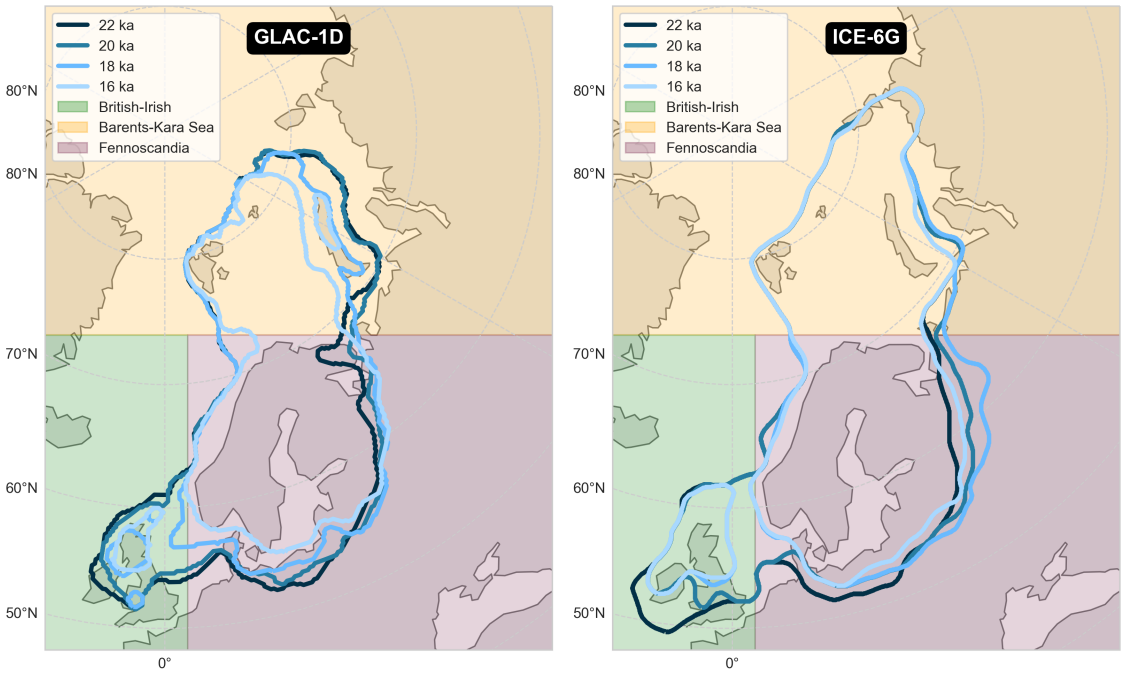

Figure 3.10: (a) GLAC-1D margins for 22, 20, 18, and 16 ka as extracted by the algorithm described in Sec. 3.9.1. (b) as in (a) but for ICE-6G. British-Irish (green), Barents-Kara Sea (yellow) and Fennoscandia (red) region divisions.

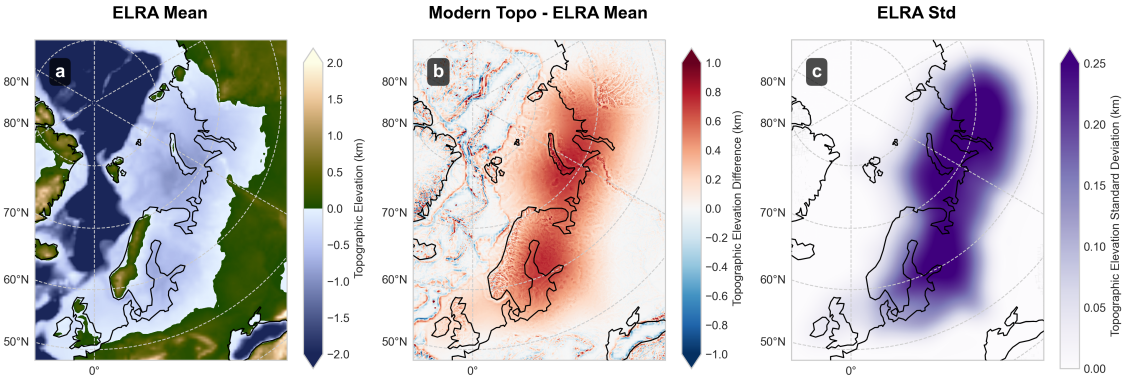

Figure 3.11: Topography deformation. Mean (a) and standard deviation (b) of topography across the full ice-sheet ensemble and (c) difference between the ensemble mean and modern-day topography.

bilinear interpolation. We then extract the ice margin from the gridded ice-thickness field using an algorithm that first identifies grid cells at the edge of the ice sheet from the ice-thickness field, then employs a pathfinding procedure to order the collected cells into an ordered polygon structure, and finally converts the ordered cell positions into coordinates. In addition a region mask, minimum considered thickness value, average ice-sheet thickness value, and a median filter smoothing may be applied as conditions.

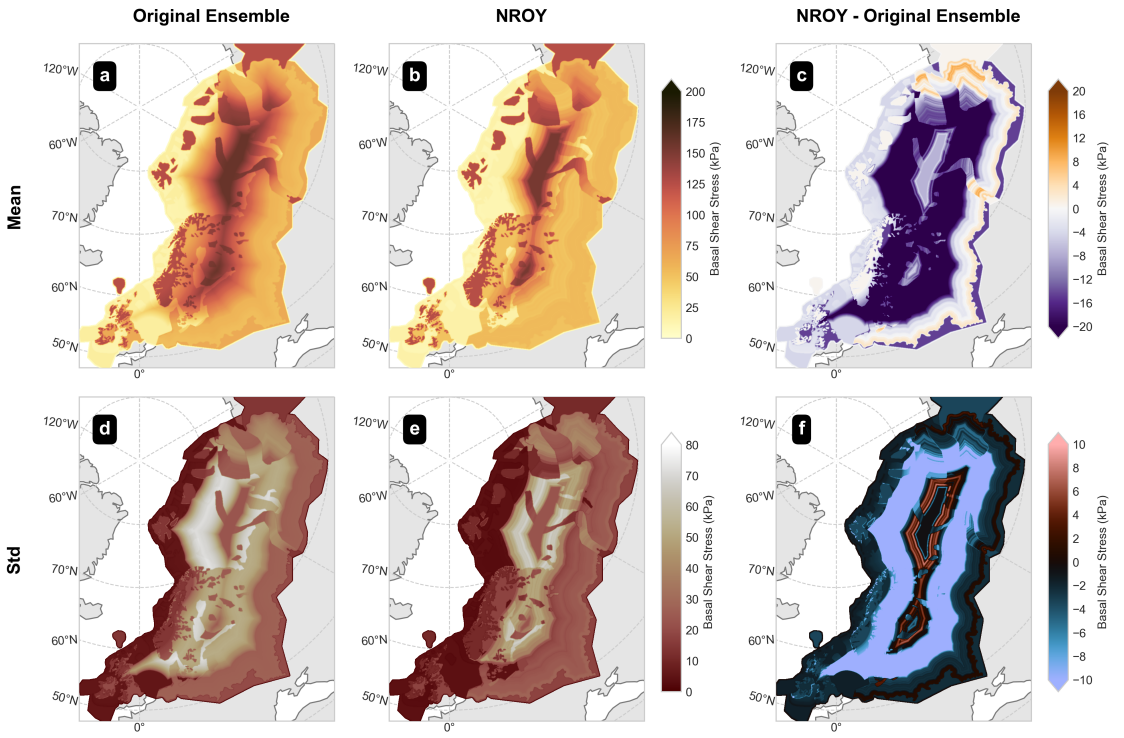

Figure 3.12: Ensemble mean basal shear stress before (a) and after (b) history matching and (c) difference between these means. Panels (d)-(f) are as in (a)-(c) but for standard deviation.

1. The 2D ice thickness is converted into a binary image (or mask), with values of 1 where ice is present, and 0 where it is not, using a minimum thickness value defined as a parameter.

2. The binary image may be optionally filtered by another mask, such as a mask defining the continental shelf, to restrict the area of the margin.

3. We perform a binary erosion morphology operation on the binary image, using a structuring element with square connectivity equal to 1, to reveal the binary shape of the ice that is 1 grid-cell smaller than the original.

4. The binary-eroded image is subtracted from the original binary image to reveal a binary outline of the ice-sheet margin.

5. Each margin cell is then checked via a recursive procedure to identify those cells adjacent to it that form part of a continuous path. The set and order of cells that form each path are then stored. Once assigned to a path, a cell is not considered by the algorithm for future paths.

6. The set of ordered cell paths is then converted, in combination with their cell coordinates, to polygon geometry objects.

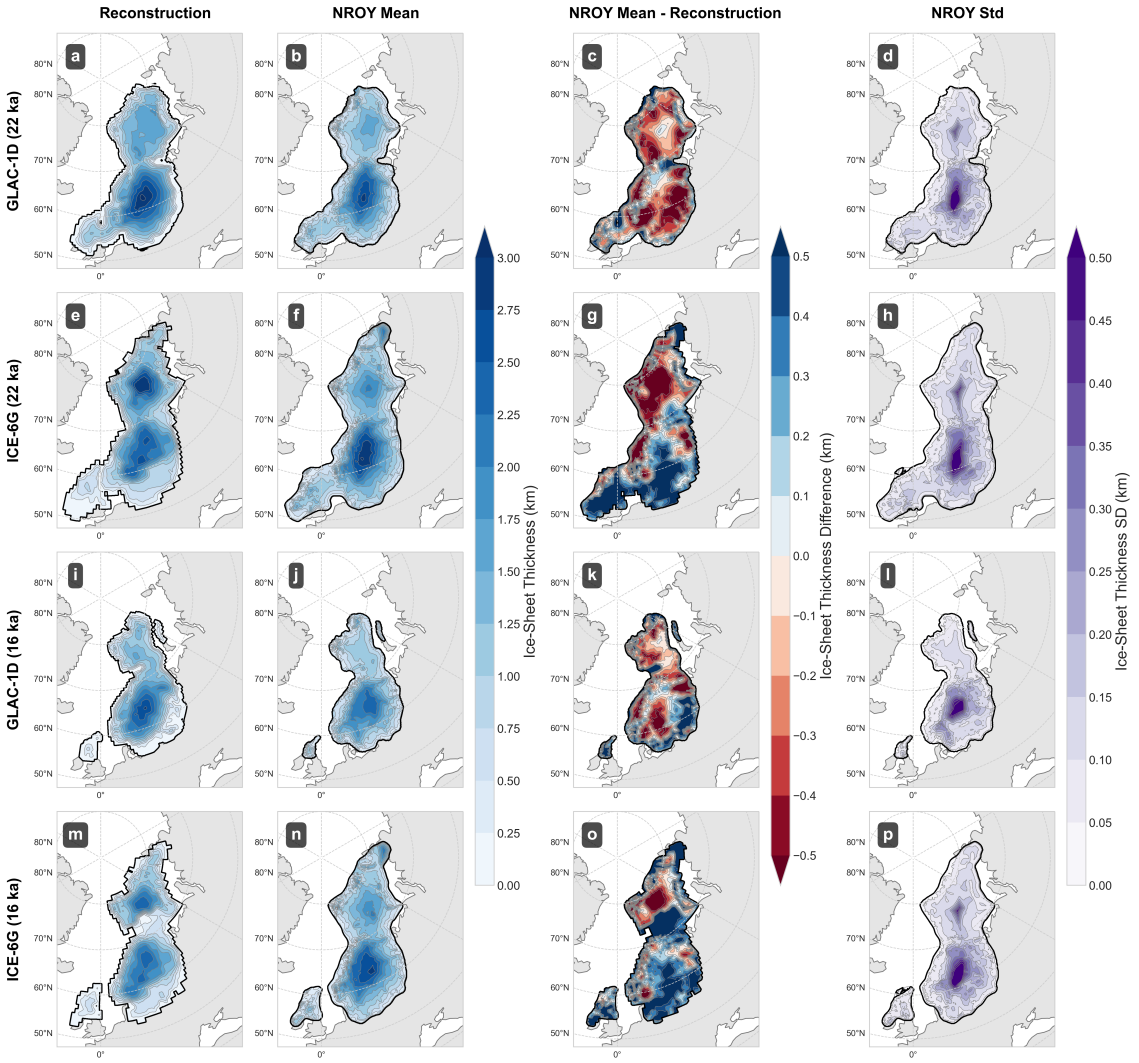

Figure 3.13: Comparison of the constrained NROY ensemble of ICESHEET$_{1D}$ and ICESHEET$_{6G}$ simulations, before removal of the model bias, against the GLAC-1D (first row: a-d) and ICE-6G (second row: e-h) reconstructions respectively, for the 22 ka time slice. (a) GLAC-1D target reconstruction. (b) Mean of the NROY ensemble of ICESHEET model outputs using the margin derived from a. (c) Difference between our ensemble mean (b) and the target reconstruction (a). (d) Standard deviation of this ensemble. Panels (i)-(p) are as in (a)-(d) but for the 16 ka time slice.

7. Each polygon may be optionally checked for the average ice-thickness value it contains, specified as a parameter, in order to exclude patches of thin, disconnected ice.

8. If an optional smoothing value is specified, an iterative smoothing procedure is performed whereby the newly calculated margin polygons are regridded onto a fine grid which is then smoothed with a median filter of a size specified by the smoothing value, and then reperforms steps 1-7 to calculate a smoothed set of margin contours.

Chapter 4

Relative Sea-Level Sensitivity in the Eurasia Region to Earth and Ice-Sheet Model Uncertainty During the Last Interglacial

4.1 Abstract

Indicators of RSL changes in northwest Eurasia during the LIG may be used to constrain the evolution of the LIG AIS. To obtain this information, these records must be corrected for the effects of GIA, driven by the spatiotemporal evolution of ice-sheet loading and the configuration of the Earth's rheological structure. However, both past ice-sheet changes and the local 1D viscoelastic Earth model are significantly uncertain. This paper sets out to determine the relative influence of each of these inputs on modelled values of LIG RSL, and how this influence varies spatially. We find that Earth model parameters are the dominant contributors to RSL uncertainty in most Eurasian regions, but the influence of ice-sheet volume on RSL values in the Barents-Kara and Baltic seas is non-negligible. Our results show that the magnitude and rate of RSL change is insensitive to the specific timing of ice-sheet retreat, as well as the configuration of the far-field North American ice sheet.

4.2 Introduction

The LIG was the last time in Earth's history that the Greenland and Antarctic ice sheets were smaller than those of today (Capron et al., 2014; Otto-Bliesner et al., 2006). Uncovering the rate, timing, and pattern of ice-sheet retreat during this period may shed light on possible future ice-sheet evolutions in response to increased polar temperatures and help to constrain the pattern of global sea-level change beyond 2300 (IPCC, 2022). Due to its location and bathymetry, the pattern of LIG RSL in some northwest Eurasian regions (Figure 4.1A) is sensitive to the evolution of the interglacial AIS, but insensitive to the melt of the GrIS, and could therefore be used to identify sources of LIG ice-sheet melt (Hay et al., 2014). In addition, some regions within northwest Eurasia, such as the North Sea, contain valuable sedimentary archives in which these past sea-level changes are recorded (Cohen et al., 2022; Zagwijn, 1983). However, such geological records reflect the cumulative contribution of multiple geophysical processes that must be quantified if they are to be used to isolate the fingerprint of LIG GrIS and AIS melt (Hay et al., 2014; Mitrovica et al., 2009).

GIA is the term used to describe a collection of processes which, as a result of surface ice-mass changes, act to modify the Earth's topography and equilibrated geometry of the ocean surface via the coupled influences of gravitational attraction and viscoelastic deformation (Farrell and Clark, 1976; Mitrovica and Milne, 2003; Whitehouse, 2018). RSL changes throughout interglacial periods are driven by both the contribution of ice-sheet melt that occurs during the interglacial, as well as the ongoing influence of GIA from ice-sheet mass changes that occurred in the glacial periods prior (Whitehouse, 2018). In regions close to former ice sheets, the contribution of ongoing GIA from previous glacial cycles to the interglacial RSL signal is known to be significant over the timescale of glacial-interglacial cycles (Dendy et al., 2017). Since records of RSL from these regions are essential for the identification of ice-sheet fingerprints (Figure 4.1B), we must therefore remove the GIA signal from such records in order to utilise them to understand interglacial ice-mass changes (Barnett et al., 2023; Dutton et al., 2015; Dyer et al., 2021). Holocene studies in locations close to or beneath former ice sheets have shown that the development of regional, near-field GIA models, driven by ice-mass changes during the preceding LGP, is an effective technique for the recovery of sea-level fingerprints from geological observations of RSL (Lin et al., 2021).

Quantification of the GIA contribution to past RSL change is possible through the use of numerically derived GIA models, constructed by iteratively solving the Sea

Level Equation. Solutions to this equation require spatiotemporal ice-sheet thickness values as input to drive the surface loading, and a model of the Earth's viscoelastic response to estimate the characteristics of surface deformation (Kendall et al., 2005). The nature of the GIA simulation is dependent on the particular combination of the global ice-sheet history and viscoelastic Earth model used, yet both the configuration of global ice-sheet mass changes during glacial-interglacial cycles prior to the LGP, including the PGP ($\sim$ 200 - 130 ka, correlated to MIS 6), and the rheological structure of the solid Earth are highly uncertain. Previous research has shown that ice-sheet changes during the PGP play a key role in determining the LIG near-field GIA simulation, making the application of GIA models to fingerprinting LIG ice-sheet melt a significant challenge (Dendy et al., 2017; Lambeck et al., 2014; Rohling et al., 2017). Previous studies of LIG GIA have approached this problem by testing a limited series of discrete, non-holistic scenarios for ice evolution and Earth model parameters which do not allow for the systematic assessment of GIA model sensitivity and uncertainty (Dendy et al., 2017; Dyer et al., 2021). In addition, the choice of ice-sheet history and Earth model is often tuned to LIG RSL databases, creating a circularity issue when extracting fingerprints from the same datasets.

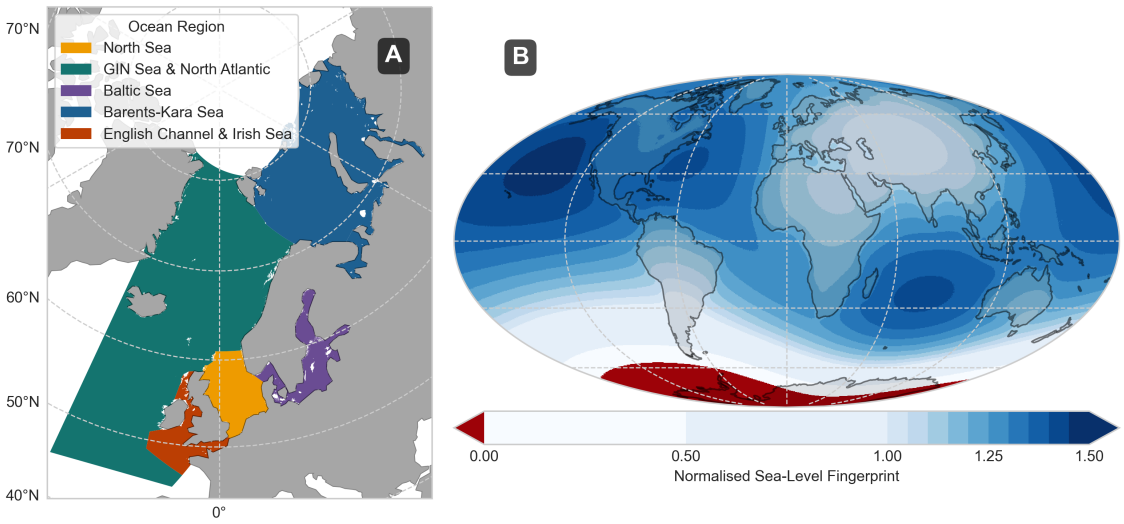

Figure 4.1: (A) Northwest Eurasian Ocean regional divisions used in this work. (B) Illustrative Antarctic sea-level fingerprint resulting from a complete collapse of the WAIS.

In this work, we develop new methodologies to enable a fully systematic assessment of RSL variability due to uncertainties in the ice-sheet evolution and viscoelastic Earth models that drive modelled LIG RSL changes, independent of sea-level data. In addition, we build upon work by Pollard et al. (2023) to explore the uncertainty in the evolution of the Eurasian ice sheet during the PGP, which is of particular importance to GIA in the North Sea and wider Eurasian region. Finally, we apply sensitivity analysis to our large ensemble of sea-level model outputs to decompose the

RSL variability into the relative contributions from each parameter, thus revealing spatial patterns of sensitivity to help guide site-specific studies on the most critical sources of RSL uncertainty.

4.3 Penultimate Deglaciation of the Eurasian Ice Sheet

The proximity of northwest Eurasian ocean regions to the expansive PGP Eurasian ice sheet means that their RSL signals are likely to be especially sensitive to mass balance changes of the Eurasian ice sheet during the Penultimate Deglaciation (Long et al., 2015). However, little is known of the ice sheet's spatiotemporal evolution during this time, with previous ice-sheet modelling work typically focusing on its maximum extent or with significant uncertainty in the ice margin position (Batchelor et al., 2019; Colleoni et al., 2016; Lambeck et al., 2006; Svendsen et al., 2004; Pollard et al., 2023). We identify three types of uncertainty in characterising the deglaciation of the penultimate Eurasian ice sheet: the maximum ice-sheet volume at the PGM; asynchrony in the pattern of the deglaciation (e.g. the eastern margin experiencing maximum extent at different times to the west); and the rate and timing of ice retreat (Toucanne et al., 2009; Ehlers et al., 2011; Ehlers and Gibbard, 2004). In order to account for each of these sources of uncertainty within our uncertainty quantification, we perform dedicated numerical modelling of the Eurasian ice-sheet complex during the Penultimate Deglaciation. This builds upon and extends the work of Pollard et al. (2023), who solely focused on modelling at the maximum ice-sheet extent.

4.3.1 Ice-Sheet Model

We generate ice-sheet geometries using ICESHEET: a simple, steady-state ice-sheet model that assumes a perfectly plastic ice-sheet rheology (Gowan et al., 2016a), and which has previously been utilised to generate ice-sheet reconstructions independently of sea-level and VLM proxy data (Bradley et al., 2023; Gowan et al., 2021). ICESHEET takes three inputs in order to produce a single, time-independent ice geometry: a parameterised basal shear-stress map, as detailed in Chapter 3; regional topography, iteratively generated using a simple topographic deformation model; and prescribed ice-sheet margin. Our methodology utilises ICESHEET to explore uncertainty in two of the three identified sources for the Eurasian Deglaciation: uncertainty in possible ice-sheet volume, which is explored through testing a range of shear-stress value configurations via its influence on ice thickness; and margin retreat asynchrony, for which we have developed a methodology for generating series

of possible margin deglaciation scenarios, described in the following section; and ice-sheet deglaciation timing, explored in Section 4.4.3.

4.3.2 Deglaciation Margins

The ICESHEET model is time-independent, meaning that it takes a single prescribed margin as input and produces a single corresponding ice geometry as output, without advancing time or evolving margin position during the course of a model simulation (Gowan et al., 2016a). Therefore, in order to generate a series of deglaciating Eurasian ice-sheet geometries for the PGP using ICESHEET, we require a prescribed series of corresponding deglaciating ice-sheet margins. To do this, we first assume that the most extensive (maximum) ice-sheet position was the MIS 6 best-estimate ice-sheet margin from Batchelor et al. (2019) which likely corresponds to the large Drenthe substage of the PGP (Toucanne et al., 2009), as modelled in Pollard et al. (2023). We also assume that the ice sheet retreated in a similar way to that of the Last Deglaciation for extents less than or equal to the LGM (Hughes et al., 2016). To bridge the gap between the MIS 6 Batchelor and LGM Hughes margins, given the very limited spatial-temporal constraints as documented in the Rohling et al. (2017) database, we develop a margin interpolation algorithm (named *ShaPy*, described in Section 2.0.2.2) which we use to generate 7 additional intermediary margins (Figure 4.2a).

Geological records of the deglaciation of the Eurasian ice sheet indicate that its pattern of retreat was likely asynchronous, with the eastern sectors deglaciating earlier than the west (Patton et al., 2017). We therefore explore the impacts of deglacial asynchrony within this interpolation regime through the introduction of two parameters: async angle A_θ, which controls the direction of maximum asynchrony; and async power A_n, which determines the magnitude of asynchrony. A value of $A_n = 1$ corresponds to no asynchrony (Figure 4.2a) and renders the value of A_θ meaningless. We set the A_θ value range, expressed in radians, to between π - 1.5π relative to the projected y-axis, spanning the full Eastern margin from the edge of the Barents-Kara Sea (π) to the beginning of the southern-European margin (1.5π), while A_n ranges from between 1 - 5 (Figure 4.2).

4.3.3 Ensemble Design

The ICESHEET model requires the input of a sheer-stress map, which is parameterised by 9 parameters that control regional shear-stress values as well as the influence of basal effects such as cold-based ice and active ice streaming distance (Pollard et al., 2023). We initially generate a 1200 member LHS of the 9 shear-stress

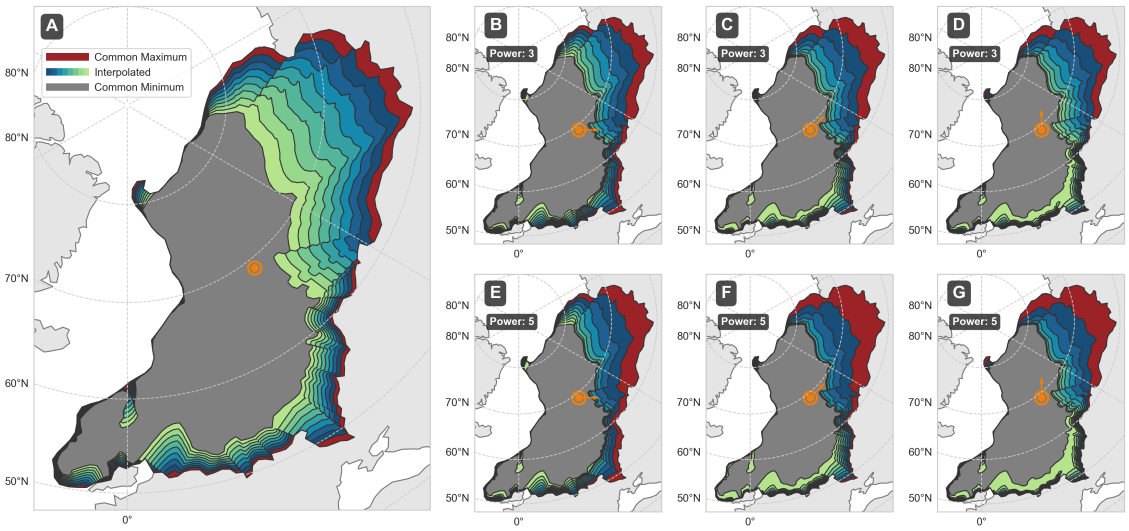

Figure 4.2: (A) 7 intermediary margins between the common maximum (Batchelor et al. (2019) MIS 6 best-estimate) and common minimum (Hughes et al. (2016) LGM) extents are generated with a margin interpolation regime. (B-D) This scheme is able to generate asynchronously deglaciating margin series by specifying the angle of maximum asynchrony (orange arrow) and magnitude of asynchrony (power). (E-G) Same as (B-D) but with a greater magnitude of asynchrony power.

parameters and 2 margin asynchrony parameters, before using the implausibility criteria developed in Pollard et al. (2023) to rule out 668 of the parameter combinations as implausible, leaving 532 remaining combinations to evaluate. Each asynchrony value pair is processed by the ice-margin interpolation algorithm to produce 532 corresponding ice-margin series. In turn, each margin series is used as input to ICESHEET, in combination with the corresponding shear-stress map configuration, to generate 532 series of ice-sheet deglaciation geometries. This initial set of ice-sheet thickness outputs was used as input to a simple deformation model in order to deform the modern-day topography with each ice-sheet load. We then performed an iteration of the ICESHEET ensemble with these deformed topography inputs in order to produce our final ensemble of deglaciation geometries. Each series of ice-sheet geometries is ordered from PGM to fully deglaciated, but the absolute timing of each configuration is not yet fixed. In section 4.4.3, we describe how we test a range of possible rates and timings of ice-sheet retreat using these modelled geometries.

4.3.4 Eurasian Ice-Sheet Simulation Results

Our ensemble has a PGM volume of 53 ± 7 m (mean $\pm$ 1 standard deviation) SLE (defined as the resulting GMSL change that would result from evenly distributing the ice-sheet volume across modern-day ocean area). The Barents-Kara Sea ice-sheet region holds the largest amount of ice by volume at 28 ± 4 m SLE, followed by

Fennoscandia at 24 ± 3 m SLE and the British-Irish ice sheet at 1.8 ± 0.1 m SLE. As the deglaciation progresses, the Barents-Kara Sea experiences the largest loss of volume, shrinking by 25 ± 7 m SLE between the invariant PGM and LGM margin positions. The Fennoscandian region has the largest average volume for all margins except for the PGM, losing only 10 ± 7 m SLE between the PGM and LGM. Over the full ensemble, the thickness of the eastern ice-sheet margin can be seen to rapidly diminish, and this is, in part, due to the presence of ensemble members with less extensive margins (larger A_n values). This also results in a relatively high thickness standard deviation of 0.8 km in this region.

In subsequent sections, we characterise a particular deglaciation ensemble member by its regional volume values at the PGM. This assumes that each member maintains a similar position within the volume distributions for subsequent deglaciation margins as its PGM position. In other words, an ensemble member with a particularly large ice-sheet volume at the PGM is assumed to have a similarly large ice-sheet volume for all subsequent margins, relative to the other ensemble members. To test this assumption, we first express each member in terms of standard deviations from the mean to quantify their relative positions within a particular margin volume distribution, so that we can then analyse the change in this position throughout the deglaciation. We find that the position of each member changes, on average, by 0.52, 0.33, and 0.30 standard deviations for the Barents-Kara Sea, Fennoscandian, and British-Irish regions. These low values make this a reasonable assumption.

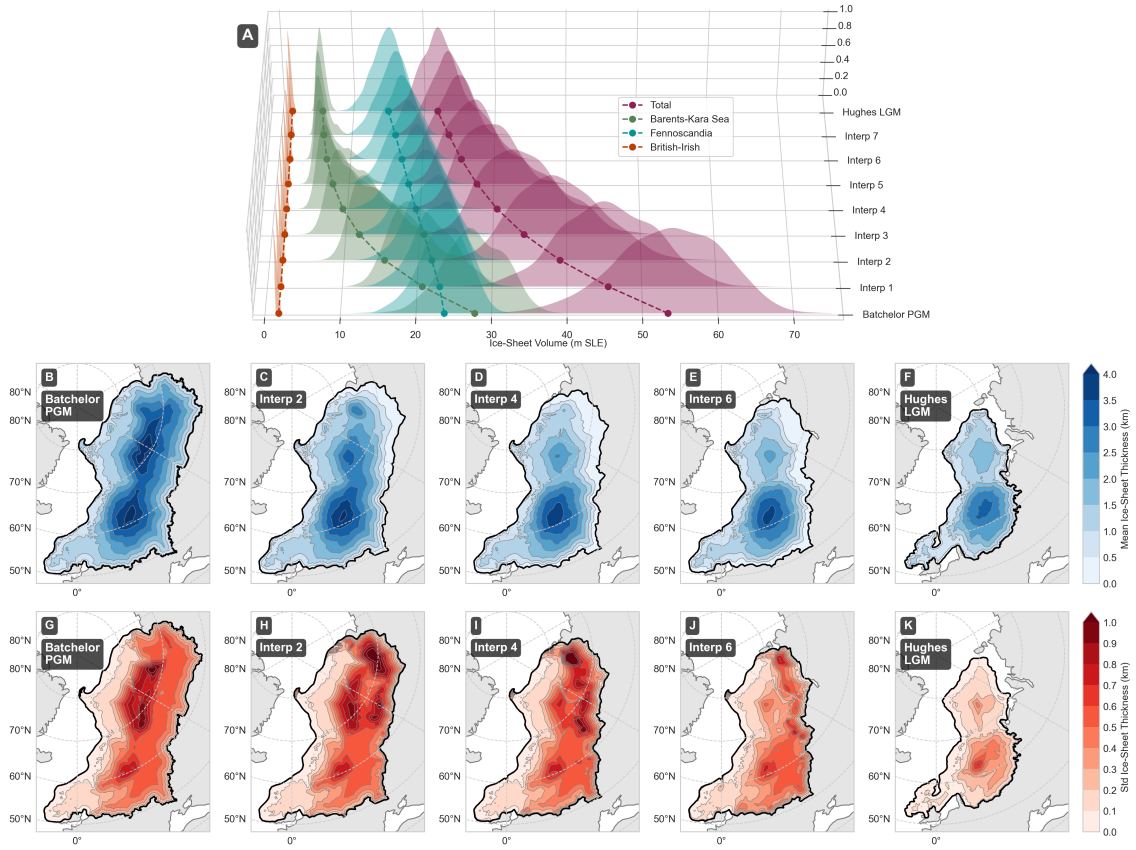

Figure 4.3: (A) Distribution of Eurasian ice-sheet volumes generated by ICESHEET, shown by region, for margins between the PGM Batchelor et al. (2019) and LGM Hughes et al. (2016) configurations. The mean volume is shown by the dotted line. Mean (B-F) and standard deviation (G-K) of ice-sheet thickness across the ensemble of model outputs is shown for 5 margins within the deglaciation series. The maximum extent across the ensemble for a given time slice is shown by the black contour.

4.4 Modelling Last Interglacial Relative Sea Level

Our new Eurasian ice-sheet deglaciation geometries, which address uncertainties in deglaciation asynchrony and ice-sheet volume, must now be combined with a global ice-sheet history and rheological Earth model as inputs to a GIA model, in order to calculate the resulting RSL ensemble and associated sensitivities. To do this, we use a numerical sea-level model combined with global-ice sheet scaling and Earth model generation algorithms to test value ranges for parameters describing the deglaciation timing, northern hemispheric ice-sheet volume, and Earth model uncertainties.

4.4.1 Glacial Isostatic Adjustment Model

We utilise a sea-level model to solve the Sea Level Equation following the implementation by Kendall et al. (2005) on a 512 by 1024 Gauss–Legendre lat-long grid (henceforth referred to as the model grid) via a temporally iterative numerical scheme.

We assume a 1D Maxwell viscoelastic Earth structure with characteristics determined by the PREM (Dziewonski and Anderson, 1981) and a simple, step-wise viscosity profile, following previous GIA models (Bradley et al., 2023; Dendy et al., 2017; Milne et al., 2006). This viscosity structure is defined by an upper mantle viscosity, lower mantle viscosity, and lithospheric thickness and we have developed an interpolation algorithm (*ViscoPy*, described in Section 2.0.2.3) to produce any 1D viscosity structure within a continuous range of values for these three parameters while preserving the location of PREM elastic and density structure discontinuities. We utilise the Earth model parameter ranges used by Bradley et al. (2023) for northwest Europe of 0.1 - 1 $\times 10^{21}$ Pa s for upper mantle viscosity, 0.1 – 5 $\times 10^{22}$ Pa s for lower mantle viscosity, and 71 – 96 km for lithospheric thickness. These values have been selected based on regional published literature for the North Sea region (Shennan et al., 2006, 2018; Bradley et al., 2011, 2009).

4.4.2 Global Ice-Sheet History

Previous studies have found that ice-sheet history inputs to reconstructions of LIG GIA should include: the PGP (194 - 130 ka) which includes the Penultimate Deglaciation, the primary driver of GIA during the LIG; the LGP (100 - 25 ka), which allows the model output to converge on modern-day topography; and at least two glacial cycles prior to the PGP, in order to drive large-scale GIA disequilibrium during the LIG (Dendy et al., 2017). We, therefore, choose to prescribe a global ice-sheet history spanning the last four glacial cycles, from 420 ka to the present day.

We construct our global ice-sheet history to follow the global ice-sheet volume evolution inferred from the $\delta^{18}O$ derived GMSL curve of Waelbroeck et al. (2002), provided at a temporal resolution of 1.5 ka, as shown in Figure 4.4. This curve is adopted over newer reconstructions, such as Shakun et al. (2015), as it has a more favourable alignment with the timing of the LIG (130 - 116 ka). We convert GMSL into a global ice-sheet volume by subtracting it from an estimate of global modern-day (pre-industrial) ice volume (72.1 m SLE), taken from the ICE-6G LGP global ice-sheet model (Peltier et al., 2015). In order to remove the impacts of any interglacial ice-sheet melt on our sensitivity results, we restrict the minimum value of global ice-sheet volume to that of modern day between 129 – 116 ka. We employ a linear interpolation procedure based upon the deglaciation portion of ICE-6G to be able to generate global thickness slices of any given total global ice-sheet volume. The deglaciation-only portion is chosen to avoid non-physical ice-mass changes that might occur while interpolating between a glaciating and deglaciating slice of similar volume. For 122 ka to present, we use the global ice-sheet volume curve of ICE-6G (Peltier et al., 2015).

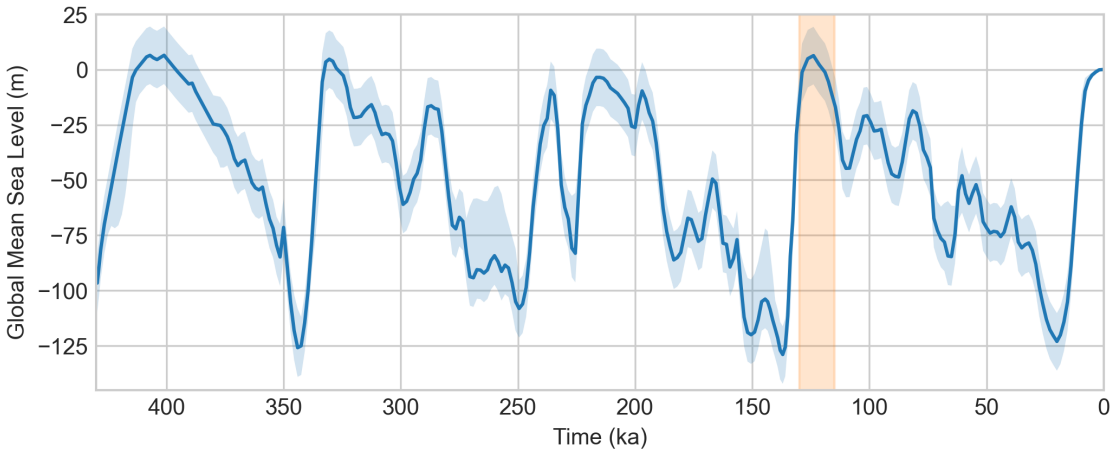

Figure 4.4: Mean (solid line) and minimum/maximum (shaded blue region) GMSL reconstruction of Waelbroeck et al. (2002) from 430 ka until present day. This reconstruction was derived from $\delta^{18}O$ records and is used in our work to infer global ice-sheet volume changes. The approximate timing of the LIG is also shown for comparison (shaded orange region).

We decrease the temporal resolution of time periods in which detailed ice-geometry changes are less impactful on LIG RSL (Table 4.1), in order to improve computational efficiency while prescribing higher resolution time steps during the Penultimate deglaciation (0.5 ka) and LIG (1 ka). This allows us to capture shorter time-scale mass changes and to facilitate high temporal-resolution analysis of RSL outputs during the LIG. Since we are using ICE-6G deglaciation geometries to construct ice-sheet histories, our current methodology has the inherent assumption that the relative distribution of global ice-sheet volume was similar to that of the Last Deglaciation for all glacial periods reconstructed. For periods prior to the PGP this assumption is likely inconsequential for the purposes of LIG GIA modelling. However, as previously discussed, it is important to account for the large difference in thickness configuration of the PGP Eurasian and, by extension as a result of balancing the delta-18O budget, North American ice-sheet complexes.

4.4.3 Eurasian and North American Ice-Sheet Components

Previous work has suggested that the timing and rate of deglaciation of both the North American and Eurasian LGP ice sheets may play an important role in controlling northwest Eurasian RSL during the Holocene (Bradley et al., 2023), and the same may also be true for the influence of the Penultimate Deglaciation on LIG RSL (Dendy et al., 2017). However, this is more challenging to constrain due to the lack of geological constraints of Penultimate Deglaciation ice-sheet changes compared to those of the Last Deglaciation (Rohling et al., 2017). To address this, we develop an experimental design that allows us to systematically produce Penultimate

Table 4.1: Description of changes in temporal resolution of ice-sheet history inputs and corresponding RSL outputs to the sea-level model.

Age (ka)	Time Period	Time Step (ka)	Motivation
420 - 220	Pre-PGP	4	Drives long-term GIA signal
220 - 145	PGP	2	PGM 'spin up'
145 - 142	PGM	1	PGM load
142 - 126	Penultimate Deglaciation	0.5	Captures deglaciation signal
126 - 114	LIG	1	High-resolution output for analysis
114 - 0	Post-LIG	2	Enables convergence iteration

Deglaciation scenarios that vary in timing and volume for both the Er and NA ice sheets.

Each deglaciation scenario is characterised by 6 parameters, 3 for the North American (NA) and 3 for the Eurasian (Er) ice sheet: deglaciation start time (T_{PGM}^{NA}, T_{PGM}^{Er}), deglaciation end time (T_{LIG}^{NA}, T_{LIG}^{Er}), and PGM volume (V_{PGM}^{NA}, V_{PGM}^{Er}). For each ice sheet, the deglaciation portion of the volume time series between T_{PGM} and T_{LIG} is prescribed as a cosine decay function beginning at V_{PGM} and ending at the LIG (modern-day) configuration. In order that the deglaciation volume curve smoothly joins with the preceding PGP curve at T_{PGM}, we make two modifications to the volume curve between 220 ka and T_{PGM}: scale in volume, such that the maximum value matches V_{PGM}; and stretch in time, such that V_{PGM} aligns with T_{PGM}. The NA volume curve is converted into an ice-sheet thickness series by interpolating ICE-6G, as described previously, while the Er volume curve uses a given series of ICESHEET-generated deglaciation geometries for interpolation instead.

4.4.4 Ensemble Design

For each global ice-history ensemble member, the Eurasian component of the Penultimate Deglaciation is derived from the corresponding series of Eurasian ice-sheet geometries, modelled with ICESHEET, as described in Section 4.3.4. Therefore, V_{PGM}^{Er} is calculated directly from the PGM geometry from this Eurasian ensemble member. For North America, we derive V_{PGM}^{NA} by subtracting the volume of all other ice sheets from the total volume at the PGM, V_{PGM}^{T}. Since the Waelbrock curve has a reported minimum/maximum value range of ±13 m at the PGM, we choose to incorporate this uncertainty by assuming V_{PGM}^{T} can be described as a

normal distribution N with a standard deviation σ of 4.3 m, such that 99.7% of the probability density is within 13 m of the mean μ. By extension,

$$V_{PGM}^{NA} \sim N(\mu = V_{PGM}^{T} - (V_{PGM}^{Er} + V_{PGM}^{Gr} + V_{PGM}^{An} + V_{PGM}^{Ot}), \sigma = 4.3)$$

and instances of V_{PGM}^{NA} are drawn from this distribution.

We design a 532-member ensemble, chosen in order to match the sample size of the previously generated Eurasian deglaciation series (Figure 4.3), by sampling over the 10 parameters controlling the PGM ice-sheet deglaciation timing and volume, Eurasian margin asynchrony, and Earth model rheology. The rheological parameters are used to calculate the Love numbers (Peltier, 1974; Kendall et al., 2005) associated with each Earth model structure. One individual parameter combination translates into a single RSL output via our combined model workflow (Figure 4.5). Our parameter sample results in 532 ice-sheet history inputs that vary in North American and Eurasian ice-sheet volumes and deglaciation patterns during the PGP (Figure 4.6).

Table 4.2: Model parameters where, for a parameter x, $U(x_{min}, x_{max})$ represents a uniform distribution with a minimum (x_{min}) and maximum (x_{max}) value, $N(\mu, \sigma)$ represents a normal distribution with mean (μ) and standard deviation (σ), and HM is a history-matched distribution.

Name	Symbol	Distribution	Unit
shear-stress map (9)	HM	-	-
Async Power	A_n	$U(1, 5)$	1
Async Angle	A_θ	$U(\pi, 1.5\pi)$	1
Upper Mantle Viscosity	ν_{UM}	$U(1 \times 10^{20}, 1 \times 10^{21})$	Pa s
Lower Mantle Viscosity	ν_{LM}	$U(2 \times 10^{21}, 1 \times 10^{23})$	Pa s
Lithospheric Thickness	L	$U(50, 120)$	km
Er Deglaciation Start Time	T_{PGM}^{Er}	$U(142, 136)$	ka
Er Deglaciation End Time	T_{LIG}^{Er}	$U(130, 126)$	ka
NA Deglaciation Start Time	T_{PGM}^{NA}	$U(136, 142)$	ka
NA Deglaciation End Time	T_{LIG}^{NA}	$U(130, 126)$	ka
NA + Er PGM Volume	V_{PGM}^{NA+Er}	$N(112, 4.3)$	m SLE

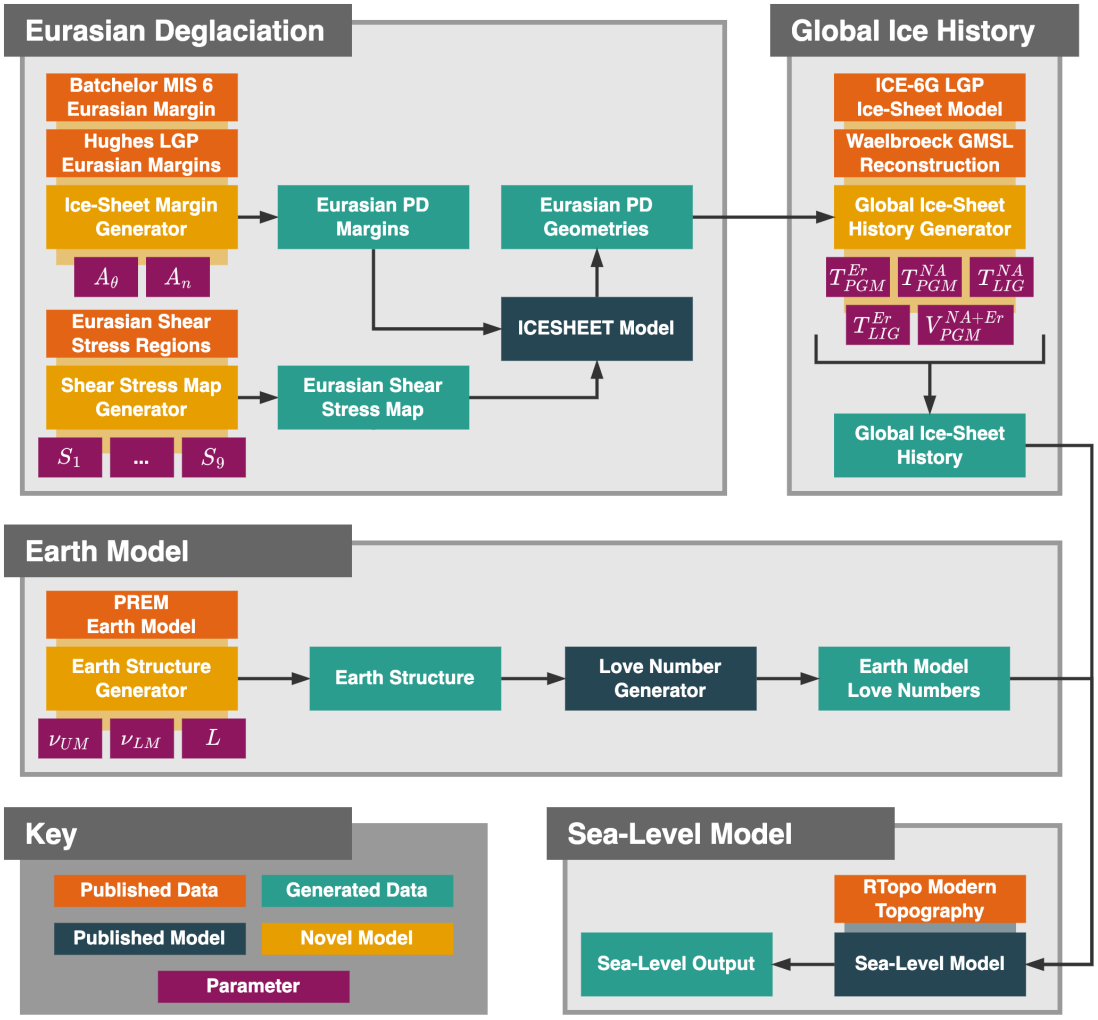

Figure 4.5: Flowchart showing the overall experimental design used in this paper. Key sections of work are grouped together. Numerical models (blue/yellow) are shown with their respective data inputs (orange/green) and parameters (purple). PD refers to the Penultimate Deglaciation.

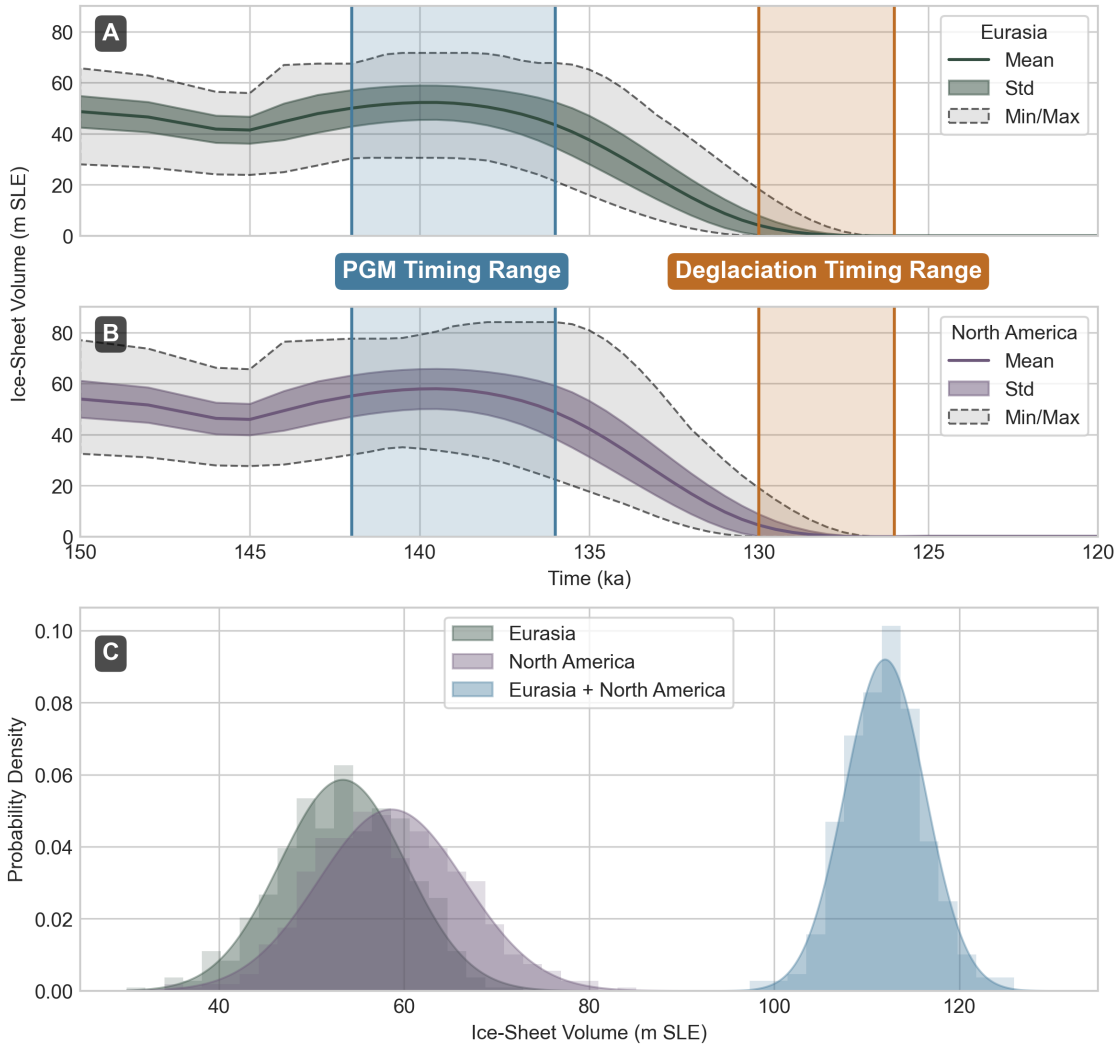

Figure 4.6: (A) Mean (solid line), standard deviation (shaded coloured region), and maximum/minimum values (grey dotted lines) of the ensemble of ice-sheet volume evolutions, shown between 150 and 120 ka, tested for the Eurasian ice sheet. (B) Same as (A) but for the North American ice sheet. (C) The probability density function of fitted normal distributions to the sample of Eurasian (derived from the ICESHEET model ensemble), total Eurasian and North American (defined from uncertainty in the Waelbroeck et al. (2002) $\delta^{18}O$ curve), and North American (resulting from the residual) ice-sheet volumes at the PGM.

4.5 Results

4.5.1 Last Interglacial Relative Sea Level

Our ensemble of 532 LIG RSL simulations show that, on average, GIA induced RSL remained significantly higher, relative to the present day (pre-industrial), throughout the LIG under areas directly covered by the Eurasian ice sheet (Figure 4.7). In the North Sea region, we find LIG RSL was almost exclusively higher than modern by an average of 30 ± 10 m, and in some places over 50 ± 30 m. However, we found that the spatial average rate of RSL change over the full Eurasian region was -2 mm yr^{-1} and was predominantly negative except for in the southern North Sea and Greenland-Iceland-Norwegian (GIN) Sea, where forebulge collapse leads to a maximum rate of change of 1 mm yr^{-1} and 5 mm yr^{-1} respectively, compared with 0 mm yr^{-1} and 2 mm yr^{-1} at present-day respectively (Kopp et al., 2015).

There is also a high level of uncertainty in our ensemble throughout the Eurasian region, particularly in locations previously covered by the PGP Eurasian ice-sheet mass. Disequilibrated topography relaxes towards isostatic equilibrium as the interglacial progresses and results in a reduction in the overall average uncertainty in RSL values later in the LIG. The average RSL standard deviation across the North Sea region reduces from ± 21 m at 126 ka to ± 14 m at 116 ka, reducing approximately linearly by ≈ 0.7 m per ka. This uncertainty is highly spatially variable and we find that the southern North Sea is has a relatively low uncertainty throughout the interglacial of $\approx \pm 5$ m, while further north areas covered by the British-Irish ice-sheet experience RSL uncertainties up to an order of magnitude greater.

4.5.2 Relative Sea-Level Sensitivity

We use sensitivity analysis (Sobol', 1990) to decompose the ensemble variance at four times throughout the LIG (126, 122, 118 and 116 ka) into per-parameter contributions, to understand the importance of each parameter on the modelled LIG RSL, as well as any large variations in the spatial influence of each parameter (Figure 4.7). Rather than using the shear stress input parameters directly, we perform our sensitivity analysis on calculated regional ice-sheet volume values for the Barents-Kara Sea, Fennoscandian, and British-Irish sections of the PGM Eurasian ice-sheet for each member of our ensemble. In addition, we choose to group parameters into Earth model, ice-sheet volume, and deglaciation timing categories to aid interpretation of our results, as detailed in Table 4.3. Our decomposition quantifies three types of parameter contributions to the RSL output variance: first-order effects, describing the independent contribution of each parameter; second-order effects, resulting

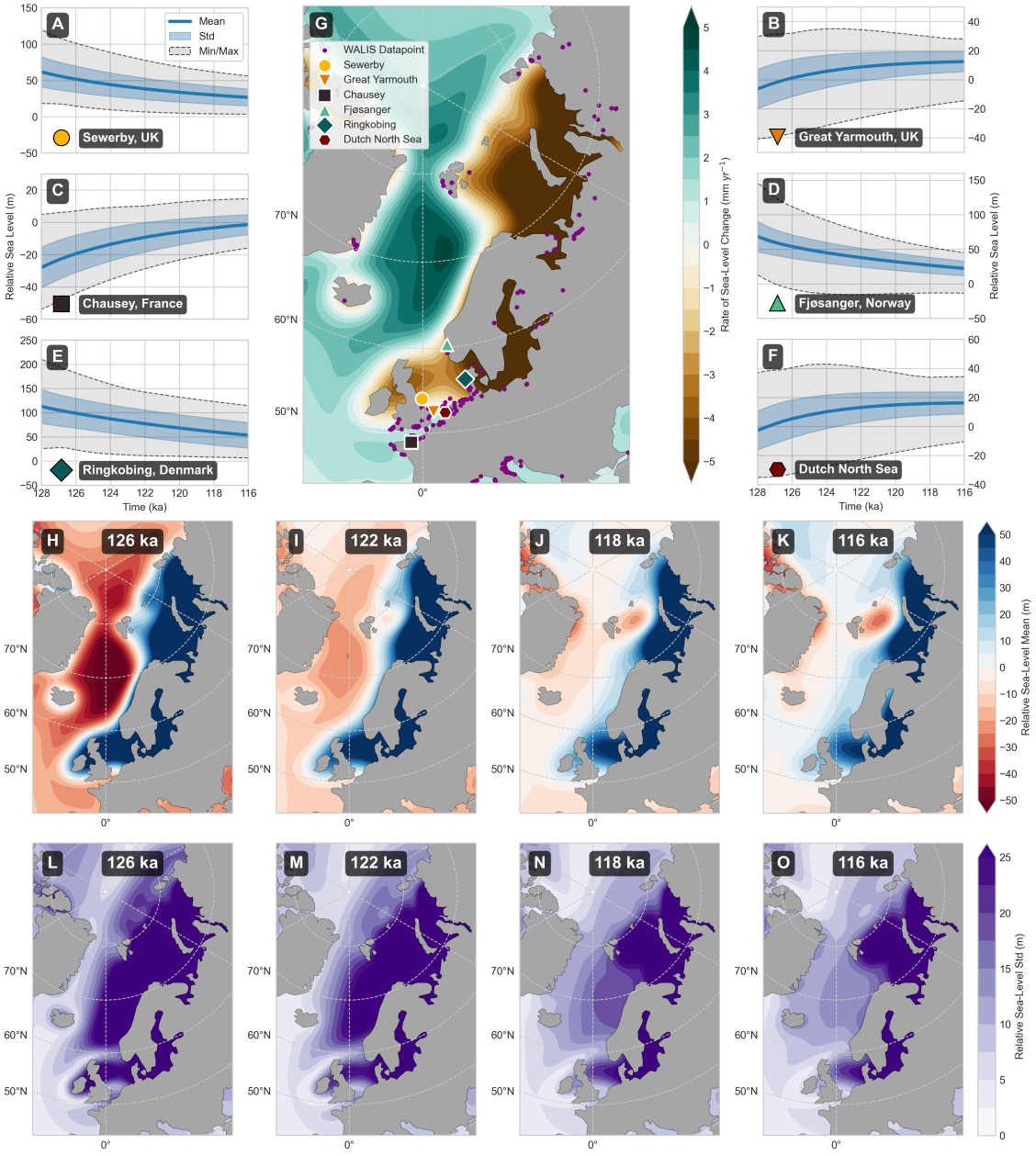

Figure 4.7: (A-F) Mean (solid line), standard deviation (shaded blue region) and minimum/maximum (grey dotted lines) values of the RSL ensemble, relative to the present day, shown for six selected locations that reflect the transects of RSL data shown Cohen et al. (2022). (G) Ensemble mean rate of Eurasian LIG RSL change. Purple points show locations of empirical RSL data from the WALIS database (Rovere et al., 2023b). The marker for location (A-F) is also plotted on this map. (H-K) Ensemble mean RSL shown for four times (126, 122, 118 and 116 ka), relative to present day. (L-O) Same as (H-K), but showing the RSL standard deviation across the ensemble.

from parameter-pair interactions; and total-order effects, representing the summed contribution of all interactions and the independent contributions for each parameter.

Table 4.3: Metrics used for sensitivity and uncertainty analysis.

Name	Symbol	Group
Upper Mantle Viscosity	ν_{UM}	Earth Model
Lower Mantle Viscosity	ν_{LM}	Earth Model
Lithospheric Thickness	L	Earth Model
Barents-Kara Sea Ice Volume	V_{BKS}^{Er}	Ice-Sheet Volume
Fennoscandian Ice Volume	V_{F}^{Er}	Ice-Sheet Volume
British-Irish Ice Volume	V_{BI}^{Er}	Ice-Sheet Volume
NA + Er PGM Volume	V_{PGM}^{NA+Er}	Ice-Sheet Volume
Async Power	A_n	Deglaciation Timing
Async Angle	A_θ	Deglaciation Timing
Er Deglaciation Start Time	T_{PGM}^{Er}	Deglaciation Timing
Er Deglaciation End Time	T_{LIG}^{Er}	Deglaciation Timing
NA Deglaciation Start Time	T_{PGM}^{NA}	Deglaciation Timing
NA Deglaciation End Time	T_{LIG}^{NA}	Deglaciation Timing

We find that the Earth model parameters make the largest first-order contribution to LIG RSL uncertainty across the Eurasian region for all times considered. The influence of the wide range of ice-sheet volumes in our ensemble is high in the Barents-Kara Sea region, contributing greater than 20 m uncertainty under the region previously loaded by the Eurasian ice sheet. However, in the Baltic Sea region, which was previously covered by the Fennoscandian portion of the ice sheet, we find that the contribution of ice-sheet mass to the RSL uncertainty significantly reduces from greater than 20 m at 126 ka to less than 3 m by 116 ka. The influence of ice-sheet deglaciation timing on uncertainty is limited to the Siberian coastline and the northern Baltic Sea region at 126 ka (Figure 4.8I), reducing to less than 5 m by 116 ka (Figure 4.8L).

There is significant variation in the magnitude and spatial scope of the first-order influence of individual Earth model parameters. We find that the upper mantle viscosity is a significant source of uncertainty in a number of regions: the central North Sea, GIN Sea, Barents Sea, and northern Kara Sea, Baltic Sea, and Siberian coastline regions (Figure 4.9A). The lower mantle viscosity RSL uncertainty contribution is concentrated around the northern Baltic Sea, where it contributes greater than

20 m, and the Fennoscandian coastline. In contrast, we find that the lithospheric thickness makes a relatively minimal contribution and, of all regions considered, is most influential in the GIN Sea, where the total-order contribution still only equates to 15% of the overall average RSL uncertainty (Figure 4.9F).

Parameter interaction effects, meaning that RSL is more sensitive to changes in multiple parameters simultaneously than those same parameter changes individually, are most influential in the Baltic Sea, Barents-Kara Sea and GIN Seas (Figure 4.12). The upper and lower mantle viscosities are most interactive in all regions, but we find that there is a strong interaction between the volume of the Barents-Kara Sea ice mass and the other ice-sheet regions, perhaps due to a larger Barents-Kara Sea ice volume co-existing with relatively large ice-sheet volumes from other regions. While also being the most sensitive, the viscosity parameters are also responsible for producing the most extreme ensemble members (quantified by the average standard deviation from the ensemble mean) for most regions. However, the Barents-Kara Sea is more influenced by the volume of the Fennoscandian and Barents-Kara Sea ice sheets than viscosity.

4.5.3 Rate of Relative Sea-Level Change Sensitivity

The rate of RSL change may be important to consider when attempting to fingerprint interglacial ice-sheet melt. Therefore, in addition to the magnitude of RSL at individual times throughout the LIG, we performed sensitivity analysis on the average rate of RSL change across the LIG. The Barents-Kara, Norwegian and Baltic Seas have the highest uncertainty in regards to the modelled rate of RSL change, reaching 4 mm yr^{-1} uncertainty in some places. The relative contributions of each parameter to the uncertainty in RSL rate of change are of similar magnitude to those previously discussed for the RSL uncertainty. However, differences between the rate of change and RSL exist in the North Sea region, where the rate is far less uncertain. We find that the Earth model contribution to uncertainty in RSL change substantially decreases in the Barents-Kara and Baltic Sea regions, while the ice-sheet volume influence remains concentrated around the Barents-Kara Sea.

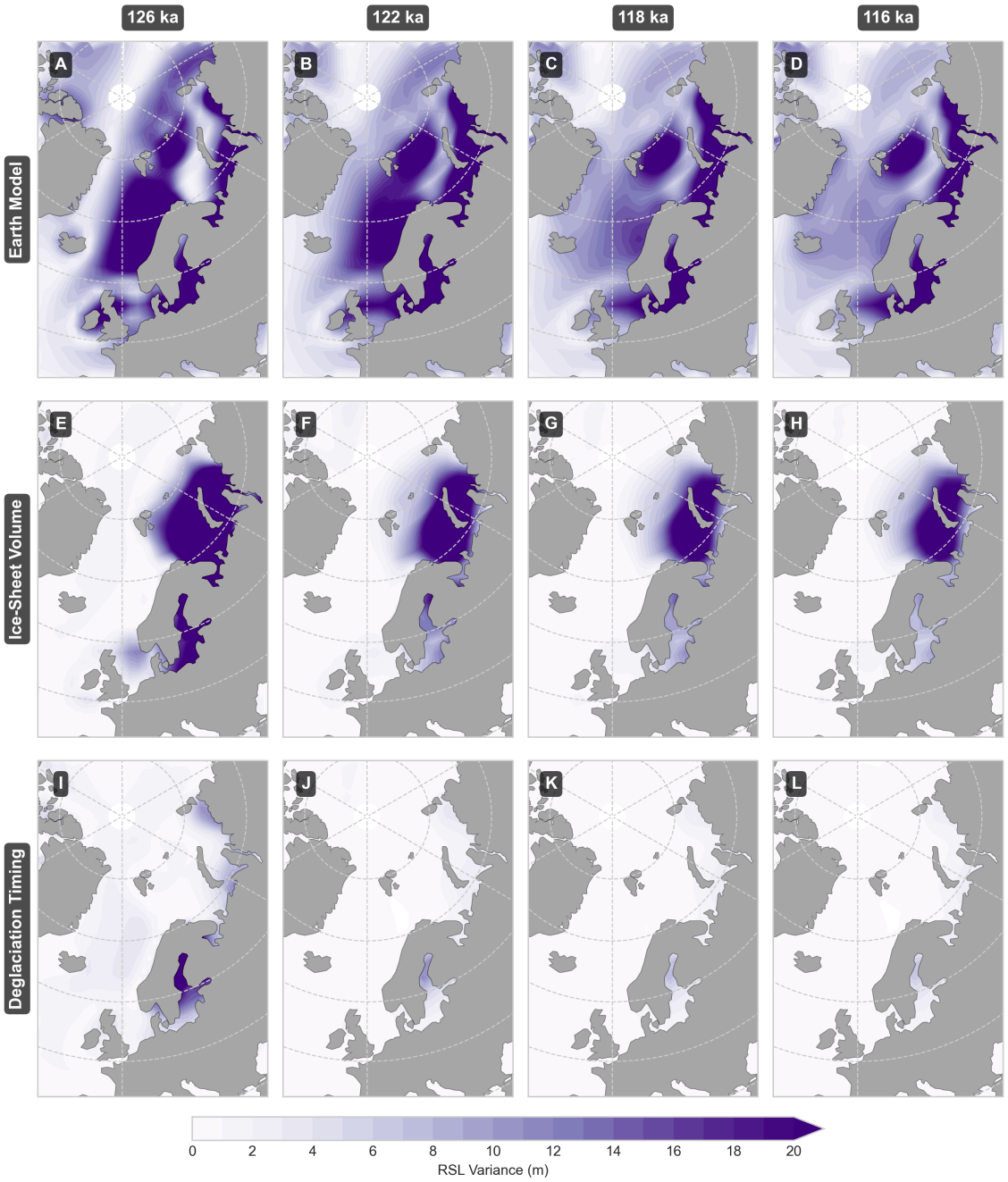

Figure 4.8: Decomposition of the RSL ensemble uncertainty at 126, 122, 118 and 116 ka. RSL uncertainty is shown as the summed sensitivities for three groups of model parameters: (A-D) Earth model, (E-H) Eurasian PGM ice-sheet volume, and (I-L) Penultimate Deglaciation timing parameters.

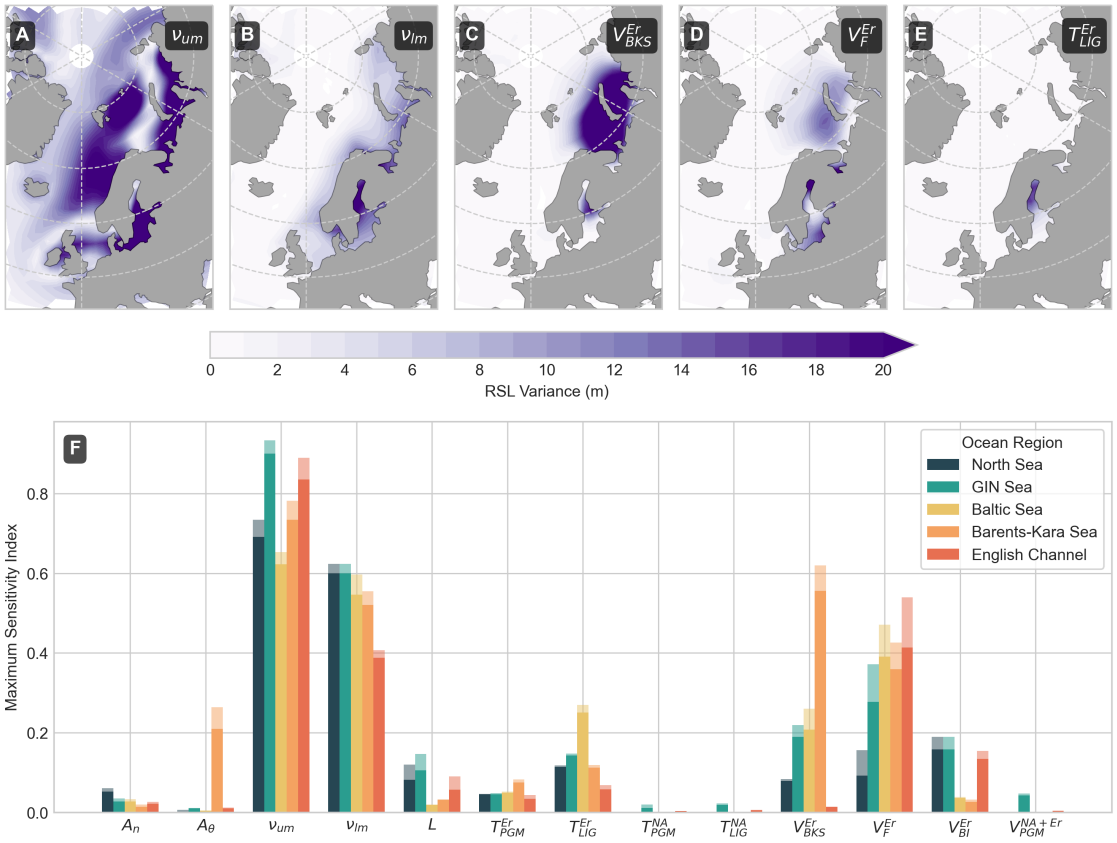

Figure 4.9: (A-E) Sensitivity decomposition of RSL uncertainty, averaged over the LIG, from the 5 most influential parameters (Table 4.3). (F) Maximum percentage 1st order parameter contribution to the time-averaged RSL variance in 5 different marine regions (where RSL will be recorded at the coastline), with the total order contribution shown as the lighter coloured bar.

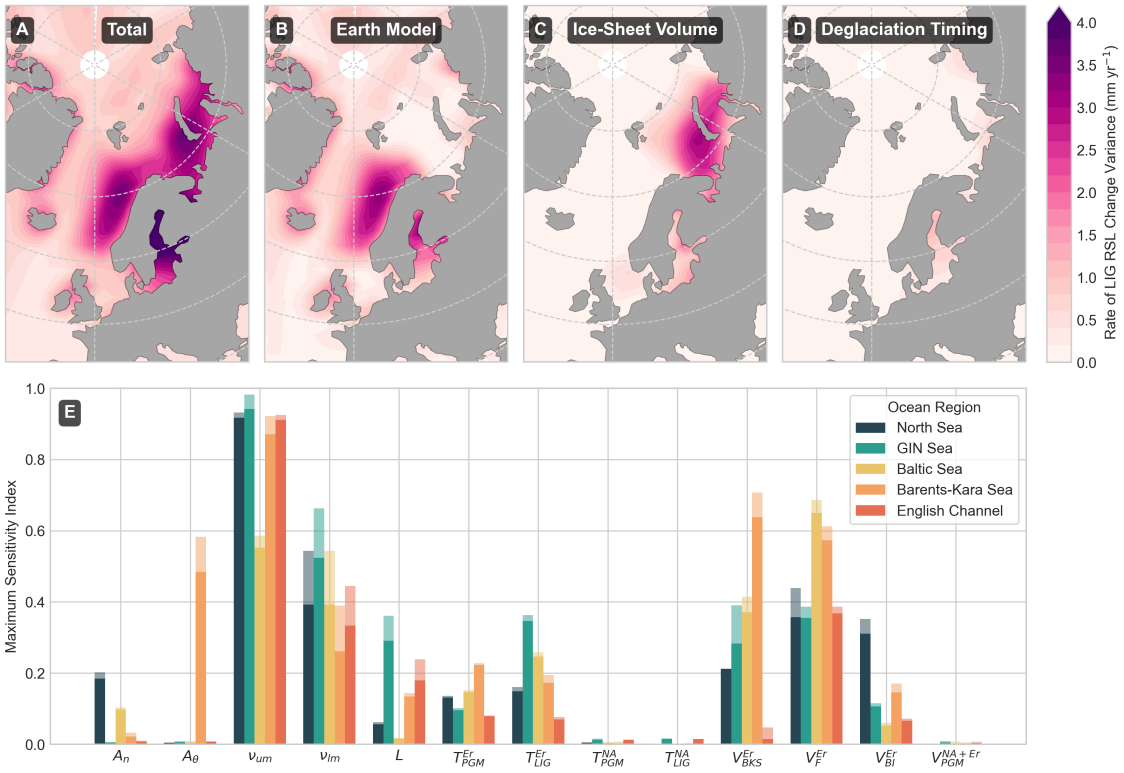

Figure 4.10: (A-D) Decomposition of the rate of LIG RSL change variance into parameter groups. (E). Maximum percentage 1st order parameter contribution to the RSL rate of change variance in 5 different ocean regions, with the total order contribution shown as the lighter coloured bar.

4.6 Discussion

We have systematically tested a suite of LIG RSL scenarios that vary in the configuration, volume, and timing of the Penultimate Deglaciation of the North American and Eurasian ice sheets; as well as in the configuration of the 1D solid Earth model. We found that RSL across northwest Eurasia during the LIG had a pattern much different to that of today due to the strong influence of GIA from ice-sheet changes during the Penultimate Deglaciation. Areas that were directly beneath the former PGM Eurasian ice sheet experienced high RSL values, in some places exceeding 50 m, such as in the Baltic Sea, central North Sea, and Barents-Kara Sea. In contrast, the GIN Sea and areas of the North Atlantic Ocean had lower RSL, likely due to the combined influence of forebulge formation and ice-mass-driven perturbation of the Earth's rotational axis. We found that the overall pattern of RSL is reasonably consistent across the LIG but that the magnitude of this signal decreases substantially in some areas due to a relaxing of the state of topographic disequilibrium set up by the preceding ice-sheet load. By 116 ka, the previously low RSL values in the GIN Sea and North Atlantic Ocean had relaxed to near modern levels, while the high RSL values in the Baltic Sea, Barents Sea, southern Kara Sea, and central North Sea persisted.

Our ensemble resulted in high levels of uncertainty in GIA induced RSL during the LIG, with an average of 34 m uncertainty over all regions at 126 ka, reducing to an average of 21 m by 116 ka. However, there is variability in the level of uncertainty between regions with the English Channel, GIN Sea, and North Sea having the lowest uncertainty (averaging 12 m, 16 m and 21 m respectively at 126 ka) while the Barents-Kara and Baltic Seas are highly uncertain (averaging 50 m and 72 m at 126 ka respectively). Parameter-wise sensitivity decomposition showed that, for almost all times and regions considered, uncertainty in the Earth model parameters dominate the RSL sensitivity and that, in particular, the upper mantle viscosity is the most important quantity in determining regional RSL. It is only in areas towards the centre of large ice-mass loading, such as the Barents-Kara Sea and areas of the Baltic Sea, that the regional volumes of the Eurasian ice sheet become more important than Earth model parameters in determining RSL. We find that the timing of the North American deglaciation plays a negligible role in determining RSL in all regions, while the timing of the Eurasian deglaciation plays a moderate role in the Baltic Sea towards the start of the LIG.

Our work suggests that data records subject to the lowest GIA uncertainty are those located in the southern North Sea, English Channel and GIN Sea regions (Figure 4.7)

and which date towards the end of the LIG. We therefore recommend that future RSL data collection focus on these regions if they wish to minimise the influence of GIA uncertainty on record data. Records collected in the Baltic Sea, central North Sea, and southern Barents-Kara Sea of any LIG age should pay particular attention to characterising Earth model uncertainty, while samples in the Baltic Sea and Barents-Kara Sea are also subject to uncertainty from the corresponding regional volume of the Eurasian ice sheet. We find that the timing of the Eurasian deglaciation plays a minor role, except for if a sample is dated at the beginning of the LIG. We find that the North American ice-sheet complex plays a negligible role in determining the overall uncertainty of northwest Eurasian RSL during the LIG but that this sensitivity is likely to change if later deglaciation timings are considered.

In order to limit the size of our ensemble parameter space, we have made several simplifying assumptions when considering the broad range of sources of uncertainty that may contribute to uncertainty in LIG RSL. We adopt the approach of similar studies by assuming a simple, 1D, globally uniform Earth structure for determining the solid Earth response to ice-sheet loading (Bradley et al., 2023; Dendy et al., 2017). We, therefore, cannot account for potential lateral variability in mantle viscosity and lithospheric thickness over our study area that would be captured through the use of a 3D Earth model. While the computational cost was infeasible within our ensemble design, we recommend the influence of 3D Earth models on LIG RSL variability be tested in future work.

Our ensemble of Eurasian ice-sheet simulations was generated assuming a single maximum ice-sheet extent for all ensemble members and, based on work by Pollard et al. (2023), including a variable PGM ice extent may have contributed up to an additional 10% variability in the Eurasian PGM ice-sheet volume. However, the inclusion of variable PGM margin would have added significant complexity to the interpretation of asynchrony parameter sensitivity and would likely have made a minor contribution to the overall uncertainty.

In generating global ice-sheet histories, we chose to use δ^{18}O as a proxy for total global ice-sheet volume due to the absence of alternative ice-volume datasets. δ^{18}O is a measure of the relative abundance of oxygen isotope ^{18}O versus ^{16}O molecules in ice or water and records can be recovered from sediment, ice-core, or biological markers reflecting values of δ^{18}O at a particular location and time. The relative abundance of oxygen isotopes in ice or water is a result of isotope fractionation during evaporation and precipitation. Thus, changes in the magnitude and global spatial pattern of δ^{18}O reflect large-scale changes in global temperature and ice-sheet volume. There are multiple sources of uncertainty in global δ^{18}O reconstructions including: interpreting

a global complication of δ^{18}O while accounting for spatio-temporal variability due to patterns of climate and ocean circulation that affect isotopic fractionation; temporal uncertainty from dating records from which δ^{18}O values have been derived; and calibrating the relationship between proxy values and the true δ^{18}O value, including the influence of local effects, such as local ocean temperature, on these relationships (Shakun et al., 2015; Waelbroeck et al., 2002). While it was not within the scope of this study, the consideration of alternative reconstructions and interpretations of δ^{18}O in our work may have resulted in a wider range of possible timing and magnitude changes in global ice-sheet volume and thus altered the range of possible RSL outputs. However, incorporating uncertainty in our δ^{18}O derived global ice-sheet volume, included by modelling the inferred combined North American and Eurasian PGM ice-sheet volume as a normally distributed parameter reflecting the δ^{18}O uncertainty assessment of Waelbroeck et al. (2002), resulted in a negligible contribution to uncertainty in LIG RSL in all regions considered.

The overall pattern of mean and variance in LIG RSL is similar to the suite of GIA scenarios tested by Barnett et al. (2023), which encompassed changes in Eurasian ice-sheet volume and Earth model configuration, but our study suggests three key findings: more extensive subsidence surrounding the British Isles, a greater RSL uncertainty in the GIN Sea at the beginning of the LIG, and more substantial subsidence in the Baltic and North Sea regions by the end of the LIG. We find a similar pattern of uncertainty in the North Sea region, likely due to the presence of an ice bridge connecting the British-Irish and Fennoscandian ice sheets, similar to that which occurred during the LGM (Gandy et al., 2021). The sensitivity experiments performed by Dendy et al. (2017) implicitly concluded that Eurasian RSL at the end of the LIG was highly dependent on the volume of the Eurasian ice-sheet at the PGM, generating absolute RSL differences of greater than 6 m in most regions when comparing model outputs using the larger Lambeck et al. (2006) Eurasian PGM geometry against the smaller LGM ICE-6G geometry (Peltier et al., 2015). While we did not test Eurasian volumes as small as ICE-6G (23.5 m SLE), we found a similar 2 - 4 m variation in RSL values in the North Sea throughout the LIG due to Eurasian volume changes, and much higher variance in regions beneath the former ice-sheet load. Their work also suggested that, beyond the former ice margin, the influence of ice-mass changes on the perturbation of the Earth's rotational axis acted to reduce RSL for larger ice sheets by greater than 6 m for an invariant Earth model. While we do not explicitly identify the contribution of rotational effects in this work, it is likely that the magnitude of the Earth model uncertain contribution dominates the contribution of rotational perturbations in the near-field northwest Eurasian region.

Utilising LIG RSL data from the near-field sedimentary archive for the purpose of developing LIG fingerprints of ice sheet melt is a major goal for the palaeo sea-level community (Dutton et al., 2015; Hay et al., 2014; Bradley et al., 2023). Our work suggests that quantifying the influence of ongoing GIA driven by the preceding deglaciation is essential to unearthing this sea-level fingerprint, but that uncertainty surrounding GIA signal may hamper efforts to use data from the Barents-Kara and Baltic Seas. We suggest that studies place their emphasis on well-quantified Earth model uncertainty in all areas; focus attention on data acquired in southwestern Eurasian regions where overall RSL uncertainty is lowest, such as the English Channel; and avoid emphasis on quantifying deglaciation timings during the PGP.

4.7 Conclusions

Quantifying the contribution and uncertainty of GIA to LIG RSL remains a challenge due to the significant uncertainties in past ice-sheet changes and the response of the solid Earth, hampering research that attempts to utilise LIG sea-level record for fingerprinting LIG ice-sheet melt. To address this, we developed a large ensemble experimental design that, by combining ice-sheet, Earth, and sea-level models, is able to systematically assess the uncertainty from two major sources: the volume, configuration, and timing of the Penultimate Deglaciation of the Eurasian and North American ice sheets; and the 1D model of the viscoelastic solid Earth structure. Utilising our ensemble, we explored the magnitude and spatial distribution of RSL uncertainty throughout the LIG and employed sensitivity decomposition to attribute the relative contribution of each input parameter to this uncertainty.

We found that the Earth model parameters have the widest spatial influence on uncertainty of both RSL and rate of RSL change, but that the Barents-Kara Sea stands out as being most influenced by the Eurasian ice-sheet volume. We find that the timing of the ice-sheet deglaciation is most influential on LIG RSL at the beginning of the interglacial and that this influence is concentrated around the Baltic Sea. Parameters controlling the timing and volume of the North American ice sheet play little part in controlling the rate of RSL uncertainty, and the asynchrony of the Eurasian ice-sheet deglaciation only influences small parts of the Kara Sea. To conclude, our findings suggest that the southern North Sea and the English Channel are regions most suitable for future data collection studies, as they are least affected by GIA uncertainty. We suggest that future work is focused on reducing uncertainty in the Earth model parameters, as they are most influential in quantifying LIG GIA in all regions except those directly under the former Eurasian ice sheet. Finally, we highlight the importance of incorporating well-quantified GIA uncertainty in

data-driven studies of LIG RSL, particularly for those aimed at quantifying RSL fingerprints.

4.8 Supplementary Figures

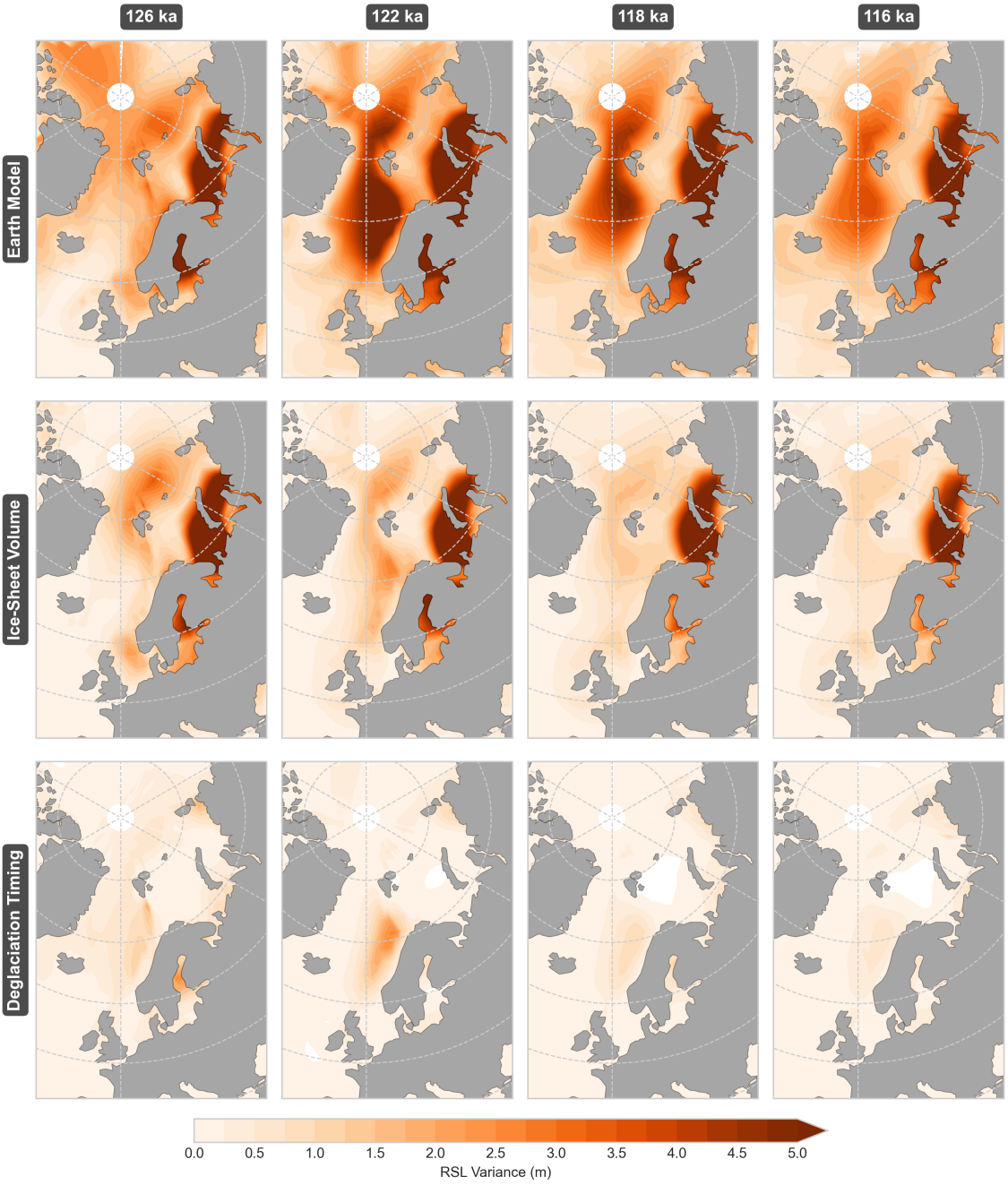

Figure 4.11: Contribution of interaction effects to RSL ensemble uncertainty at 126, 122, 118 and 116 ka. Interactions are shown as the summed sensitivities for three groups of model parameters: (A-D) Earth model, (E-H) Eurasian PGM ice-sheet volume, and (I-L) Penultimate Deglaciation timing parameters.

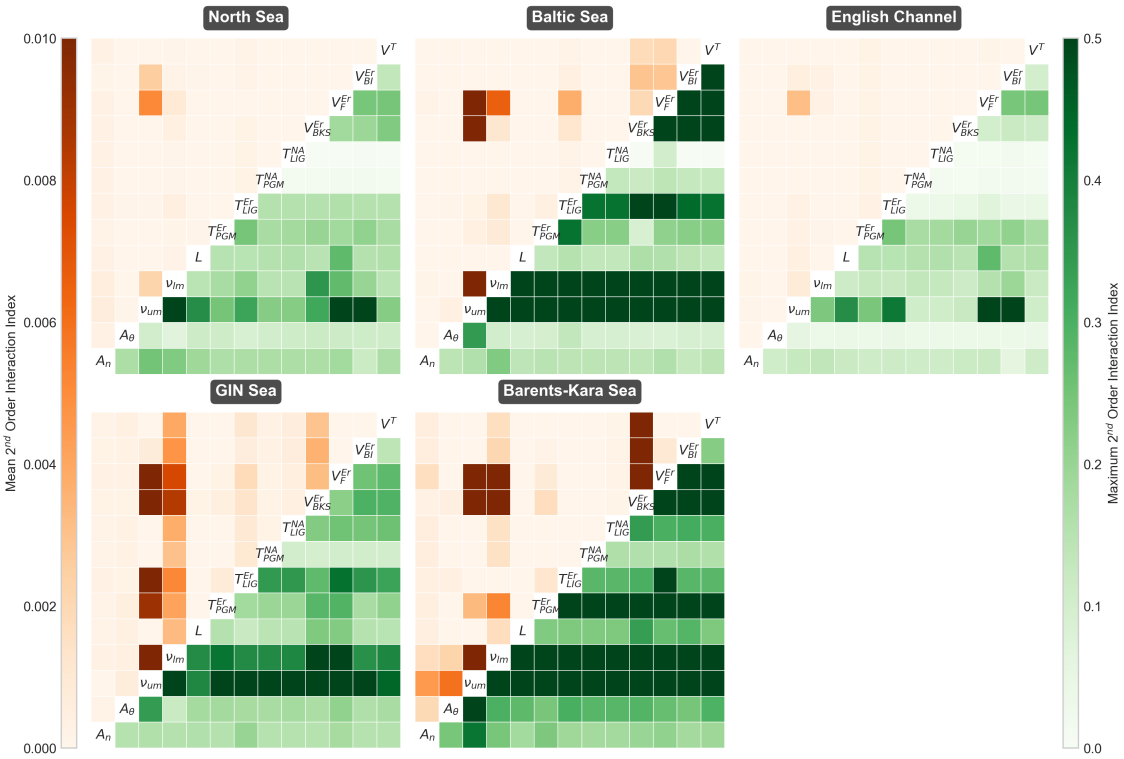

Figure 4.12: Mean (oranges) and maximum (greens) percentage contribution of 2nd order interaction effects between each parameter pair on LIG RSL uncertainty shown for each Sea region.

Chapter 5

Identifying the Antarctic Melt Contribution to Last Interglacial Sea Level from Eurasian Relative Sea-Level Records

5.1 Abstract

The high GMSL during the LIG was likely to have largely been driven by Greenland and Antarctic melt, but the timings, rates, and relative magnitudes of these contributions remain uncertain. Due to the geometry of ice-sheet fingerprints, RSL records in the Eurasian region are likely to be sensitive to ice mass changes in Antarctica while being relatively insensitive to changes in Greenland, making them ideal targets for identifying scenarios of past LIG ice-sheet melt. In this work, I produce an ensemble of Eurasian RSL models driven by regional GIA and a systematic suite of Antarctic melt scenarios in order to compare our simulations against LIG RSL records from the WALIS database. By performing regional sensitivity analysis, we identify Eurasian data regions most sensitive to AIS melt, and through the use of a bespoke Bayesian history matching framework, uncover GIA and AIS scenarios that most closely match regional RSL data within uncertainty. Our results show that data points off the coast of Wales, northwest France, and the English Channel are most sensitive to AIS melt but that all modelled RSL scenarios are able to fit the suite of RSL data within 3-sigma uncertainty. Despite this, our model-data analysis, utilising RSL data that we have identified as strongly sensitive to AIS ice-sheet changes, reveals a clear

preference for high magnitudes of total AIS melt, identifying an AIS contribution of between 3.2 - 9.3 m to the LIG GMSL highstand (*likely*, 66th percentile).

5.2 Introduction

Modern anthropogenic activity is driving wide-scale, sustained warming of Earth's climate and, in response, GMSL is projected to rise by upwards of 5 m under high emission scenarios by 2300 (IPCC, 2022). As the GrIS and AIS continue to respond to temperature changes, ice-sheet melt has become the dominant contributor to 21st century GMSL change (Gregory et al., 2013) and is driving a continued acceleration in the rates of sea-level rise (IPCC, 2022). The sources, magnitudes and rates of ice-sheet melt contributions can drastically alter patterns of RSL across the globe and, therefore, change the risk of particular locations to sea-level inundation. It is, therefore, vital to constrain the future evolution of individual ice sheets in order to accurately assess the spatial pattern of the risks posed by rising sea levels (Kopp et al., 2015). Despite this, our understanding of the response of modern-day ice sheets to future warming remains highly uncertain beyond 2300, primarily as a consequence of requiring numerical models to simulate ice-sheet behaviour outside of the window of modern observations (Pattyn and Morlighem, 2020; Robel et al., 2019). However, the Earth system has been subjected to similar warming events during previous Quaternary interglacial periods and, of these events, the LIG represents the most recent, well-studied, and data-rich past interglacial in which the GrIS and AIS were thought to be smaller than those of today (Capron et al., 2014; Otto-Bliesner et al., 2006). Constraining the evolution of the GrIS and AIS during the LIG would help to elucidate the sensitivity and response of these ice sheets to future warming; better quantify the likely rates and magnitudes of future GMSL rise; and evaluate the risk posed to local coastal population, infrastructure, and ecology, to aid decision making beyond 2300.

There is wide agreement that GMSL during the LIG was higher than those of today, but studies differ in their estimates of its magnitude, varying between 1.2 m and 10 m above present-day values, with even higher values not currently ruled out (Kopp et al., 2009; Dutton et al., 2015; Dyer et al., 2021; Fox-Kemper et al., 2021). The contribution of thermal expansion to the LIG sea-level highstand has been constrained to between 0.4 ± 0.3 m (McKay et al., 2011) and 0.8 m (Turney et al., 2020), while melt from mountain glaciers may have contributed up to 0.32 ± 0.08 m SLE (Marzeion et al., 2020) meaning that higher LIG sea levels cannot be explained without large contributions from the GrIS and/or AIS. Previous work has estimated GrIS and AIS contributions with the use of dynamic ice-sheet models driven by a

climate forcing assumed to be representative of the LIG. Such studies applied to the GrIS have resulted in wide-ranging estimates of its LIG GMSL contribution of between 0.6 m SLE (Stone et al., 2013) and 5.3 m SLE (Yau et al., 2016), depending on the climate forcing, ice-sheet model, and proxy data constraints employed in the experimental design (Cuffey and Marshall, 2000; Stone et al., 2013; Yau et al., 2016). These estimates are of similar magnitude to those inferred from recent data studies that place the GrIS contribution between 0.6 - 3.5 m SLE (Dutton et al., 2015).

AIS modelling studies have placed emphasis on identifying the distinct behaviour and drivers of the EAIS and WAIS melt. Coupled, dynamic ice-sheet simulations of the marine-based WAIS have suggested a LIG GMSL contribution of 1 - 5 m (DeConto and Pollard, 2016; Clark et al., 2020; Golledge et al., 2021), driven primarily by the ice sheet's vulnerability to Southern Ocean warming (Turney et al., 2020), but these estimates may be under-predicted by up to 30% if water expulsion from post-glacial rebound is accounted for (Pan et al., 2021). The majority of the EAIS is relatively insensitive to ocean forcing, as most of the ice sheet sits on bedrock that lies above the sea-surface elevation, and has therefore been assumed to be relatively stable (Huybrechts, 1993). Modern-day EAIS studies suggest that a warming climate may drive possible positive surface mass balance changes, in response to changes in precipitation patterns, and therefore drive ice-sheet volume growth (Harig and Simons, 2015). However, while insensitive to ocean forcing, Fogwill et al. (2014) found that the ice sheet may be vulnerable to changes in Southern-Hemispheric wind patterns and the resulting local surface warming, driving a 3 - 5 m LIG contribution from the EAIS in their numerical modelling study. AIS Penultimate Deglaciation to LIG melt scenarios in the study by Bradley et al. (2013), in which such scenarios were evaluated against ice-core derived evidence of ice thickness, estimated that the majority of EAIS change occur prior to 126 ka and found no more than a 1.1 m SLE LIG contribution from the EAIS using their reference ice-sheet model, while their adapted idealised Wilkes and Aurora basins retreat scenario contributed 1.01 m SLE.

Through the effects of GIA, the particular location and geometry of ice-sheet melt results in a distinct spatial pattern of RSL known as sea-level fingerprints (Figure 1.3) that, in turn, result in large differences in regional sensitivity to LIG AIS melt (Hay et al., 2014; Mitrovica et al., 2009). Efforts have been made to derive estimates of LIG AIS melt from records of RSL, in regions targeted for their high sensitivity to AIS changes, through the use of statistical methods (Barnett et al., 2023; Rohling et al., 2019). Such works rely on well-constrained chronologies, quantified contributions of local processes, and assumptions to be made about the contribution of GrIS and, as a result, studies typically focus on a single region or record. In one of the few studies to apply RSL data as a constraint on LIG AIS melt contribution to GMSL, Barnett

et al. (2023) utilised a database of 27 absolute-dated LIG data points (7 limiting, 20 sea-level index points), primarily located in the English Channel region, corrected for regional GIA and processes driving vertical land motion, to produce a single time series for regional LIG sea-level change. By subtracting an estimate for the GrIS contribution, the remaining time series was attributed to AIS melt and, using an estimate of the magnitude of the northwest Eurasia AIS fingerprint, was converted into an estimate for LIG AIS contribution of 5.7 m (median, 50th percentile), with a range of 3.6 to 8.7 m (central 68% probability). In other work, Dutton et al. (2015) estimate a LIG AIS contribution of 4.6 ± 1.7 m by subtracting estimated GrIS, thermosteric, and mountain glacier contributions from the sea-level signal recorded by LIG corals in the Seychelles. Significant uncertainties remain in the rate, timing and magnitudes of LIG AIS melt, as well as in the relative contributions of WAIS and EAIS, and yet these constraints are vital for realising the potential of the LIG as a rich archive of empirical ocean, ice, and climate constraints for the calibrations for future climate models that, in turn, can directly inform present-day decision-making and policy.

Previous work has been limited in three key areas: modelling studies have been limited in their range of modelled AIS scenarios due to the expensive nature of dynamic ice-sheet modelling, without the use of emulation (Gilford et al., 2020) or simple climate assumptions; data-driven studies have not fitted their inferred AIS melt scenarios against AIS models, instead extracting the AIS signal directly from data; and both approaches have been limited in the size and type of data constraints used. In this work, we develop a data-model comparison framework using a Bayesian history matching procedure that is capable of identifying the most plausible Earth model, GIA, and LIG AIS melt scenarios, accounting for model and data uncertainty when compared against LIG RSL data. We apply our approach to the northwest Eurasian region by developing a large ensemble of possible RSL patterns that we history match against an extensive, newly complied Eurasian LIG RSL database. We parameterise scenarios of LIG EAIS and WAIS melt in order to generate an ensemble of possible AIS melt histories spanning a range of timings, durations, and volumes. By combining this ensemble with a suite of possible regional GIA scenarios, driven by an ensemble of novel Penultimate Deglaciation Eurasian ice-sheet geometries and viscoelastic Earth models, we utilise a gravitationally self-consistent sea-level model to produce an ensemble of RSL simulations for the northwest Eurasian region. Sensitivity analysis of our ensemble enables us to determine the relative sensitivity of northwest Eurasian regions to AIS melt and our history matching procedure allows us to identify regions of our parameter space that are best able to match northwest Eurasian records of RSL. Finally, we combine information gained from this analysis

to focus our history-matching procedure on only those records most sensitive to Antarctic melt in order to identify the most likely ensemble of LIG AIS evolution.

5.3 Models, Methods and Data

5.3.1 Global Ice-Sheet and Earth Models

LIG RSL values resulting from AIS melt are calculated using a gravitationally self-consistent sea-level model that takes global ice-sheet thickness and a 1D viscoelastic Earth model as input in order to generate solutions to the Sea Level Equation (Kendall et al., 2005). Sea-level model calculations are performed using a pseudo-spectral algorithm up to spherical harmonic degree 512 and, as a result, model RSL and topography outputs, as well as ice-sheet history inputs, are provided on a 512 by 1024 Gauss–Legendre latitude-longitude grid (hereafter referred to as the model grid). The Earth model assumes an elastically compressible 1D Maxwell structure with a radially varying stepped viscosity profile, which is parameterised by an upper-mantle viscosity ν_{UM}, lower mantle viscosity ν_{LM}, and lithospheric thickness L and which preserves the location of PREM elastic and density structure discontinuities. As demonstrated in Chapter 4, the Earth model uncertainty is a dominant contributor to LIG RSL uncertainty in our study area and, therefore, we include systematic exploration of the viscoelastic Earth structure in our experimental design. We adopt the Earth model parameter ranges developed for the northwest European region by Bradley et al. (2023) of 0.1 - 1 $\times 10^{21}$ Pa s for ν_{UM}, 0.1 – 5 $\times 10^{22}$ Pa s for ν_{LM} and 71 – 96 $\times 10^{3}$ km for L, based upon regional published literature (Bradley et al., 2023; Dendy et al., 2017; Milne et al., 2006).

Interglacial RSL values are sensitive to ice-sheet changes from at least 3 glacial cycles prior, as shown by Dendy et al. (2017), while the sea-level model requires the ice-sheet history to extend to modern-day to enable convergence to modern topography. Therefore, we prescribe global ice-sheet changes from 420 ka until the modern day by scaling the Peltier et al. (2015) ICE-6G global ice-sheet model of the LGP to a global ice-sheet volume curve derived from the δ^{18}O reconstruction of Waelbroeck et al. (2002). Since the PGP ice-sheet configuration in North America and Eurasia was likely very different to that of the LGP we modify the PGP section of our ice history by replacing the Eurasian ice-sheet with an ensemble of deglaciation geometries, as outlined in Chapter 4, and re-scale the North American ice-sheet in order to match the total global ice-sheet budget at the PGM. Our previous study demonstrated that LIG RSL in Eurasia is relatively insensitive to the timing of North American and Eurasian deglaciation and so we prescribe a fixed PGM timing for

both the Eurasian and North American ice sheets of 139 ka and also terminate their deglaciations at 129 ka. In addition, we modify the LIG portion of our ice-sheet history such that all ice sheets assume pre-industrial configuration between 129 ka and 116 ka.

5.3.2 Last Interglacial Antarctic Melt Scenarios

We construct a range of LIG AIS melt scenarios that differ in the rate, timing, and magnitude of both WAIS and EAIS melt contributions, to test their fingerprint on LIG RSL. Our scenarios consider the evolution of WAIS and EAIS separately and are constructed from time-series of ice volume change during the LIG (that prescribe when ice is lost/gained) which are then converted into corresponding spatiotemporal evolutions of AIS ice-thickness by interpolating a series of pre-modelled AIS thickness configurations (the base model).

Our base model is the Representative Concentration Pathway (RCP) 8.5 high emission, marine ice cliff instability inclusive scenario of DeConto et al. (2021), chosen as this model spans a large range of AIS volumes, maximising the range of melt scenarios we are able to test. The model consists of 56 model time-steps spanning from the modern-day (pre-industrial) AIS configuration until 2500 which we interpolate onto the same lat-long model grid as used in our study. To prepare this model for use in our interpolation methodology, we first split the DeConto model into separate EAIS and WAIS ice-thickness series, following the MEaSUREs Antarctic Boundaries dataset (Rignot et al., 2013), before then calculating the volume of grounded ice for each region and model time step. The 56 ice-thickness configurations for EAIS and WAIS are then reordered in terms of ice-sheet volume, removing the model time-step dimension, so that their ice-thickness values can be interpolated with respect to ice-sheet volume. In its modern configuration and topography, the DeConto et al. (2021) model simulation contains 5.6 m SLE and 50.2 m SLE grounded ice volume for WAIS and EAIS respectively and, in its minimum configuration, this reduces to 1.6 m SLE for WAIS and 42.9 m SLE for EAIS. The regionally divided DeConto ice-sheet model combined with calculated grounded ice-sheet volumes allows for interpolating ice configurations that correspond to any prescribed value of grounded ice volume and, by extension, melt contribution that we require. The next step in our procedure was, therefore, to develop a methodology for generating potential scenarios of WAIS and EAIS ice-sheet melt, which, combined with the regional base ice model interpolation, can be used to generate corresponding ice-sheet histories.

We parameterise the LIG AIS melt scenarios with one set of parameters controlling the evolution of WAIS volume and another set of parameters controlling the EAIS that can be visualised in Figure 5.1. Our WAIS LIG ice-sheet melt scenarios begin with the assumption that the western portion of the AIS likely melted rapidly compared with the EAIS and may also have remained in a stable, smaller ice-sheet configuration for some time after melting (Golledge et al., 2021). To encode this behaviour, we describe WAIS melt with four parameters: melt start time T^{WA}_{melt}, the time at which melting from the default, present-day configuration occurs; melt volume V^{WA}_{melt}, describing the maximum magnitude of melting; duration of melt d^{WA}_{melt}, determining how long the transition from present-day to maximum melt configuration takes; and the stability duration d^{WA}_{stable}, which determines how long WAIS will remain in the fully melted configuration before returning to modern at 116 ka. To avoid $T^{WA}_{melt} + d^{WA}_{melt} + d^{WA}_{stable} > 116$ ka we determine d^{WA}_{stable} by the parameter p^{WA}_{stable} which determines the percentage of the LIG after $T^{WA}_{melt} + d^{WA}_{melt}$ that should remain stable. After sampling, we convert values of p^{WA}_{stable} to d^{WA}_{stable} by,

$$d^{WA}_{stable} = p^{WA}_{stable}(T^{WA}_{melt} + d^{WA}_{melt} - 116). \tag{5.1}$$

The transition between the modern configuration, pre-melt state and the fully melted state follows a quarter sine decay function (see example in Figure 5.1B) reflecting our assumption of a fast initial melting that decelerates towards V^{WA}_{melt}, while a linear transition is assumed between the end of d^{WA}_{stable} and the return to the modern state at 116 ka.

For the EAIS, we assume that changes in volume occurred more gradually and that the ice sheet likely never equilibrated. In addition, since evidence suggests the possibility of EAIS growth under modern-day warming (Harig and Simons, 2015), we do not rule out the possibility of EAIS growth during the LIG. Therefore, we allow scenarios to include negative values of EAIS volume and, for clarity, refer to EAIS parameters as determining ice-sheet change rather than melt. We do not include a period of stability as we do for the WAIS, but otherwise similarly describe EAIS scenarios with three parameters: change start time T^{EA}_{change}, change volume V^{EA}_{change}, and duration of change d^{EA}_{change}. To reflect the assumption of a more gradual EAIS evolution, we use a low degree (N=1.3) polynomial transition function but keep the assumption of linear growth from V^{EA}_{change} back to the modern-day configuration at 116 ka. For scenarios that test EAIS ice-sheet growth, we require EAIS ice thickness configurations thicker than exist in the DeConto series and so, in this case, we uniformly scale the DeConto modern (pre-industrial) grounded ice configuration to match the required volume.

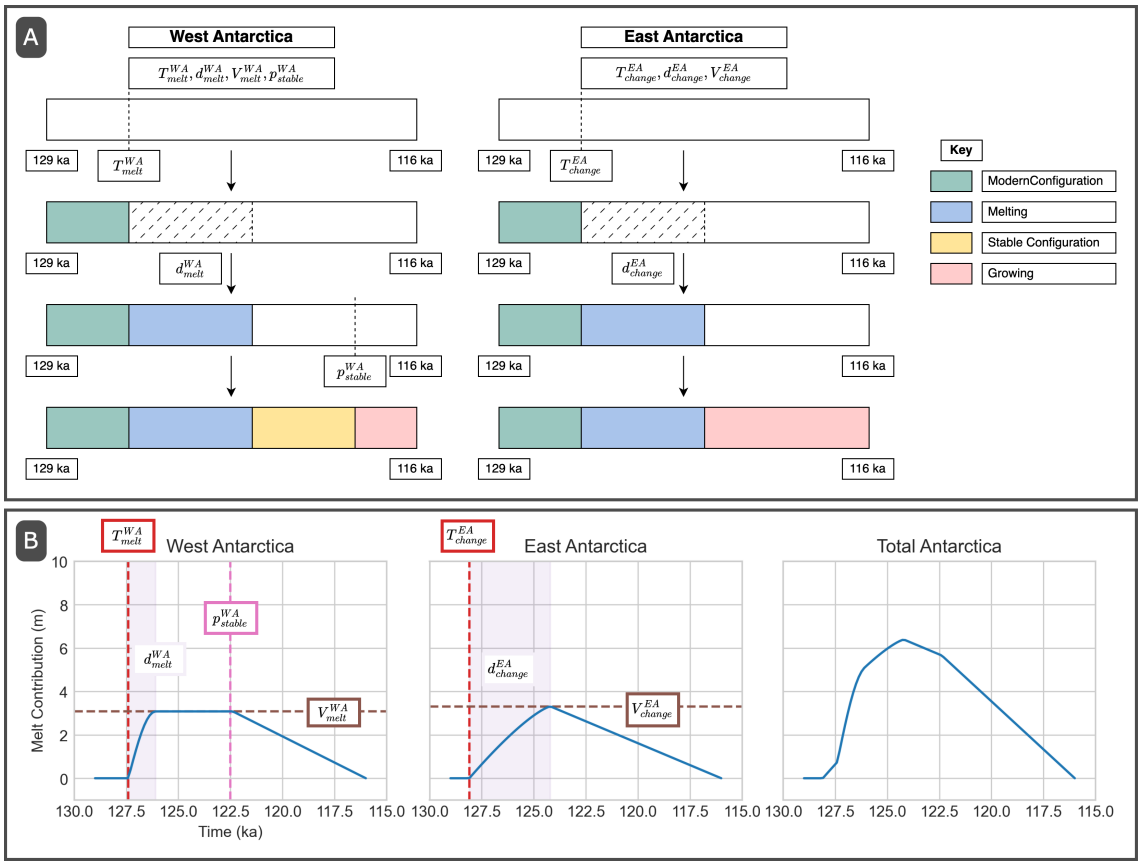

Figure 5.1: AIS melt is parameterised by the magnitude, timing, and duration of ice-sheet changes in both EAIS and WAIS. (A) This parameterisation divides the last interglacial into periods of ice-sheet melt, growth, and stability. (B) An illustrative example of an AIS melt scenario labelled with each parameter.

Table 5.1: Antarctic melt scenario parameters and their corresponding ranges.

Name	Symbol	Range	Unit
WAIS Melt Start Time	T^{WA}_{melt}	129 - 124	ka
WAIS Melt Duration	d^{WA}_{melt}	0.5 - 3	ka
WAIS Melt Volume	V^{WA}_{melt}	0 - 5.5	m SLE
WAIS Stability Percentage	p^{WA}_{stable}	0.2 - 0.8	1
EAIS Change Start Time	T^{EA}_{change}	129 - 124	ka
EAIS Change Duration	d^{EA}_{change}	1 - 9	ka
EAIS Change Volume	V^{EA}_{change}	-1 - 5	m SLE

5.3.3 Relative Sea-Level Ensemble Design

In addition to the 7 parameters controlling the evolution of LIG Antarctic melt (Table 5.1), our ensemble design consists of 3 parameters describing the viscoelastic Earth model and 3 derived parameters describing the regional ice-sheet volume of

the Eurasian ice-sheet during the Penultimate Deglaciation (Table 5.2). Chapter 4 demonstrated that the Eurasian ice-sheet volume was, in some Eurasian regions, the dominant contributor to uncertainty in LIG RSL. To account for this source of uncertainty, we design our ensemble to use the suite of 532 Eurasian deglaciation geometries as generated in Chapter 4. Alongside, we generate a 532-member LHS of our 3 Earth model parameters (Table 5.1) and 7 AIS history parameters assuming a uniform distribution across parameter ranges (Table 5.2) resulting in 532 Earth models and LIG Antarctic melt scenarios to test. We run the resulting set of 532 global ice-sheet histories and Earth model configurations with the sea-level model to produce an ensemble of RSL simulations spanning from 420 ka until the present day.

Table 5.2: Earth model and Eurasian ice-sheet model parameters where, for parameter x, $U(x_{min}, x_{max})$ represents a uniform distribution with a minimum (x_{min}) and maximum (x_{max}) value and $N(\mu, \sigma)$ represents a normal distribution with mean (μ) and standard deviation (σ).

Name	Symbol	Distribution	Unit
Upper Mantle Viscosity	ν_{UM}	$U(0.1, 1) \times 10^{21}$	Pa s
Lower Mantle Viscosity	ν_{LM}	$U(0.1, 5) \times 10^{22}$	Pa s
Lithospheric Thickness	L	$U(71, 96) \times 10^{3}$	km
Barents-Kara Sea Eurasian Ice-Sheet Volume	V^{Er}_{BKS}	$N(28, 4)$	m SLE
Fennoscandian Eurasian Ice-Sheet Volume	V^{Er}_{F}	$N(24, 3)$	m SLE
British-Irish Eurasian Ice-Sheet Volume	V^{Er}_{BI}	$N(1.8, 0.1)$	m SLE

5.3.4 Last Interglacial Sea-Level Database

Empirical observations of LIG RSL were sourced from WALIS, a state-of-the-art LIG RSL database containing 6600 RSL data points (Rovere et al., 2023b). Each RSL value, representing RSL at a specified location, can broadly be categorised as either: a sea-level index, representing a value that RSL attained; marine limiting, representing a value that RSL exceeded; or terrestrial limiting, which RSL remained below (Rovere et al., 2016). In addition, the age associated with each data point can be categorised as: absolute, which provides a specific age value with uncertainty (e.g. an OSL date); or relative (or floating), whereby the data point may have occurred at any time within a time range determined by the chronological constraint to which it is tied to (e.g. pollen biostratigraphy). We initially filtered the WALIS dataset to only include data points: (i) at locations within the northwest Eurasian region (which

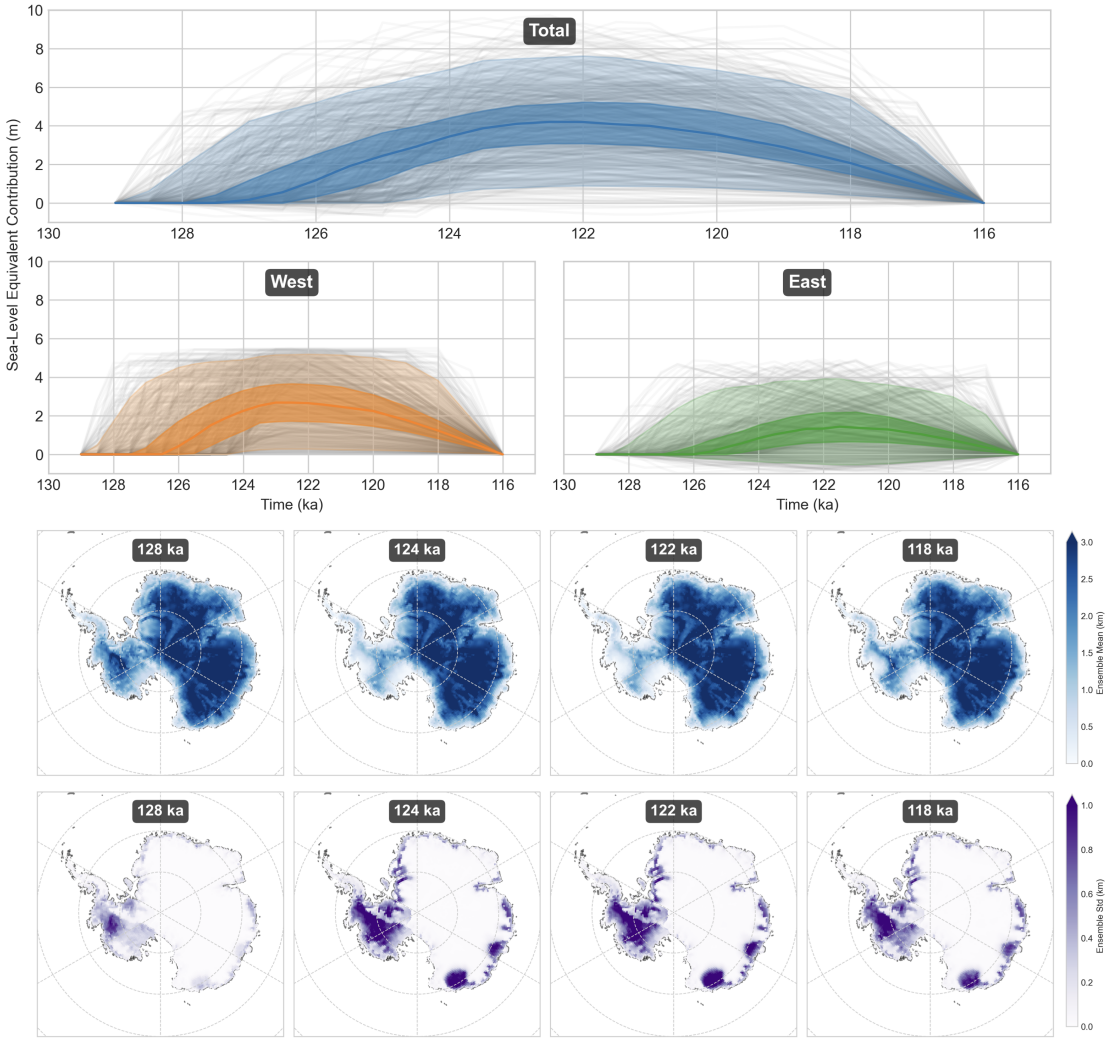

Figure 5.2: Ensemble of Antarctic melt scenarios generated with our parameterisation. (Top) WAIS, EAIS, and total AIS sea-level contributions during the LIG with ensemble 5th and 9th percentile (light shading), 32 and 68th percentile (dark shading), and median value (solid line). Individual ensemble members are shown as light grey lines. (Bottom) AIS ice-sheet thickness ensemble mean (blue) and standard deviation (purple) at 128, 124, 122, and 118 ka.

comprises the regional compilations of Cohen et al. (2022), and Dalton et al. (2022)), (ii) with an age range overlapping with the timing of LIG (129 - 116 ka, (Dutton et al., 2015)), and (iii) those data points that include a specified RSL uncertainty. After this filtering, our dataset contains 93 sea-level index, 210 marine limiting, and 14 terrestrial limiting data points, of which 120 have absolute ages and 197 have relative ages, at 141 unique locations, as shown in Figure 5.4. Also shown in Figure 5.4 are the 13 regions used to group the data points for regional-specific analysis and comparison against the RSL ensemble.

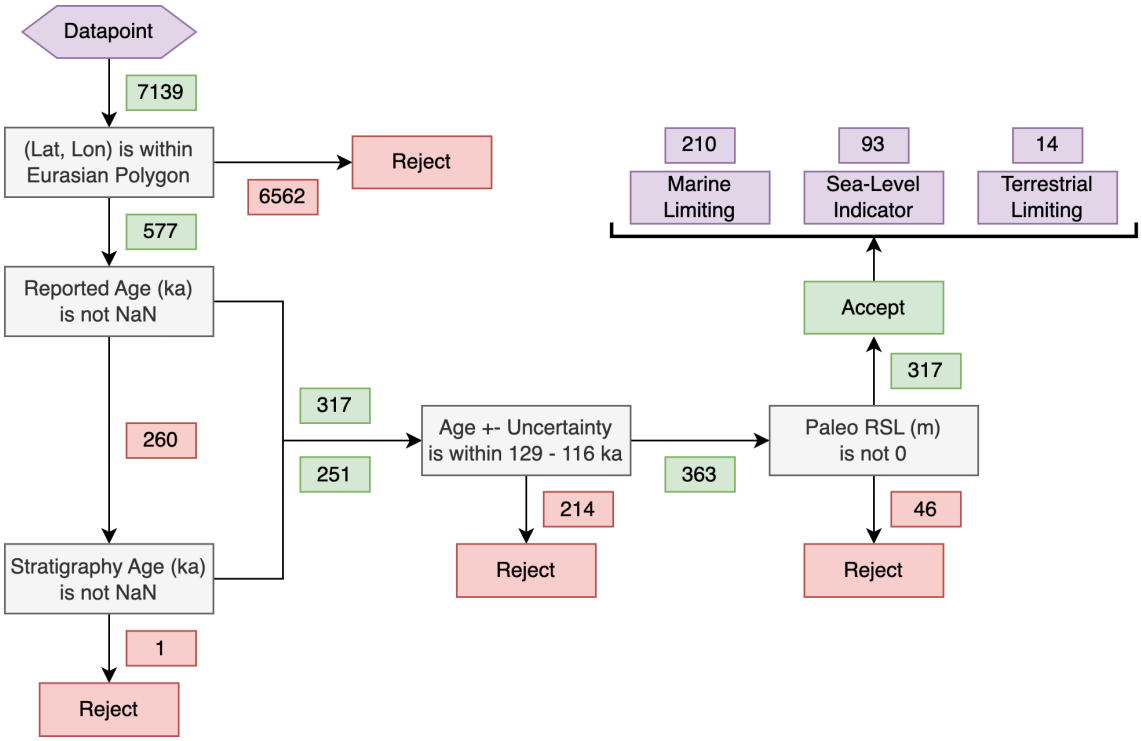

Figure 5.3: Schematic of the filtering process applied to RSL data points.

As discussed in Chapter 1.2.2.1, RSL and associated uncertainty values from WALIS represent the observed RSL as inferred from the geological record at each study site, and this value represents the influence of VLM from all local processes. Some processes cannot be quantified (e.g. tidal range changes) and are assumed the same as modern; however, in order to compare against our ensemble of GIA and Antarctic melt scenarios, we subtract the influence of dynamic topography (VLM due to mantle convection), and in the case of offshore North Sea data points, subsidence due to sediment loading, from each record, assuming that active tectonics make a negligible contribution given the distance from active plate margins. The global dynamic topography deformation dataset provided by Austermann et al. (2017) quantifies the magnitude and standard deviation of VLM due to dynamic topography since 125 ka. By converting the magnitude of dynamic topography since 125 ka into a rate, we utilise the Austermann et al. (2017) dataset to estimate the dynamic topography contribution to RSL for the WALIS data points, assuming the mean age for absolute ages and the mid-value for relative ages. Similarly, we consider the contribution of sediment loading in the southern North Sea where significant sediment has accumulated over the Quaternary (Hijma et al., 2012; Lamb et al., 2018), using the rates fields provided by Cohen et al. (2022). Figure 5.4 shows the resulting time series of data-point values plotted for each sea-level region after correcting for the VLM factors, with the exception of GIA. In this form, the database of sea-level

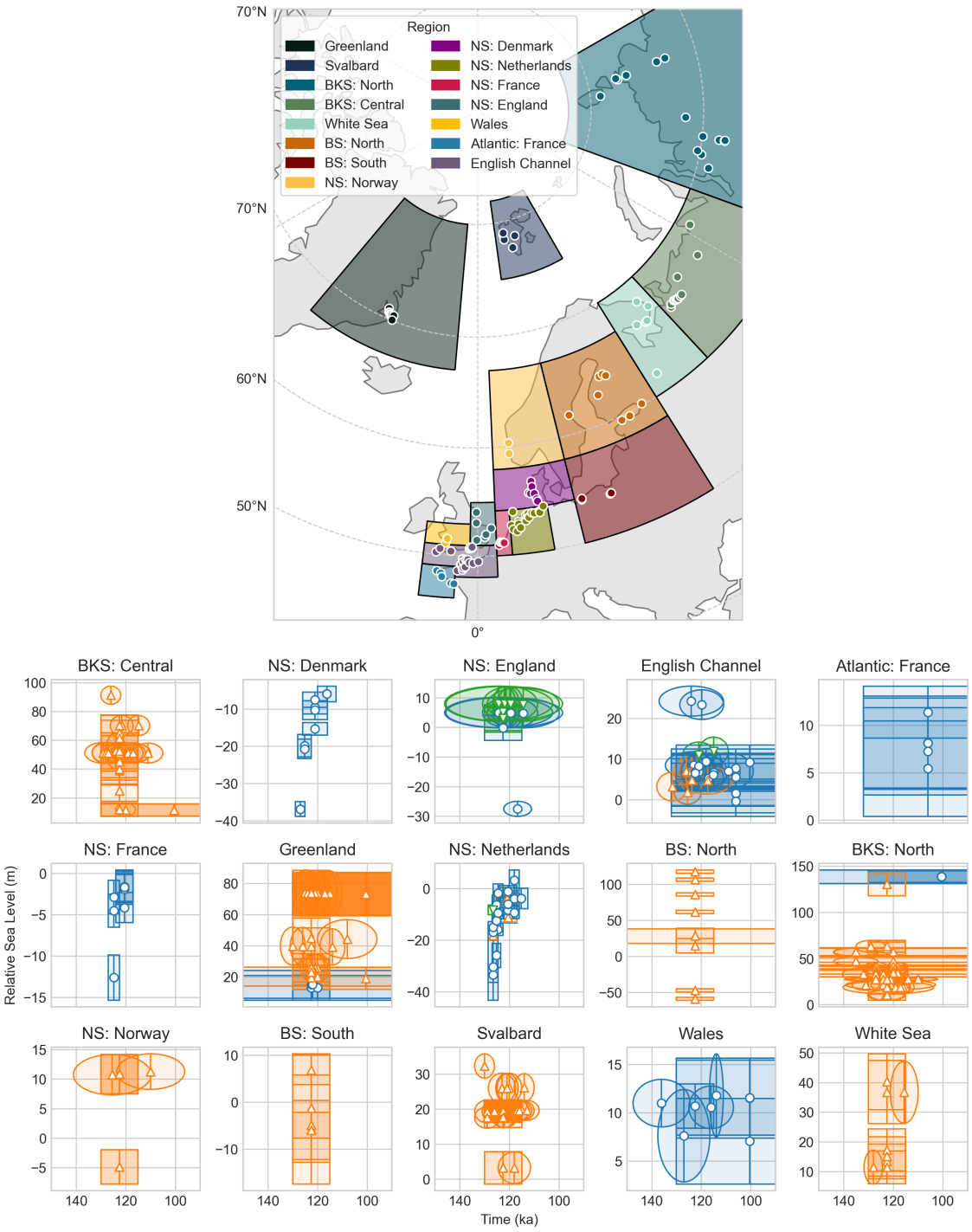

Figure 5.4: (Top) Distribution of RSL data points across northwest Eurasia grouped in 13 regions based upon similar RSL trends. (Bottom) For each region, marine limiting (orange, up-arrow marker), terrestrial limiting (green, down-arrow marker) and sea-level index points (blue, round marker) are shown with 1σ uncertainty bounds in age and RSL for absolute dated ages (curved uncertainty) and age range with 1σ RSL uncertainty for relative ages (square uncertainty).

records and their corresponding values can be compared against our modelled RSL values through a model-data comparison process known as history matching.

5.3.5 Sea-Level Data Matching Framework

History matching is a procedure used in model uncertainty quantification to rule out areas of the model parameter space (i.e. combinations of input parameter values) that are unable to match observational data within the bounds of model and data uncertainty (Vernon et al., 2022; Williamson et al., 2013; Bower et al., 2010). To compare model output and observational data, we use an implausibility metric, as used in Chapter 3, which effectively calculates the minimum distance in space and time between the modelled RSL time-series and a sea-level data point, normalised by uncertainty. For each simulation we run, we calculate an implausibility value based on the normalised distance between the model and observations. Let y be the real-world value of some quantity and z be an observation of y that differs by an error e such that $z = y + e$. Our numerical model can make a prediction of y with some parameter combination $\hat{p}$, given by $f(\hat{p})$, but since our numerical model is not a perfect representation of the real world, all predictions $f(\hat{p})$ are separated from y by model structural discrepancy ϵ such that, for the hypothetical perfect parameter combination $\hat{p}^*$, $y = f(\hat{p}^*) + \epsilon$. Therefore, $E(\epsilon)$, the expectation of ϵ, represents the model bias and $E(\epsilon) \neq 0$ indicates that $f(\hat{p})$ contains a systematic bias from observation z. In the case that f is an emulated quantity from our original numerical model, we additionally define the emulator uncertainty $Var(f(\hat{p}))$. The implausibility $I(\hat{p})$ of a parameter combination $\hat{p}$ is therefore given by,

$$I(\hat{p}) = \sqrt{\frac{(E(f(\hat{p})) - z - E(\epsilon))^2}{Var(e) + Var(\epsilon) + Var(f(\hat{p}))}} \tag{5.2}$$

A RSL data point i consists of a location $\hat{x}_i$, RSL value z_i^{RSL}, an age z_i^t, and a data type. Implausibility calculations of RSL model outputs must, therefore, account for the RSL implausibility I_i^{RSL}, temporal implausibility I_i^t, and use a different form of this function to account for the specific interpretation of each RSL and age data-type. We assume that only model values at location x_i are relevant for calculating the implausibility of data point i, and therefore let $f_i(\hat{p}, t) \equiv f(\hat{p}, t, \hat{x} = x_i)$, where t is a modelled time from the discrete set of model times T. In addition, since we are only interested in LIG simulations, we only consider the subset of modelled RSL values that fall within T_{LIG}, where $T_{LIG} = \{t \in T | t \leq 129 \text{ ka and } t \geq 116 \text{ ka}\}$.

Beginning with the temporal implausibility, a sea-level data point can be associated with either an absolute age or a relative age. In the case of absolute ages, we assume

that the age probability is normally distributed centred around the reported age z_i^t with standard deviation given by reported uncertainty $\sqrt{Var(e_i^t)}$. Using Equation 5.2 and assuming no temporal model bias or structural uncertainty, we define $I_i^t(t)$ for absolute ages to be,

$$I_i^t(t) = \sqrt{\frac{(t - z_i^t)^2}{Var(e_i^t)}} \tag{5.3}$$

In the case of relative ages, the temporal probability distribution is assumed as uniform between the lower bound t_{min} and the upper bound t_{max} of the reported age range, such that,

$$I_i^t(t) = \begin{cases} 0, \text{ if } z_i^{t_{min}} \leq t \leq z_i^{t_{max}} \\ \infty, \text{ else} \end{cases} \tag{5.4}$$

The RSL component of a data point can either be an index point, marine limiting, or terrestrial limiting. In the case of a sea level index point, RSL is assumed to be normally distributed and centred around the reported RSL value z_i^{RSL} with standard deviation given by reported uncertainty $\sqrt{Var(e_i^{RSL})}$. In this case, we can use Equation 5.2 to express I_i^{RSL} as,

$$I_i^{RSL}(\hat{p}, t) = \sqrt{\frac{(E(f_i(\hat{p}, t)) - z_i^{RSL} - E(\epsilon_i^{RSL}))^2}{Var(e_i^{RSL}) + Var(\epsilon_i^{RSL}) + Var(f_i(\hat{p}, t))}}. \tag{5.5}$$

5.3.5.1 Limiting Data Points

In the case of a limiting data point, a RSL observation value z^{RSL} represents the boundary between possible and impossible RSL values and, by extension, $Var(z^{RSL})$ represents uncertainty in the position of this boundary. Consider a RSL value at some distance above an uncertain marine limiting RSL boundary: the probability of the RSL value represents the cumulative probability of all boundary values below it whereas a RSL value above this limit is only possible for boundary positions above it. By extension, we expect that a RSL value exactly on the mean of a normally distributed boundary position should have a probability of 0.5. Using this interpretation, the probability distribution of a modelled value f around this limit can be represented as the cumulative distribution function of a normal distribution. However, in order to include this alternative probability distribution within our history-matching framework we must first think of the standard implausibility of a model value f as, effectively, the distance, in terms of standard deviations, that this

value lies away from the mean of a normal distribution given by,

$$N\left(\mu = z + E(\epsilon), \sigma = \sqrt{Var(e) + Var(\epsilon) + Var(f(\hat{p}))}\right). \tag{5.6}$$

With this interpretation, there exists a normalised probability P associated with each I, that can be calculated from the normalised probability density function associated with Equation 5.6 such that,

$$P = e^{-\frac{1}{2}I^2}. \tag{5.7}$$

By solving Equation 5.7 for I, we can express I in terms of P such that,

$$I = \sqrt{-2\log(P)}. \tag{5.8}$$

Let CDF be the cumulative distribution function associated with Equation 5.6 and, therefore, for limiting data points we can express the probability P_{lim} of a modelled RSL value $f(\hat{p})$ as,

$$P_{lim}(f(\hat{p})) = \begin{cases} CDF(f(\hat{p})), \text{ if marine limiting,} \\ 1 - CDF(f(\hat{p})), \text{ if terrestrial limiting.} \end{cases} \tag{5.9}$$

Combining Equation 5.8 and Equation 5.9 we can calculate the associated I as,

$$I(\hat{p}) = \sqrt{-2\log P_{lim}(f(\hat{p}))}. \tag{5.10}$$

5.3.5.2 Combined Implausibility

The implausibility $I_i(\hat{p}, t)$ of a model value $f_i(\hat{p}, t)$, representing the normalised model-data distance in time and space, is given by,

$$I_i(\hat{p}, t) = \sqrt{(I_i^{RSL}(\hat{p}, t))^2 + (I_i^t(t))^2} \tag{5.11}$$

Since a sea-level model ensemble member at a location $\hat{x}$ consists of a time series of RSL values, we characterise the overall implausibility of $\hat{p}$ against i as,

$$I_i(\hat{p}) = \min\{I_i(\hat{p}, t) : t \in T_{LIG}\} \tag{5.12}$$

Finally, we combine implausibility from all data points i into a single average implausibility for a given set of parameter values $\hat{p}$ by,

$$I(\hat{p}) = \text{mean}\{I_i(\hat{p}) : i \in N\} \tag{5.13}$$

5.3.6 Estimating Model Structural Discrepancy

A misfit between modelled RSL and data that is common to all ensemble members may indicate the presence of a structural model bias, such that $E(\epsilon) \neq 0$. We account for this bias in our implausibility metric by defining the terms $E(\epsilon^{RSL})$ and $Var(\epsilon^{RSL})$ in Equation 5.2. We make the assumption that $E(\epsilon^{RSL})$ and $Var(\epsilon^{RSL})$, for the LIG, are time-invariant spatial fields which we can sample from at each data location to derive $E(\epsilon_i^{RSL})$ and $Var(\epsilon_i^{RSL})$. Intuitively, this means that we assume modelled RSL may be more incorrect in some locations than others but that there is no change in this error as the LIG progresses. In reality, this bias may be larger at some times than others due to, for example, the influence of missing ice-sheet contributions. However, spatial data sparsity, when grouped by model time step would limit the temporal resolution at which these fields could be estimated. In order to estimate $E(\epsilon^{RSL})$ and $Var(\epsilon^{RSL})$ we first calculate the RSL discrepancy $d_i(\hat{p})$ at z_i^t such that,

$$d_i(\hat{p}) = f(\hat{p}, t = z_i^t) - z_i^{rsl} \tag{5.14}$$

with $d_i(\hat{p}) = 0$ if i is a limiting data point and $f(\hat{p}, t = z_i^t)$ falls on the 'possible' side of the limit boundary. By calculating $d(\hat{p}) = \text{mean}\{|d_i(\hat{p})| : i \in N\}$ we can determine the best fitting 10% of ensemble members P_{best}. We then assume that this discrepancy is representative of ϵ_i^{RSL} at each data-point location i such that $E(\epsilon_i^{RSL})$ and $Var(\epsilon_i^{RSL})$ are the mean and variance of the set $\{d_i(\hat{p}) : \hat{p} \in P_{best}\}$. In this form $E(\epsilon_i^{RSL})$ and $Var(\epsilon_i^{RSL})$ are only defined at locations i and so, to aid the physical interpretation of the structural discrepancy, we spatially interpolate onto the northwest Eurasian region using a 2D Gaussian Process with a Matern-52 kernel, the results of which are shown in Section 5.4.3.

5.4 Results and Analysis

5.4.1 Relative Sea-Level Ensemble

Our ensemble of 532 RSL outputs shows a distinctive, Eurasian ice-sheet-driven pattern of high RSL under areas previously loaded by the Eurasian ice sheet, with values exceeding 100 ± 20 m in regions such as the White Sea, and lower RSL beyond the former ice-sheet margins (Figure 5.5). A similar pattern of RSL was derived from the ensemble experiments of Chapter 4; however, we find that this new ensemble has a RSL mean that is higher in areas that are not directly under the former Eurasian ice sheet. For example, in the Atlantic and English Channel regions mean RSL values are higher by 5 m due to the added AIS contribution, while the standard deviation has remained similar, while in the GIN sea region RSL has increased by 8 m. Our

ensemble has a high rate of RSL change, averaged over the whole LIG, of up to 10 mm yr^{-1} in the GIN Sea region, while the English Channel, North Atlantic, and southern North Sea regions show more moderate rates of change of 2 mm yr^{-1}. As the LIG progresses, areas underneath the former ice-sheet load experience RSL fall as a result of isostatic rebound, averaging -3 mm yr^{-1} in the central North Sea region, and with regions such as the Barents-Kara sea experiencing rates higher than -20 mm yr^{-1}. Uncertainty in the rate of RSL change is highest in regions dominated by isostatic rebound, reaching ± 12 mm yr^{-1} in the Baltic Sea as opposed to ± 3 mm yr^{-1} in the GIN sea.

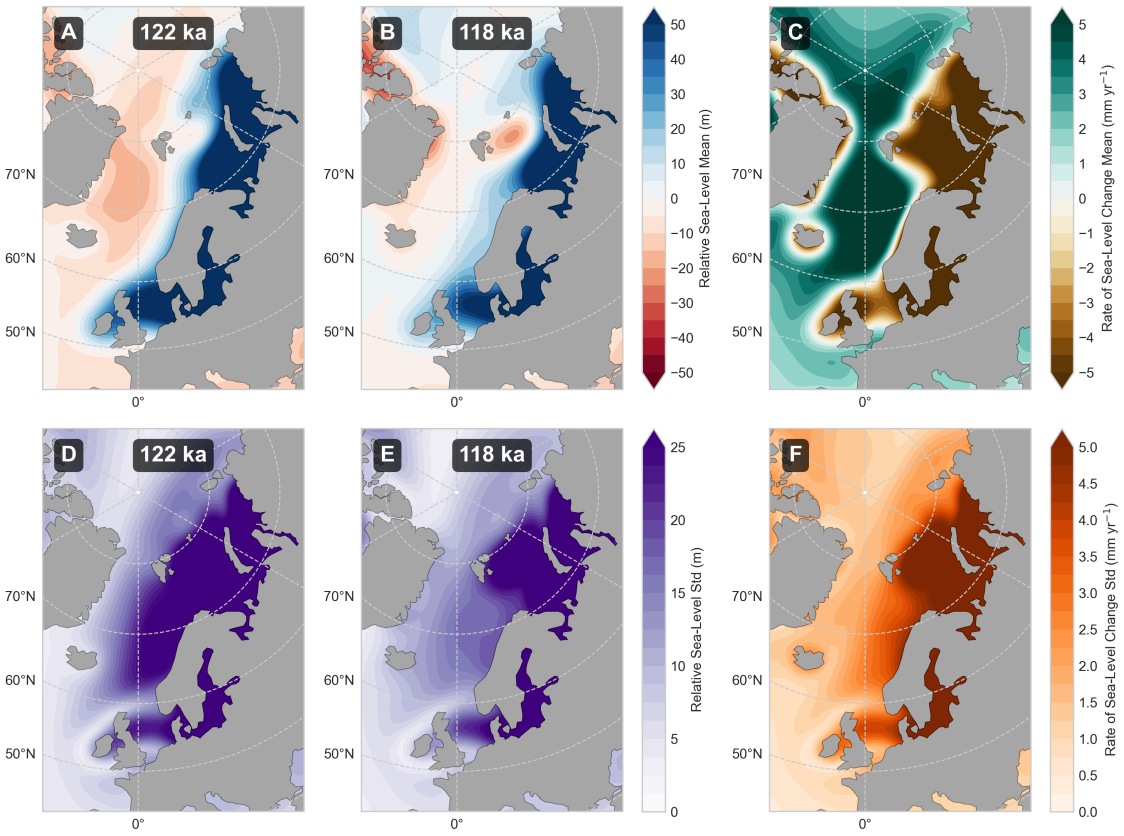

Figure 5.5: Resulting Eurasian RSL ensemble mean at (A) 122 ka, (B) 118 ka, and corresponding standard deviation at (D) 122 ka and (E) 118 ka. Panels also show the (C) mean and (F) standard deviation of the average rate of RSL change over the LIG.

Our ensemble of AIS histories have been generated by interpolating the DeConto ice-sheet model to match an ensemble of volume time-series for EAIS and WAIS (Section 5.3.2). This interpolation relied on calculated grounded ice-sheet volume values for each DeConto model time step performed by assuming modern-day topography. Since LIG topography configurations differ from modern, this assumption resulted in a mismatch between the actual sea-level contribution from each AIS ensemble member and the value prescribed from our parameterisation. To correct this, we

use the series of LIG topography configurations, outputted by the sea-level model for each ensemble member, to re-perform the grounded-ice-volume calculation at each time step, thus correcting the ensemble of sea-level contribution values. In this analysis, we find a near-linear relationship between the pre and post-corrected V^{EA}_{change} (gradient 0.97, R^2 0.998) and V^{WA}_{melt} (gradient 0.94, R^2 0.997) values, with a reduction of 0.4 m SLE and 0.3 m SLE for WAIS and EAIS volumes respectively. Subsequent results are presented using these corrected volume values.

The variance of our ensemble spans the range of possible RSL values given the specified uncertainty in viscoelastic Earth structure, Eurasian ice-sheet volume during the Penultimate Deglaciation, and the LIG evolution of AIS. In subsequent sections, we utilise this ensemble to quantify the sensitivity of each region to the evolution of AIS (sensitivity analysis), as well as to identify the region of our input parameter space most able to match observations of RSL (history matching). Sensitivity analysis requires RSL model output values at specific locations within the parameter space, while history matching is aided by far larger ensemble sizes than is feasible to directly compute with the sea-level model. Therefore, to aid both analyses, we train a Gaussian process emulator for each of the 141 unique data locations so that we are able to approximate RSL values at each location, including quantified prediction uncertainty, for arbitrary parameter input combinations.

5.4.2 Regional Sensitivity Analysis

The variance in our ensemble of Eurasian RSL results from the combined, propagated uncertainty in all of our model parameters and the magnitude of each model parameter's contribution to this variance is likely to be spatially variable. In Chapter 4, we attributed individual model-parameter contributions to this spatial pattern of uncertainty and found that viscoelastic Earth model parameters are typically dominant across Eurasia, while regions directly underneath ice-sheet loads are sensitive to respective regional volumes of the Eurasian ice sheet. Here, we perform an expanded and targeted sensitivity analysis that includes AIS parameters by utilising our suite of Gaussian process emulators to calculate Sobol sensitivity indices derived from a 1024-member Sobol sequence sample at all site locations in the filtered RSL database. We sum the individual parameter sensitivity indices at each site into a single sensitivity value for our 3 parameter groups: Earth model, Eurasian ice volume, and Antarctic ice melt scenario parameters. Finally, for each of these groups, we calculate a mean sensitivity value for each region that represents the average contribution of a given parameter group to uncertainty at data sites within a given region (as defined in Figure 5.4). Crucially, this analysis allows us to determine the sensitivity of each region's data to AIS ice-sheet melt.

Our results show that uncertainty in the Earth model parameters remains the dominant contributor to RSL uncertainty in most regions with an average contribution across all regions of 80%, compared with 12% from Eurasian ice-sheet volume and 3% from Antarctica (note that first-order contributions do not sum to 100% due to the influence of parameter interactions) as shown in Figure 5.6. The influence of GIA is particularly dominant in Greenland, likely due to lower influence from Eurasian ice-sheet changes, and in the North Sea, where it averages 91% across the Denmark, French North Sea, and Netherlands regions. The volume of the Eurasia ice sheet contributes little first-order sensitivity in these same North Sea regions, averaging 5%, but is far more dominant in the North Baltic Sea, South Baltic Sea, and White Sea regions, averaging 25%. By contrast, we find that the sensitivity to the Antarctic contribution is localised to the southwest subset of our sea-level regions where it contributes 6% to the English Channel, 4% to the English North Sea, 6% to the French Atlantic, and 16% to Wales.

Our sensitivity analysis results indicate that data points within the southwest subset of our Eurasian RSL data regions (Figure 5.4) are most sensitive to our parameterisation of AIS melt and, as such, are likely to be most informative about likely melt scenarios in our subsequent history matching analysis. We now compare our ensemble with our refined database of RSL data points in order to: (i) identify regions of systematic misfit between model and data; (ii) filter out ensemble members that do not fit the sea-level data within uncertainty; (iii) identify AIS melt scenarios and Earth model configuration that best fit the data (Section 5.4.4).

5.4.3 Model Bias

The model bias term ϵ^{RSL}, as discussed in Section 5.3.5, is a reflection of the systematic misfit between modelled and observed values of RSL. In this work, we assume that ϵ^{RSL} is a spatially variable, temporally invariant field that we estimate by calculating the discrepancy between the mean modelled RSL value of the top 10% of ensemble members based on their fit against all data points. This field is used to correct our ensemble of RSL values in locations where the systematic misfit causes the RSL ensemble to be far from the data points, thus allowing all sea-level data to fairly inform our history-matching procedure. We find that our model exhibits spatially coherent patterns of ϵ^{RSL}, demonstrating both that the empirical RSL data is regionally consistent in its measurements of RSL and that our model contains biases, likely due to misrepresented ice-sheet volume and Earth model structure, on a regional scale.

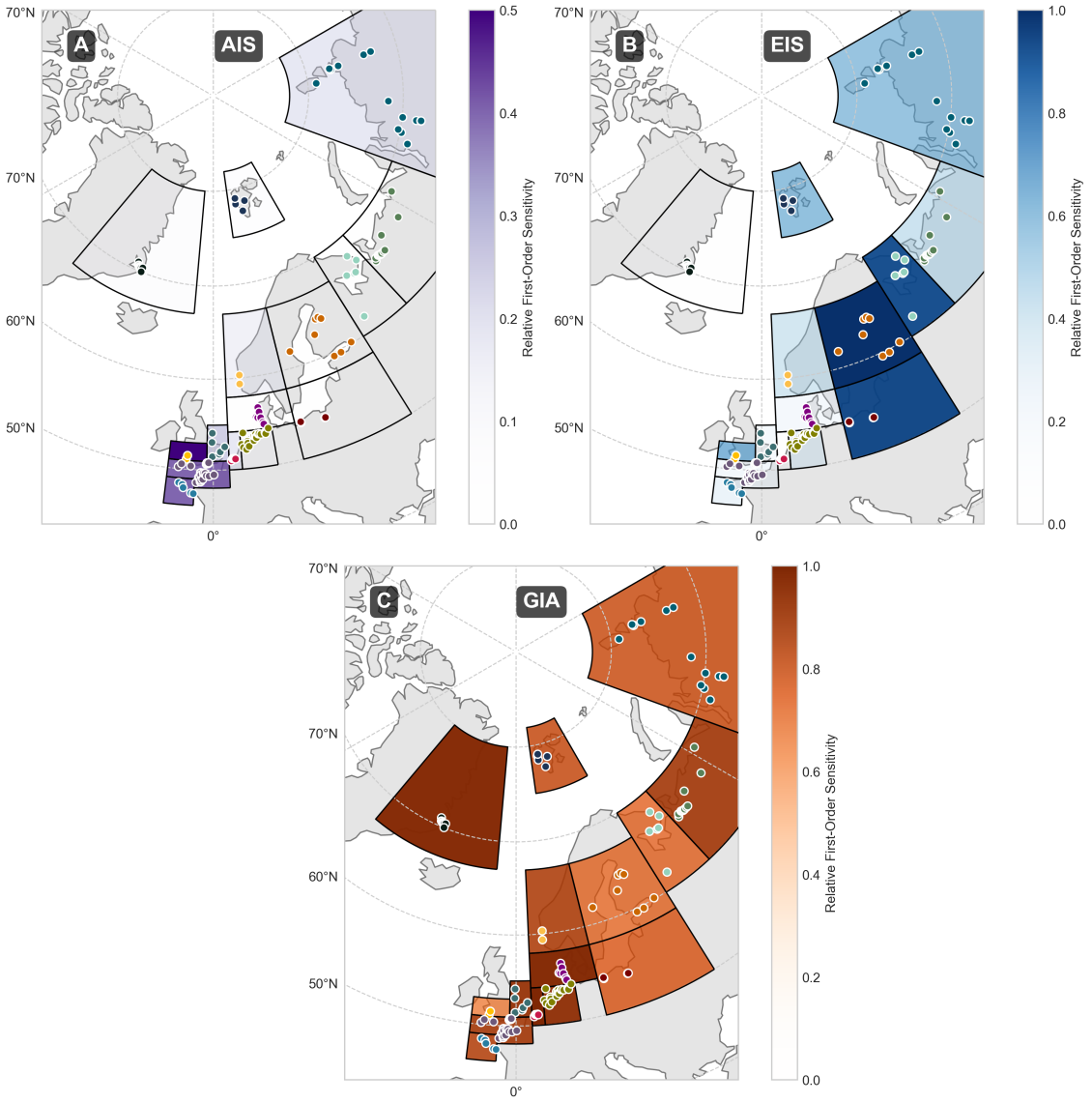

Figure 5.6: Map showing each sea-level region (defined in Figure 5.4) coloured by the magnitude of the relative first-order sensitivity contribution of (A) Antarctic, (B) Eurasian ice-sheet volume, and (C) GIA model parameters. Regional mean values are a result of mean sensitivity indices calculated at each data site.

We find that data points within the North Sea regions have a localised, negative mean model bias of $\mathcal{O}(50)$ m (of the order of 50 m), indicating that our ensemble of modelled RSL is higher than is suggested by the RSL data in these regions. However, this negative mean bias does not extend to the adjacent English Channel, Norwegian North Sea, or southern Baltic Sea region data points (Figure 5.7A). Within North Sea regions, the standard deviation (or uncertainty) of the model bias (or model structural error) is higher for data points in the Netherlands region, reaching $\mathcal{O}(10)$ m, whereas the English North Sea has an uncertainty of only $\mathcal{O}(2)$ m (Figure 5.7B). Both the mean and uncertainty in the model bias are negligible for data points in the English Channel, French Atlantic, and Wales regions, indicating that there

is a reasonable intersection between our modelled range of RSL values and data points in these regions. Most data points in the eastern data regions of Svalbard, the Norwegian North Sea, southern Baltic Sea, northern Baltic Sea, White Sea, and the central Barents-Kara Sea also show negligible mean bias, although the higher proportion of limiting data points in this region may make these data points less able to constrain any bias. However, there is a large bias variance in the northern Baltic Sea of $\mathcal{O}(10)$ m, indicating that the best-fitting subset of our ensemble has high variability in this region. The North Barents-Kara Sea and Greenland regions have a strong positive bias of $\mathcal{O}(50)$ m with low accompanying uncertainty $\mathcal{O}(2)$ m, indicating that our modelled RSL values are systematically lower than expected in this region and that this correction is reasonably uniform across the best fitting subset of ensemble members. The discrepancy calculation used to estimate a best-fitting subset of our ensemble and calculate a bias is a crude precursor to a full history matching procedure as it does not account for uncertainty in RSL data, the modelled ensemble, or the temporal data component, while also not being able to quantify the relative implausibility of specific parameter combinations. Despite this, we choose to investigate changes in the parameter distributions of our best-fitting subset versus our original ensemble in order to understand which parameters most influence our model bias. We summarise these changes by calculating a simple metric, which we refer to as a mean shift, which quantifies the change in the position of the mean parameter value relative to the parameter range of each parameter. A mean shift of 0 indicates no change in position, while -0.5 and 0.5 indicate a full shift to the lower or upper bound of the parameter range respectively. We find that the best-fitting subset is primarily characterised by lower values of ν_{UM}, associated with a mean shift of -0.4, while other parameters display an absolute shift of no more than 0.1. By repeating the bias calculation for each region, using only data from said region, we are able to calculate regional parameter shift values that represent individual regional parameter preferences. We observe large variations in these shift values across different regions but find that the viscoelastic Earth model parameters exhibit the strongest magnitude of mean shift in almost all regions (Figure 5.7C), meaning that Earth model parameters are both the largest control on model-data fit as well as having regionally variable mean parameter values.

5.4.4 Ensemble History Matching

Utilising our RSL ensemble, model-bias correction, and filtered subset of the WALIS sea-level database, we are now able to calculate the implausibility of a given sea-level model input parameter combination, with lower implausibility values corresponding to a closer model-data agreement. To perform this assessment, we utilise our suite

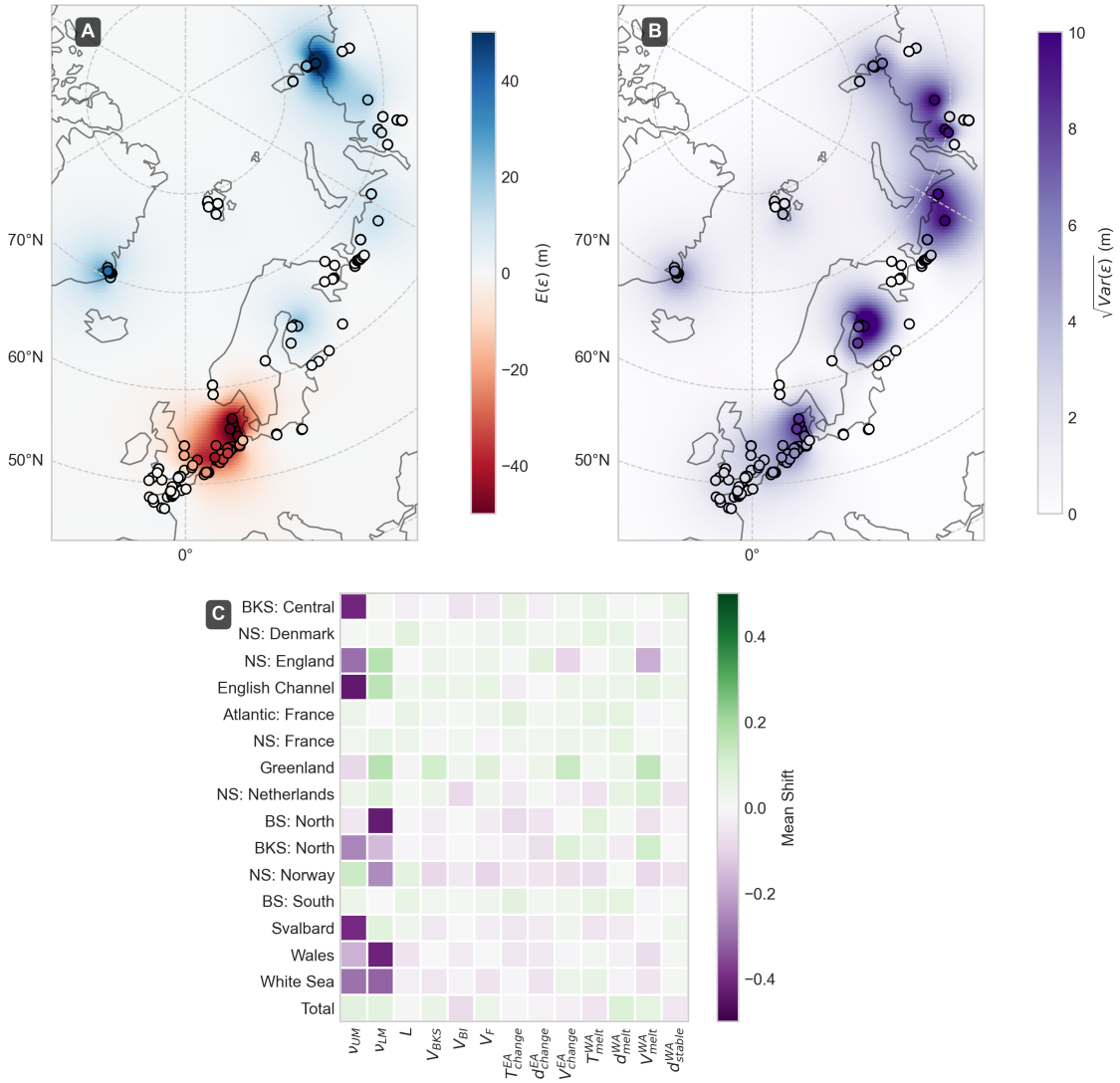

Figure 5.7: Maps showing the (A) mean and (B) standard deviation of the estimated model bias field. Data points are coloured with the calculated model bias value. (C) Matrix showing the magnitude of the shift in parameter-distribution mean in the subset of best-fitting ensemble members when compared with data from different sea-level data regions.

of Gaussian process emulators to perform a 10^4-member LHS of our parameter space at each of the 141 unique data locations. The resulting 10^4 generated LIG RSL time series are compared against the 317 data points via the history matching methodology outlined in Section 5.3.5 to calculate the implausibility value $I_i(\hat{p})$ corresponding to each parameter sample $\hat{p}$ at each location i. In order to determine the resulting overall implausibility $I(\hat{p})$ associated with each $\hat{p}$ we then calculate the mean implausibility over all i for each $\hat{p}$. In addition, since our goal is to refine parameters describing scenarios of AIS melt, we utilise the information gained from our sensitivity analysis to perform a more selective history-matching procedure using the subset of i that fall within regions most sensitive to AIS parameters: the English

Channel, English North Sea, French Atlantic, and Wales. This reduced data subset contains 70 data points (43 more than those used by Barnett et al. (2023)) consisting of 52 sea-level index points, 6 marine limiting, and 12 terrestrial limiting points, of which 37 and 33 are associated with absolute and relative ages respectively.

We find the average implausibility of all parameter combinations against all data and against the AIS sensitive regional subset to be 1.4 and 1.2 respectively, while the maximum averaged implausibility of a single parameter combination is 2.9. This means that all parameter combinations tested have an average implausibility within the 3-sigma uncertainty threshold Pukelsheim (2012) typically used in history matching (Andrianakis et al., 2015; Williamson et al., 2015) and, as a result, all parameter combinations are deemed NROY when compared against all RSL data. However, despite the classification as NROY, differences in implausibility values between sample members can still be used to extract useful information about preferred parameter distributions. We, therefore, use the 10% subset of our parameter sample with the lowest implausibility values as representative of the best-fitting subset of parameters and refer to this subset as the refined subset.

Our refined parameter space, history matched against all data regions, shows a clear preference for lower ν_{UM} values than our original range, with a mean value of 2.2×10^{20} Pa s and an upper value of 4.1×10^{20} Pa s (99th percentile), falling well below the original uniform upper bound of 10×10^{20} Pa s. We find that the higher ν_{LM} values of our original uniform range are preferred, with the lower 1st percentile falling at 1×10^{22} Pa s compared with the original 0.1×10^{22} Pa s lower bound, with the mean value shifting to 3×10^{22} Pa s. Lower values of L are preferred, but the 95th percentile still lies at 94 km and, therefore, remains close to the original upper bound of 100 km, while the mean has shifted to 84 km. The regional subset shows similar overall preferences for Earth model parameters but has a stronger preference for lower ν_{UM} with a mean and 99th percentile of 1.7×10^{20} Pa s and 2.9×10^{20} Pa s, respectively. We also find values close to the upper bound of ν_{LM} are less preferred and the L refined distribution is more similar to that of the original uniform sample.

The normally distributed regional Eurasian ice-sheet volumes show varying degrees of preference in our refined parameter set. When fitted by a normal distribution (as shown in Figure 5.8), we find that our full-data history matching prefers larger Barents-Kara Sea ice-sheet volume, with the V_{BKS} distribution shifting from an original 28 ± 4 m SLE (mean $\pm$ standard deviation) to 30 ± 3 m SLE. By contrast, there is no change within uncertainty in the preferred V_{BI} distribution, while the V_F shows a preference for a small regional ice-sheet load, reducing from 24 ± 3 m SLE to 22 ± 3 m SLE. The regional subset shows no change in the refined normal

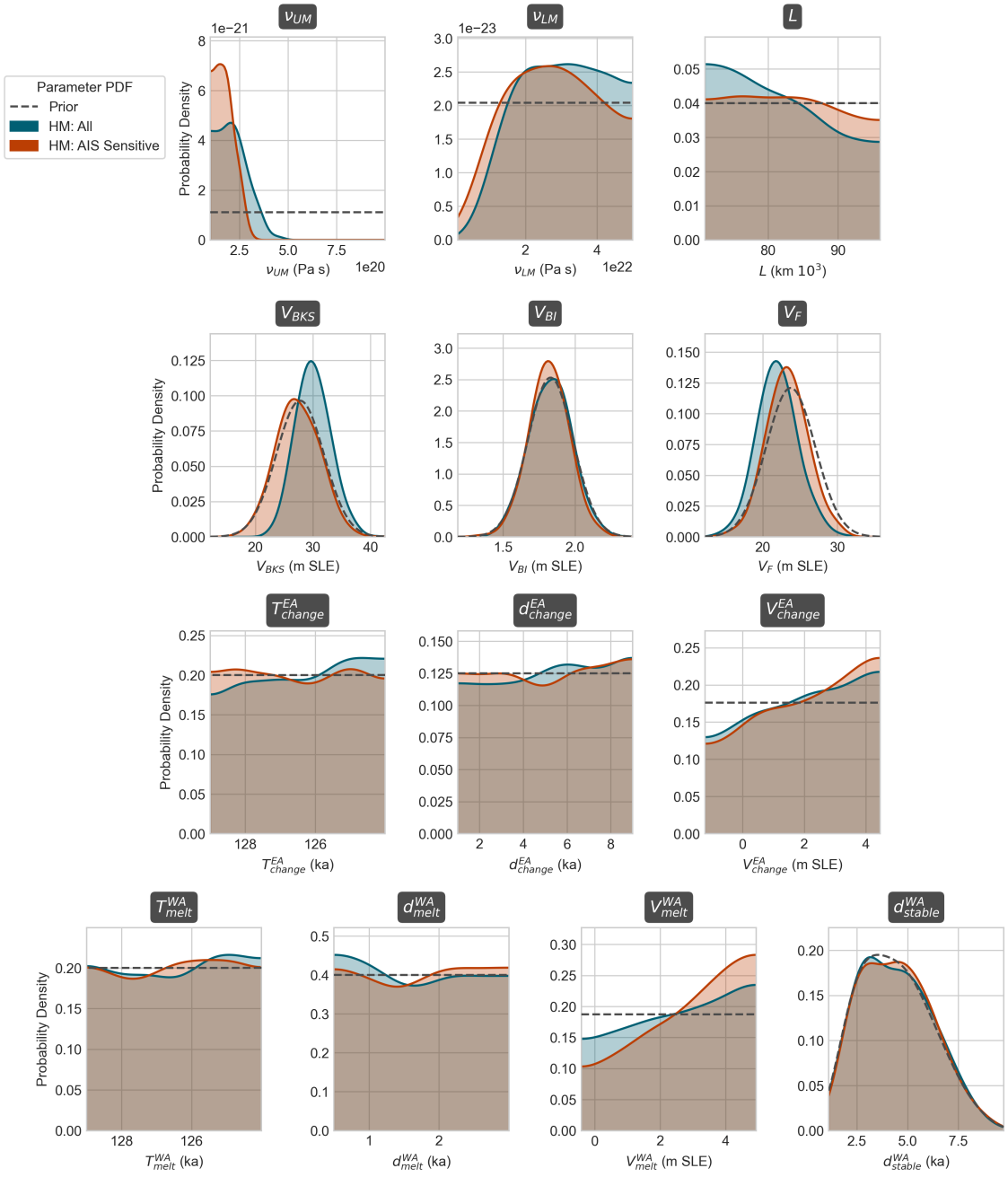

Figure 5.8: Probability density functions of the posterior model input parameter distributions are shown after history matching against RSL data from (blue) all regions and (orange) the subset of regions most sensitive to Antarctica. The dashed grey line shows the probability density functions of the original, prior parameter sample.

distributions for regional Barents-Kara Sea, British-Irish, or Fennoscandian Eurasian ice-sheet volume, within uncertainty. Our history-matching procedure reveals no significant preference for parameters controlling the timing or duration of WAIS or EAIS LIG evolution, with T^{EA}_{change}, d^{EA}_{change}, T^{WA}_{melt}, T^{WA}_{melt}, and d^{WA}_{stable} following similar distributions as the original sample. However, refined distributions from both all data regions and the subset of regions sensitivity to AIS changes reveal preferences for higher ice-sheet melt contributions for both V^{WA}_{melt} and V^{EA}_{change}. Our sensitive subset suggests a contribution of 0.5 - 4.9 m from the WAIS (*very likely*, 90th percentile) and -0.4 - 4 m from the EAIS (*very likely*) but prefers higher volume contributions of 2.1 - 4.9 m from the WAIS (*likely*, 66th percentile) and 1.1 - 4.4 m from the EAIS (*likely*), and thus a total AIS melt contribution of 3.2 - 9.3 m (*likely*). These results show that high ice-sheet melt from the EAIS and/or the WAIS produce lower values of model implausibility but may not represent data sensitivity to an East vs West source of melt and this is investigated in Section 5.5. Our resulting posterior parameter distributions for AIS scenarios, history matched against regionally sensitive data, can be inverted to produce a refined ensemble of AIS melt scenarios (Figure 5.9), demonstrating the range of tested AIS scenarios best able to match the AIS sensitive subset of northwest Eurasian RSL data.

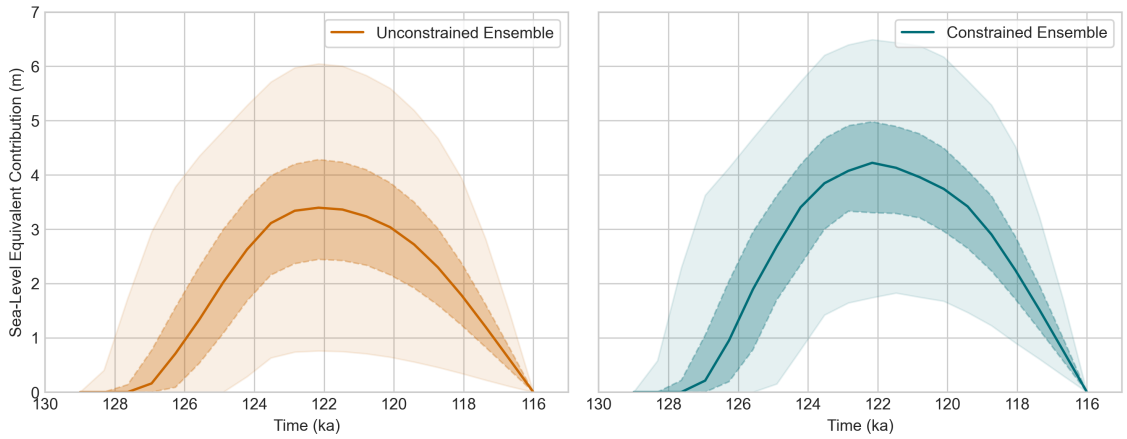

Figure 5.9: Ensemble of LIG AIS melt scenarios before (left, orange) and after (right, blue) history matching against sea-level data in regions sensitive to AIS melt. Plots show the ensemble median (solid line), 66th percentile *likely* (dark shaded region), and 90th percentile *very likely* (light shaded region) ranges of AIS sea-level equivalent volume contribution during the LIG.

5.5 Discussion

5.5.1 Antarctic Melt Scenario Methodology

We have produced a new ensemble of Eurasian RSL during the LIG that included a range of possible contributions from LIG AIS changes via our new parameterisation

of AIS melt scenarios. This parameterisation has allowed us to systematically test the timing, duration, and magnitude of LIG WAIS and EAIS volume changes based on ice-sheet thickness configurations from the DeConto et al. (2021) model. Our simple approach has utilised dynamic ice-sheet model outputs in an experimental design that differs in several ways from traditional dynamic ice-sheet modelling studies. Firstly, by utilising a pre-existing set of ice-sheet configurations, each ice-sheet input to our sea-level model is computationally inexpensive to assemble, allowing for the execution of our large-ensemble experimental design that would otherwise be computationally challenging with a coupled climate-ice model without the use of coarse model grids (Pollard et al., 2016), simplified climate inputs (Stone et al., 2013), or model emulation (Gilford et al., 2020). Secondly, we are able to test a greater range of possible ice-sheet melt scenarios than may be possible with the use of dynamic ice-sheet models since the range of ice-sheet evolutions produced by such models is constrained by the choice of implemented model physics (Pattyn and Morlighem, 2020). While in-built model physics provides useful constraints on possible ice-sheet configurations, this range is dependent on the particular model's choice of included ice-sheet physical processes, the specific numerical implementation of these processes, and the range of model boundary conditions tested (Cornford et al., 2020; Seroussi et al., 2020; Goelzer et al., 2020). In the context of the LIG, a lack of observations of the AIS physical response to changes in the ocean and climate system, and the resulting large uncertainties on dynamic model boundary conditions and parameterisation of physical processes, can cast doubt on the reliability of dynamic model-based constraints from a single model on ice-sheet behaviour (Ritz et al., 2015; Edwards et al., 2019; Crawford et al., 2021).

While our approach allows for flexibility in the range of scenarios tested it also requires prior assumptions to be made about suitable distributions of the timing, duration, and volume of LIG AIS changes, based upon previous work and understanding of WAIS and EAIS dynamics. Our range of d^{WA}_{melt} values allows for rapid WAIS retreat of up to 0.5 ka and reflects the view of previous work that the WAIS has the potential for rapid ice-sheet loss (Robel et al., 2018). The Antarctic BUttressing model Intercomparison Project (ABUMIP) of Sun et al. (2020) investigated possible rates of AIS mass loss from grounding line retreat, including marine ice sheet instability and marine ice cliff instability effects, and found multi-meter retreats over $\mathcal{O}(0.5)$ ka in all sensitivity experiments. While basins within the EAIS may also be subject to rapid responses to ocean and climate forcing they make up a smaller portion of the ice-sheet mass and, as such, we prescribe a more moderate minimum bound for d^{EA}_{change} of 1 ka since the rate of EAIS overall mass loss is likely to be lower. There is little agreement as to the timing of initial LIG WAIS and EAIS melt, as well as

the duration and timing of ice-sheet growth, and so we allow a 5 ka window for the initiation of LIG retreat, beginning at 129 ka, for both ice sheets, while also allowing a wide time window for the duration of ice growth. After running the sea-level model ensemble, our original sample of SLE contribution parameters, ranging from 0 - 5.5 m for V_{melt}^{WA} and -5 to 5 m for V_{change}^{EA}, were corrected to account for LIG topography changes, shifting their ranges to -0.25 - 5m for V_{melt}^{WA} and -1.2 - 4.5 m for V_{change}^{EA} (Section 5.4.1). After this correction, our volume ranges encompass the majority of projected ranges of mass loss from dynamic ice-sheet modelling studies of 1 - 5 m for WAIS (DeConto and Pollard, 2016; Clark et al., 2020; Golledge et al., 2021; Turney et al., 2020) and -1 to 5 m for EAIS (Harig and Simons, 2015; Fogwill et al., 2014), providing a independent constraint on these likely ice-sheet contributions during the LIG. Uplift from GIA-driven Antarctic topography deformation during the LIG may act to reduce the volume of the surrounding ocean basin thus driving additional GMSL rise, a process known as water expulsion, which may represent an underestimation of up to 30% from our sea-level contribution values for a given AIS scenario (Pan et al., 2021).

5.5.2 Regional Sensitivity

In our resulting ensemble of RSL, we have quantified the relative sensitivity of Eurasian sea-level regions to changes in the LIG AIS when compared against the contribution of uncertainty from the viscoelastic Earth model and Penultimate Deglaciation of the Eurasian ice sheet. We found that, in most regions, AIS uncertainty was dwarfed by the considerable contribution of regional GIA uncertainty and that AIS influence was only pronounced in the regions in our study area far from local ice-sheet changes. Amongst these regions, Wales had the largest sensitivity to AIS changes, likely due to the relatively small load from the British-Irish ice sheet reducing both the direct influence of ice-sheet volume uncertainty as well as consequential influences of viscoelastic deformation. The French Atlantic, English Channel, and English North Sea regions also exhibit proportionally high influence from AIS and, as they are less proximal to centres of large Eurasian ice-sheet load, thus lowering sensitivity to Eurasian ice-sheet volume. Our conclusions suggest that the southwest subset of our Eurasian data regions (Figure 5.4) has the potential to be more informative about AIS than other Eurasian regions when utilised in model-data comparison studies. This is because RSL values in these regions have a large relative sensitivity to, and a high magnitude contribution from, AIS melt. RSL data from these sites are, therefore, better positioned to refine possible scenarios of AIS melt contributions than data from regions with more significant influence from

other sources of uncertainty or from those that experienced a lower RSL contribution from Antarctica.

5.5.3 History Matching

In order to quantify the fit of our RSL ensemble against the northwest Eurasian subset of the WALIS sea-level database, we calculated the implausibility of our parameter space using a bespoke Bayesian history-matching framework that accounts for uncertainty in observed and modelled RSL values, limiting data points, and model structural error and bias. Our results show that no areas of our explored parameter space have an implausibility value that falls outside of the 3-sigma uncertainty range and, therefore, we cannot rule out any of our simulations as being implausible. As such, we concluded that current uncertainties in temporal and RSL data values, combined with the magnitude of modelled RSL uncertainty, cannot decisively identify implausible modelled RSL scenarios and, by extension, AIS melt scenarios. Despite this, we have been able to deduce information within the subset of our parameter space with the lowest 10% implausibility and, within this subset, we observed a clear preference for the choice of viscoelastic Earth model, Eurasian ice-sheet volume, and the magnitude of AIS melt. In particular, low ν_{UM} values in the best-fitting subset, contain virtually no model runs with ν_{UM} greater than 5×10^{20} Pa s, suggesting a lower viscosity Earth structure and, as a result, more pronounced (and more rapid) deformation is better able to match observational data. Our results also indicate that a thinner Eurasian lithosphere is more likely, preferring lower values of L (70 - 85 km, 66th percentile) in our full-regional history matching, combined with low ν_{UM}, although these preferences are not expressed by our southwest regional subset. The post-LGM and Holocene British-Irish ice sheet focused GIA study of Bradley et al. (2023) also showed a slight preference for higher ν_{LM} values of between 3×10^{22} Pa s and 5×10^{22} Pa s but, in contrast to our results, found a slightly better model-data fit for runs with higher ν_{UM} values of 5×10^{20} Pa s as opposed to 3×10^{20} Pa s. However, some of this difference in viscosity preference could be explained by the differences in British-Irish ice-sheet volumes between our PGM simulations and the Bradley LGM model. Our full-regional history matching also showed a pronounced preference for higher volumes of the V_{BKS}, suggesting that RSL data in the Barents-Kara Sea region have undergone high levels of subsidence. In contrast, a preference for lower V_F suggests that our mean ice-sheet load in Fennoscandia may be driving subsidence rates larger than indicated by observational constraints and, thus, our ice-sheet model may be too thick in this region.

We did not find significant preferences for parameters controlling the timing or duration of AIS mass changes and this is likely a result of the large temporal

uncertainties present in the RSL data points. However, we found a clear preference for high values of melt from both V_{melt}^{WA} and V_{change}^{EA}, especially from the subset of data regions sensitive to AIS melt. However, it is not clear from this analysis whether Eurasian sea-level data is sensitive to EAIS and WAIS sea-level contributions seperately, or simply the total AIS contribution. In order to determine whether distinct preferences for EAIS and WAIS contributions can be disentangled, we perform a pairwise implausibility calculation to identify any differences in implausibility values for equal total AIS melt contributions composed of different EAIS and WAIS contributions (Figure 5.10). Each pixel within Figure 5.10 represents the average implausibility for fixed values of both WAIS and EAIS sea-level contribution, indicated by cell position, over a 1000-member random sample of all other parameters. We used a 30-part, linear discretisation of EAIS and WAIS value ranges, resulting in a 30 by 30 pixel matrix, totalling 900 pixels and representing the evaluation of 9×10^5 parameter combinations with each of our Gaussian process emulators. Our results do not show a major distinction in preference between equal total AIS contributions with differing EAIS and WAIS contributions, and thus we conclude that it is currently not possible to distinguish the AIS source of ice-sheet melt with our current model framework and available data.

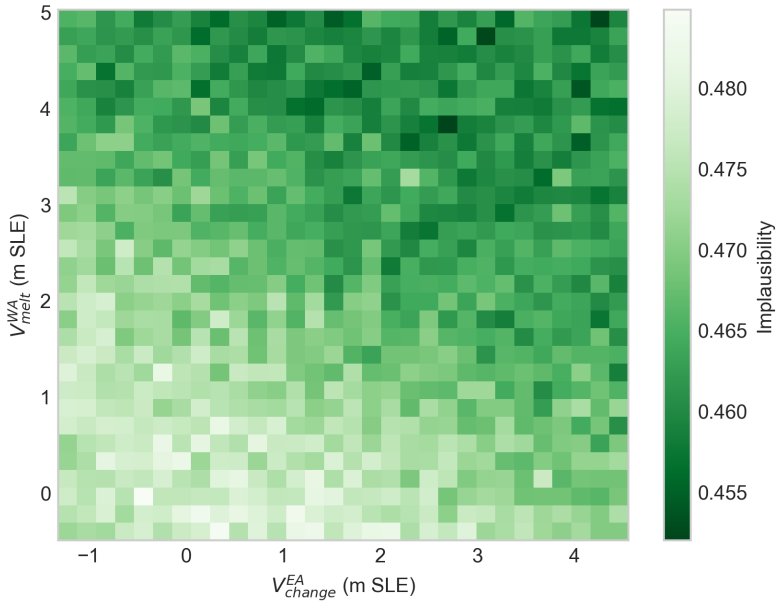

Figure 5.10: Pattern of average implausibility for EAIS and WAIS melt across their respective, discretised value ranges. Each pixel represents the average implausibility given fixed values of EAIS and WAIS sea-level contributions over a 1000-member random parameter sample of all other parameters. A darker pixel colour refers to a lower average implausibility value. The simple diagonal gradient pattern indicates that similar implausibility values are observed for similar total melt contributions, regardless of whether they are sourced from the EAIS or WAIS.

5.5.4 Model Bias

In history matching our ensemble, we accounted for the spatial pattern of the model structural error and bias, allowing the extraction of useful information from RSL records even in regions where there exists a consistent model-data mismatch. Our methodology allows us to transparently present the regional shortcomings of our model for interpretation and targeted future improvement. Prior to correcting for this systematic model bias, we found that the current range of ice-sheet and viscoelastic Earth model parameters were unable to match RSL values inferred by some rate-corrected observational records in the WALIS database. We estimated the model bias at each location by calculating the average discrepancy between the overall best-fitting 10% of ensemble members (against all records) and each sea-level record. In addition, we performed a 2D interpolation procedure in order to estimate the spatial structure of the model bias and aid interpretation, thus revealing a strong spatial structure to the model-data discrepancy. In particular, we found that modelled RSL in the southern North Sea region is over-estimated; RSL at sites beneath the former Eurasian ice sheet tended to be under-estimated; and records in the North Atlantic, English Channel and Wales regions showed good fit against our model. We found that the mean shift in parameter ranges controlling the Earth's viscoelastic structure was strongly controlled by the region against which they were compared, revealing that no one Earth model parameter combination can best match Eurasian LIG RSL data. Instead, our work shows the importance of a spatially varying Earth structure and, in future work, we suggest that studies may need to incorporate 3D Earth models into their analysis.

The discrepancy between data and our modelled North Sea RSL may reflect an overestimation of ice-sheet thickness in this region as generated by our ensemble of Eurasian Penultimate Deglaciation geometries calculated using a simple ice-sheet model (Pollard et al., 2023; Gowan et al., 2016a). This portion of the Eurasian ice sheet is known to be difficult to simulate during the Last Deglaciation, even when applying more complex ice-sheet models and available greater data constraints, due to the strong influence of dynamic ice-sheet processes that control the separation of the British-Irish and Fennoscandian ice sheet sectors and the influence of the deep Norwegian channel (Gandy et al., 2021; Clark et al., 2022; Patton et al., 2017; Bradley et al., 2011). In addition to being influenced by variation in Earth's viscosity structure, model-data discrepancy may also be influenced by the assumption of a single Eurasian PGM ice-sheet margin for all ensemble members. In Chapter 4, we found some regional sensitivity to parameters controlling the asynchrony of ice-sheet margin retreat but, since this sensitivity was relatively localised to some areas of the Barents-Kara Sea, we removed parameters controlling this influence to reduce the

size of our parameter space. As a result, reintroducing this parameterisation and expanding the assessment of margin extent and timing uncertainty to other areas of the ice-sheet margin may help to improve model-data fit in locations proximal to the ice-sheet margin.

5.5.5 Assumptions and Future Work

The sea-level fingerprints of GrIS and AIS mass loss make some areas in northwest Eurasia particularly sensitive to melt from AIS and relatively insensitive to GrIS (Hay et al., 2015; Barnett et al., 2023). We have therefore made the simplifying assumption that the Greenland contribution is negligible across the Eurasian sea-level regions we assess (Figure 1.3) and attribute observed and modelled values of RSL solely to AIS melt and GIA. LIG GrIS mass-loss estimates generally are thought to be lower than those of AIS with most studies estimating a contribution of between 0.6 and 3.5 m SLE (Letréguilly et al., 1991; Stone et al., 2013; Otto-Bliesner et al., 2006; Sommers et al., 2021) but higher contributions from GrIS of +5 m have also been suggested (Cuffey and Marshall, 2000; Yau et al., 2016). Mean fingerprint values of GrIS ice-sheet melt as calculated by Hay et al. (2014), range from between 0 - 0.5 in the Eurasian data regions that we have identified as sensitive to AIS melt. Using these values, the most likely range of GrIS melt of 0.6 - 3.5 m SLE can be translated into a theoretical contribution of 0 - 1.8 m to RSL in these regions while high GrIS melt scenarios of +5 m SLE would contribute up to +2.5 m RSL. If the thermal expansion contribution estimate of 0.4 ± 0.3 m from McKay et al. (2011) and mountain glacial melt contribution estimate of 0.32 ± 0.08 m SLE from Marzeion et al. (2020) are considered they may, combined, lower our AIS LIG contribution estimate by 0.7 ± 0.4 m, but this correction value is small compared against RSL data uncertainty.

In order to simplify the identification of Antarctic influence, our work also assumes that all other terrestrial ice-sheet deglaciation (e.g. Laurentide) are complete prior to the LIG and thus do not directly contribute to ocean water volume changes. However, Zhou and McManus (2022) have suggested that the Laurentide ice sheet may have persisted into the LIG, indicated by a Laurentide outburst flood event at 125 ka. Based on this work, Creel et al. (2023) have proposed that the Laurentide may have contributed to ongoing LIG melt. It is therefore plausible that a small proportion of our attributed AIS contribution may, in fact, be due to the combined influence of GrIS and other LIG ice-sheet melt sources, including from the Laurentide ice sheet, and a more comprehensive assessment of these contributions should be explored in future work.

5.6 Conclusions

Significant uncertainties in both observational constraints and modelled simulations make model-data comparison studies of LIG RSL a significant challenge, particularly when focused on identifying AIS ice-sheet melt. To address this problem, we developed a simple parameterisation of AIS LIG evolution that specifies the timing, duration, and magnitude of WAIS and EAIS ice-sheet changes and used this to produce a 532-member ensemble of Eurasian LIG RSL simulations that vary in viscoelastic Earth structure, the Penultimate Deglaciation of the Eurasian ice sheet, and AIS evolution. We utilise sensitivity analysis to quantify the contribution of AIS uncertainty to the variance in 15 regions of northwest Eurasian and found that AIS sensitivity was concentrated in the southwestern sector of these study areas, particularly in the English Channel, English North Sea, French Atlantic, and Wales. We compared our ensemble of RSL against data contained within the state-of-the-art WALIS RSL database (Rovere et al., 2023b) by using a comprehensive history-matching framework that accounts for structural errors in our numerical model, parameter space uncertainty, and both age and RSL uncertainty in observational constraints. In addition, we expanded this framework to incorporate information from limiting RSL data points as well as those associated with relative age constraints. Our history-matching procedure allowed us to determine the implausibility of our parameter space and, after correcting for regional model bias, we found that all of our model outputs were able to fit sea-level data within 3-sigma uncertainty.

Despite not being able to explicitly rule out portions of our parameter space, individual parameter combinations could still be compared by their relative implausibility values. When compared against RSL data within regions sensitive to AIS melt, the best-fitting 10% subset of our parameter space shows a distinct preference for high values of WAIS and EAIS melt. However, our pairwise implausibility analysis shows no meaningful change in preference between equivalent melt contributions from the WAIS or the EAIS, revealing that these contributions cannot be independently distinguished within our model-data comparison. In addition, our refined viscoelastic earth model parameter distributions showed a strong preference for low upper mantle viscosity values as well as moderate preferences for thin lithospheric thickness values and higher values of lower mantle viscosity. However, we find evidence for differences in regional viscoelastic parameter preferences, indicating a need to account for a spatially varying Earth structure across the Eurasian region. To conclude, our work suggests that, of all northwest Eurasian regions that we have considered, RSL data within the English Channel, Wales, and French Atlantic regions are most sensitive to AIS melt and that a high total AIS melt contribution of 3.2 - 9.3 m (*likely*, 66th

percentile) is best able to explain this RSL data. However, a greater quantity of high quality, low uncertainty RSL data points in regions sensitive to the AIS sea-level fingerprint, combined with more detailed assessments of temporal constraints, are needed to be able to rule out models of RSL and make decisive conclusions about the most likely patterns of LIG AIS evolution.

Chapter 6

Discussion

6.1 Review of Aims and Objectives

This thesis aimed to uncover information about the AIS during the LIG from records of RSL change in northwest Eurasia. Chapter 1 provided an overview of the current state of the literature and subdivided the overarching aim into three Research Questions (**RQ**s). After outlining key tools and techniques in Chapter 2, subsequent chapters presented work devised to address these research questions by fulfilling the five outlined Objectives (**OBJ**s). With the use of numerical ice-sheet and sea-level models, sensitivity and uncertainty analysis, and data-model comparison techniques, I have been able to address the overarching aim of this thesis. This section discusses my results, as presented in the previous chapters, and how they address the **RQ**s.

Table 6.1: Summary of research questions and the relevant thesis chapters in which they are addressed.

	Objective	Chapter(s)
RQ1	Can an uncertainty framework, utilising a simple ice-sheet model, be used to explore the range of uncertainty in ice-sheet geometry during the Penultimate Deglaciation?	3, 4
RQ2	How much does uncertainty in the ice-sheet and Earth models affect our ability to understand RSL during the Last Interglacial?	4
RQ3	Can a regional Eurasian relative sea-level dataset be used to identify the fingerprint of Antarctic ice-sheet melt during the Last Interglacial?	3, 4, 5

6.2 Answering the Research Questions

6.2.1 RQ1: Can an uncertainty framework, utilising a simple ice-sheet model, be used to explore the range of uncertainty in ice-sheet geometry during the Penultimate Deglaciation?

Before northwest Eurasian LIG RSL records could be used for the detection of Antarctic LIG sea-level contributions, it was necessary to quantify the spatiotemporal pattern of LIG GIA in Eurasia. Ongoing LIG GIA was primarily driven by ice-sheet changes from the Penultimate Deglaciation (Dendy et al., 2017) and GIA in the northwest Eurasian region likely dominated by the influence of the Eurasian ice-sheet during this time, thus constraining this ice sheet's thickness during the deglaciation required particular attention. Previous studies of Eurasian ice thickness during the Penultimate Glacial Period had focused on reconstructing the PGM only and the resulting estimates of total ice-sheet volume varied greatly depending on the modelling approach employed, such as 33 m SLE from GIA inversion of crustal rebound data (Lambeck et al., 2006), 52 m SLE from forward-dynamic-modelling based on δ^{18}O (de Boer et al., 2013), or 70 m from a dynamic ice-sheet model driven by a single climate forcing (Colleoni et al., 2016). Previous work led to three problems: (i) wide-ranging estimates of Eurasian ice-sheet volume, (ii) unquantified uncertainty in model outputs, (iii) focus on the PGM without modelling efforts extending to the Penultimate Deglaciation. The importance of the Eurasian ice sheet in driving regional GIA, combined with the significant disagreement in the present literature, led me to conclude that the propagation of ice-sheet uncertainty through to simulations of LIG RSL needed to be an essential component of my research.

Chapter 3 presented a new large-ensemble, uncertainty-focused experimental framework that could be used to assess uncertainty in ice-sheet geometries from time periods with few direct geomorphological constraints, such as the Penultimate Deglaciation. This framework was centred around the use of a simple ice-sheet model developed by Gowan et al. (2016a), known as ICESHEET, which was chosen due to its rapid execution time and small number of inputs: basal shear stress, topographic deformation, and margin extent. Chapter 3 described the parameterisation used for these inputs and explored uncertainties in their values at the PGM and Chapter 4 expanded this framework to include uncertainties in the spatial-temporal deglaciation pattern of the ice-sheet complex. While the number of model inputs was small, exploring uncertainty in the parameterisation of each input was a complex task that required

the development of numerous tools to manipulate, modify, and expand on the small amount of geological and geomorphological information available to constrain them.

Previous work had thought of the basal shear-stress map as a 'flat', mosaic-like input and could not easily explore spatial uncertainty in the layout of shear-stress regions (Gowan et al., 2016b; Reeh, 1982; Gowan et al., 2021; Fisher et al., 1985). My work utilised the Eurasian shear-stress map originally developed by Jeremey Ely for modelling the Last Deglaciation, used in the work by Gandy et al. (2018) and Clark et al. (2022), which was first simplified and extended for application to the Penultimate Glacial Period. Incorporating uncertainties in the position of ice-streaming regions (Margold et al., 2015) and basal conditions (Waller, 2001) required this map to be re-imagined as a database-style data structure, allowing input to be 'built' from successive layers thus introducing a spatially variable structure. This, in turn, necessitated the development of a Python-based module named ShearPy (Section 2.0.2.1) that could interface with this structure, apply geospatial algorithms, and overlay basal modifications to the shear-stress map. While my methodology allowed for a high degree of flexibility in shear-stress configurations, little empirical evidence was available to constrain parameter value ranges, save for those obtained from sparse individual sediment records, resulting in large parameter ranges derived from expert elicitation (Table 3.1).

The maximum extent of the Eurasian ice sheet is better constrained than the position of its margins during the subsequent PGP deglaciation (Batchelor et al., 2019; Ehlers and Gibbard, 2004; Ehlers et al., 2011; Toucanne et al., 2009), yet it was clear that significant uncertainty remains on the exact position of this maximum margin (Batchelor et al., 2019). A systematic assessment of margin positional uncertainty, as utilised within Chapters 3, required me to create a novel margin interpolation tool that could reliably linearly interpolate between two arbitrary closed polygons via the calculation of a coordinate mapping. I developed this tool as a Python-based module called ShaPy (Section 2.0.2.2) made publicly available for reuse. This same tool was used to approximate the evolution of ice margins during the Penultimate Deglaciation from an initial PGM position.

However, geomorphological evidence has suggested the Eurasian ice sheet may have deglaciated in a multi-phase, asynchronous fashion, including the Drenthe (ca. 175-160 ka) extending south of the LGM ice extent and the Warthe readvance (ca. 150-140 ka) within the Drenthe glacial maximum (Toucanne et al., 2009; Ehlers et al., 2011; Ehlers and Gibbard, 2004). Therefore some ice-sheet sectors may have reached their maximum position at the same time as others retreated (Patton et al., 2017). To incorporate deglaciation asynchrony, I expanded my interpolation tool to allow for

the rate of interpolation to vary around the shape, thus enabling parameterisation of the primary direction and magnitude of this asynchronous behaviour (Figure 2.3). Chapter 3 made the simplifying assumption that each ice-sheet margin extent tested, based on uncertainty in the MIS 6 ice-sheet margin reconstruction by Batchelor et al. (2019), represented a synchronous PGM position when it may, in fact, have been asynchronous. Yet, since our results show that incorporating margin position uncertainty did not drastically alter the modelled regional ice-sheet volume, we infer that the uncertainty introduced by the synchronicity of the PGM maximum extent is unlikely to be significant in the simulation of RSL for the LIG. On the other hand, Chapter 4 accounts for deglaciation asynchrony but, based on the negligible impact observed in Chapter 3, assumes an invariant PGM position given by the MIS 6 best-estimate of Batchelor et al. (2019). An additional caveat of the treatment of margin positions is that, since ICESHEET does not evolve dynamically, it is not possible to determine the physical validity of any given margin position if ice-sheet dynamics are considered.

Chapter 3 performed a history-matching procedure to glean insights from published reconstructions of the Last Deglaciation in order to overcome some of the physical limitations of a simple ice-sheet modelling approach, the wide range of possible ice-sheet geometries resulting from large parameter ranges, and the lack of observational constraints. The ice-sheet reconstructions of Tarasov et al. (2012) and Peltier et al. (2015) have been calibrated against observations of VLM and RSL and, therefore, by using history matching to rule out areas of the ICESHEET parameter space I have, in effect, imposed this constraining information onto the range of plausible simple ice-sheet geometries. Unfortunately, ice-sheet reconstructions often either provide no assessment of their own model uncertainty (Peltier et al., 2015) or do not make these assessments readily available (Tarasov et al., 2012) meaning that I have been unable to directly account for uncertainty in model-derived constraints, and instead used the difference between models as an approximation of this uncertainty.

Dynamic ice-sheet models are capable of resolving the evolution of the flow and geometry of an ice sheet in response to climate forcing, thus generating time-evolving ice-sheet geometries (Briggs et al., 2013; Rutt et al., 2009). However, the extent, thickness, and evolution of dynamic model simulations are highly dependent on the climate forcing used as input. Compared to the Penultimate Deglaciation, the Last Deglaciation has a relative abundance of climate and sea-level proxy data that can be used to inform climate and ice-sheet simulations. Despite this, dynamic simulations of ice sheets during the Last Deglaciation are often highly biased by errors in climate forcings (Gregoire et al., 2016). The work by Tarasov et al. (2012); Briggs et al. (2014, 2013) has tried to overcome this problem by using a complex perturbed physics

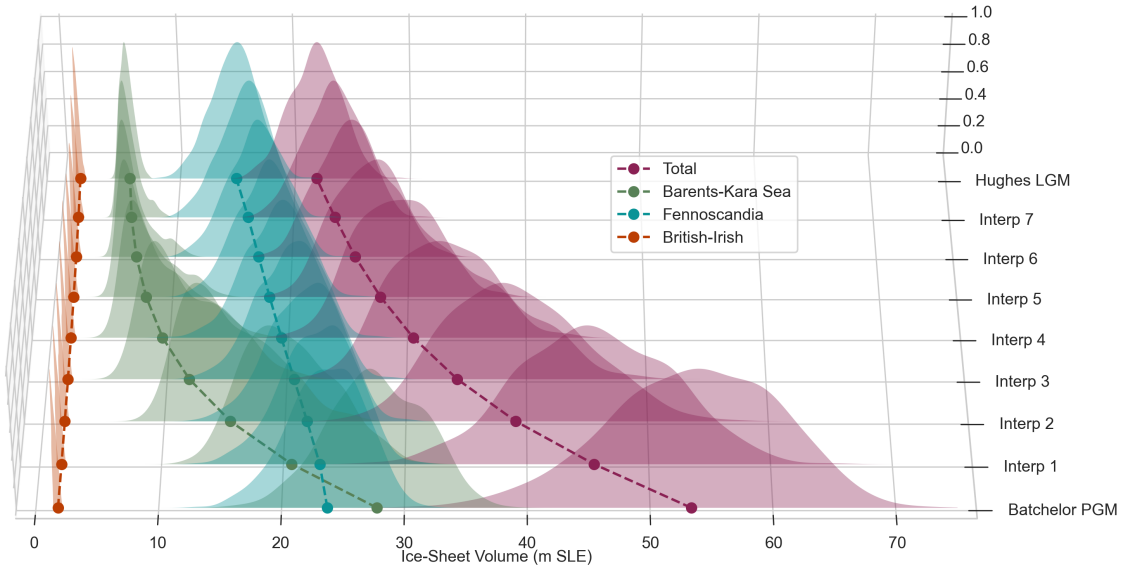

Figure 6.1: Distribution of ice-sheet volumes generated by ICESHEET, shown by region, for margins between the PGM Batchelor et al. (2019) and LGM Hughes et al. (2016) configurations. The mean volume is shown by the dotted line. Figure reproduced from Chapter 4.

ensemble experimental design in which the climate forcing is very liberally varied to force a dynamical ice sheet model to fit a large dataset of reconstructed ice sheet margins, ice thickness, near field RSL data and GPS data. Such an approach cannot be applied to the Penultimate deglaciation as there is not sufficient information on the evolution of ice sheet extent and sea level during the penultimate deglaciation. Stone et al. (2013) has used a large ensemble of thermodynamic ice-sheet model simulations to quantify uncertainty in the GrIS during the LIG. While LIG climate remains difficult to constrain (Capron et al., 2019), this work was possible due to assumptions of a relatively stable LIG climate with the majority of variability assumed to be as a result of interactions with GrIS geometry changes, approximated with an interpolation regime using three GCM climate outputs. In contrast to these studies, major uncertainties on Penultimate deglacial climate evolution, particularly the timing magnitude and evolution of greenhouse gas concentrations, make exploring uncertainty in climate inputs for use with dynamic ice-sheet models intractable. The lack of observational constraints, poorly resolved climate, the high computational expense of exploring climate uncertainty, and the over-complexity of dynamic ice-sheet models in the face of a highly unresolved Penultimate Deglaciation make the use of a simple ice-sheet model the most appropriate choice for this work.

In light of challenges that remain in constraining LIG climate, our approach is able to make transparent estimates about the range of plausible Eurasian ice-sheet geometries during the Penultimate Deglaciation for the purpose of driving a GIA

model. However, the lack of dynamics in our simulations has a number of limitations. Firstly, I assume that ice-sheet dynamics do not play an important role in determining large-scale volume distributions of ice sheets and that important dynamic-driven impacts can be approximately represented with modifications to the basal regime. However, the presence of systematic bias in my RSL ensemble in the North Sea region (Figure 5.7), an area known to be heavily influenced by dynamic ice-sheet processes (Gandy et al., 2021), suggests that the lack of resolved dynamics may impact the ability of my model to represent ice-sheet geometry and resulting RSL in some areas. Secondly, the static nature of ICESHEET means that uncertainties exist in the requirement to prescribe the temporal evolution of Eurasian Penultimate Deglaciation ice-sheet margins *a priori*. In addition, since I have generated ice-sheet margins using an interpolation regime, rather than as a result of ice-sheet dynamics (Patton et al., 2017) or geomorphological reconstruction (Batchelor et al., 2019; Hughes et al., 2016), any individual specific ice-sheet margin used may not be physically plausible. Despite this, the use of a simple method to assess uncertainty in margin evolution is warranted for the Penultimate Deglaciation as opposed to the far-larger uncertainty in extent that would result from poorly constrained dynamic ice-sheet reconstructions.

This framework has allowed the exploration of more possible scenarios than previous work and, for the first time, quantified a probability density function for Eurasian ice-sheet volume during the Penultimate Deglaciation (Figure 6.1), thus satisfying **OBJ1**. While biases indicated by RSL data, discussed in the following section, indicate that my simple approach is not able to match observational constraints in all regions (such as the North Sea) it is unlikely that a more complex, dynamic modelling approach, subject to far greater uncertainty, would improve on these issues and may, in fact, make the problem more intractable (discussed in Section 6.3). Thus, in answer to **RQ1**, I have shown that a simple ice-sheet model can, when applied within a large-ensemble uncertainty framework, be utilised to effectively and efficiently explore key uncertainties in Eurasian ice-sheet geometry both at the PGM (Chapter 3) and the Penultimate Deglaciation (Chapter 4), while incorporating geological constraining information from the better resolved Last Deglaciation through the use of a model-comparison history-matching procedure. However, I find that the lack of ice-sheet dynamics within ICESHEET does impose limitations on the reliability of simulation results in regions strongly influenced by ice-sheet dynamics and, therefore, may mean it is of less value to apply such a methodology to time periods with a better-constrained climate and ice-sheet history that could be used to drive 3D thermo-dynamic ice-sheet models (Gandy et al., 2021; Patton et al., 2017).

6.2.2 RQ2: How much does uncertainty in the ice-sheet and Earth models affect our ability to understand relative sea level during the Last Interglacial?

The pattern of northwest Eurasian LIG RSL is significantly influenced by the contribution of GIA which, in turn, is affected by uncertain changes in ice-sheet loads and the Earth's structure (Dendy et al., 2017). Understanding the uncertainty in RSL arising from model input variations was crucial before conclusions could be drawn about how well my RSL simulations matched geological data. The work within Chapters 3 and 4 developed the ensemble of Eurasian ice-sheet Penultimate Deglaciation geometries that explored uncertainties in basal shear stress, topographic deformation, and asynchrony of deglaciation. In Chapter 4, this ensemble was incorporated into a suite of global ice-sheet histories spanning 420 ka to the present day that varied in the magnitude of Eurasian and North American PGM volumes as well as in the rate and timings of the subsequent deglaciation. By combining these modelled ice-sheet histories with a set of viscoelastic Earth models, I presented an ensemble of modelled RSL histories that explore a wide range of RSL scenarios developed in order to quantify the magnitude of spatiotemporal LIG RSL uncertainty. In addition, I used this ensemble to determine the primary sources of uncertainty through the attribution of sensitivity contributions from each of the model parameters.

The results presented in this thesis showed that the combined, propagated uncertainty in Earth model parameters, ice-sheet configurations, and timings of deglaciation resulted in considerable levels of uncertainty in Eurasian LIG RSL, averaging $\mathcal{O}(10)$ m in the North Sea region and up to 30 m in the Baltic Sea. Yet this pattern was spatiotemporally variable, with the highest level of variance found in regions directly under the former ice-sheet load such as the Barents-Kara and Baltic Sea regions (Figure 4.7). The sensitivity analysis performed in Chapter 4 revealed that the sources of uncertainty are also spatiotemporally variable, but that the Earth model uncertainty was, averaged over all regions and times, by far the most dominant contributor (Figure 4.8). These high magnitudes of RSL variance combined with the results of my sensitivity decomposition reveal that uncertainty in the viscoelastic Earth model and, in locations such as the Barents-Kara Sea, the Eurasian ice-sheet load driven by the Penultimate Deglaciation are most likely to limit the ability of sea-level modelling to constrain LIG scenarios of RSL as they drive the largest uncertainty in RSL values. The work by Dendy et al. (2017) had previously demonstrated that Eurasian ice-sheet geometry uncertainty is a major contributor to uncertainty in records of RSL close to the former ice sheet and, while my work agrees with these results, I find that the influence of ice-sheet geometry uncertainty is more spatially

limited to locations directly underneath former ice-sheet loads when compared against Earth model uncertainty, particularly upper mantle viscosity (Figure 4.9). These differing conclusions can likely be explained by Dendy et al. (2017)'s focus on Earth model uncertainty in the far-field locations of Bermuda and the Seychelles, combined with their one-at-a-time experimental design making it difficult to quantify relative parameter importance to near-field RSL. Therefore, in contrast to the Dutton et al. (2015) suggestions that constraining near-field ice-sheet extent and climate are key, my work suggests that constraining Earth model uncertainty is of greatest importance for enabling the use of near-field RSL records in the reconstruction of LIG RSL changes. However, since my study is focused on quantifying uncertainty in the Eurasian ice sheet, these conclusions are likely limited to the northwest Eurasian region.

Work within Chapter 5 demonstrated spatial variation in the calculated model bias field, meaning there exist regional trends in the model's ability to fit RSL data. In addition, I found that, when compared against regional RSL data, the best-fitting subset of my ensemble expressed spatially variable preferences for Earth model parameters, particularly in the value of upper mantle viscosity (Figure 5.7). Combined, these results suggest that the assumption of a 1D Earth structure beneath Eurasia is limited in its ability to fit the RSL data and, as such, scenarios of Eurasian LIG RSL, with lower discrepancies when compared with RSL data, may be obtained with the use of a 3D Earth structure. A 3D Earth model would allow for spatial variability in these parameters but at the expense of far greater computational requirements and an expanded parameter space (Li et al., 2022; Bagge et al., 2021).

In answer to **RQ2**, my work suggests ice-sheet and Earth model uncertainty have a considerable impact on our ability to understand LIG RSL, particularly at locations under former ice-sheet loads, owing to the significant ice-sheet thickness uncertainty outlined in Chapter 3. However, in completing **OBJ2**, Chapter 4 has shown that the RSL uncertainty, when compared to regions such as the Barents-Kara Sea and Baltic Sea, is lower in Eurasian regions peripheral to the former ice sheet, such as the English Channel and French Atlantic. As a result of achieving **OBJ2**, I also demonstrated that the influence of ice-sheet uncertainty is localised; indeed, uncertainty in the Eurasian ice sheet evolution during the Penultimate Deglaciation contributed $\mathcal{O}(20)$ m to the RSL variance in Baltic Sea and White Sea regions (Figure 4.8). Despite this, the large variance in modelled LIG RSL values presented an opportunity to identify the most important model parameters in controlling Eurasian RSL and set the stage for refinement of these parameter ranges when subsequently compared against observational constraints.

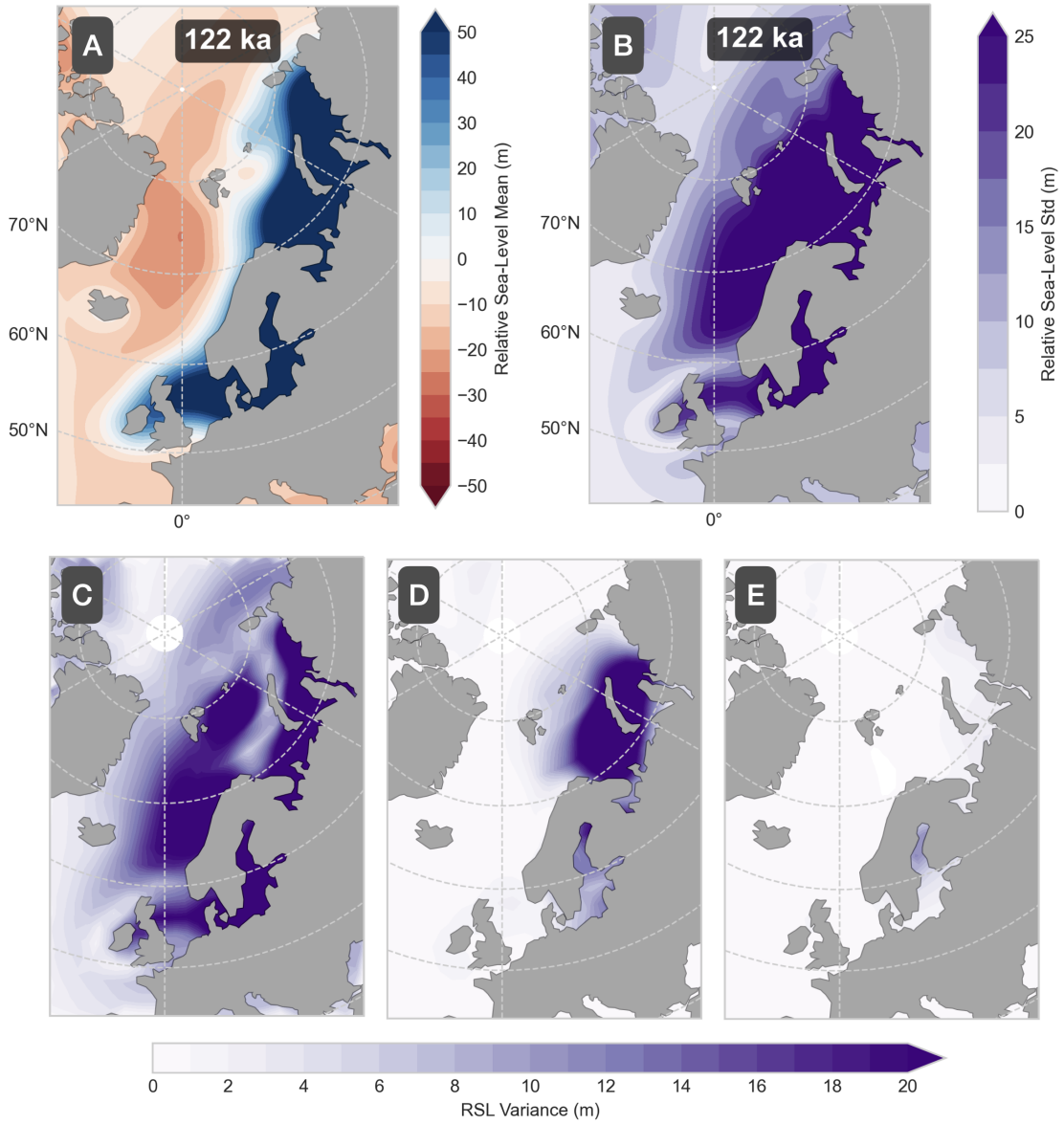

Figure 6.2: Modelled RSL ensemble (A) mean and (B) standard deviation at 122 ka. Decomposed standard deviation into first-order sensitivity contributions from parameters controlling (C) the viscoelastic Earth model, (D) volume of the Penultimate Deglaciation Eurasian ice-sheet, and (E) timing of the Penultimate Deglaciation. Figure modified from Chapter 5.

6.2.3 RQ3: Can a regional Eurasian relative sea-level dataset be used to identify the fingerprint of Antarctic ice-sheet melt during the Last Interglacial?

RSL records from the LIG reflect the magnitude of global ice-sheet melt contributions, modulated by each specific ice-sheet fingerprint at a particular data-site location (Figure 1.3). Previous work has compared LIG RSL data, corrected for regional GIA, to make inferences about LIG GMSL, such as work on Bahamian RSL data by Dyer et al. (2021), but only a limited number of studies have utilised regional RSL data to identify individual ice-sheet contributions (Barnett et al., 2023; Kopp et al., 2009). The work by Barnett et al. (2023) used a set of 27 Eurasian sea-level data points corrected for regional GIA, derived from a discrete set of scaled ice-sheet geometries and Earth models; GrIS melt (estimated to contribute less than 1 m of local sea-level change); and simple assumptions about mountain glacier and thermosteric contributions in order to infer AIS melt of 3.6 - 8.7 m (central 68% probability) from the residual Eurasian LIG RSL signal. Previous to my study, work was limited by using only a number of selective LIG sea-level data points, relying on a GIA correction derived from a sparsely explored parameter space, and not explicitly matching the resulting RSL signals to models of AIS melt. In Chapter 5, I aimed to improve on these previous methodologies in three key ways. Firstly, I incorporating the state-of-the-art WALIS sea-level database (Cohen et al., 2022; Dalton et al., 2022), 43 more data points than used by Barnett et al. (2023). Secondly, I explicitly modelling the AIS and regional GIA contribution to Eurasian RSL records by developing an ensemble of LIG AIS melt, the modelled Penultimate Deglaciation Eurasian ice-sheet (Chapter 4), and Earth model configurations. Finally, I utilised a history matching procedure to detect this contribution, accounting for model and data uncertainty, thus maximising available empirical constraints on Eurasian RSL. In doing so, Chapter 5 estimated a AIS LIG melt contribution of 3.2 - 9.3 m (*likely*, 66th percentile) from the Eurasian RSL data sensitive to AIS melt, a wider range than estimated by Barnett et al. (2023) likely due to the larger, more representative GIA uncertainty included in my study.

The first goal of Chapter 5 was to produce an ensemble of RSL values that incorporated parameters controlling the dominant sources of uncertainty in Eurasian GIA as well as AIS melt. To achieve the latter, I produced a simple parameterisation of EAIS and WAIS melt scenarios that, combined with the DeConto et al. (2021) AIS model, could be used to produce ice-sheet histories matching our specifications. By using the DeConto et al. (2021) future projection model, the RSL signal incorporates rotational feedback from changes in the AIS centre of mass that would not have been

possible by using a simpler uniform scaling, or 'deflation', of a pre-industrial ice-sheet configuration. However, while this approach, therefore, makes the assumption that AIS LIG retreat is similar to that of the DeConto model, I find that Eurasian RSL data is insensitive to the specific melt of the EAIS and WAIS ice sheets, meaning that differences in geometries between the DeConto model and an alternative ice-sheet reconstruction are unlikely to have affected my results. Sensitivity analysis revealed that the English Channel, Wales, and Atlantic regions had higher relative sensitivity to AIS melt than other Eurasian data regions (Figure 5.6). However, the raised beach deposits that are the most commonly preserved LIG RSL data in these regions (Bates et al., 2010; Coutard et al., 2006; Briant et al., 2019; Campbell et al., 2012) can provide less vertical precision than sedimentary archives (Rovere et al., 2016) preserved in the estuaries around the North Sea (Zagwijn, 1983). There must, therefore, be a balance between geophysical modelling and the vertical RSL constraints offered by the data when deciding on the most effective regions to target for LIG RSL data acquisition.

Detection of AIS melt in northwest Eurasia relies on the quality and abundance of available observational constraints. By utilising data from the WALIS database, I was able to perform the history-matching procedure on far more data points than previous studies, thus improving the spatial and temporal spread of constraints on my RSL ensemble. Despite the large number of data points, the LIG sea-level data is subject to high degrees of temporal uncertainty averaging ± 7 ka (1σ) for absolute dated sea-level data points documented in northwest Eurasia, meaning that the average data point spans the full length of the LIG within 2σ uncertainty (Figure 6.3). The high temporal uncertainty in RSL data points likely limited the work in Chapter 5 from being able to make deductions about the rate and timing of AIS melt. By contrast, the relatively low average RSL data uncertainty of ± 3 m (1σ) likely resulted in greater sensitivity to the magnitude of AIS melt in the subsequent history-matching procedure. Within my method, I make no attempt to alter the weighting of individual constraints on the history-matching procedure beyond that which is inferred directly from their reported RSL and age uncertainty. This approach allows uncertainties to be honestly presented by enabling the transparent propagation of uncertainties from data to model constraint. However, this relies on well-reported uncertainties within the literature, which varies significantly given the geological data collection period extends over several decades during which time techniques and understanding have evolved. I find that 30% of Eurasian WALIS data points have RSL uncertainties of less than 1 m, which may suggest a tendency to under-report uncertainties (Shennan, 2015), resulting in potential biases within my history matched LIG AIS melt estimates.

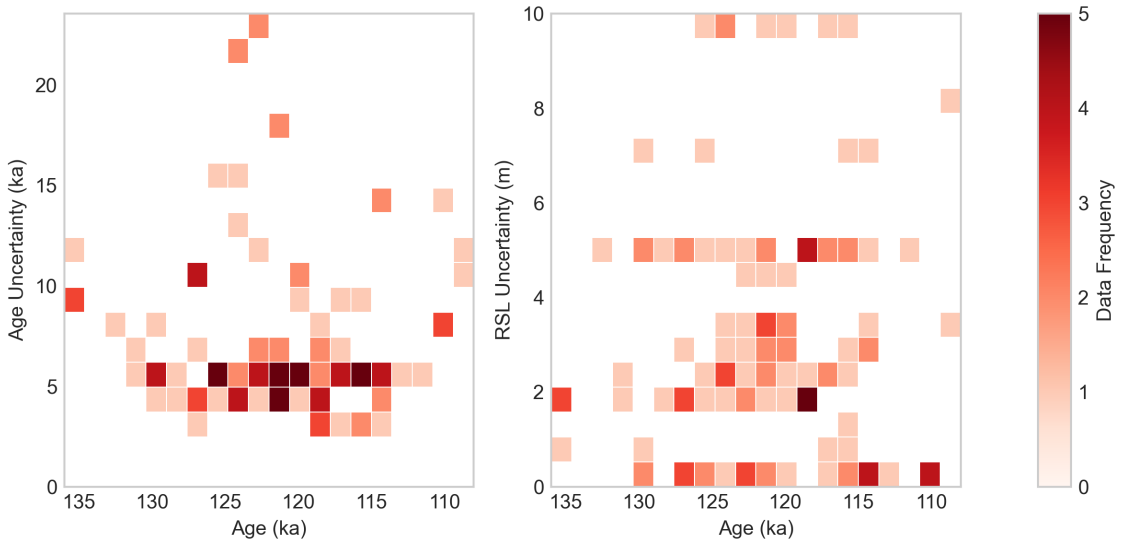

Figure 6.3: Frequency of RSL data in the filtered WALIS database (Rovere et al., 2023b) shown by age for (left) age uncertainty and (right) RSL uncertainty.

In order to utilise northwest Eurasian LIG data within the history-matching framework, I expanded the mathematics used to describe the normalised distance between model and observation to incorporate information from limiting data points and relative ages (the latter not utilised in the Barnett et al. (2023) study). To achieve this, Chapter 5 described the use of a normal cumulative density function, as opposed to a normal distribution, as an alternative distribution representing RSL implausibility for limiting data points, while the temporal implausibility for data points associated with a relative age were represented with a uniform distribution over their respective reported age ranges. This simple treatment of relative ages does not account for tie-point uncertainty, which would allow for additional constraints through the auto-correlation of relative data points tied to the same age constraint (e.g. tephra chronohorizons) as well as to data points whose age constraint is similarly auto-correlated.

Chapter 5 has achieved **OBJ4** through the use of our simple parameterisation of AIS melt and, by utilising the results of my sensitivity analysis, fulfilling **OBJ5** by identifying the best fitting subset of AIS scenarios that fit Eurasian sea-level data. In doing so, I have found that, in answer to **RQ3**, it is possible to identify the fingerprint of LIG AIS melt within a history-matching framework from northwest Eurasian RSL data but that this data is limited in its ability to inform understanding of the rate and timing of this melt, as well as in differentiating between EAIS and WAIS sources.

6.3 Limitations and Future Work

As highlighted above, my work is limited by several assumptions I have been required to make in order to navigate sparsely available temporal-spatial ice-sheet constraints, computational feasibility, and large data uncertainties. Of particular relevance to the limitations of my final modelled LIG RSL is the assumption of a 1D Earth structure. While out of the scope of this study, I suggest that well-constrained 3D GIA modelling over the northwest Eurasian region may lead to better model-data misfit in some instances (Li et al., 2022). However, in other cases, 1D models have been shown to provide a better-fit against uplift data than 3D models (Kierulf et al., 2014) and, therefore, I caution against the use of 3D models without the computing resources to adequately explore their much-expanded parameter space and pre-assessment of 1D model performance in the region of interest. At the time of writing this thesis, work is ongoing to develop methods to decrease the compute time of such models and, by extension, improve the feasibility of large ensemble 3D GIA experimental designs, such as fast, machine-learning derived approximations to the influence of 3D GIA structure for modelled RSL values (Love et al., 2023).

Model-data comparison is an essential component of reliable modelling experiments in order to validate a model's ability to match observation constraints. History matching was specifically chosen as the model-data comparison framework in this thesis so that highly uncertain LIG RSL data could still be informative, weighted by said uncertainty, and allowing for maximum data inclusivity. However, history matching is therefore reliant on the accuracy of reported data uncertainty. Efforts such as the WALIS sea-level database (Rovere et al., 2023b), and the HolSea databasing efforts for the Holocene (Khan et al., 2019), have been developed to collate and standardise the complex and expanding evidence of palaeo RSL data, but these efforts are often reliant on the accuracy of uncertainties reported within the original literature. My work is therefore subject to, and limited by, bias induced through data that may be reported as more certain than is realistic when all the uncertainties are considered (e.g. sediment compaction, palaeo tidal range, long-term tectonics). I, therefore, advocate for the honest and transparent reporting of uncertainties in empirical data studies rather than subjective filtering of data based on quality measures so that the uncertainties themselves can inform data comparison. While the error bounds on the vertical component of RSL data are typically $\mathcal{O}(1)$ m, my model-data comparison is also limited by the high temporal uncertainties reported for the sea-level data points. In this work, RSL values tied to relative age constraints (e.g., pollen biostratigraphy) are assumed to be uniformly probable across the corresponding age range and this approach could be improved in future work by assessing uncertainty in the age

tie directly and, as a result, auto-correlating the age probabilities of data points associated with the same age tie point. In doing so, the resulting reduced temporal uncertainty could be used to better constrain the timing and rate of AIS melt.

In the identification of AIS melt, I have made the assumption that all interglacial ice-sheet melt presented in Eurasia can be attributed to the AIS. While the contribution of GrIS in regions of high AIS melt sensitivity was likely small, as discussed in Chapter 5, the explicit calculation of this contribution with a bespoke Greenland parameterisation was out of the scope of this thesis. To address this, and the surfacing debate around potential ongoing interglacial contributions from North American and Eurasian ice sheets (Creel et al., 2023), I recommend future work expand on our experimental design to assess the impact of these ice sheets and thus improve the robustness of the AIS contribution estimates.

This thesis required the development of methods and tools that are likely to have applications to a variety of future work. My expanded history-matching framework is able to account for limiting data points, relative age constraints and their uncertainties, and systematic model bias, thus maximising available information regardless of sea-level data uncertainty, time period of study, or systematic model regional misfit. I recommend that future work incorporate this approach in RSL data comparison studies, particularly for periods prior to the Last Glacial where empirical constraints are limited. Future studies employing the ICESHEET model may wish to employ the ShearPy shear-stress data infrastructure tool to manage and manipulate perturbations to this input. My polygon interpolation tool, as detailed in Section 2.0.2.2, could be applied to estimate the transition between margin positions of other ice sheets and times with poorly constrained intermediary positions, including the ability to test patterns of asynchronous deglaciation. This tool could also have applications to a more general set of problems that require the use of polygon shape morphing.

In a wider context, my simulations of the Penultimate Deglaciation of the Eurasian ice sheet may have implications for studies reconstructing LIG climate and ocean circulation patterns, where the surface topography is a strong control on global wind patterns and may modulate surface temperature and ocean circulation patterns (Romé et al., 2022). Ice-sheet position and thickness can inform work understanding the past flora, fauna, and human migration patterns and my deglaciation ensemble may add additional constraints on the validity of such theories (Lister, 2004; Lauer and Weiss, 2018). My constrained ensemble of past Eurasian GIA is likely to inform the targeted development of Eurasian LIG RSL records. Finally, my deduction of AIS ice-sheet melt contributions from model-data history matching demonstrates the robustness of the fingerprinting framework (Hay et al., 2015) and LIG melt

hypotheses that serve to underpin the usefulness of the LIG to inform models of future sea-level rise. We have independently quantified AIS ice-sheet melt from a database of RSL records that agree with current estimates of AIS melt, and highlight the value of data records in constraining LIG ice-sheet changes.

6.4 Conclusions

In summary, this thesis has systematically and creatively explored the key, significant sources of uncertainty controlling RSL in the Eurasian region. Uncertainty in the spatiotemporal Eurasian ice-sheet history during the Penultimate Deglaciation was quantified with the use of a simple ice-sheet model within a large-ensemble framework combined with parameterisations of ice-sheet extent, basal shear stress, and topographic deformation. My work has demonstrated the usefulness of simple models to explore uncertainty where few empirical constraints are available and how other sources of information, such as published reconstructions of ice histories during the Last Deglaciation, can be used to inform and constrain uncertain model inputs. Simulations of the Eurasian ice sheet suggest a maximum volume of 48 ± 8 m SLE, smaller than previous work, and I present a new model of the Penultimate Deglaciation of the Eurasian ice sheet useful for driving models of GIA.

Sensitivity analysis performed with my ensemble of LIG RSL revealed that: (i) the most important source of uncertainty is, typically, in the viscoelastic Earth model, (ii) sensitivity to the volume of the Eurasian ice sheet is only dominant in regions directly under the former ice-sheet load, (iii) variation in the timing and nature of the deglaciation of the North American ice sheet had little overall effect. Using information gained from this sensitivity analysis to reduce the dimensions of our parameter space, I performed a new ensemble of simulations that included an ensemble of melt scenarios of the LIG Antarctic ice sheet with a parameterisation that tested the timing, duration and magnitude of East and West Antarctic melt. By applying a bespoke history matching procedure against a state-of-the-art database of RSL data, I found that Eurasian sea-level data in regions sensitive to Antarctic melt suggested a contribution of 3.2 - 9.3 m (*likely*, 66th percentile) but that high temporal uncertainty in RSL data limited our ability to constrain the timing or duration of this contribution. In future work, I recommend tweaking the presented methodology to reduce RSL bias by investigating variable Earth structure across Eurasia as well as including scenarios that test interglacial melt from the Greenland and, potentially, North American ice sheets.

Bibliography

Abe-Ouchi, A., Segawa, T., and Saito, F.: Climatic Conditions for Modelling the Northern Hemisphere Ice Sheets throughout the Ice Age Cycle, Clim. Past, p. 16, 2007.

Abe-Ouchi, A., Saito, F., Kawamura, K., Raymo, M. E., Okuno, J., Takahashi, K., and Blatter, H.: Insolation-Driven 100,000-Year Glacial Cycles and Hysteresis of Ice-Sheet Volume, Nature, 500, 190–193, doi:10.1038/nature12374, 2013.

Andrianakis, I., Vernon, I. R., McCreesh, N., McKinley, T. J., Oakley, J. E., Nsubuga, R. N., Goldstein, M., and White, R. G.: Bayesian History Matching of Complex Infectious Disease Models Using Emulation: A Tutorial and a Case Study on HIV in Uganda, PLOS Computational Biology, 11, e1003 968, doi:10.1371/journal.pcbi.1003968, 2015.

Archer, R., Ely, J., Heaton, T., Butcher, F., Hughes, A., and Clark, C.: Assessing Ice Sheet Models against the Landform Record: The Likelihood of Accordant Lineations Analysis (LALA) Tool, Earth Surface Processes and Landforms, 48, 2754–2771, doi:10.1002/esp.5658, 2023.

Astfalck, L., Williamson, D., Gandy, N., Gregoire, L., and Ivanovic, R.: Coexchangeable Process Modelling for Uncertainty Quantification in Joint Climate Reconstruction, 2021.

Astfalck, L. C., Cripps, E. J., Gosling, J. P., and Milne, I. A.: Emulation of Vessel Motion Simulators for Computationally Efficient Uncertainty Quantification, Ocean Engineering, 172, 726–736, doi:10.1016/j.oceaneng.2018.11.059, 2019.

Austermann, J., Mitrovica, J. X., Huybers, P., and Rovere, A.: Detection of a Dynamic Topography Signal in Last Interglacial Sea-Level Records, Science Advances, 3, e1700 457, doi:10.1126/sciadv.1700457, 2017.

Austermann, J., Hoggard, M. J., Latychev, K., Richards, F. D., and Mitrovica, J. X.: The Effect of Lateral Variations in Earth Structure on Last Interglacial Sea Level, Geophysical Journal International, 227, 1938–1960, doi:10.1093/gji/ggab289, 2021.

Bagge, M., Klemann, V., Steinberger, B., Latinović, M., and Thomas, M.: Glacial-Isostatic Adjustment Models Using Geodynamically Constrained 3D Earth Structures, Geochemistry, Geophysics, Geosystems, 22, e2021GC009 853, doi: 10.1029/2021GC009853, 2021.

Barlow, N. L. M. and Rush, G.: Late Quaternary Relative Sea-Level Changes at Mid-Latitudes, in: Encyclopedia of Quaternary Science, 3rd Edition, Elsevier, 2022.

Barlow, N. L. M., McClymont, E. L., Whitehouse, P. L., Stokes, C. R., Jamieson, S. S. R., Woodroffe, S. A., Bentley, M. J., Callard, S. L., Cofaigh, C. Ó., Evans, D. J. A., Horrocks, J. R., Lloyd, J. M., Long, A. J., Margold, M., Roberts, D. H., and Sanchez-Montes, M. L.: Lack of Evidence for a Substantial Sea-Level Fluctuation within the Last Interglacial, Nature Geoscience, 11, 627–634, doi: 10.1038/s41561-018-0195-4, 2018.

Barnett, R. L., Austermann, J., Dyer, B., Telfer, M. W., Barlow, N. L. M., Boulton, S. J., Carr, A. S., and Creel, R. C.: Constraining the Contribution of the Antarctic Ice Sheet to Last Interglacial Sea Level, Science Advances, 9, eadf0198, doi: 10.1126/sciadv.adf0198, 2023.

Batchelor, C. L., Margold, M., Krapp, M., Murton, D. K., Dalton, A. S., Gibbard, P. L., Stokes, C. R., Murton, J. B., and Manica, A.: The Configuration of Northern Hemisphere Ice Sheets through the Quaternary, Nature Communications, 10, 3713, doi:10.1038/s41467-019-11601-2, 2019.

Bates, M. R., Briant, R. M., Rhodes, E. J., Schwenninger, J.-L., and Whittaker, J. E.: A New Chronological Framework for Middle and Upper Pleistocene Landscape Evolution in the Sussex/Hampshire Coastal Corridor, UK, Proceedings of the Geologists' Association, 121, 369–392, doi:10.1016/j.pgeola.2010.02.004, 2010.

Bentley, M. J., Fogwill, C. J., Le Brocq, A. M., Hubbard, A. L., Sugden, D. E., Dunai, T. J., and Freeman, S. P.: Deglacial History of the West Antarctic Ice Sheet in the Weddell Sea Embayment: Constraints on Past Ice Volume Change, Geology, 38, 411–414, doi:10.1130/G30754.1, 2010.

Berger, A.: Milankovitch Theory and Climate, Reviews of Geophysics, 26, 624–657, doi:10.1029/RG026i004p00624, 1988.

Berger, A. and Loutre, M. F.: Insolation Values for the Climate of the Last 10 Million Years, Quaternary Science Reviews, 10, 297–317, doi:10.1016/0277-3791(91)90033-Q, 1991.

Bierman, P. R., Davis, P. T., Corbett, L. B., Lifton, N. A., and Finkel, R. C.: Cold-Based Laurentide Ice Covered New England's Highest Summits during the Last Glacial Maximum, Geology, 43, 1059–1062, doi:10.1130/G37225.1, 2015.

Bower, R. G., Goldstein, M., and Vernon, I.: Galaxy Formation: A Bayesian Uncertainty Analysis, Bayesian Analysis, 5, 619–669, doi:10.1214/10-BA524, 2010.

Bradley, S. L., Milne, G. A., Teferle, F. N., Bingley, R. M., and Orliac, E. J.: Glacial Isostatic Adjustment of the British Isles: New Constraints from GPS Measurements of Crustal Motion, Geophysical Journal International, 178, 14–22, doi:10.1111/j.1365-246X.2008.04033.x, 2009.

Bradley, S. L., Milne, G. A., Shennan, I., and Edwards, R.: An Improved Glacial Isostatic Adjustment Model for the British Isles: GLACIAL ISOSTATIC ADJUSTMENT MODEL FOR THE BRITISH ISLES, Journal of Quaternary Science, 26, 541–552, doi:10.1002/jqs.1481, 2011.

Bradley, S. L., Siddall, M., Milne, G. A., Masson-Delmotte, V., and Wolff, E.: Combining Ice Core Records and Ice Sheet Models to Explore the Evolution of the East Antarctic Ice Sheet during the Last Interglacial Period, Global and Planetary Change, 100, 278–290, doi:10.1016/j.gloplacha.2012.11.002, 2013.

Bradley, S. L., Ely, J. C., Clark, C. D., Edwards, R. J., and Shennan, I.: Reconstruction of the Palaeo-sea Level of Britain and Ireland Arising from Empirical Constraints of Ice Extent: Implications for Regional Sea Level Forecasts and North American Ice Sheet Volume, Journal of Quaternary Science, p. jqs.3523, doi:10.1002/jqs.3523, 2023.

Brain, M. J.: Past, Present and Future Perspectives of Sediment Compaction as a Driver of Relative Sea Level and Coastal Change, Current Climate Change Reports, 2, 75–85, doi:10.1007/s40641-016-0038-6, 2016.

Briant, R. M., Bates, M. R., Boreham, S., Cameron, N. G., Coope, G. R., Field, M. H., Hatch, B. M., Holmes, J. A., Keen, D. H., Kilfeather, A. A., Penkman, K. E. H., Simons, R. M. J., Schwenninger, J.-L., Wenban-Smith, F. F., Whitehouse, N. J., and Whittaker, J. E.: Early Ipswichian (Last Interglacial) Sea Level Rise in the Channel Region: Stone Point Site of Special Scientific Interest, Hampshire, England, Proceedings of the Geologists' Association, 130, 1–26, doi:10.1016/j.pgeola.2018.03.002, 2019.

Briggs, R., Pollard, D., and Tarasov, L.: A Glacial Systems Model Configured for Large Ensemble Analysis of Antarctic Deglaciation, The Cryosphere, 7, 1949–1970, doi:10.5194/tc-7-1949-2013, 2013.

Briggs, R. D., Pollard, D., and Tarasov, L.: A Data-Constrained Large Ensemble Analysis of Antarctic Evolution since the Eemian, Quaternary Science Reviews, 103, 91–115, doi:10.1016/j.quascirev.2014.09.003, 2014.

Campbell, S., Hunt, C. O., Scourse, J. D., Keen, D. H., and Stephens, N.: Quaternary of South-West England, Springer Science & Business Media, 2012.

Capron, E., Govin, A., Stone, E. J., Masson-Delmotte, V., Mulitza, S., Otto-Bliesner, B., Rasmussen, T. L., Sime, L. C., Waelbroeck, C., and Wolff, E. W.: Temporal and Spatial Structure of Multi-Millennial Temperature Changes at High Latitudes during the Last Interglacial, Quaternary Science Reviews, 103, 116–133, doi: 10.1016/j.quascirev.2014.08.018, 2014.

Capron, E., Rovere, A., Austermann, J., Axford, Y., Barlow, N. L. M., Carlson, A. E., de Vernal, A., Dutton, A., Kopp, R. E., McManus, J. F., Menviel, L., Otto-Bliesner, B. L., Robinson, A., Shakun, J. D., Tzedakis, P. C., and Wolff, E. W.: Challenges and Research Priorities to Understand Interactions between Climate, Ice Sheets and Global Mean Sea Level during Past Interglacials, Quaternary Science Reviews, 219, 308–311, doi:10.1016/j.quascirev.2019.06.030, 2019.

Celsius, A.: Anmärkning Om Vatnets Förminskande Så i Östersiön Som Vesterhafvet, Kongl., Swenska Wetenskaps Academiens Handlingar, pp. 33–50, 1743.

Clark, C. D., Ely, J. C., Hindmarsh, R. C. A., Bradley, S., Ignéczi, A., Fabel, D., Ó Cofaigh, C., Chiverrell, R. C., Scourse, J., Benetti, S., Bradwell, T., Evans, D. J. A., Roberts, D. H., Burke, M., Callard, S. L., Medialdea, A., Saher, M., Small, D., Smedley, R. K., Gasson, E., Gregoire, L., Gandy, N., Hughes, A. L. C., Ballantyne, C., Bateman, M. D., Bigg, G. R., Doole, J., Dove, D., Duller, G. A. T., Jenkins, G. T. H., Livingstone, S. L., McCarron, S., Moreton, S., Pollard, D., Praeg, D., Sejrup, H. P., Van Landeghem, K. J. J., and Wilson, P.: Growth and Retreat of the Last British–Irish Ice Sheet, 31 000 to 15 000 Years Ago: The BRITICE-CHRONO Reconstruction, Boreas, 51, 699–758, doi:10.1111/bor.12594, 2022.

Clark, P. U. and Mix, A. C.: Ice Sheets and Sea Level of the Last Glacial Maximum, Quaternary Science Reviews, p. 7, 2002.

Clark, P. U., Mitrovica, J. X., Milne, G. A., and Tamisiea, M. E.: Sea-Level Fingerprinting as a Direct Test for the Source of Global Meltwater Pulse IA, Science, 295, 2438–2441, doi:10.1126/science.1068797, 2002.

Clark, P. U., He, F., Golledge, N. R., Mitrovica, J. X., Dutton, A., Hoffman, J. S., and Dendy, S.: Oceanic Forcing of Penultimate Deglacial and Last Interglacial Sea-Level Rise, Nature, 577, 660–664, doi:10.1038/s41586-020-1931-7, 2020.

Cohen, K. M., Cartelle, V., Barnett, R., Busschers, F. S., and Barlow, N. L. M.: Last Interglacial Sea-Level Data Points from Northwest Europe, Earth System Science Data, 14, 2895–2937, doi:10.5194/essd-14-2895-2022, 2022.

Colleoni, F.: On the Late Saalian Glaciation (160 - 140 Ka): A Climate Modeling Study, Ph.D. thesis, Université Joseph-Fourier-Grenoble I; Stockholm University, 2009.

Colleoni, F., Wekerle, C., Näslund, J.-O., Brandefelt, J., and Masina, S.: Constraint on the Penultimate Glacial Maximum Northern Hemisphere Ice Topography (≈140 Kyrs BP), Quaternary Science Reviews, 137, 97–112, doi:10.1016/j.quascirev.2016.01.024, 2016.

Cornford, S. L., Seroussi, H., Asay-Davis, X. S., Gudmundsson, G. H., Arthern, R., Borstad, C., Christmann, J., Dias dos Santos, T., Feldmann, J., Goldberg, D., Hoffman, M. J., Humbert, A., Kleiner, T., Leguy, G., Lipscomb, W. H., Merino, N., Durand, G., Morlighem, M., Pollard, D., Rückamp, M., Williams, C. R., and Yu, H.: Results of the Third Marine Ice Sheet Model Intercomparison Project (MISMIP+), The Cryosphere, 14, 2283–2301, doi:10.5194/tc-14-2283-2020, 2020.

Coutard, S., Lautridou, J.-P., Rhodes, E., and Clet, M.: Tectonic, Eustatic and Climatic Significance of Raised Beaches of Val de Saire, Cotentin, Normandy, France, Quaternary Science Reviews, 25, 595–611, doi:10.1016/j.quascirev.2005.02.003, 2006.

Crawford, A. J., Benn, D. I., Todd, J., Åström, J. A., Bassis, J. N., and Zwinger, T.: Marine Ice-Cliff Instability Modeling Shows Mixed-Mode Ice-Cliff Failure and Yields Calving Rate Parameterization, Nature Communications, 12, 2701, doi:10.1038/s41467-021-23070-7, 2021.

Creel, R., Austermann, J., and Dyer, B.: Delayed Laurentide Ice Sheet Melt during the Last Interglacial Causes Sea Level Oscillation Due to Glacial Isostatic Adjustment, in: AGU23, AGU, 2023.

Cuffey, K. M. and Marshall, S. J.: Substantial Contribution to Sea-Level Rise during the Last Interglacial from the Greenland Ice Sheet, Nature, 404, 591–594, doi:10.1038/35007053, 2000.

Dalton, A. S., Margold, M., Stokes, C. R., Tarasov, L., Dyke, A. S., Adams, R. S., Allard, S., Arends, H. E., Atkinson, N., Attig, J. W., Barnett, P. J., Barnett, R. L., Batterson, M., Bernatchez, P., Borns, H. W., Breckenridge, A., Briner, J. P., Brouard, E., Campbell, J. E., Carlson, A. E., Clague, J. J., Curry, B. B., Daigneault, R.-A., Dubé-Loubert, H., Easterbrook, D. J., Franzi, D. A., Friedrich, H. G., Funder, S., Gauthier, M. S., Gowan, A. S., Harris, K. L., Hétu, B., Hooyer, T. S., Jennings, C. E., Johnson, M. D., Kehew, A. E., Kelley, S. E., Kerr, D., King, E. L., Kjeldsen, K. K., Knaeble, A. R., Lajeunesse, P., Lakeman, T. R., Lamothe, M., Larson, P., Lavoie, M., Loope, H. M., Lowell, T. V., Lusardi, B. A., Manz, L., McMartin, I., Nixon, F. C., Occhietti, S., Parkhill, M. A., Piper, D. J., Pronk, A. G., Richard, P. J., Ridge, J. C., Ross, M., Roy, M., Seaman, A., Shaw, J., Stea, R. R., Teller, J. T., Thompson, W. B., Thorleifson, L. H., Utting, D. J., Veillette, J. J., Ward, B. C., Weddle, T. K., and Wright, H. E.: An Updated Radiocarbon-Based Ice Margin Chronology for the Last Deglaciation of the North American Ice Sheet Complex, Quaternary Science Reviews, 234, 106 223, doi:10.1016/j.quascirev.2020.106223, 2020.

Dalton, A. S., Gowan, E. J., Mangerud, J., Möller, P., Lunkka, J. P., and Astakhov, V.: Last Interglacial Sea-Level Proxies in the Glaciated Northern Hemisphere, Earth System Science Data, 14, 1447–1492, doi:10.5194/essd-14-1447-2022, 2022.

Daly, R. A.: Pleistocene Changes of Level, The American Journal of Science, 10, 1925.

de Boer, B., van de Wal, R. S. W., Lourens, L. J., Bintanja, R., and Reerink, T. J.: A Continuous Simulation of Global Ice Volume over the Past 1 Million Years with 3-D Ice-Sheet Models, Climate Dynamics, 41, 1365–1384, doi:10.1007/s00382-012-1562-2, 2013.

DeConto, R. M. and Pollard, D.: Contribution of Antarctica to Past and Future Sea-Level Rise, Nature, 531, 591–597, doi:10.1038/nature17145, 2016.

DeConto, R. M., Pollard, D., Alley, R. B., Velicogna, I., Gasson, E., Gomez, N., Sadai, S., Condron, A., Gilford, D. M., Ashe, E. L., Kopp, R. E., Li, D., and Dutton, A.: The Paris Climate Agreement and Future Sea-Level Rise from Antarctica, Nature, 593, 83–89, doi:10.1038/s41586-021-03427-0, 2021.

Dendy, S., Austermann, J., Creveling, J., and Mitrovica, J.: Sensitivity of Last Interglacial Sea-Level High Stands to Ice Sheet Configuration during Marine Isotope

Stage 6, Quaternary Science Reviews, 171, 234–244, doi:10.1016/j.quascirev.2017.06.013, 2017.

Denton, G. H. and Hughes, T. J.: Reconstructing the Antarctic Ice Sheet at the Last Glacial Maximum, Quaternary Science Reviews, 21, 193–202, doi:10.1016/S0277-3791(01)00090-7, 2002.

Düsterhus, A., Rovere, A., Carlson, A. E., Horton, B. P., Klemann, V., Tarasov, L., Barlow, N. L. M., Bradwell, T., Clark, J., Dutton, A., Gehrels, W. R., Hibbert, F. D., Hijma, M. P., Khan, N., Kopp, R. E., Sivan, D., and Törnqvist, T. E.: Palaeo-Sea-Level and Palaeo-Ice-Sheet Databases: Problems, Strategies, and Perspectives, Climate of the Past, 12, 911–921, doi:10.5194/cp-12-911-2016, 2016.

Dutton, A. and Lambeck, K.: Ice Volume and Sea Level During the Last Interglacial, Science, 337, 216–219, doi:10.1126/science.1205749, 2012.

Dutton, A., Carlson, A. E., Long, A. J., Milne, G. A., Clark, P. U., DeConto, R., Horton, B. P., Rahmstorf, S., and Raymo, M. E.: Sea-Level Rise Due to Polar Ice-Sheet Mass Loss during Past Warm Periods, Science, 349, aaa4019, doi:10.1126/science.aaa4019, 2015.

Dyer, B., Austermann, J., D'Andrea, W. J., Creel, R. C., Sandstrom, M. R., Cashman, M., Rovere, A., and Raymo, M. E.: Sea-Level Trends across The Bahamas Constrain Peak Last Interglacial Ice Melt, Proceedings of the National Academy of Sciences, 118, e2026839 118, doi:10.1073/pnas.2026839118, 2021.

Dziewonski, A. M. and Anderson, D. L.: Preliminary Reference Earth Model, Physics of the Earth and Planetary Interiors, 25, 297–356, doi:10.1016/0031-9201(81)90046-7, 1981.

Edwards, T. L., Brandon, M. A., Durand, G., Edwards, N. R., Golledge, N. R., Holden, P. B., Nias, I. J., Payne, A. J., Ritz, C., and Wernecke, A.: Revisiting Antarctic Ice Loss Due to Marine Ice-Cliff Instability, Nature, 566, 58–64, doi:10.1038/s41586-019-0901-4, 2019.

Edwards, T. L., Nowicki, S., Marzeion, B., Hock, R., Goelzer, H., Seroussi, H., Jourdain, N. C., Slater, D. A., Turner, F. E., Smith, C. J., McKenna, C. M., Simon, E., Abe-Ouchi, A., Gregory, J. M., Larour, E., Lipscomb, W. H., Payne, A. J., Shepherd, A., Agosta, C., Alexander, P., Albrecht, T., Anderson, B., Asay-Davis, X., Aschwanden, A., Barthel, A., Bliss, A., Calov, R., Chambers, C., Champollion, N., Choi, Y., Cullather, R., Cuzzone, J., Dumas, C., Felikson, D., Fettweis, X., Fujita, K., Galton-Fenzi, B. K., Gladstone, R., Golledge, N. R., Greve, R., Hattermann, T., Hoffman, M. J., Humbert, A., Huss, M., Huybrechts,

P., Immerzeel, W., Kleiner, T., Kraaijenbrink, P., Le clec'h, S., Lee, V., Leguy, G. R., Little, C. M., Lowry, D. P., Malles, J.-H., Martin, D. F., Maussion, F., Morlighem, M., O'Neill, J. F., Nias, I., Pattyn, F., Pelle, T., Price, S. F., Quiquet, A., Radić, V., Reese, R., Rounce, D. R., Rückamp, M., Sakai, A., Shafer, C., Schlegel, N.-J., Shannon, S., Smith, R. S., Straneo, F., Sun, S., Tarasov, L., Trusel, L. D., Van Breedam, J., van de Wal, R., van den Broeke, M., Winkelmann, R., Zekollari, H., Zhao, C., Zhang, T., and Zwinger, T.: Projected Land Ice Contributions to Twenty-First-Century Sea Level Rise, Nature, 593, 74–82, doi: 10.1038/s41586-021-03302-y, 2021.

Ehlers, J. and Gibbard, P. L.: Quaternary Glaciations - Extent and Chronology: Part I: Europe, Elsevier, 2004.

Ehlers, J., Grube, A., Stephan, H.-J., and Wansa, S.: Chapter 13 - Pleistocene Glaciations of North Germany—New Results, in: Developments in Quaternary Sciences, edited by Ehlers, J., Gibbard, P. L., and Hughes, P. D., vol. 15 of *Quaternary Glaciations - Extent and Chronology*, pp. 149–162, Elsevier, doi: 10.1016/B978-0-444-53447-7.00013-1, 2011.

Ekman, M.: The Changing Level of the Baltic Sea during 300 Years: A Clue to Understanding the Earth, Åland Islands: Summer Institute for Historical Geophysics, 2009.

Ely, J. C., Clark, C. D., Small, D., and Hindmarsh, R. C. A.: ATAT 1.1, the Automated Timing Accordance Tool for Comparing Ice-Sheet Model Output with Geochronological Data, Geoscientific Model Development, 12, 933–953, doi: 10.5194/gmd-12-933-2019, 2019.

Farrell, W. E. and Clark, J. A.: On Postglacial Sea Level, Geophysical Journal of the Royal Astronomical Society, 46, 647–667, doi:10.1111/j.1365-246X.1976.tb01252.x, 1976.

Fisher, D. A., Reeh, N., and Langley, K.: Objective Reconstructions of the Late Wisconsinan Laurentide Ice Sheet and the Significance of Deformable Beds, Géographie physique et Quaternaire, 39, 229–238, doi:10.7202/032605ar, 1985.

Flament, N., Gurnis, M., and Müller, R. D.: A Review of Observations and Models of Dynamic Topography, Lithosphere, 5, 189–210, doi:10.1130/L245.1, 2013.

Fogwill, C. J., Turney, C. S. M., Meissner, K. J., Golledge, N. R., Spence, P., Roberts, J. L., England, M. H., Jones, R. T., and Carter, L.: Testing the Sensitivity of the East Antarctic Ice Sheet to Southern Ocean Dynamics: Past Changes and Future Implications: SENSITIVITY OF THE EAST ANTARCTIC ICE SHEET

TO SOUTHERN OCEAN DYNAMICS, Journal of Quaternary Science, 29, 91–98, doi:10.1002/jqs.2683, 2014.

Fox-Kemper, B., Hewitt, H., Xiao, C., Aealgeirsdóttir, G., Drijfhout, S., Edwards, T., Golledge, N., Hemer, M., Kopp, R., Krinner, G., Mix, A., Notz, D., Nowicki, S., Nurhati, I., Ruiz, L., Sallée, J.-B., Slangen, ABA., and Yu, Y.: Ocean, Cryosphere and Sea Level Change., in: Climate Change 2021: The Physical Science Basis. Contribution of Working Group I to the Sixth Assessment Report of the Intergovernmental Panel on Climate Change, edited by Masson-Delmotte, V., Zhai, P., Pirani, A., Connors, SL., Péan, C., Berger, S., Caud, N., Chen, Y., Goldfarb, L., Gomis, MI., Huang, M., Leitzell, K., Lonnoy, E., Matthews, JBR., Maycock, TK., Waterfield, T., Yelekci, O., Yu, R., and Zhou, B., pp. 1211–1362, Cambridge University Press, Cambridge, United Kingdom and New York, NY, USA,, doi:10.1017/9781009157896.011, 2021.

Gandy, N., Gregoire, L. J., Ely, J. C., Clark, C. D., Hodgson, D. M., Lee, V., Bradwell, T., and Ivanovic, R. F.: Marine Ice Sheet Instability and Ice Shelf Buttressing of the Minch Ice Stream, Northwest Scotland, The Cryosphere, 12, 3635–3651, doi:10.5194/tc-12-3635-2018, 2018.

Gandy, N., Gregoire, L. J., Ely, J. C., Cornford, S. L., Clark, C. D., and Hodgson, D. M.: Exploring the Ingredients Required to Successfully Model the Placement, Generation, and Evolution of Ice Streams in the British-Irish Ice Sheet, Quaternary Science Reviews, 223, 105 915, doi:10.1016/j.quascirev.2019.105915, 2019.

Gandy, N., Gregoire, L. J., Ely, J. C., Cornford, S. L., Clark, C. D., and Hodgson, D. M.: Collapse of the Last Eurasian Ice Sheet in the North Sea Modulated by Combined Processes of Ice Flow, Surface Melt, and Marine Ice Sheet Instabilities, Journal of Geophysical Research: Earth Surface, 126, doi:10.1029/2020JF005755, 2021.

Gandy, N., Astfalck, L. C., Gregoire, L. J., Ivanovic, R. F., Patterson, V. L., Sherriff-Tadano, S., Smith, R. S., Williamson, D., and Rigby, R.: De-Tuning Albedo Parameters in a Coupled Climate Ice Sheet Model to Simulate the North American Ice Sheet at the Last Glacial Maximum, Journal of Geophysical Research: Earth Surface, 128, e2023JF007 250, doi:10.1029/2023JF007250, 2023.

Gilford, D. M., Ashe, E. L., DeConto, R. M., Kopp, R. E., Pollard, D., and Rovere, A.: Could the Last Interglacial Constrain Projections of Future Antarctic Ice Mass Loss and Sea-Level Rise?, Journal of Geophysical Research: Earth Surface, 125, doi:10.1029/2019JF005418, 2020.

Goelzer, H., Nowicki, S., Payne, A., Larour, E., Seroussi, H., Lipscomb, W. H., Gregory, J., Abe-Ouchi, A., Shepherd, A., Simon, E., Agosta, C., Alexander, P., Aschwanden, A., Barthel, A., Calov, R., Chambers, C., Choi, Y., Cuzzone, J., Dumas, C., Edwards, T., Felikson, D., Fettweis, X., Golledge, N. R., Greve, R., Humbert, A., Huybrechts, P., Le clec'h, S., Lee, V., Leguy, G., Little, C., Lowry, D. P., Morlighem, M., Nias, I., Quiquet, A., Rückamp, M., Schlegel, N.-J., Slater, D. A., Smith, R. S., Straneo, F., Tarasov, L., van de Wal, R., and van den Broeke, M.: The Future Sea-Level Contribution of the Greenland Ice Sheet: A Multi-Model Ensemble Study of ISMIP6, The Cryosphere, 14, 3071–3096, doi:10.5194/tc-14-3071-2020, 2020.

Golledge, N. R., Fogwill, C. J., Mackintosh, A. N., and Buckley, K. M.: Dynamics of the Last Glacial Maximum Antarctic Ice-Sheet and Its Response to Ocean Forcing, Proceedings of the National Academy of Sciences, 109, 16 052–16 056, doi:10.1073/pnas.1205385109, 2012.

Golledge, N. R., Clark, P. U., He, F., Dutton, A., Turney, C. S. M., Fogwill, C. J., Naish, T. R., Levy, R. H., McKay, R. M., Lowry, D. P., Bertler, N. a. N., Dunbar, G. B., and Carlson, A. E.: Retreat of the Antarctic Ice Sheet During the Last Interglaciation and Implications for Future Change, Geophysical Research Letters, 48, e2021GL094 513, doi:10.1029/2021GL094513, 2021.

Gomez, N., Mitrovica, J. X., Tamisiea, M. E., and Clark, P. U.: A New Projection of Sea Level Change in Response to Collapse of Marine Sectors of the Antarctic Ice Sheet, Geophysical Journal International, 180, 623–634, doi:10.1111/j.1365-246X.2009.04419.x, 2010.

Gomez, N., Pollard, D., and Holland, D.: Sea-Level Feedback Lowers Projections of Future Antarctic Ice-Sheet Mass Loss, Nature Communications, 6, 8798, doi:10.1038/ncomms9798, 2015.

Gowan, E. J.: Model of the Western Laurentide Ice Sheet, North America, Ph.D. thesis, The Australian National University, 2014.

Gowan, E. J., Tregoning, P., Purcell, A., Lea, J., Fransner, O. J., Noormets, R., and Dowdeswell, J. A.: ICESHEET 1.0: A Program to Produce Paleo-Ice Sheet Reconstructions with Minimal Assumptions, Geoscientific Model Development, 9, 1673–1682, doi:10.5194/gmd-9-1673-2016, 2016a.

Gowan, E. J., Tregoning, P., Purcell, A., Montillet, J.-P., and McClusky, S.: A Model of the Western Laurentide Ice Sheet, Using Observations of Glacial Isostatic Adjustment, Quaternary Science Reviews, 139, 1–16, doi:10.1016/j.quascirev.2016.03.003, 2016b.

Gowan, E. J., Zhang, X., Khosravi, S., Rovere, A., Stocchi, P., Hughes, A. L. C., Gyllencreutz, R., Mangerud, J., Svendsen, J.-I., and Lohmann, G.: A New Global Ice Sheet Reconstruction for the Past 80 000 Years, Nature Communications, 12, 1199, doi:10.1038/s41467-021-21469-w, 2021.

Gregoire, L. J., Otto-Bliesner, B., Valdes, P. J., and Ivanovic, R.: Abrupt Bølling Warming and Ice Saddle Collapse Contributions to the Meltwater Pulse 1a Rapid Sea Level Rise: North American MWP1a Contribution, Geophysical Research Letters, 43, 9130–9137, doi:10.1002/2016GL070356, 2016.

Gregory, J. M., White, N. J., Church, J. A., Bierkens, M. F. P., Box, J. E., van den Broeke, M. R., Cogley, J. G., Fettweis, X., Hanna, E., Huybrechts, P., Konikow, L. F., Leclercq, P. W., Marzeion, B., Oerlemans, J., Tamisiea, M. E., Wada, Y., Wake, L. M., and van de Wal, R. S. W.: Twentieth-Century Global-Mean Sea Level Rise: Is the Whole Greater than the Sum of the Parts?, Journal of Climate, 26, 4476–4499, doi:10.1175/JCLI-D-12-00319.1, 2013.

Gregory, J. M., Griffies, S. M., Hughes, C. W., Lowe, J. A., Church, J. A., Fukimori, I., Gomez, N., Kopp, R. E., Landerer, F., Cozannet, G. L., Ponte, R. M., Stammer, D., Tamisiea, M. E., and van de Wal, R. S. W.: Concepts and Terminology for Sea Level: Mean, Variability and Change, Both Local and Global, Surveys in Geophysics, 40, 1251–1289, doi:10.1007/s10712-019-09525-z, 2019.

Gung, Y., Panning, M., and Romanowicz, B.: Global Anisotropy and the Thickness of Continents, Nature, 422, 707–711, doi:10.1038/nature01559, 2003.

Harig, C. and Simons, F. J.: Accelerated West Antarctic Ice Mass Loss Continues to Outpace East Antarctic Gains, Earth and Planetary Science Letters, 415, 134–141, doi:10.1016/j.epsl.2015.01.029, 2015.

Hay, C., Mitrovica, J. X., Gomez, N., Creveling, J. R., Austermann, J., and E. Kopp, R.: The Sea-Level Fingerprints of Ice-Sheet Collapse during Interglacial Periods, Quaternary Science Reviews, 87, 60–69, doi:10.1016/j.quascirev.2013.12.022, 2014.

Hay, C. C., Morrow, E., Kopp, R. E., and Mitrovica, J. X.: Probabilistic Reanalysis of Twentieth-Century Sea-Level Rise, Nature, 517, 481–484, doi:10.1038/nature14093, 2015.

Haywood, A. M., Valdes, P. J., Aze, T., Barlow, N., Burke, A., Dolan, A. M., von der Heydt, A. S., Hill, D. J., Jamieson, S. S. R., Otto-Bliesner, B. L., Salzmann, U., Saupe, E., and Voss, J.: What Can Palaeoclimate Modelling Do for You?, Earth Systems and Environment, 3, 1–18, doi:10.1007/s41748-019-00093-1, 2019.

Heister, T., Dannberg, J., Gassmöller, R., and Bangerth, W.: High Accuracy Mantle Convection Simulation through Modern Numerical Methods – II: Realistic Models and Problems, Geophysical Journal International, 210, 833–851, doi: 10.1093/gji/ggx195, 2017.

Herold, N., Yin, Q. Z., Karami, M. P., and Berger, A.: Modelling the Climatic Diversity of the Warm Interglacials, Quaternary Science Reviews, 56, 126–141, doi:10.1016/j.quascirev.2012.08.020, 2012.

Hijma, M. P., Cohen, K. M., Roebroeks, W., Westerhoff, W. E., and Busschers, F. S.: Pleistocene Rhine–Thames Landscapes: Geological Background for Hominin Occupation of the Southern North Sea Region, Journal of Quaternary Science, 27, 17–39, doi:10.1002/jqs.1549, 2012.

Hindmarsh, R. C. A.: Consistent Generation of Ice-Streams via Thermo-Viscous Instabilities Modulated by Membrane Stresses, Geophysical Research Letters, 36, doi:10.1029/2008GL036877, 2009.

Horton, B. P., Kopp, R. E., Garner, A. J., Hay, C. C., Khan, N. S., Roy, K., and Shaw, T. A.: Mapping Sea-Level Change in Time, Space, and Probability, Annual Review of Environment and Resources, 43, 481–521, doi:10.1146/annurev-environ-102017-025826, 2018.

Hughes, A. L. C., Gyllencreutz, R., Lohne, Ø. S., Mangerud, J., and Svendsen, J. I.: The Last Eurasian Ice Sheets – a Chronological Database and Time-slice Reconstruction, DATED-1, Boreas, 45, 1–45, doi:10.1111/bor.12142, 2016.

Hughes, P. D., Ehlers, J., and Gibbard, P. L.: Quaternary Glaciations - Extent and Chronology, Part IV - a Closer Look: Introduction, in: Quaternary Glaciations - Extent and Chronology, Part IV - A Closer Look, pp. 1–14, Elsevier BV, 2011.

Huybrechts, P.: Glaciological Modelling of the Late Cenozoic East Antarctic Ice Sheet: Stability or Dynamism?, Geografiska Annaler: Series A, Physical Geography, 75, 221–238, doi:10.1080/04353676.1993.11880395, 1993.

Huybrechts, P. and de Wolde, J.: The Dynamic Response of the Greenland and Antarctic Ice Sheets to Multiple-Century Climatic Warming, Journal of Climate, 12, 2169–2188, doi:10.1175/1520-0442(1999)012<2169:TDROTG>2.0.CO;2, 1999.

Huybrechts, P., Letreguilly, A., and Reeh, N.: The Greenland Ice Sheet and Greenhouse Warming, Palaeogeography, Palaeoclimatology, Palaeoecology, 89, 399–412, doi:10.1016/0031-0182(91)90174-P, 1991.

IPCC: The Ocean and Cryosphere in a Changing Climate: Special Report of the Intergovernmental Panel on Climate Change, Cambridge University Press, Cambridge, doi:10.1017/9781009157964, 2022.

Ivanovic, R. F., Gregoire, L. J., Kageyama, M., Roche, D. M., Valdes, P. J., Burke, A., Drummond, R., Peltier, W. R., and Tarasov, L.: Transient Climate Simulations of the Deglaciation 21–9 Thousand Years before Present (Version 1) – PMIP4 Core Experiment Design and Boundary Conditions, Geoscientific Model Development, 9, 2563–2587, doi:10.5194/gmd-9-2563-2016, 2016.

Jamieson, T. F.: On the History of the Last Geological Changes in Scotland, Quarterly Journal of the Geological Society of London, 21, 161–204, doi:10.1144/GSL.JGS.1865.021.01-02.24, 1865.

Joon, B., Laban, C., and Van Der Meer, J. J. M.: The Saalian Glaciation in the Dutch Part of the North Sea, The Saalian glaciation in the dutch part of the North sea, 69, 151–158, 1990.

Kaufmann, G., Wu, P., and Ivins, E. R.: Lateral Viscosity Variations beneath Antarctica and Their Implications on Regional Rebound Motions and Seismotectonics, Journal of Geodynamics, 39, 165–181, doi:10.1016/j.jog.2004.08.009, 2005.

Kemp, A. C., Horton, B. P., Donnelly, J. P., Mann, M. E., Vermeer, M., and Rahmstorf, S.: Climate Related Sea-Level Variations over the Past Two Millennia, Proceedings of the National Academy of Sciences, 108, 11 017–11 022, doi:10.1073/pnas.1015619108, 2011.

Kendall, R. A., Mitrovica, J. X., and Milne, G. A.: On Post-Glacial Sea Level - II. Numerical Formulation and Comparative Results on Spherically Symmetric Models, Geophysical Journal International, 161, 679–706, doi:10.1111/j.1365-246X.2005.02553.x, 2005.

Khan, N. S., Horton, B. P., Engelhart, S., Rovere, A., Vacchi, M., Ashe, E. L., Törnqvist, T. E., Dutton, A., Hijma, M. P., and Shennan, I.: Inception of a Global Atlas of Sea Levels since the Last Glacial Maximum, Quaternary Science Reviews, 220, 359–371, doi:10.1016/j.quascirev.2019.07.016, 2019.

Kierulf, H. P., Steffen, H., Simpson, M. J. R., Lidberg, M., Wu, P., and Wang, H.: A GPS Velocity Field for Fennoscandia and a Consistent Comparison to Glacial Isostatic Adjustment Models, Journal of Geophysical Research: Solid Earth, 119, 6613–6629, doi:10.1002/2013JB010889, 2014.

Knight, P. G.: The Basal Ice Layer of Glaciers and Ice Sheets, Quaternary Science Reviews, 16, 975–993, doi:10.1016/S0277-3791(97)00033-4, 1997.

Kopp, R. E., Simons, F. J., Mitrovica, J. X., Maloof, A. C., and Oppenheimer, M.: Probabilistic Assessment of Sea Level during the Last Interglacial Stage, Nature, 462, 863–867, doi:10.1038/nature08686, 2009.

Kopp, R. E., Simons, F. J., Mitrovica, J. X., Maloof, A. C., and Oppenheimer, M.: A Probabilistic Assessment of Sea Level Variations within the Last Interglacial Stage, Geophysical Journal International, 193, 711–716, doi:10.1093/gji/ggt029, 2013.

Kopp, R. E., Hay, C. C., Little, C. M., and Mitrovica, J. X.: Geographic Variability of Sea-Level Change, Current Climate Change Reports, 1, 192–204, doi:10.1007/s40641-015-0015-5, 2015.

Laban, C.: The Pleistocene Glaciations in the Dutch Sector of the North Sea. A Synthesis of Sedimentary and Seismic Data, Ph.D. thesis, University of Amsterdam, 1995.

Lamb, R. M., Harding, R., Huuse, M., Stewart, M., and Brocklehurst, S. H.: The Early Quaternary North Sea Basin, Journal of the Geological Society, 175, 275–290, doi:10.1144/jgs2017-057, 2018.

Lambeck, K., Purcell, A., Funder, S., KJaeR, K. H., Larsen, E., and Moller, P.: Constraints on the Late Saalian to Early Middle Weichselian Ice Sheet of Eurasia from Field Data and Rebound Modelling, Boreas, 35, 539–575, doi:10.1080/03009480600781875, 2006.

Lambeck, K., Rouby, H., Purcell, A., Sun, Y., and Sambridge, M.: Sea Level and Global Ice Volumes from the Last Glacial Maximum to the Holocene, Proceedings of the National Academy of Sciences, 111, 15 296–15 303, doi:10.1073/pnas.1411762111, 2014.

Lambeck, K., Purcell, A., and Zhao, S.: The North American Late Wisconsin Ice Sheet and Mantle Viscosity from Glacial Rebound Analyses, Quaternary Science Reviews, 158, 172–210, doi:10.1016/j.quascirev.2016.11.033, 2017.

Lang, J., Lauer, T., and Winsemann, J.: New Age Constraints for the Saalian Glaciation in Northern Central Europe: Implications for the Extent of Ice Sheets and Related Proglacial Lake Systems, Quaternary Science Reviews, 180, 240–259, doi:10.1016/j.quascirev.2017.11.029, 2018.

Lauer, T. and Weiss, M.: Timing of the Saalian- and Elsterian Glacial Cycles and the Implications for Middle – Pleistocene Hominin Presence in Central Europe, Scientific Reports, 8, 5111, doi:10.1038/s41598-018-23541-w, 2018.

Letréguilly, A., Reeh, N., and Huybrechts, P.: The Greenland Ice Sheet through the Last Glacial-Interglacial Cycle, Palaeogeography, Palaeoclimatology, Palaeoecology, 90, 385–394, doi:10.1016/S0031-0182(12)80037-X, 1991.

Li, T., Khan, N. S., Baranskaya, A. V., Shaw, T. A., Peltier, W. R., Stuhne, G. R., Wu, P., and Horton, B. P.: Influence of 3D Earth Structure on Glacial Isostatic Adjustment in the Russian Arctic, Journal of Geophysical Research: Solid Earth, 127, e2021JB023 631, doi:10.1029/2021JB023631, 2022.

Li, Y., Napieralski, J., and Harbor, J.: A Revised Automated Proximity and Conformity Analysis Method to Compare Predicted and Observed Spatial Boundaries of Geologic Phenomena, Computers & Geosciences, 34, 1806–1814, doi: 10.1016/j.cageo.2008.01.003, 2008.

Lin, Y., Hibbert, F. D., Whitehouse, P. L., Woodroffe, S. A., Purcell, A., Shennan, I., and Bradley, S. L.: A Reconciled Solution of Meltwater Pulse 1A Sources Using Sea-Level Fingerprinting, Nature Communications, 12, 2015, doi:10.1038/s41467-021-21990-y, 2021.

Lister, A. M.: The Impact of Quaternary Ice Ages on Mammalian Evolution, Philosophical Transactions: Biological Sciences, 359, 221–241, 2004.

Long, A. J., Barlow, N. L. M., Busschers, F. S., Cohen, K. M., Gehrels, W. R., and Wake, L. M.: Near-Field Sea-Level Variability in Northwest Europe and Ice Sheet Stability during the Last Interglacial, Quaternary Science Reviews, 126, 26–40, doi:10.1016/j.quascirev.2015.08.021, 2015.

Love, A. E. H.: The Yielding of the Earth to Disturbing Forces, Proceedings of the Royal Society of London. Series A, Containing Papers of a Mathematical and Physical Character, 82, 73–88, doi:10.1098/rspa.1909.0008, 1909.

Love, R., Milne, G. A., Ajourlou, P., Parang, S., Tarasov, L., and Latychev, K.: A Fast Surrogate Model for 3D-Earth Glacial Isostatic Adjustment Using Tensorflow (v2.8.10) Artificial Neural Networks, EGUsphere, pp. 1–25, doi:10.5194/egusphere-2023-2491, 2023.

Lowry, D. P., Krapp, M., Golledge, N. R., and Alevropoulos-Borrill, A.: The Influence of Emissions Scenarios on Future Antarctic Ice Loss Is Unlikely to Emerge This Century, Communications Earth & Environment, 2, 1–14, doi:10.1038/s43247-021-00289-2, 2021.

Lunt, D. J., Abe-Ouchi, A., Bakker, P., Berger, A., Braconnot, P., Charbit, S., Fischer, N., Herold, N., Jungclaus, J. H., Khon, V. C., Krebs-Kanzow, U., Langebroek,

P. M., Lohmann, G., Nisancioglu, K. H., Otto-Bliesner, B. L., Park, W., Pfeiffer, M., Phipps, S. J., Prange, M., Rachmayani, R., Renssen, H., Rosenbloom, N., Schneider, B., Stone, E. J., Takahashi, K., Wei, W., Yin, Q., and Zhang, Z. S.: A Multi-Model Assessment of Last Interglacial Temperatures, Climate of the Past, 9, 699–717, doi:10.5194/cp-9-699-2013, 2013.

Lyell, C.: I. The Bakerian Lecture. —On the Proofs of a Gradual Rising of the Land Certain Parts of Sweden, Philosophical Transactions of the Royal Society of London, 125, 1–38, doi:10.1098/rstl.1835.0002, 1835.

Margold, M., Stokes, C. R., and Clark, C. D.: Ice Streams in the Laurentide Ice Sheet: Identification, Characteristics and Comparison to Modern Ice Sheets, Earth-Science Reviews, 143, 117–146, doi:10.1016/j.earscirev.2015.01.011, 2015.

Marriner, N., Flaux, C., Morhange, C., and Kaniewski, D.: Nile Delta's Sinking Past: Quantifiable Links with Holocene Compaction and Climate-Driven Changes in Sediment Supply?, Geology, 40, 1083–1086, doi:10.1130/G33209.1, 2012.

Marzeion, B., Hock, R., Anderson, B., Bliss, A., Champollion, N., Fujita, K., Huss, M., Immerzeel, W. W., Kraaijenbrink, P., Malles, J.-H., Maussion, F., Radić, V., Rounce, D. R., Sakai, A., Shannon, S., van de Wal, R., and Zekollari, H.: Partitioning the Uncertainty of Ensemble Projections of Global Glacier Mass Change, Earth's Future, 8, e2019EF001 470, doi:10.1029/2019EF001470, 2020.

Mckay, M. D., Beckman, R. J., and Conover, W. J.: A Comparison of Three Methods for Selecting Values of Input Variables in the Analysis of Output From a Computer Code, Technometrics, 42, 55–61, doi:10.1080/00401706.2000.10485979, 2000.

McKay, N. P., Overpeck, J. T., and Otto-Bliesner, B. L.: The Role of Ocean Thermal Expansion in Last Interglacial Sea Level Rise: THERMAL EXPANSION IN LIG SEA LEVEL RISE, Geophysical Research Letters, 38, n/a–n/a, doi:10.1029/2011GL048280, 2011.

Meese, D. A., Gow, A. J., Alley, R. B., Zielinski, G. A., Grootes, P. M., Ram, M., Taylor, K. C., Mayewski, P. A., and Bolzan, J. F.: The Greenland Ice Sheet Project 2 Depth-Age Scale: Methods and Results, Journal of Geophysical Research: Oceans, 102, 26 411–26 423, doi:10.1029/97JC00269, 1997.

Menviel, L., Capron, E., Govin, A., Dutton, A., Tarasov, L., Abe-Ouchi, A., Drysdale, R. N., Gibbard, P. L., Gregoire, L., He, F., Ivanovic, R. F., Kageyama, M., Kawamura, K., Landais, A., Otto-Bliesner, B. L., Oyabu, I., Tzedakis, P. C., Wolff, E., and Zhang, X.: The Penultimate Deglaciation: Protocol for Paleoclimate

Modelling Intercomparison Project (PMIP) Phase 4 Transient Numerical Simulations between 140 and 127 Ka, Version 1.0, Geoscientific Model Development, 12, 3649–3685, doi:10.5194/gmd-12-3649-2019, 2019.

Milne, G., Shennan, I., Youngs, B., Waugh, A., Teferle, F., Bingley, R., Bassett, S., Cuthbert-Brown, C., and Bradley, S.: Modelling the Glacial Isostatic Adjustment of the UK Region, Philosophical Transactions of the Royal Society A: Mathematical, Physical and Engineering Sciences, 364, 931–948, doi:10.1098/rsta.2006.1747, 2006.

Milne, G. A. and Mitrovica, J. X.: Postglacial Sea-Level Change on a Rotating Earth, Geophysical Journal International, 133, 1–19, doi:10.1046/j.1365-246X.1998.1331455.x, 1998.

Milne, G. A. and Mitrovica, J. X.: Searching for Eustasy in Deglacial Sea-Level Histories, Quaternary Science Reviews, 27, 2292–2302, doi:10.1016/j.quascirev.2008.08.018, 2008.

Milne, G. A., Gehrels, W. R., Hughes, C. W., and Tamisiea, M. E.: Identifying the Causes of Sea-Level Change, Nature Geoscience, 2, 471–478, doi:10.1038/ngeo544, 2009.

Mitrovica, J. X. and Milne, G. A.: On Post-Glacial Sea Level: I. General Theory, Geophysical Journal International, 154, 253–267, doi:10.1046/j.1365-246X.2003.01942.x, 2003.

Mitrovica, J. X. and Peltier, W.: A Comparison of Methods for the Inversion of Viscoelastic Relaxation Spectra, Geophysical Journal International, 108, 410–414, doi:10.1111/j.1365-246X.1992.tb04623.x, 1992.

Mitrovica, J. X. and Peltier, W. R.: On Postglacial Geoid Subsidence over the Equatorial Oceans, Journal of Geophysical Research: Solid Earth, 96, 20 053–20 071, doi:10.1029/91JB01284, 1991.

Mitrovica, J. X., Gomez, N., and Clark, P. U.: The Sea-Level Fingerprint of West Antarctic Collapse, Science, 323, 753–753, doi:10.1126/science.1166510, 2009.

Muhs, D. R., Schumann, R. R., Groves, L. T., Simmons, K. R., and Florian, C. R.: The Marine Terraces of Santa Cruz Island, California: Implications for Glacial Isostatic Adjustment Models of Last-Interglacial Sea-Level History, Geomorphology, 389, 107 826, doi:10.1016/j.geomorph.2021.107826, 2021.

Murphy, J., Booth, B., Collins, M., Harris, G., Sexton, D., and Webb, M.: A Methodology for Probabilistic Predictions of Regional Climate Change from Perturbed

Physics Ensembles, Philosophical Transactions of the Royal Society A: Mathematical, Physical and Engineering Sciences, 365, 1993–2028, doi:10.1098/rsta.2007.2077, 2007.

Nansen, F.: The Strandflat and Isostasy, Videnskapsselskapets Skrifter. 1., Matematisk-Naturhistorisk Klasse, Jacob Dybwad, Kristiania, Norway, 1921.

NEEM community members: Eemian Interglacial Reconstructed from a Greenland Folded Ice Core, Nature, 493, 489–494, doi:10.1038/nature11789, 2013.

Nye, J. F.: A Method of Calculating the Thicknesses of the Ice-Sheets, Nature, 169, 529–530, doi:10.1038/169529a0, 1952.

O'Leary, M. J., Hearty, P. J., Thompson, W. G., Raymo, M. E., Mitrovica, J. X., and Webster, J. M.: Ice Sheet Collapse Following a Prolonged Period of Stable Sea Level during the Last Interglacial, Nature Geoscience, 6, 796–800, doi:10.1038/ngeo1890, 2013.

Otto-Bliesner, B. L., Marshall, S. J., Overpeck, J. T., Miller, G. H., Hu, A., and CAPE Last Interglacial Project members: Simulating Arctic Climate Warmth and Icefield Retreat in the Last Interglaciation, Science, 311, 1751–1753, doi:10.1126/science.1120808, 2006.

Otto-Bliesner, B. L., Rosenbloom, N., Stone, E. J., McKay, N. P., Lunt, D. J., Brady, E. C., and Overpeck, J. T.: How Warm Was the Last Interglacial? New Model–Data Comparisons, Philosophical Transactions of the Royal Society A: Mathematical, Physical and Engineering Sciences, 371, 20130 097, doi:10.1098/rsta.2013.0097, 2013.

Overland, J. E., Wang, M., Walsh, J. E., and Stroeve, J. C.: Future Arctic Climate Changes: Adaptation and Mitigation Time Scales, Earth's Future, 2, 68–74, doi:10.1002/2013EF000162, 2014.

Pan, L., Powell, E. M., Latychev, K., Mitrovica, J. X., Creveling, J. R., Gomez, N., Hoggard, M. J., and Clark, P. U.: Rapid Postglacial Rebound Amplifies Global Sea Level Rise Following West Antarctic Ice Sheet Collapse, Science Advances, 7, eabf7787, doi:10.1126/sciadv.abf7787, 2021.

Pan, L., Milne, G. A., Latychev, K., Goldberg, S. L., Austermann, J., Hoggard, M. J., and Mitrovica, J. X.: The Influence of Lateral Earth Structure on Inferences of Global Ice Volume during the Last Glacial Maximum, Quaternary Science Reviews, 290, 107 644, doi:10.1016/j.quascirev.2022.107644, 2022.

Parker, W. S.: Ensemble Modeling, Uncertainty and Robust Predictions, WIREs Climate Change, 4, 213–223, doi:10.1002/wcc.220, 2013.

Pasyanos, M. E.: Lithospheric Thickness Modeled from Long-Period Surface Wave Dispersion, Tectonophysics, 481, 38–50, doi:10.1016/j.tecto.2009.02.023, 2010.

Patton, H., Hubbard, A., Andreassen, K., Winsborrow, M., and Stroeven, A. P.: The Build-up, Configuration, and Dynamical Sensitivity of the Eurasian Ice-Sheet Complex to Late Weichselian Climatic and Oceanic Forcing, Quaternary Science Reviews, 153, 97–121, doi:10.1016/j.quascirev.2016.10.009, 2016.

Patton, H., Hubbard, A., Andreassen, K., Auriac, A., Whitehouse, P. L., Stroeven, A. P., Shackleton, C., Winsborrow, M., Heyman, J., and Hall, A. M.: Deglaciation of the Eurasian Ice Sheet Complex, Quaternary Science Reviews, 169, 148–172, doi:10.1016/j.quascirev.2017.05.019, 2017.

Pattyn, F. and Morlighem, M.: The Uncertain Future of the Antarctic Ice Sheet, Science, 367, 1331–1335, doi:10.1126/science.aaz5487, 2020.

Pedoja, K., Husson, L., Regard, V., Cobbold, P. R., Ostanciaux, E., Johnson, M. E., Kershaw, S., Saillard, M., Martinod, J., Furgerot, L., Weill, P., and Delcaillau, B.: Relative Sea-Level Fall since the Last Interglacial Stage: Are Coasts Uplifting Worldwide?, Earth-Science Reviews, 108, 1–15, doi:10.1016/j.earscirev.2011.05.002, 2011.

Pedoja, K., Husson, L., Bezos, A., Pastier, A.-M., Imran, A. M., Arias-Ruiz, C., Sarr, A.-C., Elliot, M., Pons-Branchu, E., Nexer, M., Regard, V., Hafidz, A., Robert, X., Benoit, L., Delcaillau, B., Authemayou, C., Dumoulin, C., and Choblet, G.: On the Long-Lasting Sequences of Coral Reef Terraces from SE Sulawesi (Indonesia): Distribution, Formation, and Global Significance, Quaternary Science Reviews, 188, 37–57, doi:10.1016/j.quascirev.2018.03.033, 2018.

Peltier, W.: The Impulse Response of a Maxwell Earth, Reviews of Geophysics, 12, 649, doi:10.1029/RG012i004p00649, 1974.

Peltier, W.: Mantle Viscosity and Ice-Age Ice Sheet Topography, Science, 273, 1359–1364, doi:10.1126/science.273.5280.1359, 1996.

Peltier, W.: GLOBAL GLACIAL ISOSTASY AND THE SURFACE OF THE ICE-AGE EARTH: The ICE-5G (VM2) Model and GRACE, Annual Review of Earth and Planetary Sciences, 32, 111–149, doi:10.1146/annurev.earth.32.082503.144359, 2004.

Peltier, W. and Drummond, R.: Rheological Stratification of the Lithosphere: A Direct Inference Based upon the Geodetically Observed Pattern of the Glacial Isostatic Adjustment of the North American Continent, Geophysical Research Letters, 35, L16 314, doi:10.1029/2008GL034586, 2008.

Peltier, W., Argus, D. F., and Drummond, R.: Space Geodesy Constrains Ice Age Terminal Deglaciation: The Global ICE-6G_C (VM5a) Model: Global Glacial Isostatic Adjustment, Journal of Geophysical Research: Solid Earth, 120, 450–487, doi:10.1002/2014JB011176, 2015.

Peltier, W. R.: Closure of the Budget of Global Sea Level Rise over the GRACE Era: The Importance and Magnitudes of the Required Corrections for Global Glacial Isostatic Adjustment, Quaternary Science Reviews, 28, 1658–1674, doi: 10.1016/j.quascirev.2009.04.004, 2009.

Persits, F., Ulmishek, G. F., and Steinshouer, D.: Maps Showing Geology, Oil and Gas Fields and Geologic Provinces of the Former Soviet Union, Report 97-470E, U.S. Geological Survey, Reston, VA, doi:10.3133/ofr97470E, 1997.

Peyaud, V.: Rôle de la dynamique des calottes glaciaires dans les grands changements climatiques des périodes glaciaires-interglaciaires., Ph.D. thesis, Université Joseph-Fourier-Grenoble I, 2006.

Pianosi, F., Beven, K., Freer, J., Hall, J. W., Rougier, J., Stephenson, D. B., and Wagener, T.: Sensitivity Analysis of Environmental Models: A Systematic Review with Practical Workflow, Environmental Modelling & Software, 79, 214–232, doi: 10.1016/j.envsoft.2016.02.008, 2016.

Pollard, D., Chang, W., Haran, M., Applegate, P., and DeConto, R.: Large Ensemble Modeling of the Last Deglacial Retreat of the West Antarctic Ice Sheet: Comparison of Simple and Advanced Statistical Techniques, Geoscientific Model Development, 9, 1697–1723, doi:10.5194/gmd-9-1697-2016, 2016.

Pollard, O. G., Barlow, N. L. M., Gregoire, L. J., Gomez, N., Cartelle, V., Ely, J. C., and Astfalck, L. C.: Quantifying the Uncertainty in the Eurasian Ice-Sheet Geometry at the Penultimate Glacial Maximum (Marine Isotope Stage 6), The Cryosphere, 17, 4751–4777, doi:10.5194/tc-17-4751-2023, 2023.

Powell, E., Gomez, N., Hay, C., Latychev, K., and Mitrovica, J. X.: Viscous Effects in the Solid Earth Response to Modern Antarctic Ice Mass Flux: Implications for Geodetic Studies of WAIS Stability in a Warming World, Journal of Climate, 33, 443–459, doi:10.1175/JCLI-D-19-0479.1, 2020.

Pukelsheim, F.: The Three Sigma Rule, The American Statistician, 2012.

Rasmussen, C. E. and Williams, C. K.: Gaussian Processes for Machine Learning, vol. 1, Springer, 2006.

Reeh, N.: A Plasticity Theory Approach to the Steady-State Shape of a Three-Dimensional Ice Sheet, Journal of Glaciology, 28, 431–455, doi:10.3189/S0022143000005049, 1982.

Rignot, E., Jacobs, S., Mouginot, J., and Scheuchl, B.: Ice-Shelf Melting Around Antarctica, Science, 341, 266–270, doi:10.1126/science.1235798, 2013.

Ritz, C., Edwards, T. L., Durand, G., Payne, A. J., Peyaud, V., and Hindmarsh, R. C. A.: Potential Sea-Level Rise from Antarctic Ice-Sheet Instability Constrained by Observations, Nature, 528, 115–118, doi:10.1038/nature16147, 2015.

Ritzwoller, M. H., Shapiro, N. M., Levshin, A. L., and Leahy, G. M.: Crustal and Upper Mantle Structure beneath Antarctica and Surrounding Oceans, Journal of Geophysical Research: Solid Earth, 106, 30 645–30 670, doi:10.1029/2001JB000179, 2001.

Riva, R. E. M., Gunter, B. C., Urban, T. J., Vermeersen, B. L. A., Lindenbergh, R. C., Helsen, M. M., Bamber, J. L., van de Wal, R. S. W., van den Broeke, M. R., and Schutz, B. E.: Glacial Isostatic Adjustment over Antarctica from Combined ICESat and GRACE Satellite Data, Earth and Planetary Science Letters, 288, 516–523, doi:10.1016/j.epsl.2009.10.013, 2009.

Robel, A. A., Roe, G. H., and Haseloff, M.: Response of Marine-Terminating Glaciers to Forcing: Time Scales, Sensitivities, Instabilities, and Stochastic Dynamics, Journal of Geophysical Research: Earth Surface, 123, 2205–2227, doi:10.1029/2018JF004709, 2018.

Robel, A. A., Seroussi, H., and Roe, G. H.: Marine Ice Sheet Instability Amplifies and Skews Uncertainty in Projections of Future Sea-Level Rise, Proceedings of the National Academy of Sciences, 116, 14 887–14 892, doi:10.1073/pnas.1904822116, 2019.

Rohling, E. J., Grant, K., Hemleben, Ch., Siddall, M., Hoogakker, B. A. A., Bolshaw, M., and Kucera, M.: High Rates of Sea-Level Rise during the Last Interglacial Period, Nature Geoscience, 1, 38–42, doi:10.1038/ngeo.2007.28, 2008.

Rohling, E. J., Hibbert, F. D., Williams, F. H., Grant, K. M., Marino, G., Foster, G. L., Hennekam, R., de Lange, G. J., Roberts, A. P., Yu, J., Webster, J. M., and Yokoyama, Y.: Differences between the Last Two Glacial Maxima and Implications

for Ice-Sheet, δ18O, and Sea-Level Reconstructions, Quaternary Science Reviews, 176, 1–28, doi:10.1016/j.quascirev.2017.09.009, 2017.

Rohling, E. J., Hibbert, F. D., Grant, K. M., Galaasen, E. V., Irvalı, N., Kleiven, H. F., Marino, G., Ninnemann, U., Roberts, A. P., Rosenthal, Y., Schulz, H., Williams, F. H., and Yu, J.: Asynchronous Antarctic and Greenland Ice-Volume Contributions to the Last Interglacial Sea-Level Highstand, Nature Communications, 10, 5040, doi:10.1038/s41467-019-12874-3, 2019.

Romé, Y. M., Ivanovic, R. F., Gregoire, L. J., Sherriff-Tadano, S., and Valdes, P. J.: Millennial-Scale Climate Oscillations Triggered by Deglacial Meltwater Discharge in Last Glacial Maximum Simulations, Paleoceanography and Paleoclimatology, 37, e2022PA004 451, doi:10.1029/2022PA004451, 2022.

Rovere, A., Raymo, M. E., Vacchi, M., Lorscheid, T., Stocchi, P., Gómez-Pujol, L., Harris, D. L., Casella, E., O'Leary, M. J., and Hearty, P. J.: The Analysis of Last Interglacial (MIS 5e) Relative Sea-Level Indicators: Reconstructing Sea-Level in a Warmer World, Earth-Science Reviews, 159, 404–427, doi:10.1016/j.earscirev.2016.06.006, 2016.

Rovere, A., Pico, T., Richards, F., O'Leary, M. J., Mitrovica, J. X., Goodwin, I. D., Austermann, J., and Latychev, K.: Influence of Reef Isostasy, Dynamic Topography, and Glacial Isostatic Adjustment on Sea-Level Records in Northeastern Australia, Communications Earth & Environment, 4, 1–12, doi:10.1038/s43247-023-00967-3, 2023a.

Rovere, A., Ryan, D. D., Vacchi, M., Dutton, A., Simms, A. R., and Murray-Wallace, C. V.: The World Atlas of Last Interglacial Shorelines (Version 1.0), Earth System Science Data, 15, 1–23, doi:10.5194/essd-15-1-2023, 2023b.

Rutt, I. C., Hagdorn, M., Hulton, N. R. J., and Payne, A. J.: The Glimmer Community Ice Sheet Model, Journal of Geophysical Research: Earth Surface, 114, doi:10.1029/2008JF001015, 2009.

Sainz de Murieta, E., Cunha, P. P., Cearreta, A., Murray, A. S., and Buylaert, J.-P.: The Oyambre Coastal Terrace: A Detailed Sedimentary Record of the Last Interglacial Stage in Northern Iberia (Cantabrian Coast, Spain), Journal of Quaternary Science, 36, 570–585, doi:10.1002/jqs.3317, 2021.

Saltelli, A., Ratto, M., Andres, T., Campolongo, F., Cariboni, J., Gatelli, D., Saisana, M., and Tarantola, S.: Global Sensitivity Analysis. The Primer, Wiley, 1 edn., doi:10.1002/9780470725184, 2007.

Saltelli, A., Annoni, P., Azzini, I., Campolongo, F., Ratto, M., and Tarantola, S.: Variance Based Sensitivity Analysis of Model Output. Design and Estimator for the Total Sensitivity Index, Computer Physics Communications, 181, 259–270, doi:10.1016/j.cpc.2009.09.018, 2010.

Schaffer, J., Timmermann, R., Arndt, J. E., Kristensen, S. S., Mayer, C., Morlighem, M., and Steinhage, D.: A Global, High-Resolution Data Set of Ice Sheet Topography, Cavity Geometry, and Ocean Bathymetry, Earth System Science Data, 8, 543–557, doi:10.5194/essd-8-543-2016, 2016.

Seroussi, H., Nowicki, S., Payne, A. J., Goelzer, H., Lipscomb, W. H., Abe-Ouchi, A., Agosta, C., Albrecht, T., Asay-Davis, X., Barthel, A., Calov, R., Cullather, R., Dumas, C., Galton-Fenzi, B. K., Gladstone, R., Golledge, N. R., Gregory, J. M., Greve, R., Hattermann, T., Hoffman, M. J., Humbert, A., Huybrechts, P., Jourdain, N. C., Kleiner, T., Larour, E., Leguy, G. R., Lowry, D. P., Little, C. M., Morlighem, M., Pattyn, F., Pelle, T., Price, S. F., Quiquet, A., Reese, R., Schlegel, N.-J., Shepherd, A., Simon, E., Smith, R. S., Straneo, F., Sun, S., Trusel, L. D., Van Breedam, J., van de Wal, R. S. W., Winkelmann, R., Zhao, C., Zhang, T., and Zwinger, T.: ISMIP6 Antarctica: A Multi-Model Ensemble of the Antarctic Ice Sheet Evolution over the 21st Century, The Cryosphere, 14, 3033–3070, doi:10.5194/tc-14-3033-2020, 2020.

Shakun, J. D., Lea, D. W., Lisiecki, L. E., and Raymo, M. E.: An 800-Kyr Record of Global Surface Ocean δ 18 O and Implications for Ice Volume-Temperature Coupling, Earth and Planetary Science Letters, 426, 58–68, doi:10.1016/j.epsl.2015.05.042, 2015.

Shennan, I.: Handbook of Sea-Level Research, in: Handbook of Sea-Level Research, chap. 2, pp. 3–25, John Wiley & Sons, Ltd, doi:10.1002/9781118452547.ch2, 2015.

Shennan, I., Bradley, S., Milne, G., Brooks, A., Bassett, S., and Hamilton, S.: Relative Sea-Level Changes, Glacial Isostatic Modelling and Ice-Sheet Reconstructions from the British Isles since the Last Glacial Maximum, Journal of Quaternary Science, 21, 585–599, doi:10.1002/jqs.1049, 2006.

Shennan, I., Bradley, S. L., and Edwards, R.: Relative Sea-Level Changes and Crustal Movements in Britain and Ireland since the Last Glacial Maximum, Quaternary Science Reviews, 188, 143–159, doi:10.1016/j.quascirev.2018.03.031, 2018.

Shi, X., Werner, M., Wang, Q., Yang, H., and Lohmann, G.: Simulated Mid-Holocene and Last Interglacial Climate Using Two Generations of AWI-ESM, Journal of Climate, 35, 7811–7831, doi:10.1175/JCLI-D-22-0354.1, 2022.

Shik, S. M.: A Modern Approach to the Neopleistocene Stratigraphy and Paleogeography of Central European Russia, Stratigraphy and Geological Correlation, 22, 219–230, doi:10.1134/S0869593814020075, 2014.

Simms, A. R., Rood, D. H., and Rockwell, T. K.: Correcting MIS5e and 5a Sea-Level Estimates for Tectonic Uplift, an Example from Southern California, Quaternary Science Reviews, 248, 106 571, doi:10.1016/j.quascirev.2020.106571, 2020.

Simpson, M. J. R., Milne, G. A., Huybrechts, P., and Long, A. J.: Calibrating a Glaciological Model of the Greenland Ice Sheet from the Last Glacial Maximum to Present-Day Using Field Observations of Relative Sea Level and Ice Extent, Quaternary Science Reviews, 28, 1631–1657, doi:10.1016/j.quascirev.2009.03.004, 2009.

Smith, R. C.: Uncertainty Quantification: Theory, Implementation, and Applications, SIAM, 2013.

Sobol', I. M.: On Sensitivity Estimation for Nonlinear Mathematical Models, Matematicheskoe modelirovanie, 2, 112–118, 1990.

Sokołowski, R. J., Molodkov, A., Hrynowiecka, A., Woronko, B., and Zieliński, P.: The Role of an Ice-Sheet, Glacioisostatic Movements and Climate in the Transformation of Middle Pleistocene Depositional Systems: A Case Study from the Reda Site, Northern Poland, Geografiska Annaler: Series A, Physical Geography, 103, 223–258, doi:10.1080/04353676.2021.1926241, 2021.

Sommers, A. N., Otto-Bliesner, B. L., Lipscomb, W. H., Lofverstrom, M., Shafer, S. L., Bartlein, P. J., Brady, E. C., Kluzek, E., Leguy, G., Thayer-Calder, K., and Tomas, R. A.: Retreat and Regrowth of the Greenland Ice Sheet During the Last Interglacial as Simulated by the CESM2-CISM2 Coupled Climate–Ice Sheet Model, Paleoceanography and Paleoclimatology, 36, e2021PA004 272, doi:10.1029/2021PA004272, 2021.

Spada, G. and Stocchi, P.: SELEN: A Fortran 90 Program for Solving the "Sea-Level Equation", Computers & Geosciences, 33, 538–562, doi:10.1016/j.cageo.2006.08.006, 2007.

Stephenson, S. N., White, N. J., Li, T., and Robinson, L. F.: Disentangling Interglacial Sea Level and Global Dynamic Topography: Analysis of Madagascar, Earth and Planetary Science Letters, 519, 61–69, doi:10.1016/j.epsl.2019.04.029, 2019.

Stokes, C. R. and Clark, C. D.: Geomorphological Criteria for Identifying Pleistocene Ice Streams, Annals of Glaciology, 28, 67–74, doi:10.3189/172756499781821625, 1999.

Stokes, C. R. and Clark, C. D.: Palaeo-Ice Streams, Quaternary Science Reviews, 20, 1437–1457, doi:10.1016/S0277-3791(01)00003-8, 2001.

Stokes, C. R., Tarasov, L., Blomdin, R., Cronin, T. M., Fisher, T. G., Gyllencreutz, R., Hättestrand, C., Heyman, J., Hindmarsh, R. C. A., Hughes, A. L. C., Jakobsson, M., Kirchner, N., Livingstone, S. J., Margold, M., Murton, J. B., Noormets, R., Peltier, W. R., Peteet, D. M., Piper, D. J. W., Preusser, F., Renssen, H., Roberts, D. H., Roche, D. M., Saint-Ange, F., Stroeven, A. P., and Teller, J. T.: On the Reconstruction of Palaeo-Ice Sheets: Recent Advances and Future Challenges, Quaternary Science Reviews, 125, 15–49, doi:10.1016/j.quascirev.2015.07.016, 2015.

Stone, E. J., Lunt, D. J., Annan, J. D., and Hargreaves, J. C.: Quantification of the Greenland Ice Sheet Contribution to Last Interglacial Sea Level Rise, Climate of the Past, 9, 621–639, doi:10.5194/cp-9-621-2013, 2013.

Stuhne, G. R. and Peltier, W.: Reconciling the ICE-6G_C Reconstruction of Glacial Chronology with Ice Sheet Dynamics: The Cases of Greenland and Antarctica: ICE-6G_C and ICE-Sheet Dynamics, Journal of Geophysical Research: Earth Surface, 120, 1841–1865, doi:10.1002/2015JF003580, 2015.

Stuhne, G. R. and Peltier, W.: Assimilating the ICE-6G_C Reconstruction of the Latest Quaternary Ice Age Cycle Into Numerical Simulations of the Laurentide and Fennoscandian Ice Sheets, Journal of Geophysical Research: Earth Surface, 122, 2324–2347, doi:10.1002/2017JF004359, 2017.

Sun, S., Pattyn, F., Simon, E. G., Albrecht, T., Cornford, S., Calov, R., Dumas, C., Gillet-Chaulet, F., Goelzer, H., Golledge, N. R., Greve, R., Hoffman, M. J., Humbert, A., Kazmierczak, E., Kleiner, T., Leguy, G. R., Lipscomb, W. H., Martin, D., Morlighem, M., Nowicki, S., Pollard, D., Price, S., Quiquet, A., Seroussi, H., Schlemm, T., Sutter, J., van de Wal, R. S. W., Winkelmann, R., and Zhang, T.: Antarctic Ice Sheet Response to Sudden and Sustained Ice-Shelf Collapse (ABUMIP), Journal of Glaciology, 66, 891–904, doi:10.1017/jog.2020.67, 2020.

Svendsen, J. I., Alexanderson, H., Astakhov, V. I., Demidov, I., Dowdeswell, J. A., Funder, S., Gataullin, V., Henriksen, M., Hjort, C., Houmark-Nielsen, M., Hubberten, H. W., Ingólfsson, Ó., Jakobsson, M., Kjær, K. H., Larsen, E., Lokrantz, H., Lunkka, J. P., Lysså, A., Mangerud, J., Matiouchkov, A., Murray, A., Möller, P., Niessen, F., Nikolskaya, O., Polyak, L., Saarnisto, M., Siegert, C., Siegert, M. J., Spielhagen, R. F., and Stein, R.: Late Quaternary Ice Sheet History of Northern Eurasia, Quaternary Science Reviews, 23, 1229–1271, doi:10.1016/j.quascirev.2003.12.008, 2004.

Tamisiea, M. E., Hughes, C. W., Williams, S. D. P., and Bingley, R. M.: Sea Level: Measuring the Bounding Surfaces of the Ocean, Philosophical Transactions. Series A, Mathematical, Physical, and Engineering Sciences, 372, 20130 336, doi: 10.1098/rsta.2013.0336, 2014.

Tarasov, L. and Peltier, W.: Greenland Glacial History and Local Geodynamic Consequences, Geophysical Journal International, 150, 198–229, doi:10.1046/j.1365-246X.2002.01702.x, 2002.

Tarasov, L., Dyke, A. S., Neal, R. M., and Peltier, W.: A Data-Calibrated Distribution of Deglacial Chronologies for the North American Ice Complex from Glaciological Modeling, Earth and Planetary Science Letters, 315–316, 30–40, doi:10.1016/j.epsl.2011.09.010, 2012.

Teatini, P., Tosi, L., and Strozzi, T.: Quantitative Evidence That Compaction of Holocene Sediments Drives the Present Land Subsidence of the Po Delta, Italy, Journal of Geophysical Research: Solid Earth, 116, doi:10.1029/2010JB008122, 2011.

Toucanne, S., Zaragosi, S., Bourillet, J., Cremer, M., Eynaud, F., Van Vliet-Lanoë, B., Penaud, A., Fontanier, C., Turon, J., and Cortijo, E.: Timing of Massive 'Fleuve Manche' Discharges over the Last 350kyr: Insights into the European Ice-Sheet Oscillations and the European Drainage Network from MIS 10 to 2, Quaternary Science Reviews, 28, 1238–1256, doi:10.1016/j.quascirev.2009.01.006, 2009.

Tsai, V. C., Stewart, A. L., and Thompson, A. F.: Marine Ice-Sheet Profiles and Stability under Coulomb Basal Conditions, Journal of Glaciology, 61, 205–215, doi:10.3189/2015JoG14J221, 2015.

Turney, C. S. and Jones, R. T.: Does the Agulhas Current Amplify Global Temperatures during Super-Interglacials?, Journal of Quaternary Science, 25, 839–843, doi:10.1002/jqs.1423, 2010.

Turney, C. S. M., Fogwill, C. J., Golledge, N. R., McKay, N. P., van Sebille, E., Jones, R. T., Etheridge, D., Rubino, M., Thornton, D. P., Davies, S. M., Ramsey, C. B., Thomas, Z. A., Bird, M. I., Munksgaard, N. C., Kohno, M., Woodward, J., Winter, K., Weyrich, L. S., Rootes, C. M., Millman, H., Albert, P. G., Rivera, A., van Ommen, T., Curran, M., Moy, A., Rahmstorf, S., Kawamura, K., Hillenbrand, C.-D., Weber, M. E., Manning, C. J., Young, J., and Cooper, A.: Early Last Interglacial Ocean Warming Drove Substantial Ice Mass Loss from Antarctica, Proceedings of the National Academy of Sciences, 117, 3996–4006, doi:10.1073/pnas.1902469117, 2020.

van der Wal, W., Whitehouse, P. L., and Schrama, E. J. O.: Effect of GIA Models with 3D Composite Mantle Viscosity on GRACE Mass Balance Estimates for Antarctica, Earth and Planetary Science Letters, 414, 134–143, doi:10.1016/j.epsl.2015.01.001, 2015.

Vernon, I., Owen, J., Aylett-Bullock, J., Cuesta-Lazaro, C., Frawley, J., Quera-Bofarull, A., Sedgewick, A., Shi, D., Truong, H., Turner, M., Walker, J., Caulfield, T., Fong, K., and Krauss, F.: Bayesian Emulation and History Matching of JUNE, Philosophical Transactions of the Royal Society A: Mathematical, Physical and Engineering Sciences, 380, 20220 039, doi:10.1098/rsta.2022.0039, 2022.

Waelbroeck, C., Labeyrie, L., Michel, E., Duplessy, J., McManus, J., Lambeck, K., Balbon, E., and Labracherie, M.: Sea-Level and Deep Water Temperature Changes Derived from Benthic Foraminifera Isotopic Records, Quaternary Science Reviews, 21, 295–305, doi:10.1016/S0277-3791(01)00101-9, 2002.

Wahr, J., Molenaar, M., and Bryan, F.: Time Variability of the Earth's Gravity Field: Hydrological and Oceanic Effects and Their Possible Detection Using GRACE, Journal of Geophysical Research: Solid Earth, 103, 30 205–30 229, doi:10.1029/98JB02844, 1998.

Waller, R. I.: The Influence of Basal Processes on the Dynamic Behaviour of Cold-Based Glaciers, Quaternary International, 86, 117–128, doi:10.1016/S1040-6182(01)00054-4, 2001.

Weertman, J.: On the Sliding of Glaciers, Journal of Glaciology, 3, 33–38, doi:10.3189/S0022143000024709, 1957.

Wekerle, C., Colleoni, F., Näslund, J.-O., Brandefelt, J., and Masina, S.: Numerical Reconstructions of the Penultimate Glacial Maximum Northern Hemisphere Ice Sheets: Sensitivity to Climate Forcing and Model Parameters, Journal of Glaciology, 62, 607–622, doi:10.1017/jog.2016.45, 2016.

Whitehouse, P. L.: Glacial Isostatic Adjustment Modelling: Historical Perspectives, Recent Advances, and Future Directions, Earth Surface Dynamics, 6, 401–429, doi:10.5194/esurf-6-401-2018, 2018.

Williamson, D.: Exploratory Ensemble Designs for Environmental Models Using K-Extended Latin Hypercubes, Environmetrics, 26, 268–283, doi:10.1002/env.2335, 2015.

Williamson, D., Goldstein, M., Allison, L., Blaker, A., Challenor, P., Jackson, L., and Yamazaki, K.: History Matching for Exploring and Reducing Climate Model

Parameter Space Using Observations and a Large Perturbed Physics Ensemble, Climate Dynamics, 41, 1703–1729, doi:10.1007/s00382-013-1896-4, 2013.

Williamson, D., Blaker, A. T., Hampton, C., and Salter, J.: Identifying and Removing Structural Biases in Climate Models with History Matching, Climate Dynamics, 45, 1299–1324, doi:10.1007/s00382-014-2378-z, 2015.

Williamson, D. B., Blaker, A. T., and Sinha, B.: Tuning without Over-Tuning: Parametric Uncertainty Quantification for the NEMO Ocean Model, Geoscientific Model Development, 10, 1789–1816, doi:10.5194/gmd-10-1789-2017, 2017.

Wolstencroft, M., Shen, Z., Törnqvist, T. E., Milne, G. A., and Kulp, M.: Understanding Subsidence in the Mississippi Delta Region Due to Sediment, Ice, and Ocean Loading: Insights from Geophysical Modeling, Journal of Geophysical Research: Solid Earth, 119, 3838–3856, doi:10.1002/2013JB010928, 2014.

Woodward, R. S.: On the Form and Position of the Sea Level, Tech. rep., Washington: Government Printing Office, 1888.

Woodworth, P. L., Melet, A., Marcos, M., Ray, R. D., Wöppelmann, G., Sasaki, Y. N., Cirano, M., Hibbert, A., Huthnance, J. M., Monserrat, S., and Merrifield, M. A.: Forcing Factors Affecting Sea Level Changes at the Coast, Surveys in Geophysics, 40, 1351–1397, doi:10.1007/s10712-019-09531-1, 2019.

Yau, A. M., Bender, M. L., Robinson, A., and Brook, E. J.: Reconstructing the Last Interglacial at Summit, Greenland: Insights from GISP2, Proceedings of the National Academy of Sciences, 113, 9710–9715, doi:10.1073/pnas.1524766113, 2016.

Yin, Q. and Berger, A.: Interglacial Analogues of the Holocene and Its Natural near Future, Quaternary Science Reviews, 120, 28–46, doi:10.1016/j.quascirev.2015.04.008, 2015.

Yokoyama, Y. and Purcell, A.: On the Geophysical Processes Impacting Palaeo-Sea-Level Observations, Geoscience Letters, 8, 13, doi:10.1186/s40562-021-00184-w, 2021.

Yousefi, M., Wan, J., Pan, L., Gomez, N., Latychev, K., Mitrovica, J. X., Pollard, D., and DeConto, R. M.: The Influence of the Solid Earth on the Contribution of Marine Sections of the Antarctic Ice Sheet to Future Sea-Level Change, Geophysical Research Letters, 49, e2021GL097525, doi:10.1029/2021GL097525, 2022.

Zagwijn, W. H.: Sea-Level Changes in the Netherlands during the Eemian, Sea-level changes in the Netherlands during the Eemian, 62, 437–450, 1983.

Zhao, H. and Kowalski, J.: Topographic Uncertainty Quantification for Flow-like Landslide Models via Stochastic Simulations, Natural Hazards and Earth System Sciences, 20, 1441–1461, doi:10.5194/nhess-20-1441-2020, 2020.

Zhou, Y. and McManus, J.: Extensive Evidence for a Last Interglacial Laurentide Outburst (LILO) Event, Geology, 50, 934–938, doi:10.1130/G49956.1, 2022.

Zoccarato, C., Minderhoud, P. S. J., and Teatini, P.: The Role of Sedimentation and Natural Compaction in a Prograding Delta: Insights from the Mega Mekong Delta, Vietnam, Scientific Reports, 8, 11 437, doi:10.1038/s41598-018-29734-7, 2018.